University of Nottingham
UK | CHINA | MALAYSIA

Investigating challenges in producing adherent Boron Nitride PVD coatings for tooling and additive manufacturing applications

Timothy P. Cooper, MEng. (Hons)

Thesis submitted to the University of Nottingham for the degree of Doctor of Philosophy

Supervisors: Prof Adam Clare, Prof David Grant & Dr James Murray

September 2023

Declaration

I, Timothy P. Cooper, hereby certify that this thesis has been completed by myself and that it is a record of my own work over the period from October 2018 to September 2023.

Except where specific reference is made to other sources or collaborators, the work presented in this thesis is the original work of the author. It has not been submitted, in whole or part for any other degree.

Timothy P. Cooper

Acknowledgements

This PhD has been a long and hard journey through many upsets and troubles, and I can hardly accept that I have made it this far, but I am glad to have pushed through and reached this point, both for the sense of achievement of making it though, but also for the relief that the worst is over.

I could not have made it this far without the guidance of my supervisors Prof Adam Clare, Prof David Grant, and Dr James Murray. My thanks to them for giving me this opportunity and putting up with me over these years.

I would also like to thank the people that I have worked alongside over the years, Matt Wadge and Zakhar Kudrynskyi, your friendship, encouragement and knowledge have been so appreciated, and I look forward to working with you in the future.

To my family, you have helped me throughout, and I am so grateful that I have been gifted with such love and support.

To Johan Bos, your friendship, support and patience have been invaluable when I've been ranting on about how stressed and tired I am all the time.

And, if I may be somewhat religious here, my thanks to the Father God that I believe and trust in, that I am loved by Him and cannot be separated from his grace and mercy, through his son Jesus Christ.

Abstract

Magnetron Sputtering Physical Vapour Deposition (MS-PVD) is a process capable of depositing thin (< 10 µm) layers of myriad materials onto vacuum stable components. Boron Nitride (BN) is a ceramic with potential for use in surface coating and alloy doping due to its desirable mechanical properties. Multiple issues prevent adoption of BN as a coating material, related to its low deposition rate, low adherence, and the intensive processing required.

The work presented in this thesis investigated the deposition of BN onto powder and planar substrates, developing the knowledge of BN in Additive Manufacturing (AM) and Tooling applications.

Chapter 4 focused on developing a coating rig for depositing thin films onto powdery materials. Prior to the deposition of BN onto powder, three preliminary studies were undertaken.

Zn coatings were deposited onto Cu powder (D_{50}: 39.4 and 7.3 µm), and Ag powder (D_{50}: 28.7 µm) was coated with Ti. The common goal was reflectance reduction at 1070 nm, a wavelength used in Laser Powder Bed Fusion (LPBF), an AM process. Reflectivity was reduced by 38.4 % for the Cu-Zn and 25.7 % for the Ag-Ti, dependent on powder size distribution and sputtering power. This was due to different agitation, time exposed to coating flux and dependence on cohesive vs gravitational forces. Agglomeration of the Ag was exacerbated by higher power, dependent on surface moisture, lack of surface oxides, and snowballing of agglomerates. In-situ drying partially solved this issue.

316L powders were coated with Cu and BN, comparing agitation via rotation and vibration. Neither agitation was successfully deposited uniform coatings across the powder, flow mechanisms were suggested. The deposition of BN onto the 316L powder was insufficient for full analysis of ceramic deposition onto powders.

Chapter 5 focused on the development of a novel adhesion interlayer for c-BN coatings, combating high internal stresses remaining from coating, and ambient degradation, onto steel substrates at low temperatures. A single process was used with a 4 magnetron industrial coater. This interlayer consisted of a fully blended gradient Cr-CrC-C-BCN layer with BN top layer. c-BN nucleation methodology adapted from literature only formed amorphous mixed phase films (~300 nm thick BN) as identified via HRTEM, however these were stable in atmosphere for > 18 months. Significant surface coverage/homogeneity issues were present in all samples.

Chapter 6 iterated the methodology of Chapter 5, moving to a rotational coating setup for intensification of coating parameters via Closed Field Magnetron Sputtering (CFUBMS), first step investigation in coating higher numbers of components, and improved surface coverage. Varied substrate bias voltage (60-180 V), pulsing parameters and gas flows were used in the final BN layer deposition to produce different phases such as Wurtzite phase BN and Extra-Diamond phase BN. Potential mechanisms related to the ratio and energy of ion bombardment to the flux of arriving coating material were discussed. All coatings deposited with different parameter sets except one degraded in ambient conditions over time, and showed insufficient hardness for tooling applications.

Publications

Included in this thesis:

Papers

M. D. Wadge, M. Lowther, **T. P. Cooper**, W. J. Reynolds, A. Speidel, L. N. Carter, D. Rabbitt, Z. R. Kudrynskyi, R. M. Felfel, I. Ahmed, A. T. Clare, D. M. Grant, L. M. Grover, S. C. Cox, "Tailoring absorptivity of highly reflective Ag powders by pulsed-DC magnetron sputtering for additive manufacturing processes", Journal of Materials Processing Technology , vol. 317, Article 117985, Aug. 2023, https://doi.org/10.1016/j.jmatprotec.2023.117985

A. Speidel, M. D. Wadge, L. Gargalis, **T. P. Cooper**, W. J. Reynolds, D. M. Grant, R. Hague, A. T. Clare, J. W. Murray, "The interaction of volatile metal coatings during the laser powder bed fusion of copper", Journal of Materials Processing Technology, vol. 299, Article 117332, Jan. 2022, https://doi.org/10.1016/j.jmatprotec.2021.117332

Not included in this thesis:

Papers

M. D. Wadge, M. Bird, A. Sankowski, H. Constantin, M. W. Fay, **T. P. Cooper**, J. N. O'Shea, A. N. Khlobystov, D. Walsh, L. Johnson, R. M. Felfel, I. Ahmed, D. M. Grant, "Nanostructured, Alkaline Titanate-Converted and Heat-Treated Ti6Al4V Microspheres via Wet-Chemical Alkaline Modification and their ORR Electrocatalytic Response", Advanced Materials Interfaces, vol. 10, iss. 5, Feb. 2023, https://doi.org/10.1002/admi.202201523

J. Felton, E. Blundo, Z. Kudrynskyi, S. Ling, J. Bradford, G. Pettinari, **T. Cooper**, M. Wadge, Z. Kovalyuk, A. Polimeni, P. Beton, D. Grant, G. Walker, A. Patanè, "Hydrogen-Induced Conversion of SnS2 into SnS or Sn: A Route to Create SnS2/SnS

Heterostructures", Small, vol. 18, iss 33, Jul. 2022, https://doi.org/10.1002/smll.202202661

L. Astolfi, D. A. Hutchins, R. L. Watson, P. J. Thomas, M. Ricci, L. Nie, S. Freear, **T. P. Cooper**, A. T. Clare, S. Laureti, "Optimised polymer trapped-air lenses for ultrasound focusing in water exploiting Fabry-Pérot resonance", Ultrasonics, vol. 125, Article 106781, Sep. 2022, https://doi.org/10.1016/j.ultras.2022.106781

M. D. Wadge, M. J. Carrington, H. Constantin, K. Orange, J. Greaves, Md. T. Islam, K. M. Zakir Hossain, **T. P. Cooper**, Z. R. Kudrynskyi, R. M. Felfel, I. Ahmed, D. M. Grant, "Characterization of potential nanoporous sodium titanate film formation on Ti6Al4V and TiO2 microspherical substrates via wet-chemical alkaline conversion", Materials Characterisation, vol. 185, Article 111760, Mar. 2022, https://doi.org/10.1016/j.matchar.2022.111760

L. Nie, D. A. Hutchins, L. Astolfi, **T. P. Cooper**, A. T. Clare, C. Adams, R. L. Watson, P. J. Thomas, D. M. J. Cowell, J. R. McLaughlan, S. Laureti, M. Ricci, S. Freear, "A Metallic Additively-Manufactured Metamaterial for Enhanced Monitoring of Acoustic Cavitation-Based Therapeutic Ultrasound", Advanced Engineering Materials, vol. 24, Iss. 4, Article 2100972, Dec. 2021, https://doi.org/10.1002/adem.202100972

Conferences

Z. R. Kudrynskyi, **T. P. Cooper**, M. D. Wadge, J. Kerfoot, V. V. Korolkov and D. M. Grant, "High dielectric breakdown strength of nano- and micrometer-thick magnetron sputtered AlN films probed by conductive atomic force microscopy", 12th EASN International Conference on Innovation in Aviation and Space for opening New Horizons

Table of Contents

1. Introduction

Magnetron Sputtering Physical Vapour Deposition (MS-PVD) is a plasma coating manufacturing process capable of depositing myriad materials, both metals and ceramics, onto any vacuum stable components and materials. It finds uses in many application fields, such as tooling, aerospace, biomedical and automotive and additive manufacturing industries [1, 2]. A key advantage of this technique is the minimal harmful waste products compared to chemical based coating methods.

MS processes operate in a vacuum chamber, where the substrates to be coated are situated. A target, consisting of the desired coating material, is placed within line of site of the substrates. An inert gas, typically Ar, is introduced into the chamber, a potential is applied to the target, and a plasma is ignited. As the target is negatively charged, ions from the plasma are accelerated to the target surface, colliding and removing (sputtering) material, that then coats the substrates.

Boron Nitride (BN) is a ceramic material with highly desirable mechanical properties. The hardness in the cubic phase (c-BN), second to only to diamond, the low solubility of carbon in BN, and the greater oxidation resistance at higher temperatures compared to diamond make it a prime candidate for the modification and coating of tool materials [3]. Furthermore, the lubricity of the hexagonal phase, sometimes called ‘white graphite’ is desirable for inclusion in alloys to improve surface friction and wear behaviour of materials manufactured from powder feedstocks [4, 5].

When considering the tooling industry, demands for shorter turnaround times in machining of components, and new development of hard to machine and mould material stocks drives the need for new tool coating materials to meet the challenge. BN is a possible material solution due to the aforementioned desirable properties. Furthermore the rapidly expanding Additive Manufacturing industry is driving the

development of new alloys suitable for manufacturing complex components not previously realisable via traditional subtractive manufacturing methods.

Coating substrates with BN, and specifically the formation of c-BN coatings raises a number of challenges. Firstly, the deposition rates when sputtering ceramic materials are generally low [2], due to the need for the use of alternating potential Radio Frequency power supplies. Secondly, when attempting to form c-BN coatings, an intense bombardment of ions from the plasma and a high deposition temperature is required, which creates large internal stresses in the coating, leading to delamination. Thirdly, the resultant BN films can be susceptible to attack from moisture in ambient environments, leading to degradation of the films [3].

Further development of existing coating methodologies is needed, to produce BN coatings, with the desired phase and structure, that adhere to substrate materials. A key gap in the published literature is the deposition of the coatings onto steel substrates and in the use of low deposition temperatures combined with high current of low energy ions to the growing film surface. This is applicable to tool steel substrates, in order to avoid degradation and alteration of the heat treatment and tempering of the steel.

Aims and Objectives:

The aims of this thesis are to deposit adherent thin films of ceramic Boron Nitride across two different substrate morphologies, powder and planar, for application in the rapidly developing field of Additive Manufacturing and the established field of Tooling. These coatings are intended to have properties such as high hardness, low wear rate, high adhesion to substrates, and hot oxidation resistance. This thesis aims to investigate and clarify mechanisms occurring in the deposition processes.

The objectives set for achieving the aims for this project are listed below:

- Deposit coatings using Magnetron Sputtering (a Physical Vapour Deposition technique).
- Develop an existing custom built PVD rig to investigate the coating of powders with different materials.
    - First coat powders with metals for assessment and analysis of powder agitation and coating morphology.
    - Once these investigations are complete, coat 316L stainless steel powder with ceramic Boron Nitride via Radio Frequency sputtering.
    - Use the powder coated with Boron Nitride to produce weld tracks via Laser Powder Bed Fusion.
- Use Magnetron Sputtering equipment to deposit BN directly onto planar substrates, confirming issues with adhesion and deposition morphology.
- Develop a novel interlayer for the improvement of coating adhesion and prevention of degradation, to steel substrates when depositing BN in the cubic phase.
- Alter the coating methodology to investigate coating of larger numbers of samples through rotation of substrates in the PVD equipment.
- Investigate the effects of high ion current at low deposition temperature when depositing BN, utilizing the ion bombardment advantages of Closed Field Unbalanced Magnetron Sputtering and Pulsed Direct Current bias.

2. Literature Review

2.1 Physical Vapour Deposition (PVD)

PVD is an umbrella term for a group of established and state of the art processes for the coating of myriad materials and parts with thin films in vacuum environments. The 'physical' aspect of the techniques come from the use of ions produced in a plasma or an ion gun. These ions are directed to the surface of a material (via an electric field), bombarding the surface and vaporising material through a transfer of momentum, this is called sputtering, see Figure 1.

.

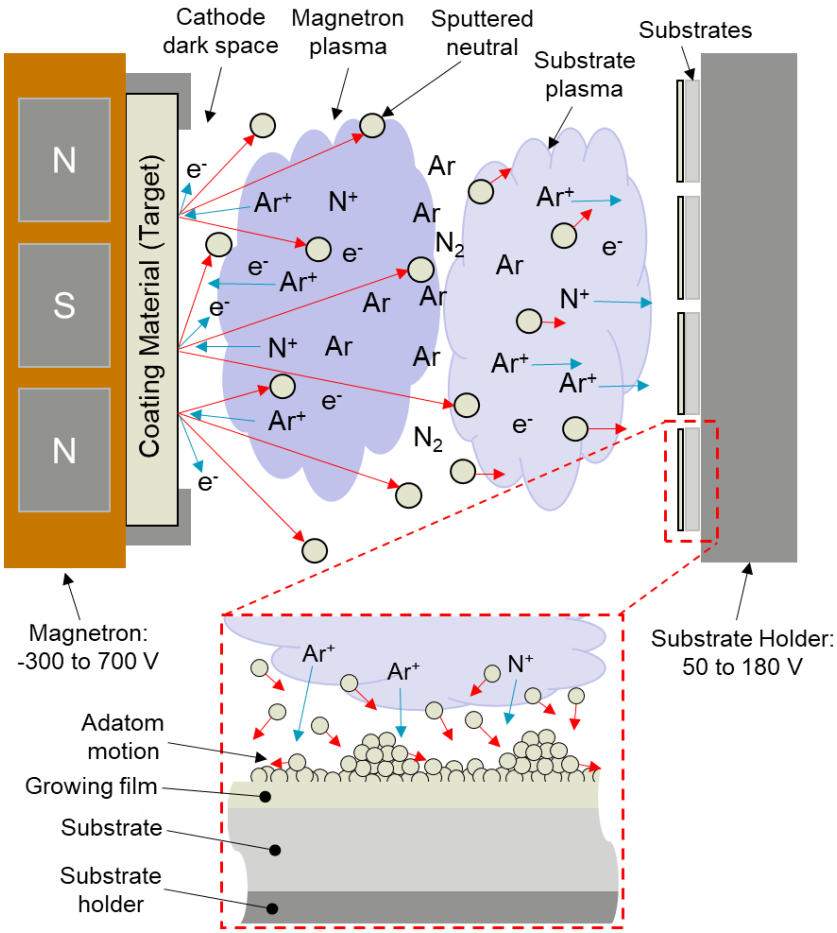

Figure 1 - Schematic identifying the different components of a magnetron sputtering setup, the two plasma fields form neutral regions of excited ions, electrons and neutral sputtered material, inset shows the interaction of ions and neutrals with the substrate.

The coating material then travels and condenses on the chosen substrate at a distance from the source [6]. This is in contrast to Chemical Vapour Deposition (CVD), which uses chemical reactions to produce coating material, which then deposits on the substrates.

In PVD the solid coating material is called the target, as the ions are bombarding it, and can be any material that is stable in a vacuum environment. This is a key advantage of sputtering processes, as pure metals, alloys, compounds and ceramics can be deposited using these techniques. Because plasma processes are inherently inefficient, with ~80% energy lost to heat [1], water cooling is employed, in direct contact with the rearside of the target. Coatings deposited via PVD processes are typically < 10 µm, with films as thin as 10 nm deposited using optimised processes, with thickness dependent on requirements in the desired application.

2.1.1 Diode Sputtering

This technique refers to the simplest (and first developed) sputtering setup, where a potential (several kV) is applied to a target in a vacuum chamber, with a flow of noble gas (typically Argon) at a pressure in the > 10 mTorr range. The target forms the cathode (-ve), and the chamber and/or the substrate holder forms the anode (+ve). Electrons are emitted from the target, and there are free electrons present in the gas, due to cosmic and ultraviolet radiation. When a sufficient potential is applied, these electrons gain enough energy to ionise the Ar, forming positive ions, an avalanche of ionisation then occurs. Note the gas is only partially ionised, as neutral gas atoms are still present in the distribution.

The ionisation of the gas creates a glow discharge, as some electrons in the plasma recollide with the ions leading to photon emission due to bremsstrahlung (breaking radiation), and the de-excitation of electrons to ground state in atoms [7]. This gives the typical light emission seen in ‘neon’ signs (different gases produce different

wavelengths and therefore colours). Due to the distribution of charges within the plasma, the overall charge of the plasma is quasi-neutral [8, 9].

The positive ions are accelerated to the target, bombarding the surface, releasing neutral sputtered atoms (coating material), and further electrons (called secondary emission) which contribute to sustain the plasma field. The neutral sputtered atoms travel through the gas and condense on the substrate surface. The sputtering yield from the target is described as the number of atoms sputtered per incident ion [10]. In addition to these emissions, a proportion of the ions will be neutralised and backscattered away from the target to the substrate.

There exists a compromise related to the working pressure in the vacuum chamber. In order to stimulate a glow discharge that is sustainable, the pressure needs to be sufficient for electron-atom collisions to occur, forming ions. At too low pressures the probability of ionisation through collisions to form a glow discharge is too low. However, once a discharge has started, and material is sputtered from the target, the pressure of the gas must be low enough to allow (relatively) unimpeded travel of coating neutrals through to the substrate, without colliding with Ar ions or neutrals [1].

The mean free path is a simple mechanism for demonstrating this [11] and represents the average distance that an atom can travel in a gas (consisting of the same element) before a collision occurs. Equation 1. below allows calculation of this:

$$\lambda = \frac{k_B \times T}{\sqrt{2} \times \pi \times p \times d^2} \qquad (1)$$

Where k_B = Boltzmann's constant (JK^{-1}), T = Temperature (K), p = Gas pressure (Pa) and d = Atomic diameter (m). Atomic radii are taken from Slater [12] and Mantina et al. [13] for Ar, B and N, values for path length in cm are contained in Table 1.

The path length is increased for lower pressures and higher temperatures, allowing greater flux of coating material to the substrate, however, with the same influences

affecting the electron free paths, and increasing these, the ionisation efficiency is low. When an appropriate balance is found, the deposition rates are generally low [14].

Table 1 - Calculated mean free paths of Argon, Boron and Nitrogen at different temperatures and pressures, path values in cm equation from [11].

Temp (°C)	0.9 mTorr (0.11 Pa)	1 mTorr (0.13 Pa)	2 mTorr (0.27 Pa)	3 mTorr (0.40 Pa)
Argon				
0	5.00	4.50	2.25	1.50
100	6.83	6.15	3.07	2.05
200	8.66	7.79	3.90	2.60
300	10.49	9.44	4.72	3.15
Boron				
0	4.79	4.31	2.16	1.44
100	6.55	5.89	2.95	1.96
200	8.30	7.47	3.74	2.49
300	10.06	9.05	4.53	3.02
Nitrogen				
0	7.35	6.62	3.31	2.21
100	10.05	9.04	4.52	3.01
200	12.74	11.47	5.73	3.82
300	15.43	13.89	6.95	4.63

2.1.2 Magnetron Sputtering (MS)

Therefore, a development was needed to increase the ionisation efficiency of plasmas, whilst maintaining the low vacuum conditions necessary for material transfer to the substrate surface. This was achieved through the use of magnetrons [1].

With magnetrons the target material is attached to (typically) a number of permanent magnets, which produce a magnetic field in the region in front of the target, see Figure 2 b) and c). The magnetic field forms what is described as an electron ‘trap’, as primary and secondary electrons ejected from the cathode, which have sufficient energy to travel to the anode or the chamber walls, instead orbit around the field lines in a helical motion. This is due to the Lorentz force, which is applied to a charge

moving in a magnetic field, perpendicular to the motion of the particle and the magnetic field lines (according to Fleming's right hand rule), see Figure 2 a). This increases the path length of the electron within the plasma (called drift), and for a constant gas pressure and mean free path, the probability of ionisation is increased [14, 15].

Figure 2 b) shows a circular target/magnetron, highlighting the 3D arrangement of magnetic field lines. The electron motion is constrained to a ring, above the target, forming intense plasma. As the plasma is intense in this region, the majority of material is preferentially sputtered from the target in proximity to this, forming a depression in the target over time, called the racetrack. Whilst this increases the deposition rate by an order of magnitude [16] it also leads to inefficient use of target material. As the sputtering is localised relative to diode sputtering, which occurs uniformly across the target surface, the target rapidly erodes in the racetrack. Given that water cooling is employed to cool the rear of targets, this erosion must be monitored in order to avoid burning through the target thickness. Targets therefore have a limited lifetime, with the majority of material volume unsputtered by the end of target use. It should be noted that innovations in magnetron design have allowed increased target usage, but the pros and cons of these designs will not be considered here.

The higher ionisation efficiency allows the use of lower gas pressures (0.8-8 mTorr), and therefore higher mean free paths for sputtered material, further improving deposition rates. The requirement for high voltages (~kV) to sustain discharge is also removed, and as such lower voltage (200-700 V) power supplies can be used, reducing cost, simplifying system design and improving safety.

Whilst the majority of ion bombardment occurs at the target, some ion bombardment of the substrate and growing film leads to beneficial modification [9], the mechanisms of ion interaction will be presented later.

Subsequent to the discovery of this, further magnetron development was undertaken, focused on increasing the current of low energy ions reaching the substrate. The three general stages of this are displayed in Figure 2 c), modified from Kelly and Arnell [2]. The Conventional Magnetron represents the first stage of development, and operates as described previously. Here the inner and outer magnets produce a field of similar strength (ergo 'balanced'), with the majority of field lines terminating at both ends, leading to the electron motion being restricted close to the surface of the target, and low (< 1 mA/cm^2) current density on the substrate.

When using magnets of different strengths, the field lines do not terminate on the target surface. In Type-1 Unbalanced Magnetrons, Figure 2 c), where the centre pole is stronger than the perimeter pole, field lines extend from the centre outwards away from the substrate, reducing substrate current. Further development led to Type-2 Unbalanced Magnetrons, where the imbalance between the magnet strengths is optimised, the outer pole is stronger than the centre pole and the field lines are directed to the substrate, extending the plasma field. This greatly increases the current density at the substrate [14, 17].

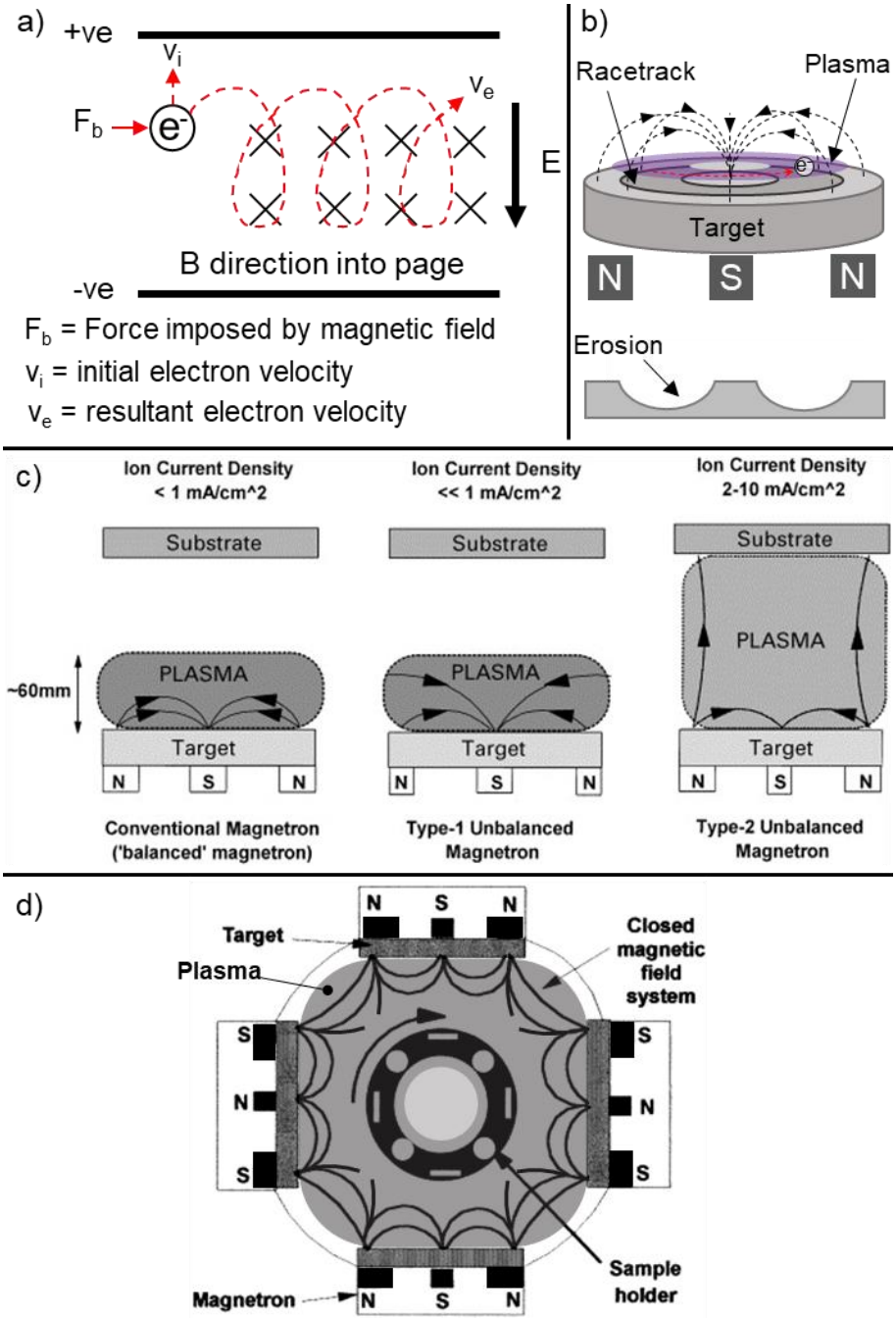

Figure 2 - Schematics demonstrating magnetic fields of different types of magnetron and magnetron arrangements, a) simple schematic of electron motion in an electromagnetic field b) magnetic field lines, plasma ring, electron motion and racetrack on a circular magnetron, c) modified from Kelly and Arnell [2], field lines of three magnetrons, with differences in 'unbalance', extend field lines away from and towards the substrate c) modified from Laing et al. [18], orthogonal arrangement of Type-2 unbalanced magnetrons, field lines are joined up forming a closed field.

2.1.3 Closed Field Unbalanced Magnetron Sputtering (CFUBMS)

In order to improve the homogeneity of coatings and uniformly coat the surfaces of components with complex geometry, substrates are translated through the flux of material from the magnetron. This is usually achieved by either linearly moving substrates past magnetrons, as in a production line, or by rotating substrates past magnetrons as in Figure 2 d). This creates issues with ion bombardment of substrates, as with the use of isolated Type 2 magnetrons bombardment is restricted to regions in front of magnetrons, and parameters are not equivalent in different regions of the chamber [19]. A further development, patented and published in the seminal work by Teer Coatings LtD [18, 20] was to link the magnetic fields of magnetrons, forming a closed field, see Figure 2 d).

This closed field means that the magnetic field lines extend between and connect the magnetrons, the plasma species are therefore not lost to thermalisation at distance from the magnetron [21]. Instead, the ionisation is sustained along and across the field lines, even when no power is applied to alternate magnetrons. This results in increased homogeneity of bombardment throughout the chamber, and a higher overall current of low energy ions [2, 22]. The ion current enhancement is shown in Figure 3.

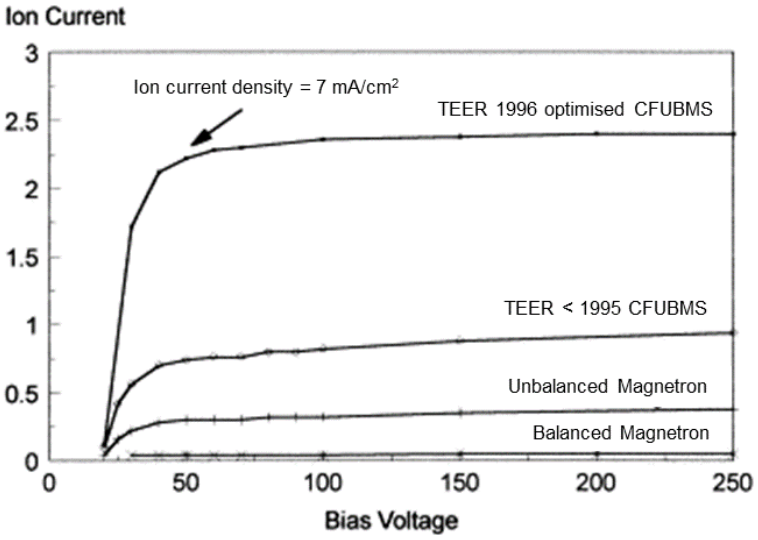

Figure 3 - Differences in ion current between different magnetron types and arrangements, the use of highly unbalanced magnetrons combined with a closed field arrangement leads to a ~25 times increase over balanced magnetrons. Modified from Laing et al. [18].

2.1.4 Power supplies

Typically, three types of power are used in sputtering, these are outlined below.

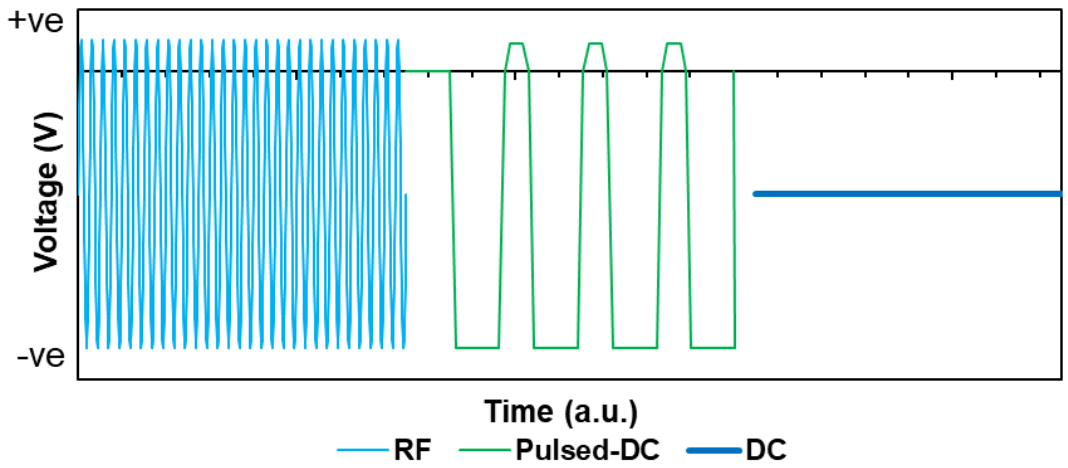

Figure 4 – Example idealised voltage waveforms applied to the target from different power supplies used in sputtering (Not to scale), Radio Frequency (13.56 MHz) waveforms are nominally sinusoidal, Pulsed-DC (mid-frequency, 20-300 kHz) has unequal forward and reverse pulse times, with a small positive voltage in the off-pulse, DC is nominally constant negative voltage.

Direct Current (DC)

Direct current power supplies are the most common supplies used for sputtering. When sputtering conductive materials such as metals and alloys high deposition rates are achievable (several µm/h dependent on setup). A constant negative voltage is applied to the target, leading to a constant current, and constant sputtering of target material. Note that in reality it is typical to use either power or current setpoint control, with the power supplies independently controlling the other variables to maintain the setpoint.

However, DC power cannot be used for depositing materials that are non-conductive, as applying a negative voltage to the target will accumulate positive (ionic) charge on the surface, with no plasma formation as current cannot flow. Sufficient charge accumulation can then lead to arc formation, causing damage to equipment and/or previously deposited coatings, and ejecting undesirable droplets from the target.

Pulsed Direct Current (PDC)

Pulsed DC power supplies, with voltage waveform shown in Figure 4, were developed to tackle the issue of target poisoning during reactive sputtering processes, detailed in 2.1.7, and operate at mid-frequencies (10-300 kHz) [23]. Note that the square waveform shown Figure 4 is idealised, in practice when sputtering the supply is current controlled and as such the voltage peaks to initiate the pulse discharge and when the current starts to flow, the voltage reduces to provide the setpoint current.

These supplies operate either in Unipolar or Bipolar pulsed mode, the former refers to waveforms that are simple pulsed negative voltages, the latter alternates short positive pulse with longer negative pulses (as shown in Figure 4). Bipolar power supplies are used predominantly.

The Bipolar PDC is distinct from Alternating Current (AC) in that the positive and negative pulses are asymmetric; they differ in both duration and amplitude. Typically

the positive pulse has a voltage of 10-20 % of the negative voltage, and the positive pulse will have a shorter duration than the negative [24]. The inclusion of a short positive pulse removes accumulated positive charge from the target surface, so that in the following negative pulse ions are not repelled from non-conductive regions by same-charge influences [25]. This allows removal of poisoned material created in the previous negative pulse. The voltage, frequency and pulse width are the parameters modified by the user.

Radio Frequency (RF)

The final type of power commonly used in magnetron sputtering is the RF power supply. As the name indicates, this is a pulsed supply operating at a radio frequency, in sputtering this is typically 13.56 MHz. An example waveform is shown in Figure 4, note not to scale. The waveform is symmetric in time in contrast to PDC. In order to efficiently transfer power to the target from the power supply, the impedance of the load needs to be 'matched' to the power supply, which operates optimally with a 50 Ω load [26]. Therefore matching units with variable capacitance are inserted between the power supply and the load.

This high frequency pulsing was developed to sputter materials that are non-conductive, such as BN, Al_2O_3, SiO_2 and glasses, in order to deposit dielectric thin films [10].

The mobility of electrons in the plasma is much higher relative to the mobility of ions, this is due to the lower mass of electrons. As the electric field is oscillating, the electrons also oscillate relative to the gas atoms, leading to increased collisions in the plasma sheath and increased ionisation efficiency [14, 15]. As a result, RF plasmas can operate at a lower pressure than DC and PDC plasmas, beneficial for sputtering materials with low sputter yield such as ceramics, as the mean free path can be increased at lower pressures [24].

Additionally, due to the superior mobility of the electrons relative to the ions in the plasma (asymmetric current), whilst the voltage applied by the power supply is alternating between positive and negative, the target actually maintains an average negative potential, allowing sputtering to occur. This is because the ion current during the negative portion of the cycle is insufficient for full neutralisation of the target, and in the positive portion of the cycle, the electron current is sufficient to negatively charge the target, as the non-conductive target is essentially a capacitor plate [10, 16]. However, given that the applied voltage is alternating, there is the potential to sputter from the substrate. In order to prevent this, the substrate area, including the substrate holder, fixtures and jigging must have a larger surface area than the target [7].

2.1.5 Nucleation and Growth of coatings

As the sputtered material reaches the substrate, a number of different nucleation and growth mechanisms can occur. These are generalised into three models as presented in Figure 5. In the first, proposed by Frank and van der Merwe [27], the material deposits uniformly over the surface of the substrate in monolayers, due to a low (<9 %) mismatch in lattice parameters. The Volmer-Weber model depicts material depositing in islands, with preferential growth leading to coalescence and intergrowth of competing islands. The Stranski-Krastanov model combines the two previous models, suggesting that at a critical layer thickness the mode shifts from monolayer to island growth. This is due to an increase in strain in the coating as thickness increases [28].

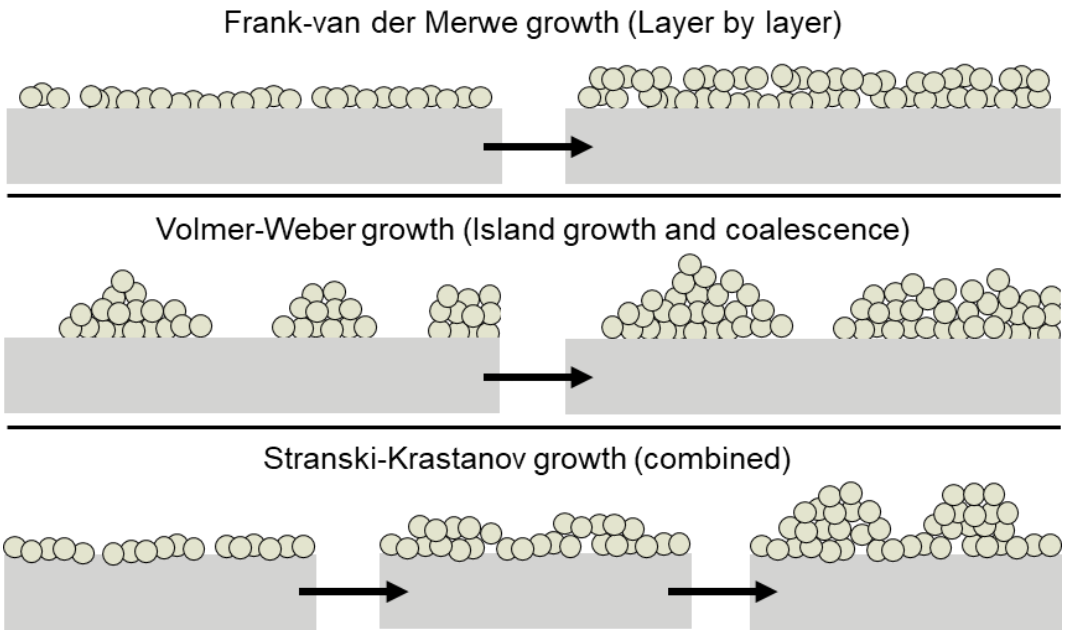

Figure 5 - The general growth models of PVD coatings in the early stages of deposition, van der Merwe growth is where monolayers grow consecutively on the surface with good coverage, Volmer-Weber growth exhibits island growth, where initial coverage is low and as the deposition proceeds islands enlarge and coalesce, Stranski-Krastanov growth is a combination of the two, where intially layer growth is seen, transfering to island growth as deposition proceeds [8, 28].

As the coating grows (> 25 nm), different structures form, dependent on the chosen process parameters and the effects of these. A growth Structure Zone Diagram (SZD), highly cited and recognised in the field of thin film development, was developed by Thornton [29] (iterated from the diagram from Movchan and Demchishin [30]) and modified diagrams have been proposed by Kelly and Arnell [2, 22, 31] and Anders [32] to relate reduced (grouping of independent) parameters to observed structures, see Figure 7. It is important to emphasise that these are highly generalised diagrams, produced based on metallic materials in the majority, and therefore are only a guide. Each material combination and equipment setup with produce varied structures.

The fundamental mechanism governing the structures formed in thin film coatings is the motion of adatoms (shortened term for ‘adsorbed atom’). These are depicted in Figure 6. When an atom arrives at the surface, it transfers energy and is held by weak

bonding to another atom(s), the atom is adsorbed. If the atom subsequently forms a strong bond with an atom(s) on the surface, it is said to be chemisorbed [8]. An adatom has a higher mobility across the surface of the growing film compared to a chemisorbed atom. When adatoms have sufficient energy after arriving at the surface, they can move from locations with low substrate-adatom interaction, to locations with higher surface-adatom interaction, such as geometric or lattice defects [33]. Some atoms will also gain enough energy, either through thermal or kinetic energy transfer, to leave the surface. The Sticking Coefficient is the ratio of the number of atoms arriving at the surface to the number of atoms adhering to the surface [8].

Considering the Thornton diagram in Figure 7 a), there are 4 zones, 1, T, 2 and 3, related to two parameters, Ar pressure and Homologous temperature. Here, homologous temperature refers to the ratio between the substrate temperature T and the melting temperature of the coating material T_m. In Zone 1, T_h is low (< 0.3) and as such thermal driven surface diffusion of adatoms is low, atoms rest where they deposit, leading to geometrically defined structures. The geometry, either defects (scratches, pits, nodules etc) on the surface [34-36], or protrusions or depressions from previously deposited material (see Figure 5, Volmer-Weber/Stranski-Krastanov nucleation) leads to tapered porous structures. This porosity is due to the formation of voids because regions of coating are shadowed by adjacent islands, such that material flux preferentially adsorbs onto the islands, eventually overcoating and sealing a void. This growth is also present at higher T_h (~ 0.3), and higher Ar pressures (> 10 mTorr), as whilst the thermal energy on the surface is increased, the kinetic energy of arriving flux is reduced due to higher probability of collisions with gas atoms in the travel from target to substrate (reduced mean free path) [29].

Zone T, transition, exists in the ~0.1-0.5 T_h range, varied with Ar pressure. This growth is characterised as having a similar tapered fibrous structure to Zone 1, however the thermal driven surface diffusion leads to elimination of the shadowing effect. The

adatoms are not immediately ‘frozen’ (or quenched) in place and can migrate to form a denser, less porous structure. A further increase in T_h (~0.4-0.8) leads to Zone 2, where expansion of the fibrous structures, increasing in width, form columnar grains as adatoms can readily diffuse to low energy positions, allowing epitaxial growth to occur rather than disordered abundant nucleation of new crystallites.

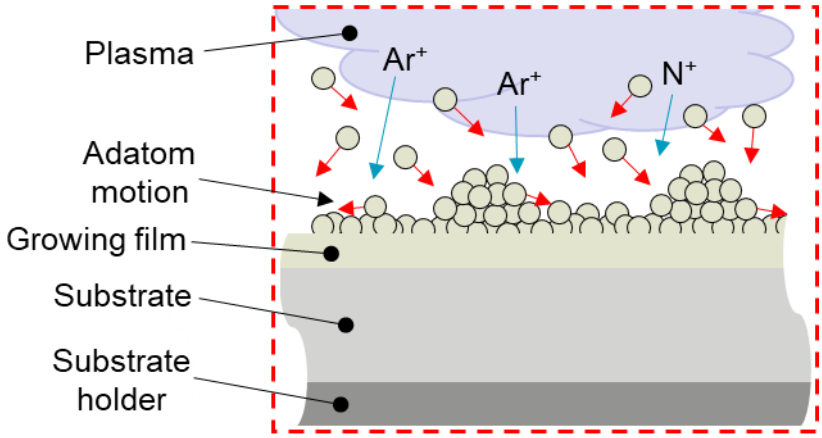

Figure 6 - Schematic illustrating adatom motion across the surface of a growing thin film. Shown in context in Figure 1. Ion bombardment and substrate heating transfers energy to adsorbed material, promoting rearrangement.

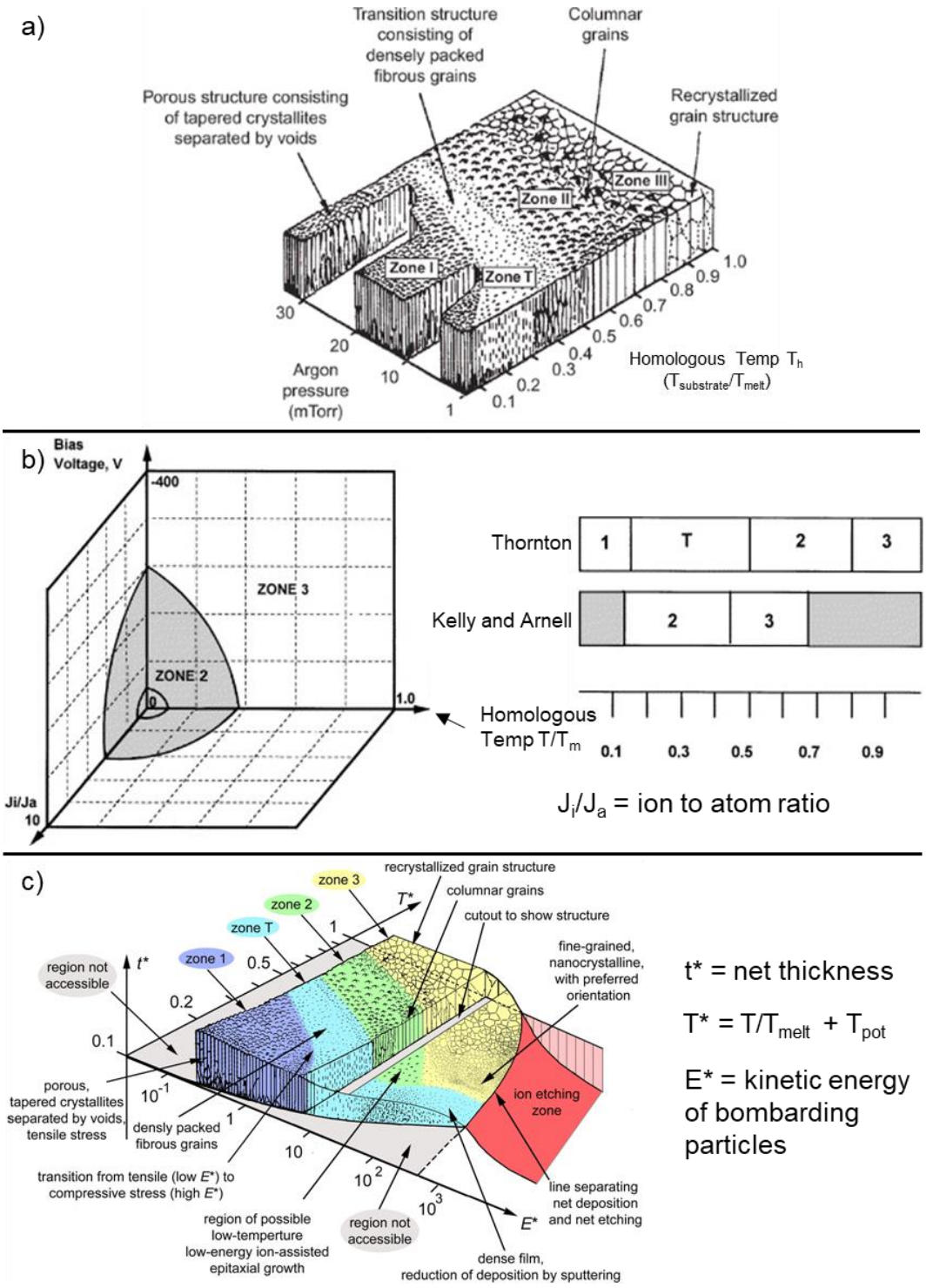

Figure 7 - Structure Zone Diagrams (SZDs) for the growth of magnetron sputtered coatings, a) highly cited diagram relating the pressure and the homologous temperature T_h to growth structures, adapted from Thornton [29] by Mattox [33], b) modification of the Thornton diagram to include the influence of ion energy (driven by bias voltage) and ion to atom ratio in high ion current CFUBMS setups, adapted from Kelly and Arnell [31] c) iteration on the Thornton diagram focused on including high energy bombardment, a thickness axis is added to allow negative net deposition, the temperature axis is modified to include thermal transfer (T_{pot}) from bombardment and the pressure axis is modified to more appropriately define kinetic energy from bombardment, adapted from Anders [32].

It should be noted however, that whilst these columnar structures are called columnar grains, it is unlikely for the whole macro structure to be composed of a single crystal, and as such these are polycrystalline [33].

Zone 3 (> 0.7 T_h) is indicative of growth where the thermal contribution to the coating from the substrate is sufficient to allow bulk diffusive mechanisms to dominate. As such, coatings with Zone 3 structures have equiaxed grains, where the size of the grain perpendicular to the substrate plane is similar to the size parallel to the substrate. The properties of coatings with Zone 3 structures move towards those of bulk annealed materials.

The use of Ar pressure in this diagram overlooks multiple key variables, such as effects of material flux to the surface, and the kinetic energy transferred to the surface from this flux. As such, an iteration has been made by Kelly and Arnell, see Figure 7 b), related to the Closed Field Unbalanced Magnetron Sputtering technique, described previously in 2.1.3. This technique enables homogenous surface bombardment with a high ion current.

The primary change with respect to the Thornton diagram is the split of the Ar pressure axis into two axes, the bias substrate voltage (voltage applied to the substrate to encourage ion bombardment) and ion to atom ratio (J_i/J_a in the diagram). This effectively defines the ion current and the ion energy in relation to observed structures. The results seen by Kelly and Arnell when bombarding the growing film with low energy ions were that the onset for Zone 2 and Zone 3 growth occurs at a lower homologous temperature. Zone 1 and Zone T growth was also not observed. The higher ion to deposited atom ratio is the driving force for this, allowing lower deposition temperatures to be used for achieving Zone 2 and 3 growth. It should be noted that the materials investigated were metallic (Al, Zr and W) and such there could be deviations when depositing ceramics or compounds.

The Anders diagram, Figure 7 c), was also developed in order to extend the Thornton diagram to include ion bombardment effects, however with the focus on High Power Impulse Magnetron Sputtering (HIPIMS). This technique will not be considered in-depth in this review, but is relevant as the substrates experience a high degree of bombardment, due to ionisation of coating material in the transfer from target to substrate, not present in typical magnetron sputtering. Due to these points, a thickness axis has been added, enabling description of structure formation close to the resputter limit (where the net deposition is almost negative, as material is resputtered/etched from the substrate).

Coating substrate/layer interfaces

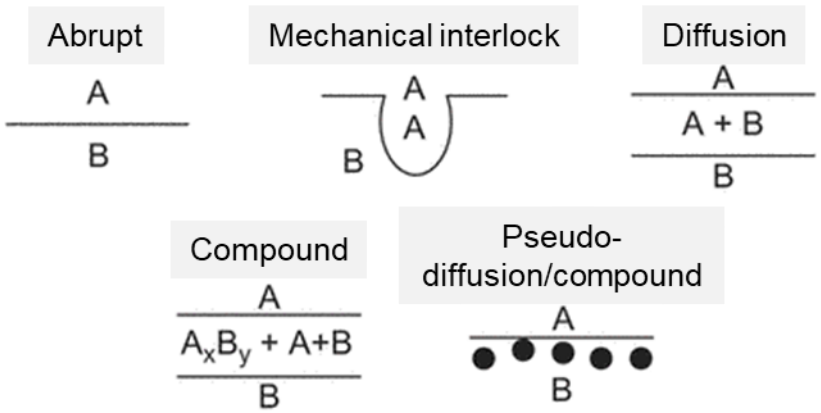

Figure 8 - Different types of interfaces between layers in a coating substrate/interlayer system, see text for details, modified from Mattox [33].

When depositing coatings onto substrates, a key region of interest is the interface between the substrate and the coating, or in multilayer systems, the interface between layers. The design of this region will have considerable impacts on the adhesion of the layers, as differences in material properties, such as expansion coefficients, or chemical resistances, will lead to degradation mechanisms via mechanical or chemical changes. Figure 8 contains the typical interfaces between layers of a coating system. The first, and most simple, is the abrupt interface, where one material is

deposited on top of one another, and is defined by material properties changing within one or two atomic spacings (< 0.8 nm). This will limit the adhesion of the layer, as there is limited interaction volume, and is dependent on the chemical bonding of between the materials. Crack propagation along the interface is unobstructed. As such this interface is only used in situations where the sharp change in properties is required, with low demands on adhesion strength.

The second, Mechanical Interlocking, in contrast to the abrupt interface, is defined by the geometry of the preceding layer, typical of textured or roughened surfaces. The adhesion is improved by deposition of material into valleys and scratches in the material, see Figure 8, creating a complex route for crack propagation. The limitation of this interface is in the coating conformity, as without sufficient adatom mobility, deep troughs will be overcoated to form voids, which can be stress concentration points and therefore crack formation sites [33]. Mechanical interlocking is, however, not really a separate type of interface, as no real surface is perfectly smooth, and as such there will always be an interlocking effect regardless of the desired interface type.

The following three types of interface are variants on a theme, and are defined by different amounts of diffusion, mixing and reaction of materials at the interface. A Diffusion interface is formed when there is physical mixing of the materials at the interface, and is time and temperature dependent. This interface is graded, and is formed when mutually soluble materials are deposited on top of one another at sufficient temperature for diffusion to occur. The compound interface takes this a step further, where the materials both diffuse and react with each other, forming compounds, as is detailed in the schematic in Figure 8.

Both the diffusion and compound interfaces require both time and temperature to form. Given that one of the key advantages of PVD is the low (< 500°) deposition temperatures, the use of increased temperatures to enable diffusion mechanisms

could be limiting to process applications. Instead, Pseudodiffusion/compound interfaces can be formed at lower temperatures by concurrent deposition of different materials from individual sources, or via reactive sputtering (detailed in 2.1.7). Therefore graded interfaces can be directly deposited according to design, rather than via passive diffusion based methodology. Furthermore, as the mixing of the material components is related to the deposition ratio, metastable phases which are richer than equilibrium solubilities are accessible. The use of ion bombardment promotes further mixing of material through adatom rearrangement and resputtering of surface material.

The use of diffuse or graded interfaces means that the mechanical properties of the two (or more) materials change gradually over the thickness of the interface. If there are differences in properties such as thermal or volume expansions, related to cooling from the deposition temperature to room temperature, or reactions between coating components leading to higher or lower density compounds respectively, the stresses caused by these can be contained by the graded interface [10, 33]. Whether the interface that forms is a solid solution of segregated material or a compound is dependent on the specific material combination.

2.1.6 Bias assisted deposition (Ion Plating)

As previously mentioned, concurrent bombardment of growing films with ions leads to beneficial material modification mechanisms. The development of unbalanced magnetrons was driven by this advantage. Negative substrate biasing is a further technique that can be used to increase ion bombardment of the substrates [10]. This involves applying a negative potential, DC, PDC or RF to the substrates, of lower magnitude than that applied to the target, as sputtering of previously deposited coating is not the goal. Furthermore, as opposed to sputtering from the target, which is typically carried out in current or power setpoint control, substrate biasing is varied through voltage control. The negative biasing of the substrate accelerates ions to the

substrate with a wide range of energies, due to collisions and energy transfer in the plasma. Increasing the voltage increases the energy of the ions, albeit still with a wide range.

Prior to the development of PDC supplies, DC and RF supplies were primarily used for this purpose. However, as previously outlined, these both have drawbacks. DC supplies are not suitable for deposition of non-conductive material. At the outset of the coating run, the DC supply with provide a ready supply of ions to the film, but as the substrates and holders are coated, the nonconductivity will prevent current flow, leading to a reduced bombardment. RF supplies solve this issue, but impedance matching units are required in order to provide the power supplies with the optimum 50 Ω load. Given that in industrial or high volume coating there is a need for complex jigging and substrate fixturing, and variations of these run to run, the use of matching units with limited variability leads to increasing cost and complexity. The development of PDC supplies overcame these issues, as matching units are not required, and the bipolar pulsing prevents charge build-up.

In coating processes the initial step involves the use of ion bombardment to clean substrates. A relatively large potential, typically 300-1000 V, highly dependent on process setup, is applied to the substrates in this step, transferring enough energy to ions to sputter contaminants, remaining from previous wet cleaning stages, from the surface. These contaminants could be moisture, adsorbed gases or passively formed oxide layers typically observed on metals such as Cr and Ti (~5 nm thick). Furthermore, ion bombardment of the surface can also introduce atomic level roughening. The removal of contaminants and modification of the surface all improve the adhesion of the following coating, and is an essential part of the Bias assisted PVD process [9].

Following cleaning, the voltage is lowered to < 300 V, in order modify rather than resputter the deposited coating. The ion bombardment can cause multiple

mechanisms to occur. The thermal energy of the ions impacting the substrate will transfer, raising the temperature, though most of the thermal energy transferred to the samples is through electron backscattering from the target. The kinetic energy, which is the predominant energy transferred by the ions leads to ion peening, where the density of the deposited material is increased by the recoil of atoms, voids are removed and compressive stresses form, increasing surface toughness. As well as modification of chemisorbed atoms, adsorbed atoms, as mentioned previously in 2.1.5, are displaced and rearranged due to energy transfer, and defects in the surface are created which promote nucleation and reaction. The increase in densification and nucleation density also lead to a finer grain structure, and therefore higher strength and hardness via the Hall Petch effect. The microscale roughness of the final coating surface can also be reduced or lowered due to increased density and reduced grain size [10, 19].

The development of both the CFUBMS setup and the use of PDC power supplies for bias sputtering has been found to provide increased current of low energy ions to the substrate [37, 38]. Cooke et al. [38] in their study on PDC vs DC bias sputtering in a closed field system (4 orthogonal magnetrons) found that the ion current (taken as the current displayed on the power supply front panel) was ~13.5x greater for PDC than DC (500 V, 300 kHz frequency and 1500 ns pulse width), see Figure 9 a). This is explained by Kelly et al. [37] to be due to an increase in ionisation due to higher electron mobility when pulsing, forming a second glow discharge at the substrate. Furthermore, Kelly et al. found that with DC, the current saturates with an applied voltage between 100-200 V, whereas with PDC the current continues to rise with increased voltage, see Figure 9 b).

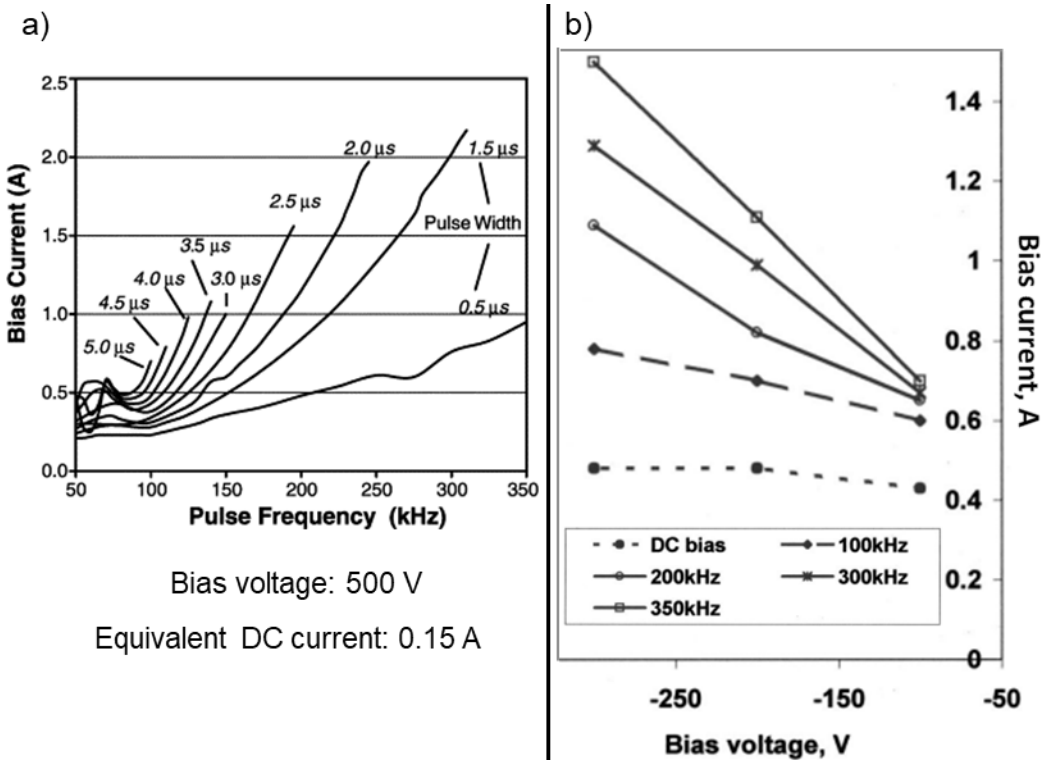

Figure 9 - Pulsed DC vs DC substrate biasing, a) the relationship between the frequency and pulse width and the ion current drawn at the substrate (fixed voltage), DC current is lower than all pulsed parameters tested, modified from Cooke et al. [38], b) effect of increasing voltage on the ion current for pulsed and non-pulsed DC, current continues to rise with an increase in voltage for PDC, wheras DC saturates, modified from Kelly et al. [37].

2.1.7 Reactive Sputtering

As mentioned previously, sputtering is highly adaptable, and can deposit coatings from metals, alloys, ceramics and compounds. However, if a coating material, typically a ceramic or compound, is not able to be produced in solid target form, or it is undesirable to sputter from a ceramic or compound target there is an alternative.

A process called Reactive sputtering can be used, where a pure or simplified compound target can be sputtered, and reacted with an additional gas that is entered into the inert Ar plasma in the chamber. Many gases can be used for reactive sputtering, commonly N_2, O_2 and hydrocarbon containing gases such as butane (C_4H_{10}) are used to form nitrides, oxides and carbides (including Diamond like Carbon) coatings respectively [10]. Furthermore, if compound targets are sputtered,

elements can dissociate from one another, as is the case with BN, and a reactive gas can be input to replenish dissociated material in order to achieve a desired stoichiometry [15, 39].

An example of reactive sputtering is the deposition of Alumina (Al_2O_3) coatings, which are typically sputtered from pure Al targets, with additional O_2 gas flow [24, 40]. However, as reviewed by Berg and Nyberg [23], the use of Direct Current (DC) power will lead to issues with the efficiency of the process. As the reactive gas is introduced, it will chemisorb onto the surface of the target, 'poisoning' it. In the case of Al_2O_3 and other dielectric materials, this will reduce the sputter rate, eventually leading to a non-conductive target surface, no secondary electron emission and extinguished plasma [10]. The gas flow therefore needs to be optimised to avoid this. Figure 10 contains curves related to the deposition rate and target voltage as reactive gas flow is varied. This is a complex issue, as hysteresis loops are present. As flow is increased the deposition rate (Figure 10 a)) is reduced gradually, the partial pressure of the gas is relatively unchanged, as all the reactive gas is 'used up' in coating formation. This region is called 'metallic mode' sputtering, and corresponds to high deposition rates.

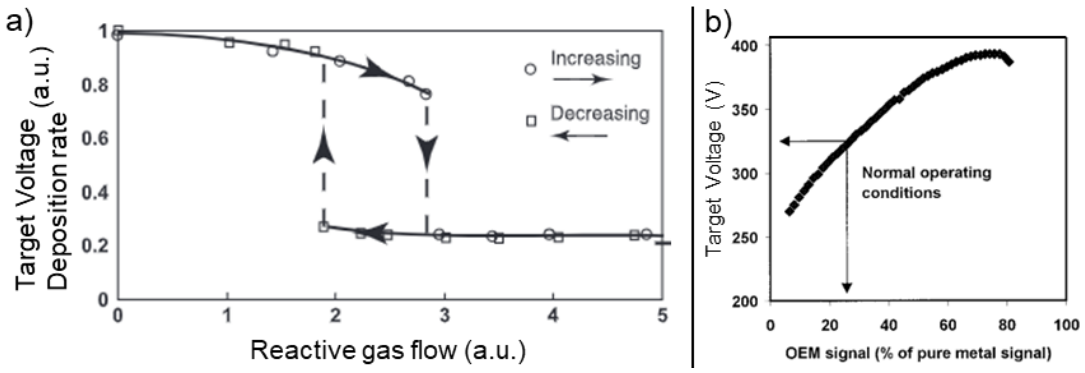

Figure 10 – a) general curve of target voltage or deposition rate responding to increases and decreases in reactive gas flow. The curve has a hysteresis loop, indicating different behaviour when flow is lowered following a rise, modified from Berg and Nyberg [23], b) Measured voltages on a target as the reactive gas flow is increased (shown here as the variation in Optical Emission of metal ions in the target plasma) modified from Kelly and Arnell [24].

It is unlikely that such a low flow of reactive gas will lead to the desired stoichiometry in the deposited coating, though this will of course vary situation to situation, and as such the gas flow must be raised. To avoid a drop in deposition rate due to target poisoning, as is evident at a flow of ~3 in Figure 10 a), the target must be operated in a 'partially poisoned' mode as described by Kelly et al. [24], maintaining stoichiometry whilst avoiding a severe voltage drop.

2.1.8 Ion Beam Assisted Deposition (IBAD)

An additional form of coating bombardment, through the use of ion beams, will be briefly considered here. Instead of using the biasing of substrates to accelerate ions to the surface of the growing film, an independent source of ions accelerated from an ion gun, see Figure 11, can be used [21].

There are a number of key differences between ion beam bombardment and bias assisted bombardment, this is because the operation of the ion gun is in relative isolation to the production of coating material in a hybrid ion gun/plasma system, whereas in a solely plasma based system the bombardment and sputtering are interdependent.

The first difference is that the energy of the ions can be controlled within a narrow range by the acceleration voltage. This is in contrast to the ions accelerated from the plasma by the bias potential, which have a wide range of energies. Furthermore, the ion current can be directly controlled by the gas input to the ion gun, whereas the modification of ion current in bias assisted sputtering relies on varying the bias voltage, which also varies current, and gas pressure, which will also affect the sputtering at the target. Independently varying ion energy and current in bias assisted sputtering is therefore more complex, and the measurement of ion energies and currents varied throughout the chamber in plasma based processes is also non-trivial [41-43].

The final difference is that due to the line of site nature of the ion beam, it is not conducive to use in situations where there are large areas of complex geometry, in contrast to the use of bias, which can uniformly bombard in a closed field system, as detailed previously [7, 21].

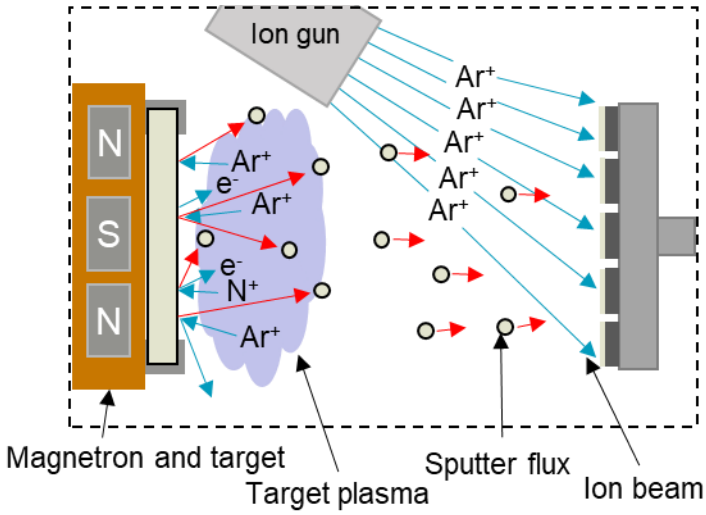

Figure 11 - Simple ion beam assisted magnetron sputtering setup, the ion gun provides a relatively monoenergetic beam of ions to the growing film at a controlled current.

2.2 Additive Manufacturing (AM)

AM processes are distinct from traditional manufacturing processes such as machining in that material is supplied to form the component/part, rather than removing (subtracting) material. Furthermore, when considering processes which require a mould or die to arrive at net or near net shape, such as casting, forging or injection moulding, AM has the advantage of being completely mould-less.

This allows freedom of design and manufacture for the creation of complex parts with optimised geometry and topology, with reduced material waste. These key attributes of AM allow previously un-manufacturable parts with high-strength to weight ratio for applications in the aerospace and automotive industries [44], among many others, to be realised [45].

2.2.1 Laser Powder Bed Fusion (LPBF)

The particular type of AM that will be considered in this project will be Laser Powder Bed Fusion (also known as Selective Laser Melting), a general schematic of which is shown in Figure 12. This process, as with the majority of 2.5 dimensional AM techniques, requires a CAD model of the part to be sliced into layers for iterative layer-by-layer manufacture.

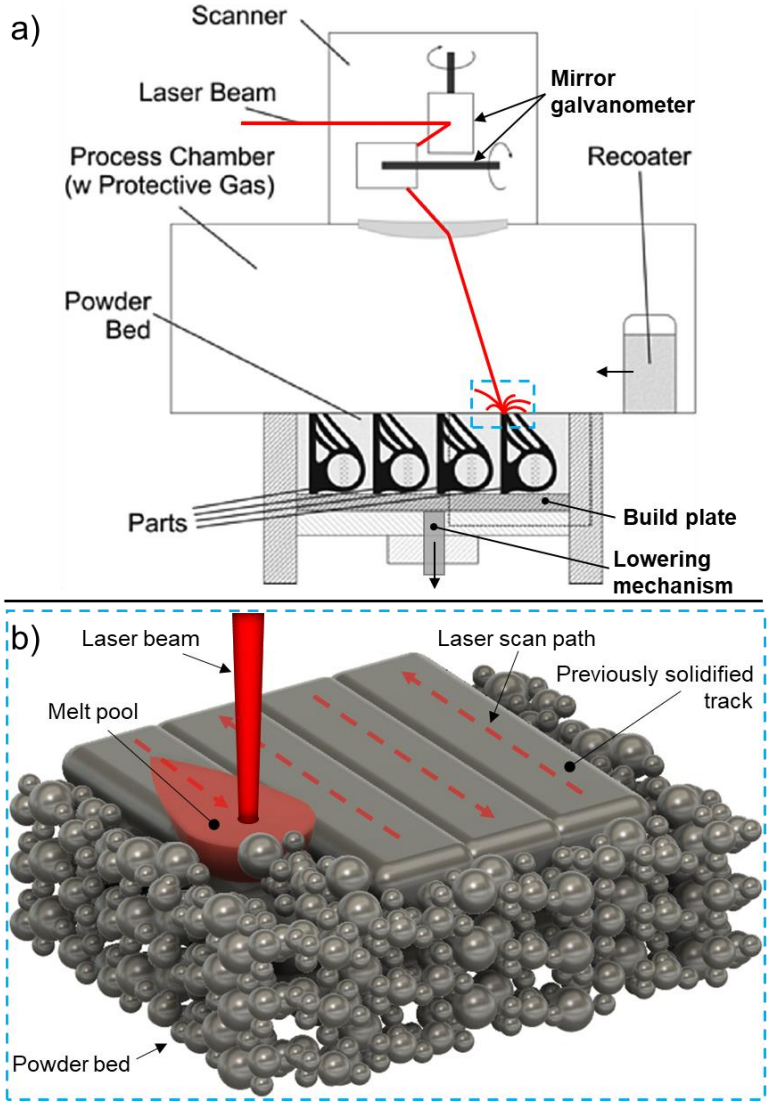

Figure 12 - Schematics detailing the LPBF process, a) modified from Herzog et al. [46] general schematic of equipment, a laser rasters across the surface of a powder bed, selectively melting powder in tracks, on the completion of a scan path, the build plate is lowered, a fresh layer of powder is drawn over the top by the recoater and the laser scans again, b) solidifying further tracks, remelting and incorporating with previous layers.

A layer of metal powder is deposited with the recoater, which consists of a blade or roller, carrying powder from a hopper, covering the build area. The layer is then selectively melted by a laser, scanning across the powder surface according to the path programmed for the CAD layer. The build plate is then lowered, a new powder layer deposited, and the process repeated, see Figure 12 [46].

Whilst the parameters for manufacturing parts for multiple materials, such as 316L and Ti6Al4V, have been optimised for production, many materials pose challenges for manufacture via LPBF [47]. Metals such as Cu and Ag are two such materials. As studied by Gargalis et al. [48], the optimisation of parameters in the LPBF of Cu is challenging, as the reflectivity and absorptivity at the commonly used ~1070 nm laser wavelength is high and low respectively [49]. This combined with the relatively high thermal conductivity of Cu (400 and 15 $Wm^{-1}K^{-1}$ for Cu [50] and Ti [51] respectively) means that any energy that is absorbed is rapidly transferred away from the melt pool to the surrounding powder bed. This leads to lack of fusion defects, unmelted powder particles and void formation in parts. This has been shown by Silbernagel et al. [52] who used a 200 W laser to produce parts with 85.8 % density, and observed defects.

These issues can be partially overcome by using higher laser powers and by optimising parameters, as shown by Ikeshoji et al. [53] and Jadhav et al. who used 800 W and 500 W lasers to produce 96% and 99 % dense parts respectively. There are drawbacks to this technique, however, as optimal process windows are narrow, and whilst this shows improvement for pure Cu, the use of higher laser powers may not transfer to mixed material systems used to form alloys. With higher powers there will also be an increased risk of damage to sensitive optical components in the system [54].

An alternative to modifying the equipment used for the LPBF is to modify the powder feedstock [55]. Given that the reflectance and absorption, at least for the initial energy transfer by the laser prior to the melt pool formation, is dependent on powder surface

properties, the modification of the powder particle surface is the objective. Jadhav et al. have investigated multiple routes for powder modification of Cu for LPBF. Two studies were based on furnace heating of powders, the first was with oxidised powder formed by heating Cu powder in a furnace in air [56], the second formed a coating on a CuCr1 powder by diffusion of Cr to the surface by heating in a N_2 atmosphere [57]. Both approaches increased the optical absorptivity at the ~1080 nm wavelength, and whilst the maximum laser power for their equipment (500 W) was necessary for dense (> 98%) parts, a higher scan speed could be used than with pure Cu.

Actively coating the surfaces of Cu powders by depositing new material also shows promise in this field, with powder coated via immersion plating (a wet chemical process) with Sn [50] and Ni [58], also demonstrating reduced porosity. However, Jadhav et al. [50] noted that S contamination from the coating process introduced cracking in the parts. Magnetron sputtering was used by Lassègue et al. [59] to deposit pure CrZr coatings on Cu powder. The part density increased (87.9 to 94.3% for Cu and Cu-CrZr respectively) and the authors noted that the final elemental composition of the printed cubes was comparable to pure copper (~99.5 wt% Cu). A key gap in the published literature is the mechanism that occurs when the laser interacts with a coated particle.

As mentioned previously, there are potential issues with the use of optimised process parameters for one material for the manufacturing of components containing multiple materials. Given that production of alloy powders by atomisation techniques can be complex, a simpler solution is to mix powders of different elements to form alloys [60, 61]. However, mixing different materials in powder form for alloy manufacture in LPBF leads to a number of issues. Firstly, the optimum LPBF parameter spaces for the materials can be different, especially when considering difficult to process materials such as Cu and Ag. Secondly, in creating alloys with powders with different size distributions, material densities and powder morphologies, there is an increased risk

of segregation of powder during the layer recoating step, as found by Mussato et al. [62] and Shaheen et al. [63].

In tackling the first issue, differing optimal parameter spaces, coating the powder of one material with a layer of the other has the potential to consolidate LPBF process parameter windows. For example, Ti-Ag alloys are promising candidates for biomaterials used in AM orthopaedic implants as reviewed by Lowther et al. [64]. Ti and Ti alloys are prevalent in implant manufacture, and alloying could utilise the antimicrobial properties of Ag. However, the reflectance at the incident wavelength of ~1070 nm is 0.31 and 0.85 for Ti [65] and Ag [66] respectively and the thermal conductivity at 1235 K is 15 and 360 $Wm^{-1}K^{-1}$ for Ti [51] and Ag [67] respectively. If a simply mixed powder was used the layer on the powder bed surface will not melt, solidify, and consolidate uniformly as the properties differ, leading to lack of melting and/or fusion or excessive vaporisation at the extremes.

For the second issue, in process demixing due to differences in material and powder properties, the use of separate powders is not always optimal. Instead, introducing alloying material to the surface of the powder is a potential route to avoid these issues. The use of Boron Nitride in powder mixtures has been studied for improvement in sliding wear of components manufactured via powder metallurgy. Mahathanabodee et al. [4, 5] introduced hexagonal BN powder into 316L powder to form composite materials by sintering. Fu et al. [68] prepared coatings using cubic BN powder mixed with Ti6Al4V powder in laser cladding. In both authors' work, the surface mechanical properties of the materials were modified. The 316L/BN sintered composites [4, 5] had a lower friction coefficient (35-45 % reduction, depending on BN content), but conversely had a higher wear rate. The Ti6Al4V/BN laser clad coatings [68] showed an approximate ~2.3 increased hardness over the Ti6Al4V substrate. However, for both the 316L/BN and Ti6Al4V/BN materials there were issues with consolidation of the material, with void formation and porosity leading to fracture and pull out of

different phases in the wear tracks. The coating of the BN onto the matrix forming powder feedstock could homogenise the properties of the alloy, and would eliminate the possibility of powder segregation in the LPBF powder bed when recoating.

2.3 Coating of Powders

2.3.1 Coating via Magnetron Sputtering

2.3.1.1 Material combinations

The highly adaptable nature and ability to deposit metals and ceramics means that MS processes are attractive for powder surface modification. Furthermore, given that relatively few waste products are formed in MS processes (inert gas exhausting, readily recyclable target materials) they are attractive compared to chemical based powder modification. Table 2 contains a summary of the literature published on PVD coating of powders, with details of the studies where available. The table is not exhaustive, as there are many coating parameters that will influence the resultant material, but for brevity the key information: materials, powder size, equipment setup details and coating thickness have been included.

Note that in order to narrow the field of research, studies using particle sizes < 1 µm (most notably from the Japanese research group led by Abe Takayuki), and studies where particles have been modified by plasma treatment (where there is no deposition of material from a target) have been omitted.

Table 2 - Collation of published literature on the MS coating of powdery materials (> 1 µm), N-A indicates where the publication could not be accessed, and details are taken from the abstract, where multiple publications are from a single research group, they have been collated according to the surname of the author most frequently involved.

Coating Material	Powder Material	Powder size (µm)	Barrel Shape (angle)	Rotation	Vibration	Powder Quantity	Coating Thickness	Research Group	Reference
V, SS, Fe, Cr	Mg	D_{50}:30 D_{50}:26	Tilted double cup	Y (52rpm)	N	7 g	Not stated	Nottingham	2017 [69]
Zn	Cu	D_{10}:15.4 D_{50}:39.4 D_{90}:59.6	Cylinder (45°)	Y (24rpm)	N	5 g	~1 µm		2022 [70]
		D_{10}:3.1 D_{50}:7.3 D_{90}:19.0					2-3 µm		
Ti	Ag	D_{10}:17.4 D_{50}:28.7 D_{90}:45.3	Cylinder (45°)	Y (24rpm)	N	5 g	Not stated		2023 [71]
Pt	Glass MS	100	Pan (H)	N	Y (Ultrasonic, via piezo-crystal)	N-A	6 µm	Meyer	1980 [72]
Pt/PtO	Glass MS	Not stated	Pan (H)	N	Y (Ultrasonic, via piezo-crystal)	Not stated	2 µm		1981 [73]
N-A	Glass MS	N-A	N-A	N-A	Y (Ultrasonic, via piezo-crystal)	N-A	N-A		1981 [74]
N-A	N-A	N-A	Drum	Y	N-A	N-A	N-A	Ensinger	1994 [75]

Coating Material	Powder Material	Powder size (µm)	Barrel Shape (angle)	Rotation	Vibration	Powder Quantity	Coating Thickness	Research Group	Reference
Au	Al_2O_3	30-300	Conical drum with Fins (‘Wing drum’)	Y (0-200rpm)	N	3 g	Not stated		1994 [76]
Au	Al_2O_3	N-A	Conical drum with Fins (‘Wing drum’)	N-A	N-A	N-A	N-A		1994 [77]
N-A	N-A	N-A	N-A	N-A	N-A	N-A	N-A		1995 [78]
Au Pd	Al_2O_3	3-500	Conical drum with Fins (‘Wing drum’)	Y	N	0.5 g	Nodules		1998 [79]
Pt	Al_2O_3 WC	100 20	Conical drum with Fins (‘Wing drum’)	Y	N	0.5-1 g	Nodules		1999 [80]
Pt Au	Al_2O_3 WC	100 20	Conical drum with Fins (‘Wing drum’)	Y (60rpm)	N	0.5 g	Nodules		2003 [81]
304	WC	9-10	Cylinder (H)	Y (3rpm)	Y (1.6 Hz)	100 g	Not stated	Vieira	2003 [82]
304L	WC	D_{50}: 9.1	Cylinder (H)	Y (3rpm)	Y (1.6 Hz)	100 g	~0.4 µm		2006 [83]
304	316L Cu-sph	D_{50}: 7.7	Not stated	Not stated	Not stated	50 g	Not stated		2007 [84]

Coating Material	Powder Material	Powder size (µm)	Barrel Shape (angle)	Rotation	Vibration	Powder Quantity	Coating Thickness	Research Group	Reference
	Cu-irr	D_{50}: 28.7 D_{50}: 19.8							
Ni/Fe/Cr	WC	2-10	Cylinder (H)	Y (3rpm)	Y (1.6 Hz)	100 g	Not stated		2008 [85]
316L	316L	Not stated	Not stated	N	Y 'High Frequency'	Not stated	Not stated		2008 [86]
Cu 304L 304L	316L Cu-sph Cu-irr	D_{50}:7.7 D_{50}:28.7 D_{50}:19.8	Not stated	N	Y 'High Frequency'	Not stated	Not stated		2009 [87]
Cu	WC	9	Not stated	Not stated	Not stated	Not stated	Not stated		2013 [88]
Cu, Ag, Ni, Ti, Co, multilayer Co-Ni and Co-Ni-Ag	Fly-ash spheres, Al_2O_3	40-200	Cup (H)	Wobbling	Y (600-1800 Hz)	2 g	8-100 nm	Yu	2007 [89]
Co, Ni, Cu, Ag	Fly-ash spheres	30-80	Cup (H)	Wobbling (20rpm)	Y (Ultrasonic)	1 g	10-134 nm		2007 [90]
Cu	Fly-ash spheres	30-90	Cup (H)	Wobbling (20rpm)	Y (Ultrasonic)	Not stated	~51 nm		2007 [91]
Cu	SiC, Polymer	40 4	Cup (H)	Wobbling (20rpm)	Y (Ultrasonic)	4 g	Not stated		2008 [92]

Coating Material	Powder Material	Powder size (µm)	Barrel Shape (angle)	Rotation	Vibration	Powder Quantity	Coating Thickness	Research Group	Reference
Ni	Fly-ash spheres	20-100	Cup (H)	Wobbling (15rpm)	Y (Ultrasonic)	1 g	26-85 nm		2009 [93]
TiO_2	Fly-ash spheres	Not stated	Cup (H)	Wobbling (20rpm)	Y (Ultrasonic)	1 g	16-264 nm		2011 [94]
Multilayer Ti/Al/Cu	Alumina	40-63	Angled drum	Y	N	Not stated	Not stated	Smirnov	2014 [95]
Multilayer Ti/Al/Cu	Alumina	40-63	Horizontal cup	Not stated	Not stated	Not stated	Not stated		2017 [96]
Pd	ZrNi	500	Cylinder (H)	Y (30rpm)	N	2.7 g	< 270 nm (Calc.)	Abe	2003 [97]
Pt	Al_2O_3	20, 80, 120	Hexagonal (H)	Y (0-20rpm)	N	6 g	Not stated		2004 [98]
Pt	Polymer	5, 12, 50	Hexagonal (H)	Y (20rpm)	N	3 g	10-50 nm		2005 [99]
TiO_2	SiO_2	110	Hexagonal (H)	Y (3.5rpm)	N	Not stated	40-60 nm		2006 [100]
WO_3	SiO_2	110	Hexagonal (H)	Y	N	Not stated	24-40 nm		2006 [101]
Au, Ag, Pd, Cu, Ni	Polymer	15, 5	Hexagonal (H)	Y (4rpm)	N	3 g	9-42 nm		2007 [102]
Au	Metallic	Screws, Nuts etc	Hexagonal (H)	Y (1.7rpm)	N	N/A	~2.7 µm		2007 [103]
SnO_2	Al flakes	130	Hexagonal (H)	Y (3.5rpm)	N	10 g	65-200 nm		2007 [104]

Coating Material	Powder Material	Powder size (µm)	Barrel Shape (angle)	Rotation	Vibration	Powder Quantity	Coating Thickness	Research Group	Reference
WO_3	SiO_2	110	Hexagonal (H)	Y (3.5rpm)	N	Not stated	24-40 nm		2007 [101]
TiN	Al	130, 30	Hexagonal (H)	Y (4rpm)	N	6 g	~200 nm		2008 [105]
WC	Polymer	15	Hexagonal (H)	Y (4rpm)	N	Not stated	~80 nm		2008 [106]
Pt	SiO_2	0.3-12 (mean 4.9)	Hexagonal (H)	Y (4.2rpm)	N	2 g	Nanoparticles		2008 [107]
DLC	Polymer	50	Hexagonal (H)	Y (4.3rpm)	N	Not stated	~500 nm		2012 [108]
Cu/Zn	Zeolite (Al_2O_3/SiO_2)	Not stated	Hexagonal (H)	Y (3.5rpm)	N	Not stated	Nanoparticles		2013 [109]
Ru	Zeolite (Al_2O_3/SiO_2)	5	Hexagonal (H)	Y (4.2rpm)	Y	3 g	Nanoparticles		2014 [110]
Co/Pd	Zeolite (Al_2O_3/SiO_2)	Not stated	Hexagonal (H) + stirrer	Y (4.2rpm)	Y	3 g	Nanoparticles		2014 [111]
Cu/Zn	Zeolite (Al_2O_3/SiO_2)	Not stated	Hexagonal (H)	Y (3.5rpm)	Y	Not stated	Nanoparticles		2014 [112]
Co	Zeolite (Al_2O_3/SiO_2)	Not stated	Hexagonal (H)	Y	Y	5 g	Nanoparticles		2015 [113]
Au	Al_2O_3	Average 4.6	Hexagonal (H)	Y (4.3rpm)	N	10 g	~41.5 nm		2016 [114]
Pd-Co	Cu	< 75	Hexagonal (H)	Y (4.3rpm)	N	10 g	Uniform Nanoparticles		2017 [115]

Coating Material	Powder Material	Powder size (µm)	Barrel Shape (angle)	Rotation	Vibration	Powder Quantity	Coating Thickness	Research Group	Reference
Mo	Diamond C Fibres	100-600	Cup with fins (20-40°)	Y, 2-fold, 3-5 + 18-30	N	1.25-2.5 cm^3	10-80 nm	Eisenmenger-Sittner	2009 [116]
Mo	Diamond	100-120	Not stated	Y	N	Not stated	2.5-15 nm		2009 [117]
Pt Cu	Hollow Glass MS	~14	Various cups (45°)	Y (26-60rpm)	Y (Tapping rods)	16 cm^3	1.5-4 nm		2010 [118]
Ti, Al, TiO_2, Al_2O_3, Pt, Cu	Hollow Glass MS	2-70	Double cone concussion drum with fins (45°)	Y	Y (concussion)	< 20 ml	30-50 nm		2013 [119]
Cu	Hollow Glass MS, Mg, Diamond	19-135	Double cone concussion drum	Y	Y (concussion)	1 L	13-54 nm		2016 [120]
Cr	SA508 steel	Mean 9.83	Double cone concussion drum (45°)	Y (25rpm)	Y (concussion)	2.2 kg	~7 nm		2022 [121]
Au, Al, Mo	Hollow Glass MS	50-500	N/A	N	Levitation and vibration (20-60 Hz)	Not stated	< 2µm	Other	1979 [122]
Pt	TiO_2	Not stated	Dish (H)	N	Y	Not stated	Nanoclusters		1989 [123]
Ni/Pt	Al_2O_3	N-A	N-A	N-A	N-A	N-A	N-A		1991 [124]
Be/Cu	Polymer	N-A	Pan	N	Y	N-A	7-120 µm		1997 [125]

Coating Material	Powder Material	Powder size (µm)	Barrel Shape (angle)	Rotation	Vibration	Powder Quantity	Coating Thickness	Research Group	Reference
Cu	SiC	35-170	Petri dish (40°)	Y	N	Not stated	Not stated		1997 [126]
Ar/C/Cu	Glass MS	2-1000	Cup	N	Y (120 Hz)	Not stated	N/A		1998 [127]
Al	Fe	2	RF plasma suspension	N	N	Not stated	150-200 nm		1998 [128]
Au, Pd, W	Hollow Glass MS	N-A	N-A	N-A	Y (Tapping)	N-A	N-A		2004 [129]
Au	Al_2O_3	< 44	Double cylinder concussion (45°)	Y (43rpm)	Concussion	Not stated	Nanoparticles		2005 [130]
Ti/Al	Hollow Glass MS	70-120	Cylinder (H)	Y	N	2 litres	< 400 nm		2006 [131]
TiO_2, V_2O_3	Hollow ZrO_2/SiO_2	250-425	Cylinder (H)	Y	N	Not stated	15-30 nm		2007 [132]
Al	Ti-37.5Si	D_{10}:1.5 D_{50}:19.9 D_{90}:60.2	Not stated	Not stated	Not stated	Not stated	Not stated		2008 [133]
Al, Al/SnO	Glass spheres	213-250 1-75	Horizontal cup	N	Y (not stated)	20-30 g	10-200 nm		2013 [134]
Pt	C	Not stated	Cup	Y (10rpm)	Y (2-3 Hz)	0.5-0.65 g	Nanoparticles		2013 [135]
CrZr	Cu	D_{10}:10.1	Not stated	Not stated	Not stated	Not stated	32-445 nm		2021 [59]

Of the 71 publications contained in Table 2, 59 are focused on the deposition of metallic coatings, 12 of ceramic coatings, 14 use metallic substrates, 49 use ceramic substrates and 6 use polymer substrates. Of the ceramic coatings deposited, 11 are deposited reactively from metallic targets (such as Tungsten Carbide (WC) in the publication by Akamaru et al. [106]) and only 1, tin oxide by Baechle et al. [134] has been deposited directly from a ceramic target using RF plasma. Therefore, at the outset, there is a clear gap in knowledge of depositing ceramic coatings using RF power, such as BN, onto the surface of powdery substrates via magnetron sputtering, and also a deficit of studies of coating metallic powders, relative to ceramics.

There are varied applications investigated using powders coated via MS. A large number of publications (21) focus on applications of coated powders to catalytic processes, where the large surface areas (relative to planar surfaces) are beneficial for efficient reactions. These publications involve deposition of noble metals such as Pt, Ru and Pd, onto ceramic substrates. It should be noted that whilst the number of publications is high, they do not necessarily contribute extensively to the body of knowledge of MS coating of powders, rather they focus on the applications of the powders.

The repurposing of waste materials, specifically hollow ash spheres [89, 94, 136], has been investigated for low density electromagnetic and UV radiation attenuation. The modification of ceramic Al_2O_3 powder feedstock materials for plasma spraying, focused on improving adhesion of the sprayed coatings by adding metal layers to the powder, has also been carried out [95, 96]. Other applications include improved flowability, advantageous in powder metallurgy processes [84, 87], improved binder distribution and material doping in sintering of hard metal [83, 85, 88] and the aforementioned applications in AM [59, 70, 71].

A small number of publications (6, [89, 95, 96, 131, 134, 137]) have attempted to deposit multilayers, consisting of different materials, onto powder particles. This has

been aimed at wetting and improving adhesion of the top layer onto the powder with an interlayer.

2.3.1.2 Coating morphology

There are a number of coating morphologies that have been produced in published studies. The general nucleation and growth of MS coatings on powders is similar to that detailed in Section 2.1.5. However, the key variation is in the surface coverage of the individual particles, whether a uniform coating is applied to create a core-shell particle, where the substrate is the core and coating is the shell, or whether isolated regions of coating material exist on the surface. For both, the growth structures are of interest in order to determine the formation and deposition mechanisms, and the behaviour in subsequent applications will vary.

When considering the published literature, and the coatings that have been deposited, a clear distinction in the morphology of the coatings can be immediately seen, dependent on the geometry and the density of the powder particles, see Figure 13 and Figure 14, for the Scanning Electron Microscope (SEM) images of uncoated powders and coated powders respectively.

In many studies, specifically those carried out with glass microsphere and coal ash sphere substrates, see Table 2, the starting feedstock is of a regular spherical shape, with smooth surfaces and low density, Figure 13 a). Comparatively, powders of irregular shapes, such as the SiC coated by Yu et al. [92] Figure 13 b), or even those produced via atomisation techniques, such as the Cu powder coated by Lassègue et al. [59], 13 c)/d) cause issues with coating, due to the increased roughness, and interlocking of the particles in the powder bulk, detailed in Section 2.3.2. As such, see Figure 14, the surface coverage and uniformity of the coating on the spherical particles is high 14 a), and the coverage for the irregular, angled faces of non-spherical particles 14 b), is low.

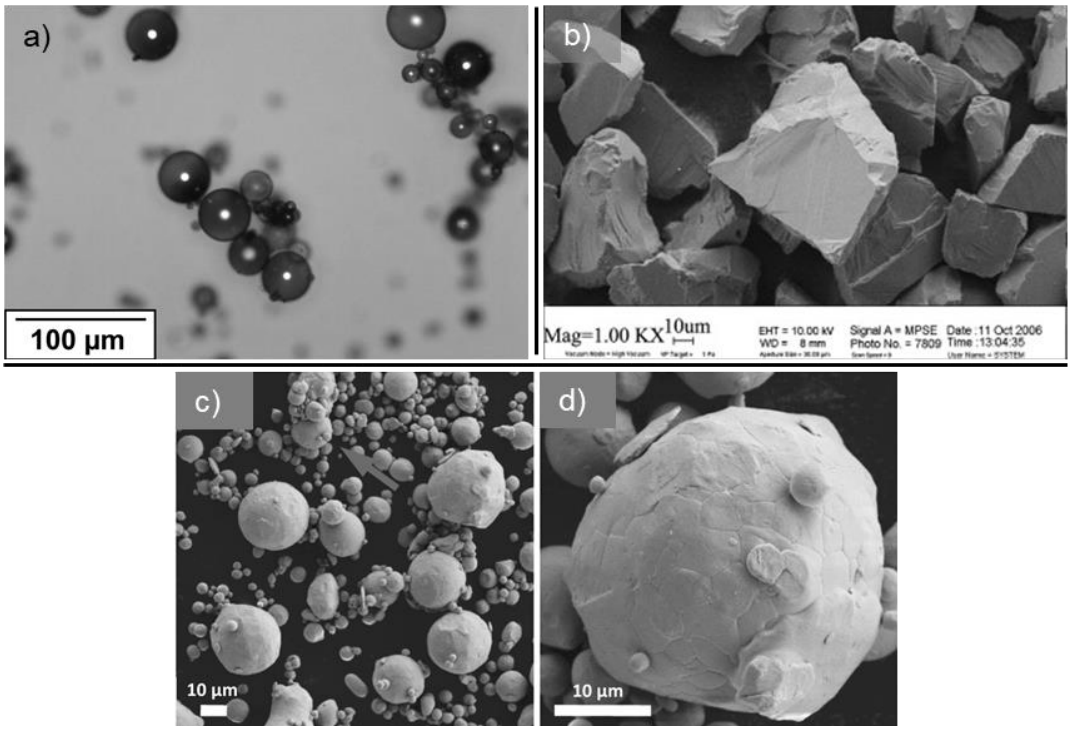

Figure 13 - Images of powder substrate materials used in studies from literature, the geometry differences and surface morphology are apparent, a) optical image of glass microspheres, highly spherical and smooth, modified from Schmid et al. [118], b) SEM image of irregular SiC particles, modified from Yu et al. [92], c) and d) SEM images of gas atomised Cu powder, the particles are somewhat spherical, with satelites and irregular surface morphology, modified from Lassègue et al. [59].

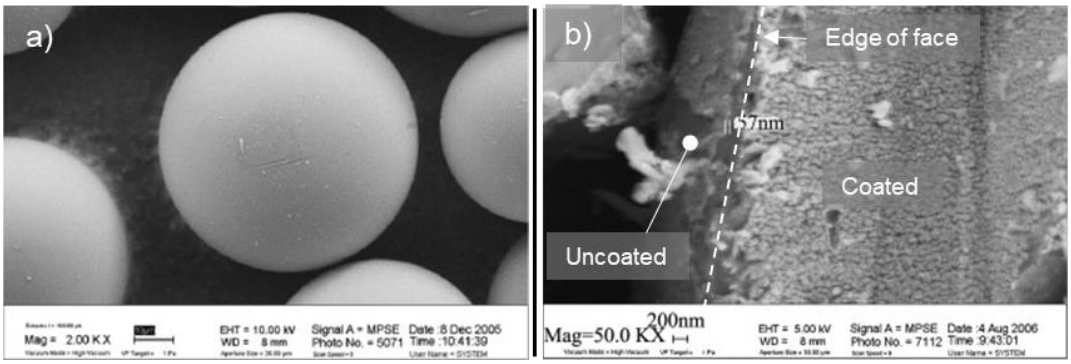

Figure 14 - Comparison of the surface coverage of two different shaped particle feedstocks, subsequent to coating via MS, a) total surface coverage of smooth spherical ash sphere, modified from Xu et al. [89] , b) non-uniform coating of surface on irregular SiC particle where one face is well covered, and the other is not, modified from Yu et al. with annotations [92].

When considering the thickness of coatings deposited on powders, and the typical thickness of coatings deposited via magnetron sputtering processes (10 nm - 10 µm), it is helpful to consider the surface area being treated. Take a bulk sample, 1 kg of Ag, in the form of a cube, this cube will have a surface area of 125 cm^2 (using a

density of 0.01049 kg/cm^3). If the same mass of powder is considered, the surface area is much greater, at 2.38 x 10^6 cm^2 (taken from powder size analysis in Chapter 4). It is clear then why the majority of coatings reported in Table 2 are < 100 nm, as it is not practical to deposit the volume of material required for thicker coatings in reasonable process durations.

2.3.2 Powder agitation during PVD coating

As the majority of this large surface area will inevitably be obscured and buried within the bulk of powder, and as magnetron sputtering is a line of sight process, the powder needs to be agitated. This is in order to turnover the planar exposed surface and therefore facilitate deposition onto all of the powder particles and also the whole surface of each individual particle.

There have been multiple techniques and equipment designs used to agitate powder during MS coating, which are summarised in Figure 15. The Japanese group led by Abe T. initially used a horizontal (where the central axis is parallel to the ground) cylinder, with a magnetron inserted along the central axis, directed to the internal wall, Figure 15 a). In their study on coating irregular ZrNi alloy powder with Pd [97], they found that rotating the barrel (30 rpm) agitated the powder sufficiently to coat the particles in the population. However, this was only stated, and only an image and corresponding Energy Dispersive X-ray Spectroscopy (EDX) maps for Pd, Ni and Zr for an individual particle were presented. X-ray Diffraction (XRD) patterns of the coated powder did indicate the presence of a crystalline Pd phase.

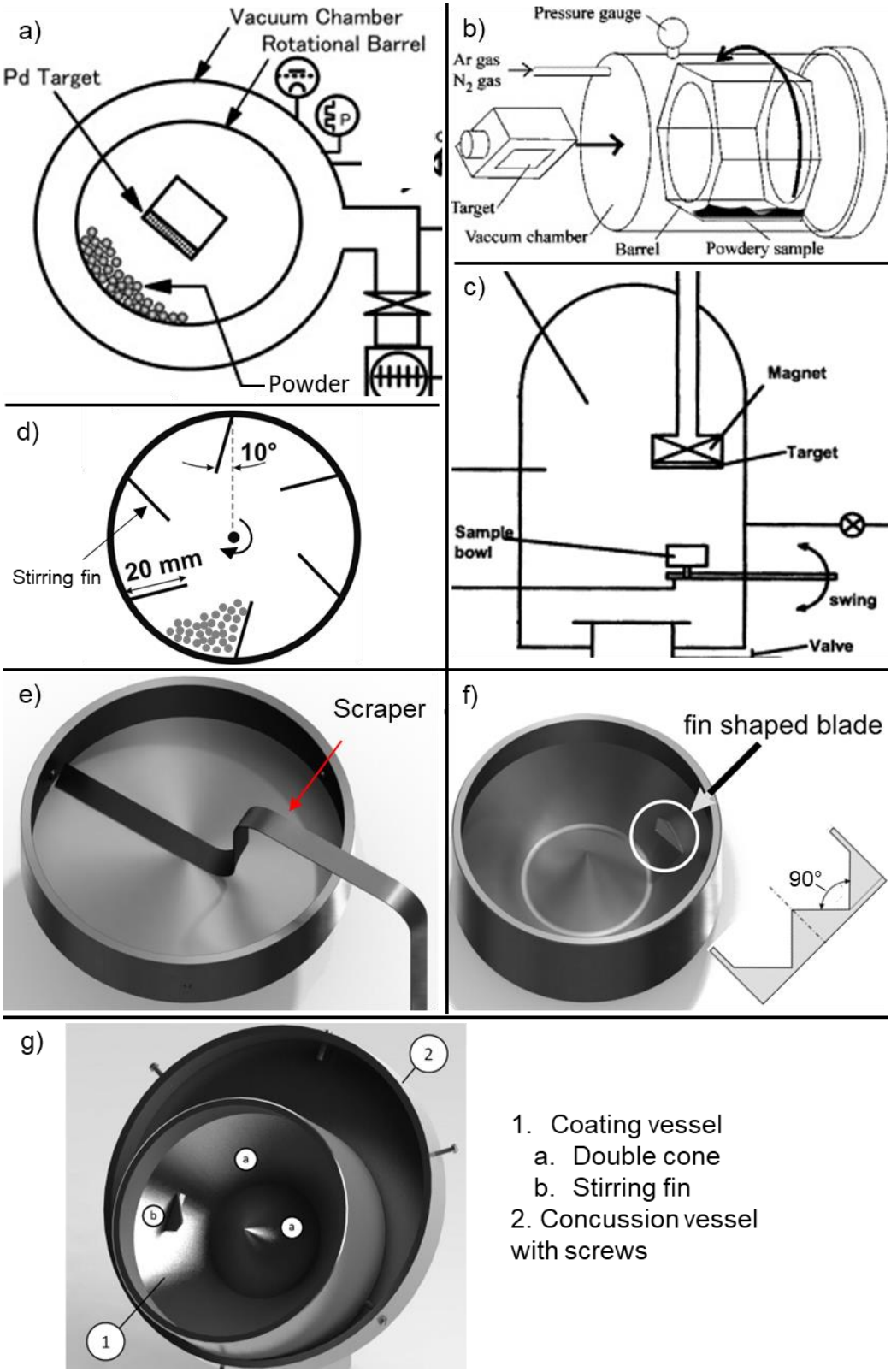

Figure 15 - Summary of the arrangements and vessels of PVD equipment used for coating powder, a) horizontal cylindrical barrel with coaxial magnetron and rotation, modified from Hara et al. [97], b) hexagonal horizontal barrel, with rotation and vibration, modified from, Abe et al. [98], c) vibrating cup with top down magnetron, modified from Xu et al. [89], d) angled cup with stirring fins, modified from Hell et al. [116], e) angled cup with scraper, modified from Schmid et al. [118], f) double cone cup with fin, modified from Schmid et al. [118], g) double cone cup with fin contained in concussion vessel, modified from Schmid et al. [119].

Subsequent to this, see Figure 15 b), a change in setup was made, to instead use a hexagonal shaped barrel [98]. The rotation of the barrel (4rpm) when coating both irregular and spherical Al_2O_3 with Pt promoted improved agitation and turnover relative to the cylindrical barrel. The authors suggested this was due to the angled edges of the hexagonal barrel, which carried powder up the surface of the container and dropped it when gravitational forces overcame the surface friction. They proposed that the smooth surface of the cylindrical barrel did not provide enough influence from friction alone to achieve this powder translation. Qualitative data in the form of optical and SEM images were used to confirm the improvement in coating across the powder population.

An alternative setup, used by the Chinese group involving Yu X., instead uses a horizontal cup, with agitation provided by a vibration generator and by tilting/swinging the cup back and forth. The coating flux is directed from a magnetron above the cup [89]. The majority of their studies, see Table 2, involve deposition of coatings onto spherical ash particles. Using this apparatus, they achieve smooth, uniform coatings across the spheres, see example in Figure 14 a) (from Xu et al. [89]), and show optical images of many particles to show coating present across the population [90, 92]. However, when coating irregular Al_2O_3 particles, as seen in Figure 14 b), coating was not uniform across the particle surfaces, and the optical images presented by the authors confirm that not all of the particles were coated.

The group led by Eisenmenger-Sittner [116-121] has carried out multiple studies focused on the alteration of barrel geometry to improve agitation of powder. In one study, Hell et al. [116], investigated the use of angled (20-40°) cups (rotating) in combination with fins configurations, see Figure 15 d). When coating diamond particles with Mo the use of these fins did turnover the powder, seen visually, however subsequent to coating it was found that uncoated powder had accumulated and adhered to the surface of the cups at the point at which the fins met the cup surface.

They also varied the amount of powder, and found that, as explained previously, a greater coating duration was required to coat a larger powder volume with increased surface area. A secondary effect of the increased batch size was in the reduction of powder adhesion to the cup surface. The authors attributed this to a greater quantity of particles, with a larger powder bulk momentum impacting the adhered particles, removing them from the wall/base of the cup. Additionally, when varying the angle of the cup, the maximum angle of 40° produced populations with fewer uncoated particles (assessed from contrast in optical images).

Further investigations from this group, Schmid et al. [118], tested a number of different container geometries, two of which are shown in Figure 15 e) and f). When using glass microspheres (~ 14 µm), the authors found that in atmosphere the spheres readily cascaded when the container was rotated at an angle, however, when under vacuum the spheres agglomerated and formed clumps. This was attributed to the evaporation of moisture from the powder, which had acted as a lubricant in atmosphere and had evaporated in the vacuum environment.

The container design shown in Figure 15 f) was presented in the study by Schmid et al. [118] and used in conjunction with the setup in Figure 15 g) in the publications by Schmid et al. [119], Eder et al. [120] and Unnikrishnan et al. [121]. The design used a cone placed at the centre of a drum with sides converging to the centre. The use of this geometry, when angling the assembly, means that, depending on the angle, all surfaces are non- horizontal at all times, or alternate between horizontal and vertical per rotation. Essentially this removes regions for powder to accumulate, by having particles on a slope. The authors found that with this setup the powder was continuously in motion, and adherence to the container walls was minimised. However, clumping of the powder (glass microspheres coated with Pt) still occurred.

The iteration on this concept, Figure 15 g), introduced a second container, surrounding the powder barrel. This second container (with screws fixed radially from

the outer rim) was rotated, and the powder barrel sat inside, dragged around by and bounced over the screws. The authors found that the clusters seen previously were periodically broken up by the concussion of the containers [119].

2.3.3 Alternative powder coating techniques

Summaries of a number of coating techniques for use with powder are contained below, to the author's current knowledge, there are no publications reporting the coating of powders with BN.

Electroless Plating

This process utilises Redox (Reduction and Oxidation) reactions, where reactants gain or lose electrons in liquid solutions to form thin films on substrate materials, and as such, when compared to Electroplating, requires no additional potential to be applied. The reactions occur at the substrate surface, which can be seeded with a catalyst material to aid/increase the rate of reaction [138, 139].

Li et al. and Geng et al. [140-142] plated Al and Ti6Al4V powder with Ni and Co, presenting a possible solution to modifying powders in large quantities (1 kg <) for LPBF. The authors used Sodium Citrate ($Na_3C_6H_5O_7$) and Sodium Hypophosphite (NaH_2PO_2) as a pH controller and a reducer respectively, and used either Nickel Chloride ($NiCl_2$) or Cobalt Sulphate ($CoSO_4$) as the source of metal. The surface morphology of all powder samples showed 'decoration' of the particles with coating material (< 1 µm in size) rather than complete core-shell coating, with an increase of particle density when adding more of the metal source to the coating bath.

The advantages of Electroless coating are that the equipment setup is relatively simple, the correct reactants need to be chosen, and suitable containers, but no additional power supplies or vacuum or temperature controlled environment is needed. Furthermore, as this is a wet chemical process, all of the substrate powder surface is exposed to the deposition, allowing for uniform coverage, and the process

is readily scalable. However, as with all chemical methods, the handling, processing and disposal of hazardous chemicals, and the potential lack of suitable reactants for a desired coating, limit this process.

Chemical Vapour Deposition (CVD)

Chemical vapour deposition, as detailed previously, utilises reactants in the vapour phase to form coatings on substrate surfaces. These processes vary widely, but typically involve passing the first precursor though a heated chamber, where substrates are placed, allowing the material to adsorb/chemisorb onto the surface. A second (or more) reactant/s is then passed across the first, reacting to form the coating. The temperatures used in CVD processes tend to be higher than those used in magnetron sputtering, in order to crack the reactants, maximise the rate of reaction, and promote interaction with the substrate material [3, 55].

Zhang et al. [143, 144] investigated the coating of c-BN powder with SiO_2, for applications in Spark Plasma Sintering. In their first investigation ([144]) the authors deposited 10-20 nm thick coatings across the surface of irregular 2-4 µm powder by supplying Tetraethyl Orthosilicate ($Si(OC_2H_5)_4$) at 973 K. The powder was exposed to the coating material by rotating the coating vessel, causing turnover of the powder. The authors then identified that the addition of the SiO_2 layer to the c-BN powder inhibited the unwanted phase transformation to h-BN during sintering, and in their second study increased the thickness of the coating into the 50-300 nm range. The corresponding micrographs of the sintered composites showed uniformly distributed SiO_2 throughout, however no investigation of the uniformity of the coating across individual powder surfaces and the whole population was reported.

Karches et al. [145] also deposited a ceramic material (Al_2O_3 onto SiC) via CVD, however the authors used Plasma-Enhanced CVD, by exciting/cracking the reactant (Aluminium-tri-sec-butoxide $Al(OC_4H_9)_3$) and carrier (Ar) gas with coupled

microwaves. The SiC substrate powder and reactants were circulated in a cyclone by the Ar stream, passing through the plasma region.

From observation of the particles after different process durations, the authors determined that the coating material (≤ 1.3 µm) first deposited as fine nano particles on the surface, coalescing to form a dense film as the process proceeded. The authors also noted that the interaction between powder particles and the walls of the reactor led to localised abrading of the particles and coating from the edges of the irregular particles, rounding them off and exposing the substrate. This also led to blocking of the filtered reactor apertures with fine particles.

The use of CVD and variations thereof does show potential for the coating of powders, however the issues with adequate agitation of the substrate powder to enable coating of the whole surface of individual particles and uniformly across the powder population are still present. Furthermore, as with electroless deposition, the availability of suitable reactants and the hazards associated with these (and the exhaust products) can pose problems.

Sol-gel coating

Sol-gel coating techniques are summarised as chemical processes which involve the deposition of solutions of materials, by submerging, dipping, spinning or aerosol methods, which then undergo sol-gel transitions to form colloidal suspensions, and then solid coatings as the material dries. These coatings tend to be thin, ≤ 1 µm, though can be thicker, and are used for optical, electronic and protective and catalytic applications [21, 146, 147]. Multiple application and drying cycles can be performed to build thicker or multilayered films.

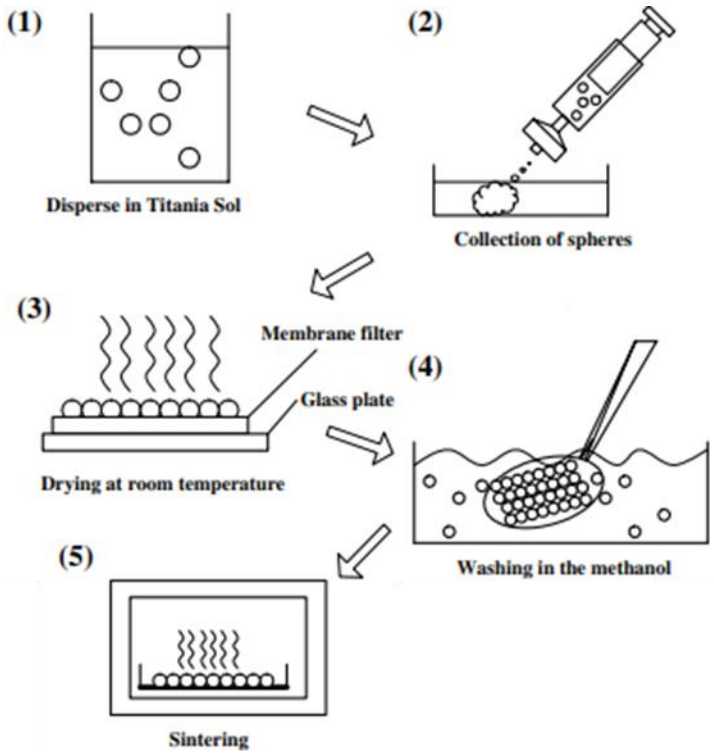

Figure 16 - The sol-gel powder coating process stages, 1) the powder is dispersed in the coating sol (colloid solution), 2) the spheres are removed from the excess liquid, 3) the coated particles are deposited on a glass plate for drying and consolidating the gel into a solid coating, 4) the plate and particles are washed in solvent to separate the coated product, modified from Haraguchi et al. [148].

Haraguchi et al. [148] have coated SiO_2 powder with TiO_2 using a sol-gel process, the steps of which are detailed in Figure 16. The authors used monodisperse SiO_2 with a size of 10 µm, submerging the powder in a solution containing Titanium Tetraethoxide ($Ti(OC_2H_5)_4$). The particles were submerged for several hours to allow a gel to cover the surface, and then were removed and placed on a glass plate to dry at room temperature. They were subsequently washed in methanol to separate them from the glass, and finally sintered at 400-800 °C to consolidate the coating. From SEM observations, the authors identified the thickness of the coatings to be < 100 nm and composed of nanoparticles.

No publications on the coating of powder particles with BN was found for inclusion in this review, however depositing BN via sol-gel processes is possible, as shown by Kayani et al. [149]. In their study, the authors used Boron Nitrate and Boric Acid

dissolved in water, with ammonia as a pH stabiliser, investigating variations in the sol composition. They succeeded in depositing BN, and annealing at 300 °C formed a predominantly (002) oriented h-BN structure, assessed by XRD, when using Boric Acid. The film thicknesses were in the 3-4 μm range, and no surface or cross-section analysis was presented to analyse the porosity or surface morphology.

As with electroless plating, sol-gel processes are highly scalable and, in the case of powder substrates, are only limited by the container size and volume of solution. Furthermore, as they are wet chemical processes, the penetration and coverage of coating material into the complex powder bulk is an advantage, as long as sufficient agitation is provided. However, in order to consolidate a non-porous coating, the drying stage/s of the process must be optimised to avoid agglomeration of powder, and which, in the case of the high-temperature resistant BN ceramic, could lead to undesirable phase transformation and contamination.

2.4 Boron Nitride (BN)

Boron Nitride is an engineering ceramic, with many desirable properties for multiple applications. The Cubic form of BN (c-BN) has high hardness (30-70 GPa [3, 150, 151]), second only to diamond, desirable in tooling applications, where hardness and wear resistance are required to extend tool life.

Additionally, BN has hot (< 1300°C) oxidation resistance [3], with high thermal conductivity [152-154], and can be used for machining carbon containing materials, as the solubility of C in BN is low [155, 156]. The electrical properties of c-BN (such as the high breakdown strength, 8 MV/cm [153]) also have potential applications in the field of electrical insulation materials and semiconductors.

2.4.1 Phases

There are a number of BN phases, separated by the arrangement and types of bonding which form different structures, diagrams of which are shown in Figure 17.

Hexagonal (h-BN), Turbostratic (t-BN) and Rhombohedral (r-BN) structures are composed of solely sp2 bonding. The h-BN phase is composed of layered hexagons, with alternating B and N atoms, the layers repeat in an A-A'-A order, where A' refers to a layer with the same in plane bonding as A, but it is rotated by 30° around the c-axis [157]. Weak (relative to the covalent bonding) van der Waals bonds connect the layers. Analogous to Graphitic Carbon, h-BN is lubricious, sometimes called 'white graphite', and is used for applications where non-conductive dry lubricant is required.

t-BN, not pictured in Figure 17, is a disordered form of h-BN, where the in-plane structure is preserved, however the c-axis of the individual layers is angled, giving rise to a curved layer structure as shown via High Resolution Transmission Electron Microscopy (HRTEM) imaging by Li et al. [158]. t-BN structures are predominately observed in materials, specifically thin films, with low crystallinity [3]. r-BN again

preserves the in-plane bonding of h-BN, but in-plane translation of the basal planes leads to an A-B-C stacking arrangement.

The Cubic (c-BN) and Wurtzite (w-BN) structures are formed of sp3 bonds and analogous to cubic and hexagonal diamond, with A-B-C and A-A'-A stacking respectively [153]. Explosion phase BN (E-BN), named due to the method of formation used in its discovery by Batsanov [159], now called Extra-diamond phase, is a less understood BN structure. It was proposed by Olszyna et al. [160] that this consisted of a hexagonal structure with an A-B-A stacking sequence, and mixed sp2/sp3 bonding with a 1:1 ratio. Subsequently, Pokropivny [161] proposed that the structure was instead a fullerene derivative (see Figure 17) formed of sp3 bonds.

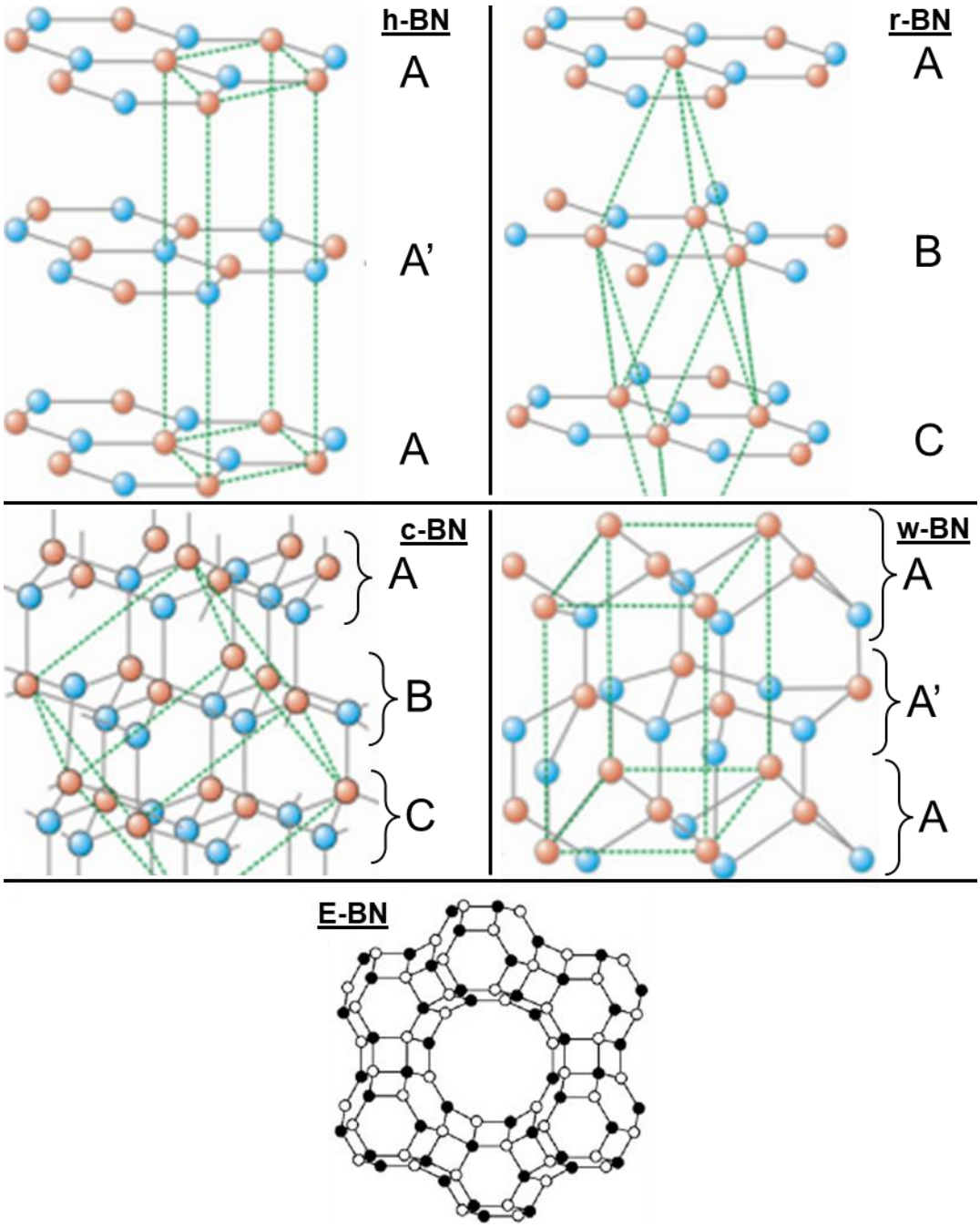

Figure 17 - The 5 main phases/structures of BN, and the layer sequences they follow, h-BN and r-BN contain sp2 bonds, c-BN and w-BN contain sp3 bonds, E-BN contains both sp2 and sp3 bonds in a 1:1 ratio, h-, r-, c- and w-BN diagrams modified from [157], E-BN diagram modified from Pokropivny [161]. The colours of B and N atoms are not specified as the structures are 1:1 stoichiometric and as such either colour can be either element.

2.4.2 Boron Nitride PVD

2.4.2.1 Requirements for depositing c-BN

As BN is a non-conductive ceramic, deposition from BN targets via magnetron sputtering requires the use of RF power, and therefore as with all ceramic materials it deposits at low rates. Alternatively, to utilise the greater deposition rates achievable with DC sputtering, heated B targets (where the heating increases the electrical conductivity, as shown by Hahn et al. [162]) or conductive Boron Carbide (B_4C) targets can be used [163]. However all three options have drawbacks, as the heating of a B target has the potential to damage the permanent magnets in magnetrons, and the use of a C containing target will inevitably lead to doping of the resultant film with undesirable C content.

When depositing BN the structures (summarised in Figure 17) formed are highly dependent on the parameters used. As reviewed in the seminal publications by Mirkarimi et al. [3], Kulisch and Ulrich [43] and Reinke et al. [164] there are many interdependent variables, focused on the energy input to the nucleating or growing film, that contribute to formation of these structures. For nucleating and growing the cubic phase, c-BN, it has been found that significant energy input via ion bombardment is required. In addition to the kinetic and thermal energy provided by ions, heating of the substrate has been shown to influence the formation of c-BN. Without energy input amorphous films with h-BN bonding have been shown to form by Abbas et al., using no applied substrate bias and at room temperature [165].

Both bias assisted sputtering and ion beam assisted sputtering have been used for depositing BN films, and whilst this thesis focuses on the former, results from the latter inform on the mechanisms and parameter thresholds for producing c-BN. Mirkarimi et al. [3] in their review produced a general diagram showing the parameter spaces for nucleating c-BN in thin films, see Figure 18 a). As can be seen from this figure, at low ion energies and ion current, h-BN structures are formed. As the two parameters are increased this transfers into a region where c-BN structures are formed. A further increase leads to a situation where the ion bombardment is sufficient

to remove material previously deposited, leading to low c-BN content and a no growth condition.

It should be noted at this stage that the type of biasing, whether RF or PDC is sometimes not stated by authors in literature, and if PDC is used full parameters (pulse width and frequency) are sometimes not complete. The studies prior to the year 2000 are assumed to have been carried out with RF bias.

Kulisch and Ulrich [43] collated parameters and results from coatings produced via IBAD, see Figure 18 c), where the authors have related the ion/atom ratio and the ion energy to produce a quantitative diagram similar to that of Mirkarimi. Note that, as described in Section 2.1.8, these parameters/metrics are relatively simple to gather in IBAD processes compared to the measurement of ion energies and fluxes in non-static plasma setups, and so relating this diagram to studies concerning bias assisted deposition is difficult. Regardless, both parameter space diagrams depict similar trends for formation of the hexagonal and cubic structures of BN. In their review the authors also suggested a set of limiting parameters for c-BN formation, which were a minimum substrate temperature of 120 °C, ion to B atom ratio of 0.6, and ion energy of 55 eV.

An additional complication in the deposition of c-BN thin films is caused by the residual stress in the coatings. The high intensity of bombardment introduces large compressive stresses, for example ~4-11 GPa for a film grown on Si substrate at 150 V bias/350 °C by Abendroth et al. [166], or an extreme value of 29 GPa for a film grown at 200 V/350 °C by Sell et al. [167]. These internal stresses, if not accommodated or relieved, lead to delamination of the coating from the substrate material, as the coating ‘wants’ to expand, and therefore buckles and peels [3, 168]. Generally, when depositing films via PVD, an increase in thickness will lead to an increase in the internal stress [27], this is also true when depositing BN, and this

combined with the aforementioned stress produced when promoting c-BN formation is a major barrier to the realisation of thick (> 1 µm) c-BN films.

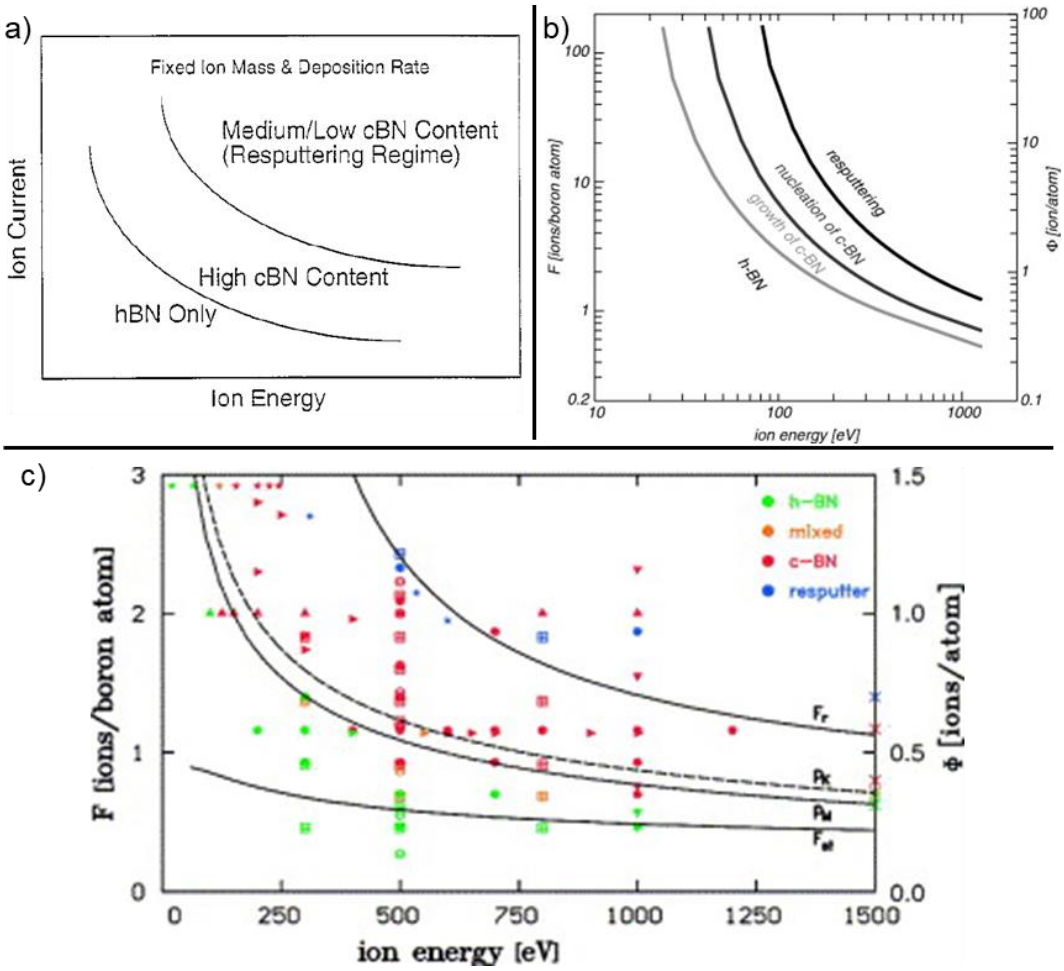

Figure 18 - General a), modified from Mirkarimi et al. [3], semi-quantitative b), modified from Kulisch et al. [169] and quantitative IBAD c), modified from Kulisch and Ulrich [43] parameter spaces for the nucleation of c-BN films, at low ion energy and low ion current (or ion/atom flux) only h-BN nucleates, increasing these parameters promotes the nucleation of c-BN, leading to mixed phases, followed by cubic phase, and finally resputtering of the film.

One technique for reducing the residual stress, and also something that has distinguished the mechanism of nucleation from the growth mechanism of c-BN thin films is the use of a varied substrate bias. Hahn et al. [170] deposited films at 350°C on Si with 80-90% cubic content by setting the substrate bias at 150 V for a short period (1 min), in order to nucleate the cubic phase, and then lowering the substrate bias for the growth of the coating. The authors found that a drop in cubic content only

occurred at growth voltages lower than 60 V. They concluded that the mechanism for growing c-BN film subsequent to nucleation was epitaxial above a certain bombardment momentum threshold.

Litvinov et al. [171, 172] also observed the reduced bias phenomenon. When depositing BN on Si at a very high temperature (1000 °C), the authors nucleated the cubic phase at 96 V,and observed cubic growth in films with biases lowered to 56 V. In addition to this, the reduction in bias also led to both increased deposition rate (as less resputtering of the film occurred) and improved crystallinity as observed from the sharp Reflection High Electron Energy Diffraction (RHEED) patterns.

Multiple parameter changes were investigated by Gao et al. [173]. The authors firstly observed an increase in the cubic content (measured from the FTIR spectra) with increased deposition time. At 10 min the cubic F_2TO (~1065 cm^{-1}) phonon mode was dominated by the h-BN E_{1u}TO (~1367 cm^{-1}) mode, and as the time was increased by steps of 10 min to 40 min the cubic mode became more prominent. Furthermore, the authors investigated the two-step bias nucleation and growth technique in conjunction with the effect of changing Ar:N_2 ratio. After depositing a thin nucleation layer of c-BN at 250 V and 470 °C, films were grown at different bias voltages and Ar flows. When pure N_2 was used, the threshold bias for cubic growth was higher than the threshold bias when using mixed Ar and N_2 flows, 150 V and 125 V respectively. This can be explained by the difference in momentum, as suggested by Hahn et al. [170] and reviewed by Kulisch and Ulrich [43]. The mass of N is lower than Ar, so for a constant momentum (or kinetic energy) threshold a decrease in mass will require an increase in velocity, and therefore accelerating (bias) voltage.

This reduced ion bombardment technique has also been utilised by Bewilogua et al. [174] who used 200/130 V to nucleate/grow at 600 °C, by Wang et al. [175] who used 350/200 V to nucleate/grow, Jiang et al. [176] who used comparatively low bias

voltages of 75/50 V to nucleate/grow at 300 °C and Li et al. who used 120/50V at 450 °C [158, 177].

2.4.2.2 Phase characterisation

As the bonding in Boron Nitride is sensitive to infrared radiation, a common technique used to analyse coatings is Fourier Transform Infrared Spectroscopy (FTIR). As reviewed by Mirkarimi et al. [3], the frequencies absorbed by thin film Boron Nitride can shift due to defects, thickness effects and internal stresses. Compressive internal stresses shift the peaks to higher wavenumber, and tensile to lower wavenumber. Additionally, the crystallinity of the material also changes the width of the peaks, with nanocrystallinity and amorphous content broadening the peaks. As such, to build up a clear picture of the different peak values corresponding to different vibrational modes present in the different BN structures, values reported in literature were collated and are shown in Table 3.

Similarly, X-ray Photoelectron Spectroscopy (XPS) is a technique used for probing the near surface (~ 10 nm) region of a sample. This technique provides information on the bonding present in this region, via the calculation of binding energies of ejected photoelectrons. The values corresponding to sp2 and sp3 bonding, that have been reported in literature, are contained in Table 4. Furthermore, due to the differences in bonding, where sp2 bonds include a π bond, a plasmon peak ~9 eV above the B1s and N1s peak is present for sp2 bonding. Distributions calculated from these values are contained in Table 5.

From the relative intensities of the peaks corresponding to the c-BN F_2TO (~1065 cm^{-1}) and h-BN $E_{1u}TO$ (~1367 cm^{-1}) modes, an approximation for the c-BN content in a BN thin film can be calculated via the Equation 2. below [3]:

$$\%cBN \approx \frac{I_{1065}}{I_{1065} + I_{1367}} \qquad (2)$$

Table 3 - FTIR peak positions and corresponding vibration modes gathered from BN published in literature, unless specified the data is from thin film coatings, some values that are not reported in the original publication are estimated based on reading the FTIR spectra. Nominal BN values are taken from the review by Mirkarimi et. al. [3].

Vibration mode	Wavenumber (cm^{-1})	Reference
c-BN F_2TO 1065 [3]	< 1050	[178-181]
	1050-1059	[162, 176, 182-185]
	1060-1069	[3, 170, 176, 177, 186, 187]
	1070-1089	[151, 176, 177, 184, 188-190]
	1090-1100	[151, 162] [166]
	1100	[163, 191-197]
	1100 <	[180]
	Value unreported	[198]
c-BN F_2LO 1340 [3]	1302-1305	[199]
	1310	[3]
	1340 (approximated)	[182]
w-BN A_1LO 1090 [3]	No values reported	
w-BN E_1TO 1120 [3]	1120	[181]
	1125	[200]
	1130	[181]
	1171	[201]
	Value unreported	[202]
w-BN E_1LO 1230 [3]	1224	[179]
	1250	[200]
h-BN A_{2u}TO 783 [3] B-N inter-plane bending	< 750	[189, 203, 204]
	770	[181]
	780	[3, 166, 186, 187, 192, 202, 205, 206]
	781-800	[180, 184, 197, 207]
	800	[162, 191, 193, 194]
	800 <	[185, 206]
	Value unreported	[151, 170, 188, 190, 195, 198]
h-BN A_{2u}LO 828 [3] B-N-B out of phase stretching	820	[204]
h-BN E_{1u}TO 1367 [3] B-N in-plane stretching	< 1340	[181, 189]
	1370	[3, 187, 205]
	1380-1389	[156, 181, 192, 197, 202, 207]
	1390-1399	[151, 184, 186]
	1400	[162, 166, 191, 193, 194, 196]
	1400 <	[180, 203, 206]
	Value unreported	[170, 188, 190, 195, 198]
h-BN E_{1u}LO 1610 [3]	1600, 1610	[208], [204]
	Value not reported	[193]
E-BN	450	[161]
	550	[161]
	700	[161]
	800	[161]
	907, 927, 940, 960	[201], [180], [161], [181, 209]
	1030	[161]
	1110	[161]

Vibration mode	Wavenumber (cm^{-1})	Reference
	1200	[161]
	1224-1234	[181]
	1250-1252, 1260 (Tensile B-N)	[160, 180, 209, 210], [201]
	1400, 1409	[161], [201]
	1450-1480, 1492	[160, 181, 209, 210]
	1500	[181]
	1580 (Tensile B-N)	[160, 201]
	1600, 1645, 1650, 1675	[161, 181, 209, 210]
	1785	[181]
	2000-2500 (intermolecular mode)	[181]
	3750	[181]
B_2-NH/B-NH_2 (NH/NH_2 stretching)	~3240 (Shoulder) 3370, 3392 ~3430 3435-3565	[206] [160], [204] [206] [211, 212]
N-H Wagging	820	[204]
B-H Bond stretching	2485 2505	[213] [211, 212]
B-OH Out of plane torsion	520	[211, 212]
B-OH/B-OH_2 Hydroxyl stretching	3204, 3208 ~3000-3500 ~3500-3600 3690	[204], [203] [213] [206, 214] [211, 212]
B-OH	832	[204]
B-OH in-plane bending	1000-1300	[213]
BO_3 B-O bond stretching	1200-1550 1300-1450, 1465	[215] [213], [204]
BO_4 B-O bond stretching	1100-850 883	[215] [204]
B-O-B bond bending	690-770 713	[215] [204]
O-B-O	490	[206]
B-N-O	920-930 1100-1160 1181	[206, 216] [206, 215] [203]
Boron Oxide	Values unreported	[216]

Table 4 - B1s and N1s components reported in literature for sp2 and sp3 bonding in boron nitride gathered from XPS.

Element	Component	Component/ eV (FWHM)	Reference
B1s	B-B	187.1	[217] No fitting
		187.9	[202]
		188.0	[163]

Element	Component	Component/ eV (FWHM)	Reference
	B-H	189.3 (1.99), 189.2 (2.28)	[218]
	B-N sp2	189.7	[179]
		189.8	[217] No fitting
		190.2, 190.0, 189.8, 189.6, 189.5	[204]
		190.0	[219]
		190.1	[220]
		190.2	[202] Partial fitting
		190.3	[218]
		190.3 ± 0.1	[176]
		190.5	[179]
		190.5	[221] No fitting
		190.5	[222]
		190.6	[223]
		190.7 (2.06)	[218]
		190.78	[224]
		191.2	[225]
	B-N sp3	190.5	[221] No fitting
		190.5-190.9	[226]
		190.7 ± 0.1	[176]
		190.2-190.8	[217] No fitting
		190.8	[220]
		190.8	[175]
		191	[227] No fitting
		191.0	[219]
		191.0	[163] Partial fitting
		191.5	[205] Partial fitting
		191.8	[179]
	π plasmon	+ 9	[176, 217, 226, 227]
	Bulk plasmon	+ 25	[176, 227]
N1s	N-B sp2	397.2	[179]
		397.7, 397.7, 398.0, 398.0	[204]
		397.7 ± 0.1	[176]
		398.0	[219]
		398.2	[223]
		398.3	[222]
		398.3	[225]
		398.37	[224]
		398.4	[228] No fitting
		398	[227] No fitting
		398.2	[163] Partial fitting
		398.5	[202], [221] Partial fitting
	N-B sp3	397.9-398.5	[226]
		398	[227] No fitting
		398.3 ± 0.1	[176]
		398.4	[228] No fitting
		398.5	[217], [221] No fitting
		399.0	[219]
		399.5	[179]

Element	Component	Component/ eV (FWHM)	Reference
	π plasmon	+ 9	[176, 226, 227]
	Bulk plasmon	+ 25	[176, 227]

Table 5 - Distributions of the sp2 and sp3 components of B1s and N1s energy levels in XPS of boron nitride

	sp2 component	sp3 component
B1s	190.2 ± 0.4	190.9 ± 0.4
N1s	398.0 ± 0.3	398.5 ± 0.5

2.4.2.3 Hexagonal to Cubic transformation

It has been observed by many groups ([158, 163, 177, 188, 229-234]) that the mechanism of cubic nucleation is typically composed of a sequence of layers. These layers, as observed via HRTEM [3, 177], see Figure 19, are composed of a thin layer of amorphous BN, followed by a layer of turbostratic BN, and then cubic BN, with the former two having thicknesses of 2 nm and a varied 2-5 nm in the investigation by Kester et al. [188]. An additional layer is also observed at the surface consisting of t-BN/h-BN.

This sequence is one explanation for the time dependent variation in c-BN FTIR intensity mentioned previously in the study by Gao et al. [173]. Furthermore, in the deposition of c-BN thin films it is well recognised that a 1:1 ratio of B:N is required to form the cubic phase, as this phase a has a 1:1 stoichiometry, and a deficit in either element will lead to the formation of sub-stoichiometric structures [235].

As to the underlying mechanism of cubic phase nucleation, and the appearance of the layer sequence, there are a number of theories proposed, which will be briefly described. One mechanism is called the ‘Sputter mechanism’, as proposed by Reinke et al. [164, 236] [237]. Reinke et al. have found that when intentionally sputtering

previously deposited t-BN/h-BN and c-BN with ion beams, the sputtering yield is approximately 1.5 times higher for the former [164]. Therefore they suggest that as BN is deposited on the substrate, there is initially mixed sp2 and sp3 bonding, and as the deposited material is bombarded by ions and neutrals, the sp2 bonded material preferentially resputters from the substrate, leaving the sp3 material intact.

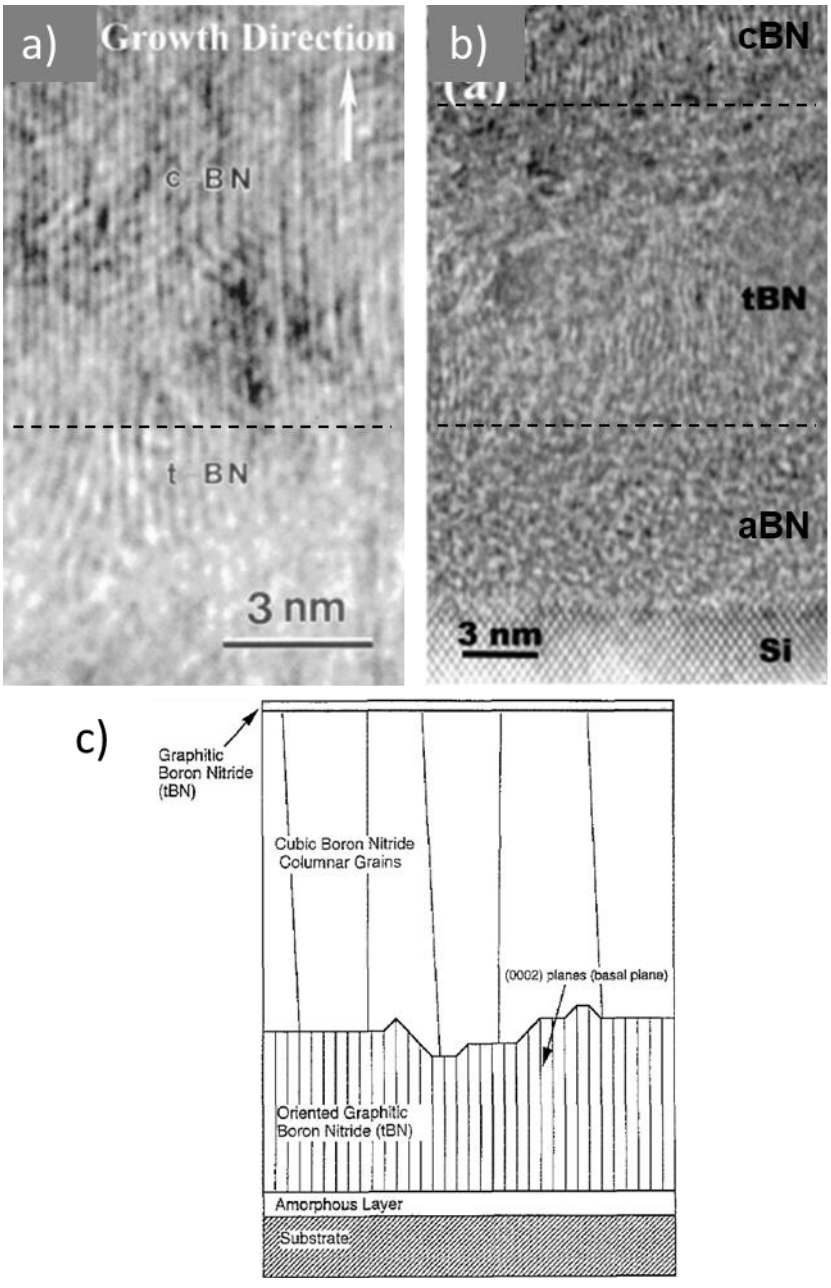

Figure 19 – The sequence of layers in c-BN nucleation, initially a thin layer of amorphous material is deposited, onto which oriented t-BN (disrupted h-BN) grows, subsequent to this cubic columnar grains form and grow perpendicular to the substrate, a) and b) HRTEM images modified from Li et al. [177], c) schematic modified from Mirkarimi et al. [3].

However, this does not satisfactorily explain the layer sequence observed in HRTEM, as from this mechanism there should be no remaining sp2 bonded material, whereas there is typically a t-BN layer, Figure 19.

Hofsäss et al. [238] have suggested an alternative mechanism based around phenomena seen in the ion bombardment of C films. The authors call this the 'Thermal Spike' mechanism and relate the interaction of implanted ions with coating material to the structures formed. They suggest that as the ions lose energy through collisions within the lattice, and at a certain point are terminated, they transfer any remaining energy to the surrounding material in the form of phonons (lattice or bonding vibrations). These localised vibrations increase the temperature and pressure to a threshold where c-BN is stable. Following this the temperature is quenched to the surrounding material, hence the name thermal spike, and the c-BN bonding remains [3].

Mirkarimi et al. [3] however, suggest that these thermal spikes are more likely to cause annealing of the film, and the release of stress and stabilisation of sp2 bonding. The stress relief is contradictory to their, in conjunction with McKenzie et al., suggestion of a mechanism, called the Stress mechanism, which fundamentally relies on stress to promote c-BN structures [239-241].

The stress mechanism is related to 'peening' of the surface by ions during deposition. This bombardment densifies the material through knock-on ion/atom collisions and through increased adatom motion (as described in Section 2.1.6) , reducing voids and introducing compressive stress in the film. From data collated on the compressive stress in deposited films compared to c-BN content (in the review by Mirkarimi [3]), an approximate stress threshold of 4-5 GPa was determined. This suggested mechanism therefore involves the modification of sp2 bonded material to form sp3 bonded material, which is corroborated by the often observed thin sp2 layer at the surface of a complete film, as this finally deposited material has not been modified.

2.4.2.4 Moisture degradation

In addition to the difficulty in adhering c-BN films to substrates due to the high internal stresses, BN films have been observed to react in ambient conditions, leading to degradation and delamination [169].

Cardinale et al. [242] systematically investigated the degradation of c-BN films in different environments. They observed that under vacuum, dry nitrogen, and importantly dry oxygen the films remained adhered and no delamination mechanism was seen. When stored in either ambient or intentionally humid environments, however, the films delaminated, in 2 weeks for the former and 3-4 days for the latter. This simple test identified that the degradation mechanism was not driven by oxidation of films, but rather by water vapour.

Thus, the authors concluded that the delamination of their films was due to a combination of factors. Firstly, the residual compressive stresses from deposition led to a stressed film, remaining adhered due to the strength of the substrate containing the stress. Secondly, as the film was exposed to moisture, the water diffused through the film along the grain boundaries, reaching the sequential interface layers (Figure 19), reacting and causing an increase in volume. This volume increase combined with the internal stress caused delamination. Equation 3. for the reaction suggested by Cardinale et al. is shown below:

$$\frac{13}{2}O_2 + 8BN + H_2O \rightarrow [(B_2O_3)_2(OH)] + 4N_2 \qquad (3)$$

This reaction was also suggested by Batsanov in the degradation of E-BN material [243].

Kim et al. [244] in their study of the delamination and degradation mechanism offer a competing view to that of Cardinale et al. [242]. The authors suggest that the rate at which degradation was seen on their samples in humid air was too high for the

mechanism to be solely dependent on diffusion of reactants through the film thickness to the a-BN/t-BN/c-BN interface. Instead, they suggest that reaction with moisture occurs at cracks and other geometrical roughness defects at the surface, leading to volume expansion, and widening of the defect, providing a path to the interface. In agreement with this, in their study Moller et al. [168] witnessed instantaneous buckling of films when breathing onto them, supporting the suggestion that a separate infiltration mechanism is in play.

It should also be noted that Cardinale et al. deposited their coatings onto large Si substrates, and subsequently scribed and snapped them into smaller pieces for distribution into different environments. This method will obviously expose the edges (cross-sections) of films, influencing the reaction of the interface with moisture.

2.4.2.5 Substrates

The research into the deposition of c-BN films has predominantly been undertaken with Si substrates. Apart from the use in applications related to electronics, Si provides a stable, smooth substrate with a well-defined structure for investigating film formation. However, limiting the research to one substrate is not conducive to the expansion of knowledge. Other substrates, a summary of which is contained in Table 6, have been investigated, through the breadth of knowledge with the combination of these coating substrate systems is not wide. This is likely due to the aforementioned issues in film adherence, and the potential reluctance of researchers to publish ‘bad’ results in attempting to solve these issues.

Table 6 - A brief summary of substrate use in c-BN coating investigations, Si is used in the majority, with other materials comparatively under investigated.

Substrate Material	Reference
Si	[151, 163, 166, 173, 174, 176, 177, 187, 199, 202, 219, 231, 232, 245-247]
Glass	[156, 248]
Ni	[185, 188, 220]
Cu	[188, 220]

WC	[174, 231, 234, 249]
Steel	[174, 201]
AlN	[157]
Diamond	[153]

2.4.2.6 Interlayer Selections

As well as the use of two-step bias bombardment techniques to reduce residual stresses in c-BN coatings, a major area of research is in the investigation of interlayers between the substrate and the BN film. These interlayers are beneficial for multiple reasons, primarily as an attempt to avoid the formation of the a-BN/t-BN interface layer, and also to contain the residual stress present in the c-BN layer.

As mentioned in Section 2.4.2.1, instead of depositing from an h-BN target using RF power, some groups have opted to use conductive B_4C targets sputtered with DC power. This has led to the development and investigation of boron carbide interlayers to improve the adhesion of subsequent BN layers.

Yamamoto et al. [163] succeeded in depositing up to 2.7 µm thick BN films at varied 300-600°C temperature which were predominantly (not quantified) cubic phase. They used a graded BCN interlayer of 350 nm thickness in between the Si substrate and the BN layer, where the N_2 gas flow was increased to form the gradient. In addition to this they also utilised the two-step bias, nucleating at 200 V and reducing ‘by a few tens of volts’ for the growth step.

From HRTEM imaging of the film cross-section, the authors saw that the thin a-BN layer typically seen at the start of cubic phase nucleation was not present. Instead, the t-BN was observed to grow on top of the amorphous B_4C/N gradient layer, and then cubic phase nucleated on top of the t-BN. The c-BN was columnar, containing crystals of ~10 nm size. The use of the B_4C target meant that whilst the majority of

the top layer was composed of B and N, there was approximately 5 at% C present in the c-BN. The authors do not mention any degradation of the film in ambient conditions.

In a further study [231], the same group transferred their interlayer methodology to tungsten carbide (WC) substrates. Intriguingly, the authors also mention that they used high speed steel substrates, but present no data for this. In depositing their multilayer system onto WC they found that they needed to deposit a titanium interlayer (500 nm), prior to the B_4C gradient layer, and also extend the duration/thickness of this from the previous 350 nm to 1-1.7 µm. Confusingly, they carried out a repeat of HRTEM imaging on the coated Si substrate (without Ti layer) rather than the WC based system. Regardless, the maximum c-BN thickness deposited on WC was 700 nm as measured by Secondary Ion Mass Spectroscopy, less than on Si.

In a subsequent study [174], the authors suggest that the stability of their coatings in ambient conditions is due to the density of the columnar c-BN structures, which they suggest reduces water diffusion to the interface. Furthermore, in testing the coating in turning (machining on a lathe) tests against graphite cast iron, the coating was observed to fail by an abrasive wear mechanism, rather than by chipping and delamination from the tool face, indicating successful adhesion using this interlayer system.

Wong et al. [234] have used Zr to form an interlayer system to adhere c-BN films to WC substrates in addition to in-situ post deposition annealing. Note that this study was carried out via ion beam sputtering with ion beam bombardment of the growing film, rather than the use of magnetrons and substrate biasing, but has been included in this review due to the interlayer selection. The authors deposited ~360 nm of Zr, followed by ~122 nm of sp2 BN and ~480 nm of sp3 BN at 680°C. They then annealed the sample at 850°C in-situ, promoting inter-diffusion of the layers. From HRTEM

images, it was observed that the Zr and sp2 BN layers had diffused to form a mixed layer, and that c-BN extended directly from the interface of the Zr/sp2-BN. The authors do not indicate whether degradation from moisture occurred.

The use of a TiN interlayer prior to a BCN-BN coating was investigated by Bejarano et al. [228]. The authors deposited the TiN (300 nm) onto Si substrates in a separate coating system and then transferred the prepared substrates to lab-scale equipment for the subsequent coating layers. They deposited a 4.6 µm layer of c-BN (note that they provided no HRTEM or FTIR data to confirm cubic content) on top of the interlayer by using 16 alternating B_4C and BCN layers (~300 nm each). There was no observed delamination of the film, and the authers suggested that the change in mechanical properties over the thickness of the film was smoother than for a thin abrupt change in layer, and as such this promoted adhesion. It was not discussed whether the alternating layers contributed to this improved adhesion rather than just the thick (~5 µm) interlayer.

Finally, as well as modification of the layer structure by introducing adhesion interlayers, the doping of BN films with minor (< 10 at%) amounts of elements in addition to B and N has been investigated. Researchers based in Sweden and Germany have included oxygen in their c-BN films deposited on Si substrates. Latterman et al. [250] and Ulrich et al. [251, 252] modified their Ar/N_2 gas flows with 1 % O_2 flow, and nucleated and grew c-BN at 350 V bias. The O content in the resulting ~2 µm thick c-BN layer was 4.6 at%, but despite this the film maintained close to the 1:1 B:N stoichiometry required for c-BN formation. The cubic content was not quantified, and the intensity of the c-BN mode in FTIR (~1065 cm^{-1}) was only slightly higher than the h-BN mode (1367 cm^{-1}), however the film stress was measured and had reduced to 9 GPa form 29 GPa as measured in their previous work without O addition [167].

2.4.3 Alternative BN deposition

Two alternative processes for depositing BN containing coatings are summarised below, with the advantages and disadvantages highlighted.

CVD

Kimura et al. [253] formed BN coatings using diborane (B_2H_6) and ammonia (NH_3) in a H_2 atmosphere at a temperature of 1050°C onto Si substrates. These films had a thickness in the range of 0.4-1.8 µm and their electrical properties (conductivity) were modified when exposed to water vapour. The authors do not report what phase their films were, but noted that the films were unchanged after storage in atmosphere and multiple moisture cycles.

Guimon et al. [218, 254], in contrast, used BF_3 and NH_3 as reactants to form their coatings at 1000°C, composed of t-BN/h-BN, onto SiC substrates. In their XPS analysis, they reported that there was a significant contribution from O to the composition (6 and 17 at% for the two samples produced), throughout the film, not indicative of surface level contamination.

In their review Mirkarimi et al. [3] note that the first processes used for depositing c-BN coatings were Plasma Enhanced CVD processes. These operate differently to traditional CVD, and as highlighted by the more recent study by Chakrabarty et al. [179], use RF or microwave frequency supplies to excite plasma, with this activating the reactants rather than the thermal input via heating. This also allows the acceleration of reactants and carrier/inert gas atoms to the substrates via biasing, critical in forming the cubic phase. Chakrabarty et al. produced BN coatings composed of mixed phases, with the wurtzite predominant when applying bias (400 V), giving a hardness of 25.0 ± 4.3 GPa. The authors do not state whether the coatings remained adhered in ambient conditions over time.

Whilst CVD in its basic form (non plasma-enhanced) is simpler and cheaper to set up than sputtering equipment, the requirement for bombardment and therefore plasma negates this advantage over magnetron sputtering. Furthermore, the need for increased temperatures, despite the use of plasma, also prevents the use of temperature sensitive substrate materials. Finally the main detraction from the use of CVD, as correctly pointed out by Mirkarimi et al. is that the reactants and exhaust products can be highly hazardous, Diborane is explosive, and Boron Trifluoride is toxic.

Thermal and Plasma Spraying

Another alternative method for producing BN containing coatings is via Spraying, with variants of this such as High-Velocity Oxy-Fuel spraying (HVOF) and Plasma spraying [21], utilising the high temperature stability, hardness and lubricity of the material [255]. Note that these techniques typically are not used to form pure coatings, with different feedstock materials and binders combined to form adherent layers on substrates. The essence of the techniques are that a feedstock material, in powder form, is accelerated by a combusting fuel, or via flow of gas with an electrical potential applied, to propel the material and impact the surface of the substrate, see Figure 20.

An example of the deposition of (relatively) pure BN is in the plasma spraying by Madhav Reddy et al. [256]. The temperature and velocity of the sprayed material was 4200 K and 500 m/s respectively, with the plasma gas consisting of pure N_2 or a N_2/H_2 90/10% mixture. Note that the authors were not intending to deposit a coating, and were instead investigating the phase transformation to c-BN through the spraying process, but this has been included in this review to demonstrate that c-BN can be formed by these techniques.

The authors used an amorphous BNCO feedstock material (with short range sp2 bonding), adding additional boric acid (H_3BO_3) and elemental B to increase B content

in the final material. The use of these meant that the final deposits contained BN, but were also contaminated by C and O, in one sample the approximate ratio (determined via EELS) was 40B:40N:< 20C at%. Furthermore, the c-BN formation was inefficient, with a maximum of 8 % c-BN volume attained, in grains < 20 nm in size. They suggested that the use of an amorphous feedstock lowered the pressure requirements for the transition to c-BN, and prevented an interstitial h-BN structure forming.

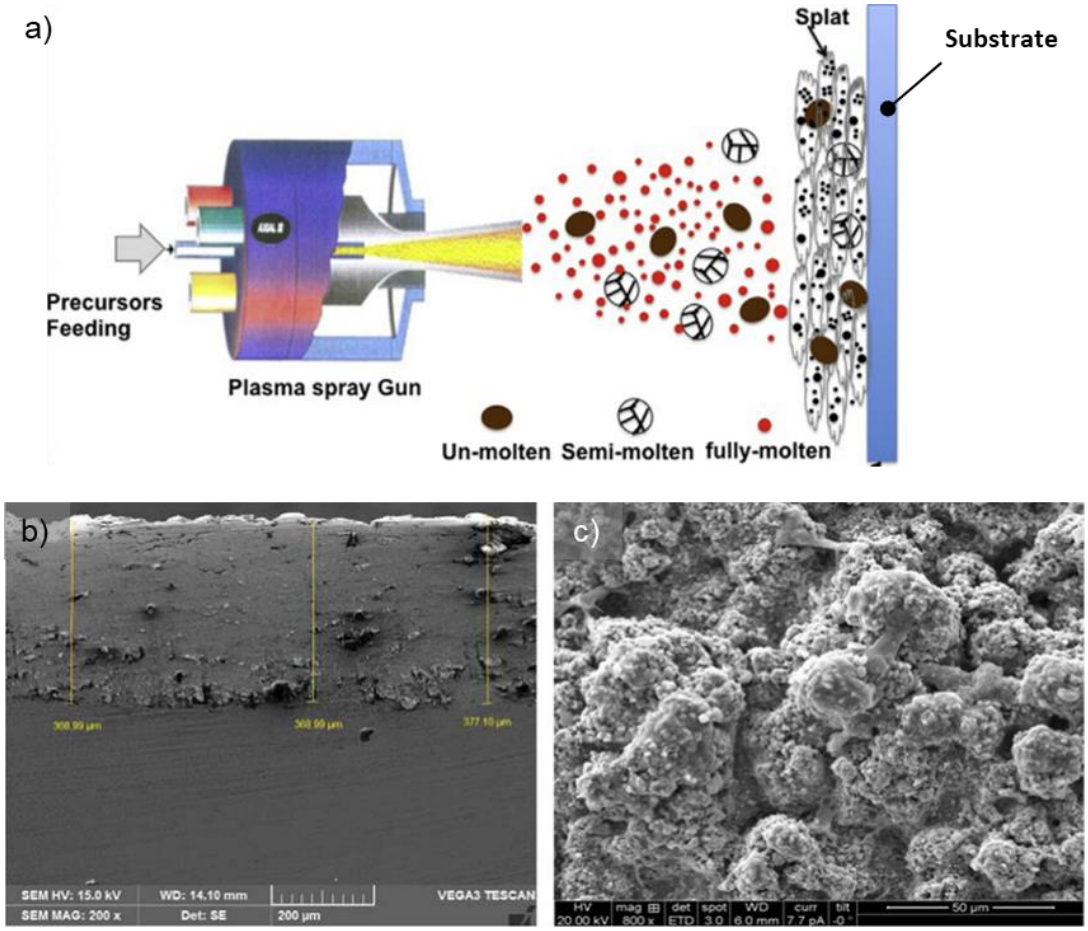

Figure 20 – a) Schematic detailing the plasma spray process, modified from Madhav Reddy et al. [256]. The powder precursors are fed into a gun, mixed and heated with a carrier gas, a plasma is then formed and the material, in a mixture of states, is accelerated to the substrate, forming splats, b) cross-section, and c) surface SEM images of Inconel 718/c-BN coating, modified from Shivalingaiah et al. [257].

Shivalingaiah et al. [257] and Padmavathi et al. [258] both studied the addition of BN powder (c-BN specifically for the former) to metal and ceramic powder feedstocks. The former increased c-BN content from 0 to 20 wt% in an Inconel 718 feedstock, and the latter added 10 wt% BN to two metal carbide feedstocks. Predictably, given that c-BN has a high hardness, the increase in wt% in the Inconel matrix powder increased the hardness of the resulting coating by 0.47 GPa (20 wt% c-BN) to 5.15 GPa. Though given that pure c-BN PVD/CVD coatings can have hardnesses in the 30-70 GPa range [3, 150, 151], this is not significant. In contrast, the BN added to the Tungsten and Chromium Carbide coatings investigated by Padmavathi et al. [258] modified the wear properties of the coatings. The BN doped material exhibited a lower coefficient of friction and sliding rather than ploughing behaviour in wear tests. From this it would be logical to assume that the BN was in the hexagonal phase.

However, as is seen in the studies referenced, the morphology and scale of sprayed coatings is different to that of PVD and CVD coatings. As the material feedstock is powder, the deposition rate is limited by the feedrate, and as such can be much higher, with thicknesses greater than the typical 0-10 µm of thin films (~300 µm in Figure 20 c), an advantage. However, whilst coatings deposited via CVD and PVD are built up atomically, sprayed coatings tend to deposit in ‘splats’ with a mixture of molten, partially molten and solid particles impacting the substrate, see Figure 20 a) [256]. There is also the possibility for carrier gas to become trapped in the growing coating, leading to porosity ~2 % in study by Padmavathi et al. [258].

The nature of this deposition mechanism leads to a lower density of deposit, with many routes for crack propagation, unsuitable for producing coatings from BN without additional contaminating binders. The rough surface finish as seen in the papers by Shivalingaiah et al. [257] and Padmavathi et al. [258] is also unsuitable for tool coatings, as this will create an uneven cutting edge, and sub-par surface finish on the machined component.

2.5 Summary

This review has highlighted the current status of published literature focused around the deposition of BN coatings onto powder and planar substrates. The review has predominantly considered well established PVD processes, which are relatively clean and lack the substance hazards of chemical based techniques. The desirable material properties of BN, it's hardness, hot oxidation resistance and reduced reactance with ferrous materials over diamond, and its electrical properties, have been presented.

From this, multiple gaps in the current knowledge have been identified. BN coatings, in particular those with c-BN structures, are difficult to deposit, and require intensive parameters in order to nucleate and grow. The investigation of low temperature deposition of c-BN has been underinvestigated. Furthermore, there has been mixed success in the use of adhesion interlayers, particularly related to Boron Carbide. The potential avenues for investigation in this are related to the transfer of these existing coating methodologies and parameter spaces onto uninvestigated substrate materials such as steel. As seen in the Aims and Objectives (1. Introduction), it is proposed to investigate the use of a novel interlayer, drawing on the work in literature, to improve adherence of BN to steel substrates. This will also inform on the mechanisms of c-BN formation in coatings, intending to contribute to previously suggested mechanisms, none of which fully explain the nucleation and growth of c-BN coatings. This work will is presented in *Chapters 5* and *6.*

Furthermore, it has been identified that the majority of investigation into BN and specifically c-BN deposition onto planar substrates has taken place in highly controlled research equipment. As such there is a need for assessing the first steps in scaling up BN deposition for larger batches, applicable to applications such as tooling. The objective corresponding to this intends to address this gap through the use of large volume industrial coating equipment, this is presented in *Chapter 6*.

From the review of coating of powdery substrates via PVD, an exciting opportunity for modifying powder feedstocks for additive manufacturing processes has been identified. The understanding of how material is transferred to the surface of particles and the growth of coatings is still missing key components. The role of agitation in aiding the coverage of the total powder particle surface also requires further investigation. Finally the apparent lack of investigation into the coating of powdery substrates with BN is a clear gap in the current knowledge, and must be analsyed for homogeneous doping of ceramic materials via PVD. The objectives drawn from these gaps are focused around developing existing powder coating equipment, first investigating the deposition of metallic materials, which are simpler to deposit than ceramics, before moving to the more complex deposition of BN. This work is presented in *Chapter 4*.

3. Materials and Methodology

Introduction

This chapter details the equipment and parameters used for the deposition and post-processing of boron nitride thin film coatings, with interlayers and modification techniques, on multiple substrates, and the deposition of coatings onto powder. The analysis techniques used to characterise the material are briefly described and explained, highlighting the information each technique provides, in order to facilitate the understanding of the results in later sections.

3.1 Substrate Material and Preparation

Coatings were deposited onto both flat surfaces and powders, the material and preparation subsections that follow have been separated accordingly. Flat surfaces are referred to as 2D from this point onward as the lateral dimensions of the surface are considered infinite compared to the coating thickness and the depth of interaction with the substrate. Powders are separated from this as the investigations are focused on the deposition of coatings onto 3D surfaces.

3.1.1 2D substrates

Multiple 2D substrate materials were used in this project. 316L steel sheet (1 mm thickness, Smiths Metal Centres, Nottingham) was guillotined from sheet into 10x10 mm squares. M42 steel (10 mm diameter round and 25 mm square, West York Steel) was Wire EDM'd into 2 mm thick plates.

Steel surfaces were prepared for coating by grinding with Silicon Carbide abrasive papers with decreasing grit size, P240, P400, P800, P1200, P2500 and P4000 (MetPrep). This was followed by polishing using 1 µm (RS Components) and 0.25 µm (RS Components) diamond paste on cloths. In between each abrasive size substrates were cleaned with detergent and air dried to remove remaining abrasive. Following

this preparation, some 316L substrates were separated into a second group and then abrasive grit blasted to introduce uniformly random morphology to the surface. Samples were blasted with Alumina Grit (Guyson Media, F70 grade, 212 µm particle size) at a pressure of 3 bar and distance of 50 mm for approximately 5 seconds each.

Glass slides (thickness 1 mm, Agar Scientific) and Silicon wafers (Single crystal (100) orientation, double side polished, Inseto (UK) Ltd) were used with surface morphology as received. These substrates were scribed with a diamond scribe and shattered into pieces approximately 10x10 mm to maximise the total number of samples coated.

Following surface preparation all samples were ultrasonicated in Acetone followed by Industrial Methylated Spirit (IMS) for 10 min each, then dried with compressed air.

3.1.2 Powder

Multiple powder materials were used as substrates in this thesis, with details summarised below.

Gas atomised pure Cu powders (>99.9 %, ECKA Granules, Germany) in two size distributions were used, named Cu-Coarse (D10: 15.4 µm, D50: 39.4 µm, D90: 59.6 µm) and Cu-Fine (D10: 3.1 µm, D50: 7.3 µm, D90: 19.0 µm). 5 g of powder was used per batch.

Nitrogen gas atomised pure Ag-999 powder (Cookson Precious Metals LtD.) with a size distribution (nominal 15-45 µm) displayed in Figure 21. 5g was also used per batch.

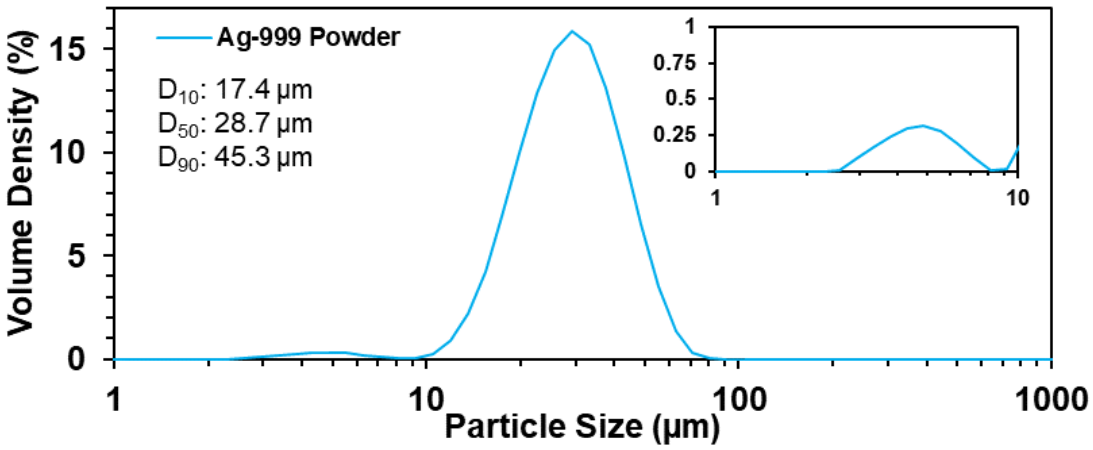

Figure 21 - Particle size distribution for the as-received Ag-999 powder.

Gas atomised 316L austenitic stainless steel powder, CT PowderRange 316L F (Carpenter Additive) was also used for the powder coating trials in this project. This powder has a size distribution that is optimised for SLM additive manufacturing. Composition and distribution from the manufacturer data sheet are shown in Table 7 and Table 8 [259].

The powder was mechanically sieved into two ranges, see Figure 22, using a 25 µm sieve, for assessing the behaviour of the lower and upper ranges, named 316L-Coarse and 316L-Fine. 5g was used per coating batch.

Table 7 - Elemental composition in wt % of the 316L powder used as the substrate in the powder coating trials [259].

Composition (wt %)											
C	Cr	Cu	Fe	Mn	Mo	N	Ni	O	P	S	Si
0.030	17.0-18.0	0.8	Bal	2.00	2.00-2.50	0.10	12.0-13.0	0.10	0.030	0.015	0.8

Table 8 - Particle size distribution values for the as supplied 316L powder [259].

Size	Value
-15 µm	5 Volume %
+45 µm	3 Weight %
D10	18-24 µm
D50	32.5-34.4 µm

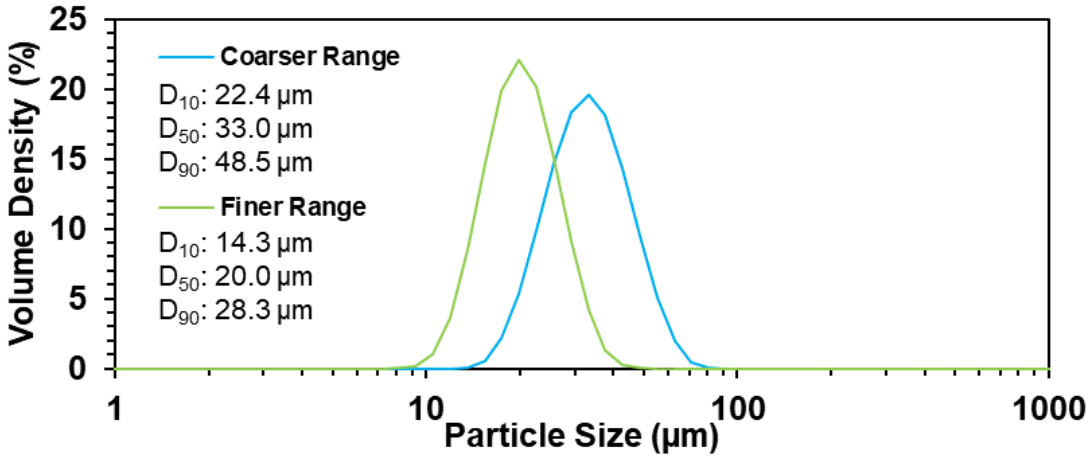

Figure 22 - Particle size distributions for the sieved 316L powder, 316L-Coarse and 316L-Fine.

3.2 Magnetron Sputtering Physical Vapour Deposition

Two different PVD coating systems were used in this project, with use defined by the type of substrate used, 2D substrates or powders.

3.2.1 TEER Coatings Ltd. UDP 650 – 2D substrates

This magnetron sputtering equipment is a programmable industrial coating rig capable of both large-scale production and laboratory-scale research, and uses Closed-field Unbalanced Magnetron Sputtering as is outlined in Section 2.1.3. A schematic setup of this equipment is shown in Figure 23 a), with photo in Figure 23 b), and consists of 4 magnetrons arranged at 90° angles around a circular substrate holder. This substrate holder can be rotated to allow the substrates to pass in front of each magnetron.

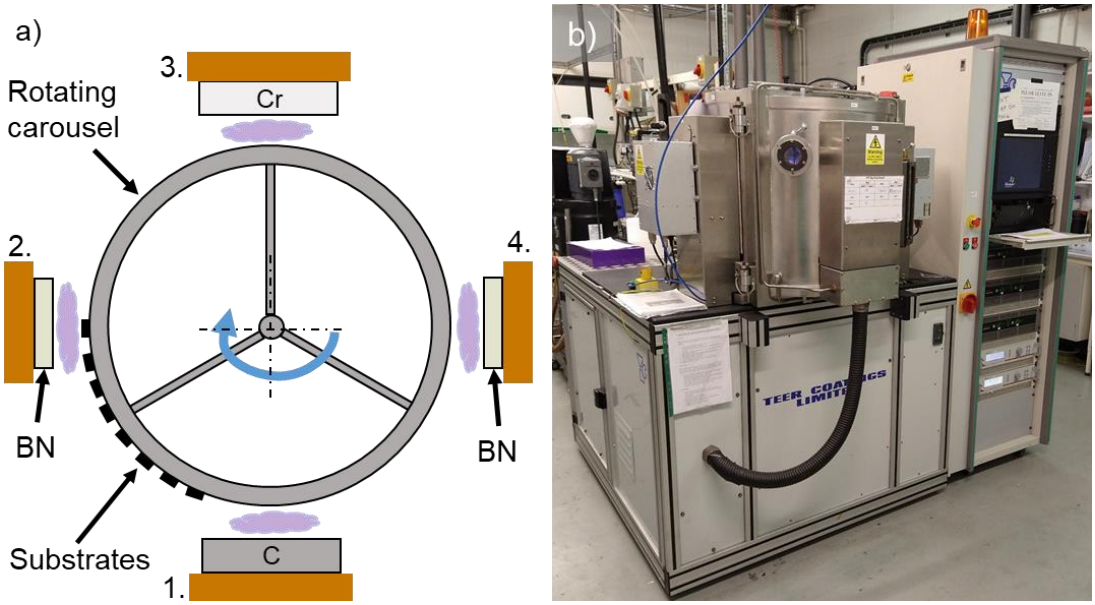

Figure 23 - a) Schematic of the TEER UDP 650 system, highlighting the 4 magnetron setup and rotating substrate holder, b) Photo of the system in the lab.

The magnetrons, hereafter labelled 'Mag #' corresponding to the numbering in Figure 23 a), are connected to independent power supplies allowing full control of each target individually. DC power can be applied to all of the magnetrons, and RF power can be applied to Mag 2 and Mag 4. Rectangular targets were used with DC power on Mag 1 and Mag 3 with dimensions 380 x 175 x 12 mm. Circular targets were used with RF power on Mag 2 and Mag 4 with dimensions 57 mm diameter and 3 mm thickness. Target materials used in this project are detailed in Table 9.

Table 9 - Magnetron sputter target materials used for depositing thin film coatings.

Material	Purity	Dimensions	Supplier
Boron Nitride	99.5%	57 mm Ø, 3 mm thick	Kurt J. Lesker Company, Testbourne Materials
Boron	99.9%	57 mm Ø, 3 mm thick	Kurt J. Lesker Company
Graphite (C)	99.5%	380 x 175 x 12 mm	TEER Coatings Ltd.
Chromium	99.5%	380 x 175 x 12 mm	TEER Coatings Ltd.
Aluminium	99.5%	380 x 175 x 12 mm	TEER Coatings Ltd.
Titanium	99.6%	380 x 175 x 12 mm	TEER Coatings Ltd.

The substrate holder can be held at a floating potential or a negative bias (0-600 V) can be applied via a power supply independent to the magnetrons. This substrate bias can be configured as DC or PDC, all substrate bias used in this project was PDC to reduce the probability of charge accumulation and subsequent arcing from the holder. Substrates were attached to the substrate holder via double sided Copper Tape (Agar Scientific), or were rested on ledges attached to the substrate holder, see Figure 24 a) and b).

Figure 24 - Photos of the two different arrangements of substrates on the holder, substrates are uncoated, a) stuck to the holder using double side adhesive copper tape, materials from top to bottom, silicon, steel, glass b) resting on bent stainless steel ledges, 2 steel coupons.

Gas was introduced into the chamber via Mass Flow Controllers (MFCs), with up to 4 gases connected to the equipment, and up to 3 usable at one time. The gases used in this work were Argon (99.999% purity, Pureshield BOC) and Nitrogen (Oxygen Free 99.998% purity, BOC).

The key advantage of using this industrial equipment is the ability to program recipes through a custom LabView interface. This allows precise control of the target power, gas flows, layer times and substrate rotation which facilitates blending, reactive and multilayer coating steps. An example of the recipe software interface is shown in Figure 25. Furthermore, data is logged and saved by the software for convenient analysis at a later date.

As detailed in Chapter 5 and 6, the design of the magnetrons used for BN deposition was unsuitable, and required modification. An attachment was designed and implemented as shown in Figure 26.

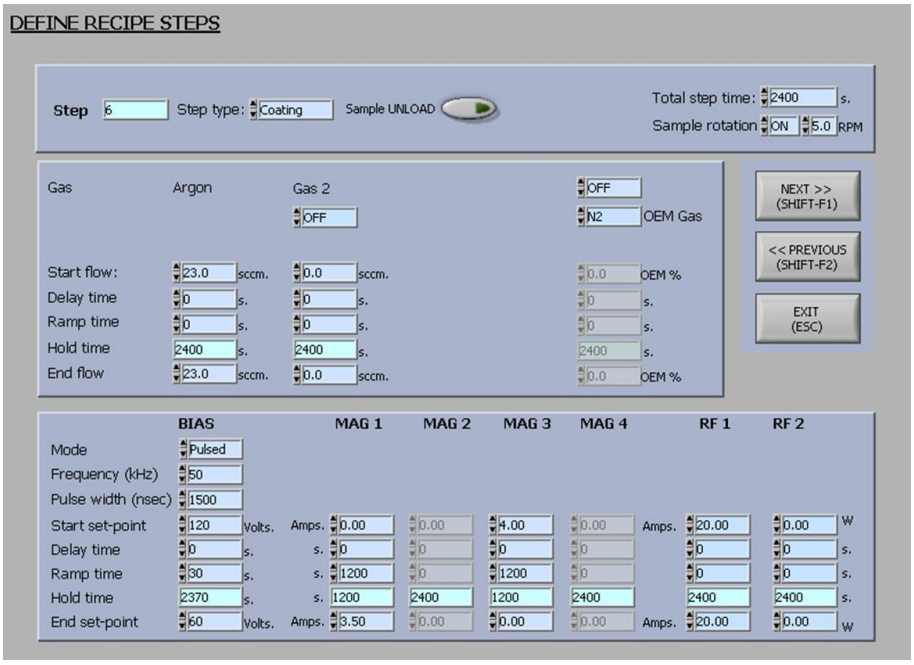

Figure 25 - Screenshot of the recipe construction software for the TEER UDP650 PVD system, each parameter can be ramped up and down, with hold times to delay changes in each step of the process, allowing creation of multilayered systems and blended interlayers. The step shown is the CrC-C step of the blended multilayer.

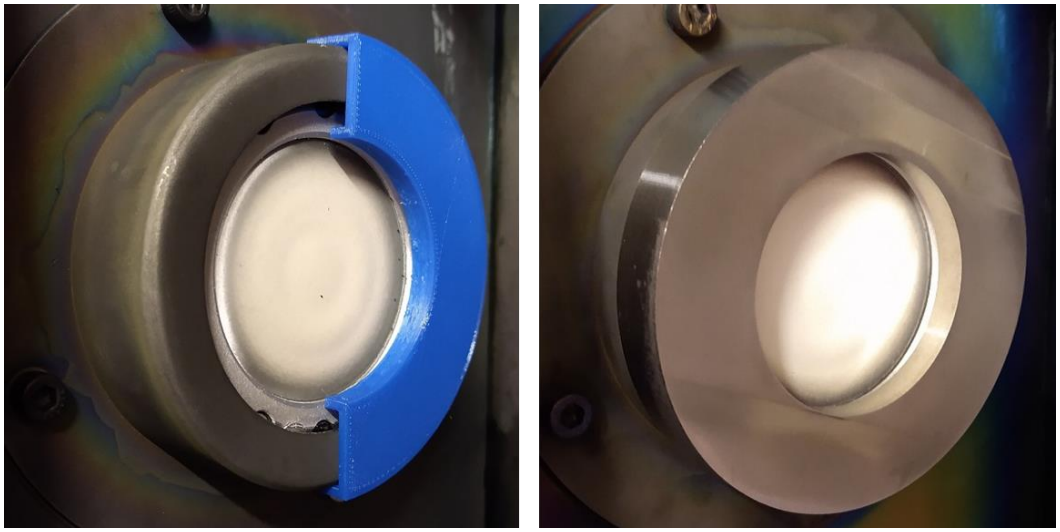

Figure 26 - Photos of the 3D printed prototype (left) and final machined 316L (right) magnetron shield attachment for the reduction of sputtering from the clamp ring, and prevention of substrate contamination, the 57 mm BN target is visible.

3.2.1.1 Multilayer Coating Structure and Parameters

The parameters used in the deposition of single and multilayer BN coatings are contained in Table 10 and Table 11 below, for the top layer and interlayer parameters respectively.

Table 10 - Summary of the sputtering parameters for the top layers of the BN coatings deposited onto planar substrates using the TEER UDP650 system, each coating is assigned a number for clarity.

No	Multi - layer	Top layer motion	BN Targets (Duration)	Ar:N_2 (sccm)	Bias Voltage (V)	Pulse Frequency (kHz)	Reverse time (ns)
1	N	Static	1 (6 h)	50:12	60	250	500
2	N	Static	1 (24 h)	50:0	60	250	500
3	N	Static	1 (6 h)	50:12	60	250	500
4	N	Static	1 (4 h)	50:12	150 - 120	250	500
5	Y	Static	1 (6 h)	30:15	180 - 150	250	500
6	Y	Static	1 (12 h)	30:15	180 - 150	250	500
7	Y	Static	1 (18 h)	30:15	180 - 150	250	500
8	Y	Rotation	2 (24 h)	15:5	60	250	500
9	Y	Rotation	2 (24 h)	15:5	100	250	500
10	Y	Rotation	2 (24 h)	15:5	180 - 150	250	500
11	Y	Rotation	2 (24 h)	30:25	180 - 150	250	500
12	Y	Rotation	2 (24 h)	30:25	180 - 150	50	1500

Table 11 - Summary of the sputtering parameters for the Cr-CrC-C-BCN adhesion interlayer applied to planar substrates as part of Coatings 5-12.

Layer	Target Setpoint	Substrate Bias (V)	Ar: N_2 (sccm)	Layer duration
Chromium	Cr (4 A)	120	23:0	900 s
Chromium Carbide	Ramp Cr (4-0 A) Ramp C (0-3.5 A)	60	23:0	1200 s
Carbon	C (3.5 A)	60	23:0	1200 s
Boron Carbon Nitride	Ramp C (3.5-0 A) BN (175 W)	60	30:15	2400 s

Due to restrictions on availability of equipment and the difficulty of getting accurate measurements, not all of the coating thicknesses were measured, those that were are contained in the corresponding results sections.

3.2.2 UoN Custom Barrel Coater – Powder substrates

The powder coating equipment used in this project is a bespoke rig built in-house at the University of Nottingham. The equipment, photo in Figure 27, consists of a cylindrical vacuum chamber, angled at 45°, containing a rotating barrel where powder is agitated and coated. The chamber has a diameter of 300 mm and depth 300 mm, and barrel has diameter 127 mm and depth 102 mm (5” x 4”). The powder barrel is rotated by a DC motor attached to a feedthrough into the chamber.

A single circular magnetron (Angstrom Sciences ONYX) with 2” target size is angled into a barrel containing powder, as shown in Figure 28, maintaining a target-powder distance of 90±1 mm. Target materials are contained within Table 12.

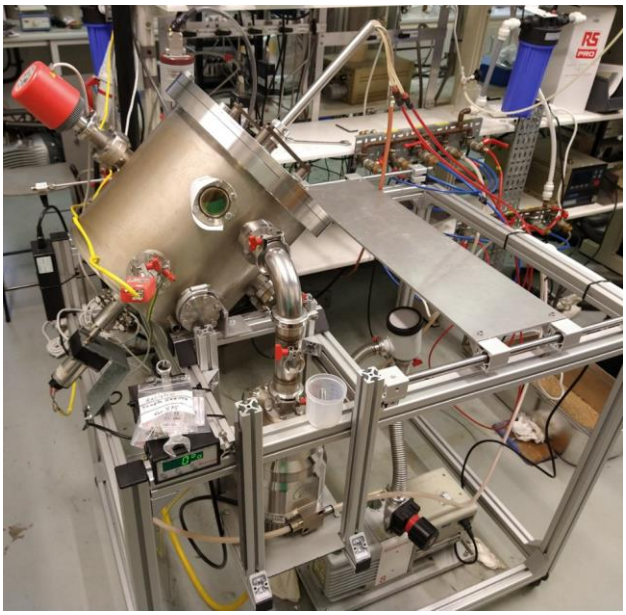

Figure 27 - Photo of the University of Nottingham powder coating equipment, chamber held at 45° to allow powder rotation and agitation.

Table 12 - Sputter target materials used for coating powders.

Material	Purity	Dimensions	Supplier
Zinc	99.99%	2.00" Ø, 0.250 thick	Angstrom Sciences Inc.
Titanium	99.90%	2.00" Ø, 0.250 thick	Kurt J. Lesker Company
Copper	99.95%	2.00" Ø, 0.250 thick	Kurt J. Lesker Company
Boron Nitride	99.50%	2.00" Ø, 0.250 thick	Kurt J. Lesker Company

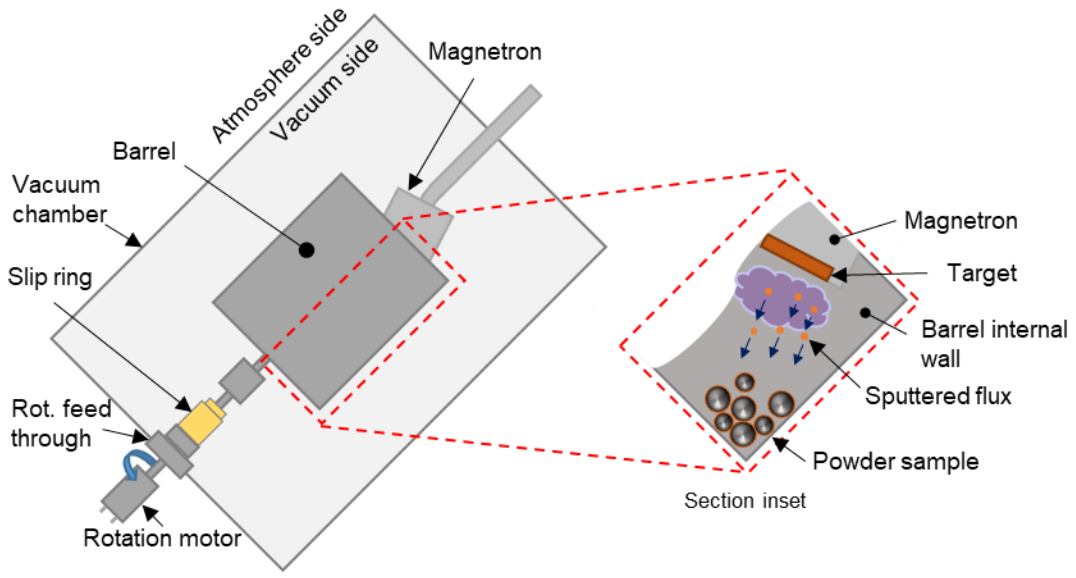

Figure 28 – Cross-section of the powder coating equipment, the chamber is held at 45° to horizontal and the barrel can be rotated to promote agitation of the powder, the magnetron is angled towards the base of the barrel to coat the accumulated powder, powder particles are enlarged to ease visualisation.

From this point onward samples will be named as 'Substrate powder-Coating material' e.g. 'Ag-Ti'. For all powder coating trials the chamber was pumped to a base pressure of ~6 x 10^{-5} Torr by rotary and turbomolecular pumps.

Gas flow into the chamber was altered with the use of a Mass Flow Controller (MFC) (MKS 1179A). This was powered by a four-channel ratio controller power supply (MKS 247C), receiving logic control from a pressure controller (MKS Type 250), which monitored the gas pressure using a temperature controlled capacitive manometer (MKS Baratron 627B). PDC power was applied to the target by an ENI RPG-50 power supply at a frequency of 150 kHz and pulse width of 2016 ns. When using the BN non-conductive target, RF power from a RF Plasma Products RF5S power supply was applied through an impedance matching unit at a frequency of 13.56 MHz.

3.2.2.1 Powder Coating Parameters

Parameters for the powder coating trials are summarised in Table 13, in the corresponding sections these are used for different powder size distributions where applicable.

Table 13 - Sputtering and motion parameters for the powder coating trials in this thesis.

Material	Gas Flow (sccm)	Power (W)	Duration (h)	Rotation (24 RPM)	Vibration	Dried
Cu-Zn	10	100	1	Y	N	N
Ag-Ti	17	50	3	Y	N	N
Ag-Ti	17	100	1	Y	N	N
Ag-Ti	17	50	3	Y	N	Y
316L-Cu	17	100	1	Y	N	N
316L-Cu	17	100	1	N	Y	N
316L-Cu	17	100	1	Y	N	Y
316L-BN	7:7 (Ar:N_2)	70 (RF)	24	Y	N	Y
316L-BN	7:7 (Ar:N_2)	70 (RF)	48	Y	N	Y

3.3 Materials Characterisation

3.3.1 Electron Microscopy

Electron microscopy techniques allow data to be gathered from the effects of electron beam interactions with materials.

Scanning Electron Microscopy (SEM)

Scanning electron microscopy uses a low energy, low current electron beam (5-30 kV, ~50-100 µA), produced by thermionic emission from either a Tungsten filament or Lanthanum Hexaboride (LaB_6) element, or when using a Field Emission Gun (FEG) SEM, by field emission from a narrow tungsten tip.

The electron beam interacts with the sample surface as is demonstrated in Figure 29. The electron beam scans across the surface, rastering, to collect data from an area. Multiple signals can be detected, to gain different insights into the sample material.

For imaging purposes, two types of electron signals are used, Secondary Electrons and Backscattered electrons.

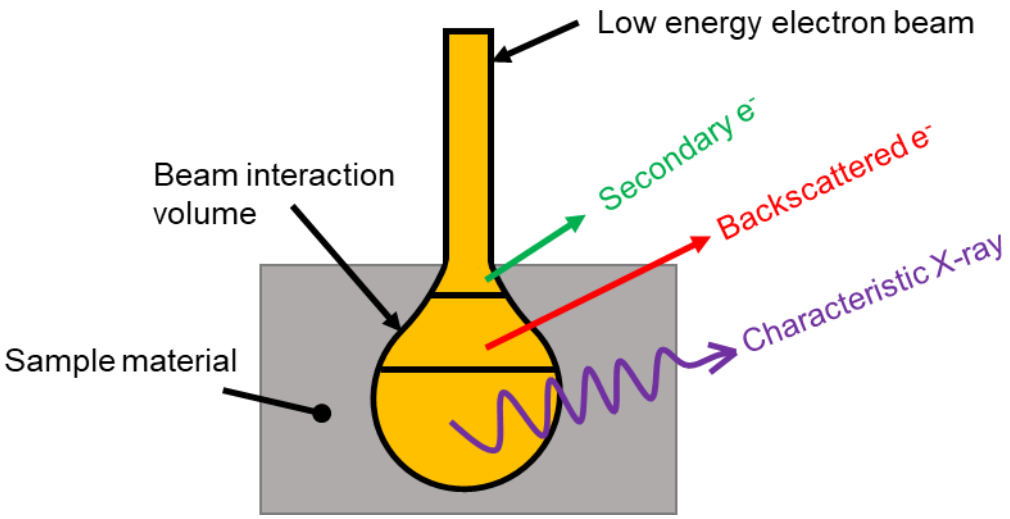

Figure 29 - Schematic showing the interaction volume of the SEM electron beam with the near surface region of a sample, 3 signals are indicated, Secondary and Backscattered electrons, and Characteristic X-rays.

Secondary electrons are produced when the incident beam inelastically removes electrons from the sample. These secondary electrons are low energy (< 50 eV) and as such can only be detected from the very near surface region of the sample. Due to the restricted depth that these electrons can escape from and be detected, secondary electron imaging provides high resolution detail of the topography and texture of the sample surface.

Conversely, backscattered electrons are produced elastically, as the incident beam passes close to the nucleus the electrons are ‘scattered back’, through 180°. As the scattering is dependent on the nucleus, molecular weight influences the backscattered signal, with heavier elements scattering more electrons, leading to brighter regions. As such, this technique creates images with contrast between heavier and lighter elements. Furthermore, as these are higher energy electrons than secondary, they can be detected from deeper regions.

Imaging in Secondary and Backscattered modes was carried out on a JEOL 7000F FEG-SEM with an accelerating voltage of 15 kV and 10 mm working distance. For surface characterisation samples were attached to SEM stubs with conductive carbon tape (Agar Scientific), and when examining cross-sections samples were mounted in black Conducto-Mount resin (MetPrep). All samples were analysed as prepared, with no additional Carbon, Gold or Platinum coatings applied.

Energy Dispersive X-ray Spectroscopy (EDX/EDS)

Elemental identification can be performed by the detection of X-rays from the interaction volume of the electron beam, see Figure 29. The incident electron beam removes electrons from lower electron shells, following this electrons from higher energy shells drop into the vacancies, releasing X-ray photons in the process. These X-rays are characteristic to the element, as the energy level difference is related to the size of the nucleus. From these signals the elemental composition of samples can be qualitatively and quantitatively (when compared to reference samples) assessed.

EDX analysis was also carried out on the JEOL 7000F FEG-SEM at 10 kV, working distance 11.5 mm with an Oxford Instruments X-ray detector. Oxford Instruments Aztec software was used for data acquisition, all scans ran for minimum 60 s live time.

It should be noted here that in analysis of low mass elements, such as B and C, the signal detected is generally of low amplitude, and as such the results need to be treated with an appropriate level of confidence.

Focused Ion Beam

The focused ion beam technique, in contrast to electron beam imaging, uses a beam of ions, typically Ga, to both image and modify the surface of a sample. Due to the much larger mass of a Ga ion relative to an electron, it is possible to selectively remove material from the surface of a sample via sputtering mechanisms. The ion beam can also be used to activate reactive gases, in a technique called Ion Beam

Assisted Chemical Vapour Deposition (IACVD), and deposit material from the gas onto the sample.

Using both the deposition and removal of material with the ion beam, small (< 20 µm width and depth) sections of samples can be machined and removed from the bulk sample for further analysis via TEM, described below.

Firstly, a protective layer is deposited on the surface, using a Pt or W containing gas as the material feed. Then trenches are milled either side of the region of interest, and the base and sides of the section, now called the lamella, are cut. Prior to full separation from the bulk sample, a probe is inserted, placed in contact with the lamellae, and welded on using the aforementioned IACVD. The lamella is then welded to a TEM sample holder and the probe removed. Final thinning of the lamella to electron transparency (< 100 nm) is then carried out.

The FIB instrument used in this project was a FEI Quanta 200 Dual Beam Microscope, operated by Dr Chris Parmenter at the Nano and Microscale Research Centre (nMRC), University of Nottingham.

Transmission Electron Microscopy (TEM)

In contrast to SEMs which capture data from the surface of samples, transmission electron microscopes capture data from the interaction of an electron beam travelling through thin samples (~50-100nm) using high energy electron beams (~200kV accelerating voltages). TEM techniques produce images at a much higher resolution than SEM imaging techniques, as the wavelength of the electron beam is smaller.

Three different types of imaging are of interest when using TEM. These are Bright-field (BF), Dark Field (DF) and Scanning (STEM), schematics of which are shown in Figure 30 a)-c).

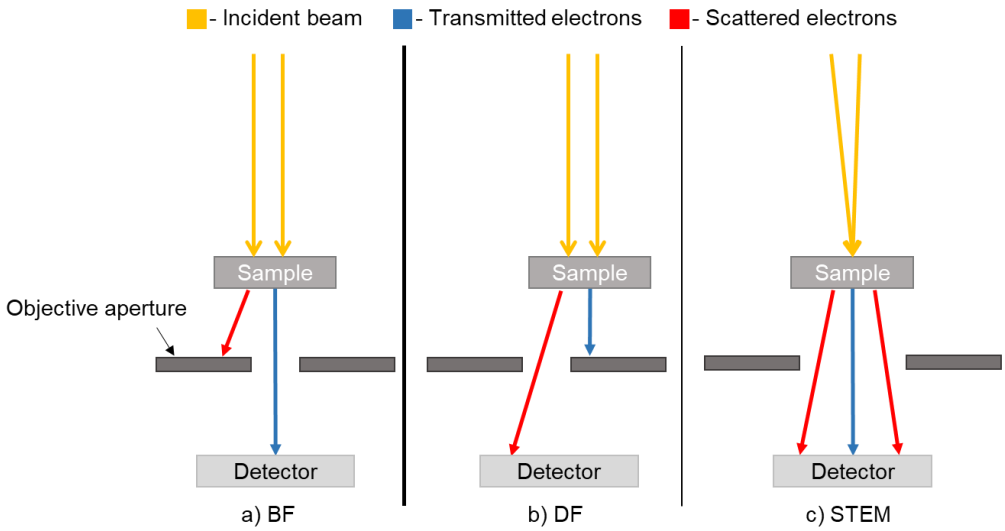

Figure 30 - Schematic of the TEM setup showing the incident high energy electron beam, sample, aperture and detector, a) In Bright Field mode the transmitted electrons are detected, showing contrast with the regions which scatter electrons, b) Dark Field mode shows contrast between high mass regions, c) Scanning TEM allows multiple detectors to be combined to build up images from different signals.

As the electron beam passes through the sample, there will be regions which transmit the beam, and regions which scatter the beam. By placing a detector behind the sample, Figure 30 a), the transmitted electrons can be collected, appearing as bright areas in the image, whereas the regions which have scattered the electron beam will appear as dark, shadowed areas, this is Bright Field imaging. As with SEM backscattered imaging, the atomic mass influences the scattering of the electron beam, creating mass contrast in the image.

Dark Field imaging is the ‘inverse’ of this method, where the aperture between the sample and detector is shifted (or the angle of the electron beam changed) such that the scattered electrons are detected rather than the transmitted electrons. This provides larger contrast between high mass elements.

With BF and DF imaging in ‘conventional’ TEM, the electron beam is perpendicular to the substrate surface, in parallel beams, however in STEM, the beam is focused to a point on the surface, as in SEM. The use of the scanning beam, and multiple detectors, allows multiple signals to contribute to the overall image.

TEM in this project was carried out using a JEOL 2100+ TEM operated by Dr Mike Fay at the Nano and Microscale Research Centre (nMRC), University of Nottingham.

3.3.2 X-ray Diffraction (XRD)

This technique provides data on the phases and compounds present in the sample according to peaks in a pattern. When collimated X-rays are directed onto the surface of a sample at a particular angle, the crystal lattice spacing, or parameter d, determines the angle at which the x-rays are refracted from the near surface of the sample, according to Bragg's law, Equation 4., see Figure 31.

$$n\lambda = 2d \sin\theta \qquad (4)$$

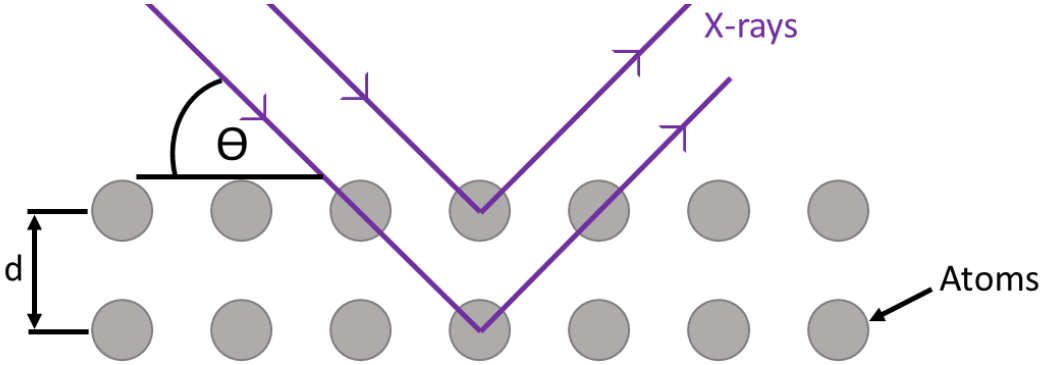

Figure 31 - Schematic of the diffraction of X-rays by atoms in a crystal lattice during XRD analysis, the extra distance travelled by the x-ray reflected by the lower atom must be an integer of the wavelength to constructively interfere.

If the d spacing of the lattice is such that the extra distance travelled by the x-ray transmitted through the lattice; and reflected by the lower lattice point compared to the ray reflected at the surface is an integer multiple of the wavelength, the reflected rays will have the same phase and will constructively interfere [260].

The x-rays are most commonly emitted from a copper source bombarded by electrons thermoionically released from a tungsten element. These diffracted x-rays can be used to characterise materials according to the varying d spacings of different phases present in the sample.

Glancing angle, sometimes referred to as glancing or grazing angle or incidence, X-ray diffraction is a technique developed to inspect the near surface region of a material, suited to analysing thin films. The x-ray source is held at a low angle to the substrate, and uses collimation to form a parallel beam, the detector scans from low to high angles. This technique utilises much longer detector dwell times at each angle compared to standard Bragg-Brentano scanning, to compensate for the reduced signal from the substrate due to the low angle beam interacting with a lower volume of material.

The Scherrer equation, see Equation 5. below, can be used to approximate the size of sub-micrometre crystals, useful for thin films which typically contain nanocrystallinity.

$$L = {}^{k\lambda}/_{\beta \cos \theta} \qquad (5)$$

Where L is the average crystallite size, k is a shape factor (0.94), λ is the wavelength of the Cu-Kα X-rays (0.15406 nm) and θ is the Bragg angle.

XRD analysis was carried out using a Bruker D8 Advance DaVinci, with parameters summarised in Table 14, collected data was compared to Powder Diffraction Files (PDFs).

Table 14 - The range of parameters used for glancing angle XRD.

2Θ range	20 - 90°
Θ value	1.0 - 1.2°
Step size	0.02 - 0.04°
Step dwell time	5 - 22s
Rotation	On

3.3.3 Fourier Transform Infrared Spectroscopy (FTIR)

FTIR uses the vibration of covalent bonds when exposed to infrared radiation to provide data on the material bonding in a sample [261-263].

The sample is exposed to an infrared source, and a detector measures the wavenumbers of the radiation transmitted through the sample. The radiation wavenumber ranges that are selectively absorbed by the sample correspond to known bond vibration modes. From these peaks (or troughs) in the produced spectrum, the bonding and phases present in the sample can be identified.

By using an Attenuated Total Reflectance crystal attachment, materials and samples that do not transmit the IR through the entirety of the sample, or where only a selected depth is of interest, can be analysed. This is the case in film-substrate systems, where the coating phase and bonding are of interest, these can be analysed as a whole, rather than detaching the film from the substrate.

A Bruker Tensor 27 Spectrometer with diamond ATR crystal and ZnSe prism was used for this work, with absorbance in the wavenumber range 600 - 4000 cm^{-1} (wavelength 0.3 - 12.5 nm) measured. Samples were pressed firmly into contact with the diamond crystal when analysing. OPUS software was used for instrument control, with background subtraction and ATR correction.

3.3.4 X-ray Photoelectron Spectroscopy (XPS)

XPS is a technique that is used for analysing the near surface (~10 nm depth) of a material, by measuring the energies of electrons removed from the surface by X-rays, due to the photoelectric effect. As the energy of the X-rays are known, and the kinetic energy of the photoelectrons are measured, the binding energy can be calculated, see Equation 6. below [264].

$$E_{Binding} = E_{Photon} - (E_{Kinetic} + \emptyset) \qquad (6)$$

Where $E_{Binding}$ is the binding energy of the electron, E_{Photon} is the energy of the impinging X-rays, $E_{Kinetic}$ is the measured energy of the ejected photoelectron, and ϕ is an instrument correction factor.

The instrument used in this work was a VG Scientific ESCALAB Mk II, using an Al anode, at 12 kV voltage and 20 mA current. Survey scans were carried out with a step size of 1 eV, 0.2s dwell time with 2 scans. High-resolution scans were carried out with step size of 0.2 eV, 0.4s dwell time with 5 scans. The instrument was operated by Dr Hannah Constantin.

CasaXPS software was used for analysis, all spectra were charge corrected to C at 284.8 eV. Peak fitting was carried out with Gaussian/Lorentzian 70/30% lineshapes, a Shirley background, with FWHM fixed for all the components in a peak.

3.3.5 Inductively Coupled Plasma-Optical Emission Spectroscopy (ICP-OES)

ICP-OES is a technique for assessing the quantities of elements in a sample material. This is achieved by detecting the characteristic wavelengths emitted from these elements in a plasma, typically an RF Argon plasma. This technique can be used for analysing solid, liquid and gas samples, however, these must be inserted into the plasma in dried aerosol form to enable the plasma to interact and excite the materials.

In the plasma, energy is transferred to the atoms, exciting electrons to higher energy levels. When the electrons return to a lower energy level, the characteristic energy corresponding to that transfer is emitted as a photon of a specific wavelength. This is then detected by the equipment, and a library of element wavelengths is used to identify the element. Ratios of counts per second are used to report the composition of a sample [265].

An Agilent 5110 instrument was used in this thesis, with nominal masses of solid samples digested in nitric acid (5 wt%) in order to allow effective insertion into the plasma.

3.3.6 Contact Stylus Profilometry

Contact Stylus Profilometry is a technique used to collect data about the texture of a surface, by dragging a tip attached to an instrumented stylus across the surface. This stylus is connected to a piezoelectric element that precisely transforms the movement of the tip into voltages that can be measured. In this work profilometry was used for assessing the deposition rates of different materials, and for final film thickness measurements.

A KLA Tencor D-120 Nano stylus profilometer was used for coating thickness measurements, with a tip radius of 2.5 µm, force of 5 mg, acquisition distance of 1mm and travel speed of 0.03 mm/s. Coated glass slide samples were prepared by applying Kapton tape to one half of the surface to mask from the coating process. The tape was then removed to create a sharp edge allowing the difference in coating and substrate height to be measured, see Figure 32.

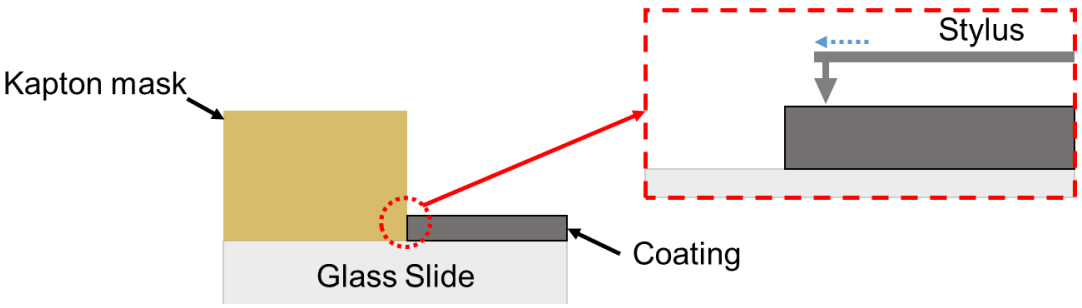

Figure 32 - Schematic of the stylus profilometry measurement, a glass slide partially masked with kapton tape, with inset showing the revealed edge when the tape is removed, and direction of stylus motion during measurement, coating thickness enlarged to ease visualisation.

3.3.7 Nanoindentation

Indentation testing provides data on the hardness of a material. Nanoindentation uses this principle and reduces it for low depth penetration. This is essential when investigating the surface hardness of a material whilst limiting the contribution from the material bulk and as such is used for assessing the mechanical properties of thin film coatings.

A Micro Materials NanoTest P3 Nanoindenter was used for the indentation measurements of thin film coatings, using a Modified Berkovich indenter. Indents were made to varied target depths, at 0.1 mNs^{-1} loading and unloading rate, with a dwell time of 20s at depth. Testing was conducted to BS EN ISO 14577:2015 [266].

Unless otherwise stated for each surface measurement a 3 x 3 array of indents was carried out for assembling data, the spacing between indents was set at 5 µm.

4. PVD Coating of powders

As outlined in Section 2.3.1.1 there is a lack of investigations published in literature focused on the deposition of ceramic materials via RF magnetron sputtering onto powdery materials. Furthermore, whilst there has been non-uniform coating and agglomeration witnessed in the coating of powders, understanding of the mechanisms responsible for this, and the dependencies have not been clearly presented. This chapter aims to add to this gap in knowledge by the deposition of metals coatings via PDC and by depositing a typical ceramic material, BN, which has potential applications in alloy modification, onto 316L, widely investigated in LPBF of components.

Prior to the deposition of BN, the untested equipment built for powder coating at the University of Nottingham, outlined below and in Section 3.2.2, was tested by coating metal powders with metal coating materials. This testing contributed critical underlying technical and experimental work to the publication of two studies.

The first, based around the mechanism occuring when a laser in LPBF interacts with a coated powder, utilised Zn as the coating material and Cu as the powder substrate [70]. This material combination was chosen due to the issues with Cu use in LPBF, as outlined in Section 2.2, the lower reflectivity of Zn at the laser wavelength of ~1070 nm, and the common use of Zn and Cu in brass.

The second, with a similar focus on reflectivity reduction, investigated the coating of Ag powder with Ti, with potential applications, as outlined in 2.2, in the production of Ti-Ag alloys via LPBF for use in orthopaedic implants [71].

Following this a further study of powder flow, and attempted optimisation of powder agitation was carried out, followed by coating with Boron Nitride.

4.1 Coating Methodology

As described in Section 3.2.2, a custom in house built sputtering rig was used for the deposition of materials onto powder substrates. This equipment consisted of a cylindrical vacuum chamber, held at a 45° angle. The container that held the powder was a cylindrical barrel, open at one end, with a single 2 inch magnetron angled into the opening, see Figure 33.

As will be detailed in the following results sections, two types of agitation were investigated, rotation and vibration. Additionally, in-situ drying was assessed.

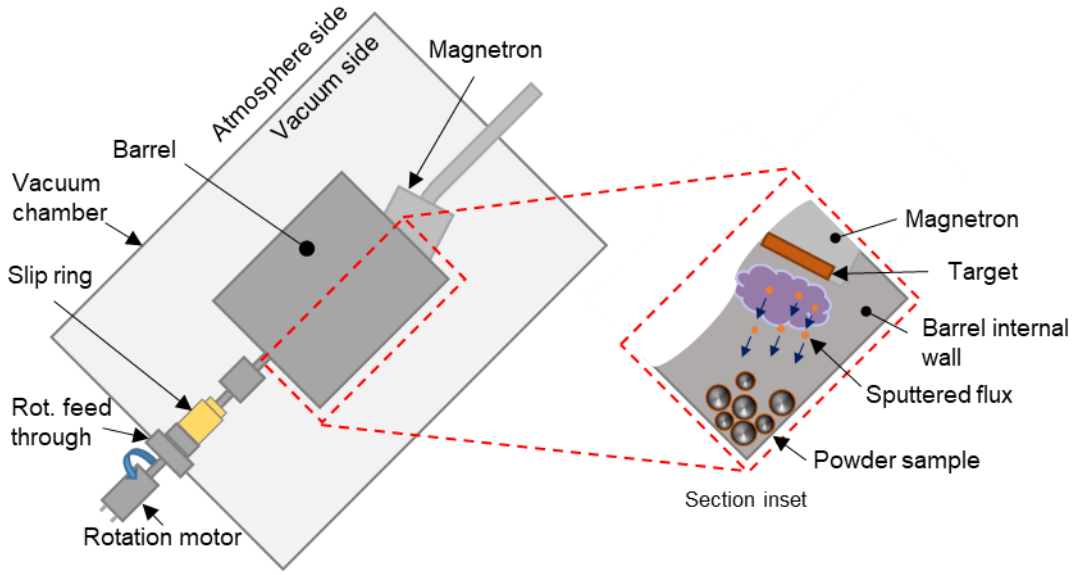

Figure 33 - Cross-section of powder coating equipment, the chamber is held at 45° to horizontal and the barrel can be rotated to promote agitation of the powder, the magnetron is angled towards the base of the barrel to coat the accumulated powder, powder particles are enlarged to ease visualisation.

4.2 Results

4.2.1 Zn coated Cu powder (Cu-Zn)

The two focuses of this study were on the reduction of the reflectivity of Cu powders used in LPBF manufacturing, and in the dependence and effect of powder size distribution on the ability to coat powders via PVD. The Cu powders used here are named Cu-Fine (D10: 3.1 µm, D50: 7.3 µm, D90: 19.0 µm) and Cu-Coarse (D10: 15.4

µm, D50: 39.4 µm, D90: 59.6 µm). Coating parameters were: 100 W target power, 10 sccm Ar flow, 1 h duration with 24 RPM rotation for both powder distributions.

These parameters were chosen as Zn readily deposits in this time-frame with this power, the rotation showed movement of the powder without ejecting particles from the container, and the gas flow sustained plasma without creating a high pressure which would reduce the mean free path of sputtered material.

Figure 34 contains a photo comparing the appearance of the Cu-Coarse powder to the coated Cu-Zn-Coarse powder, this was an initial indication of the success of the coating process. Additionally, the powder flowability had improved (qualitatively) compared to the as-received uncoated powder.

Figure 34 - Photo of two powders in glass vials, left) uncoated Cu-Coarse, right) Cu-Zn-Coarse coated with Zn, with distinct change in colour.

As shown in Figure 35 the diffuse reflectance, measured over the ultraviolet-visible-near infrared range (200-1200 nm), was reduced for the 2 coated powders, Cu-Zn-Coarse and Cu-Zn-Fine. Both uncoated Cu powders had a high reflectance in the red and NIR range (> 700nm), with 75.1% and 67.5% for the Cu-Fine and Cu-Coarse respectively at a wavelength of 1070 nm (commonly used in LPBF processes). After coating with Zn, reflectance reduced across the whole spectra, with the reflectance

at 1070 nm reduced to 40.6% for Cu-Zn-Fine and reduced a greater amount, to 29.1%, for Cu-Zn-Coarse respectively.

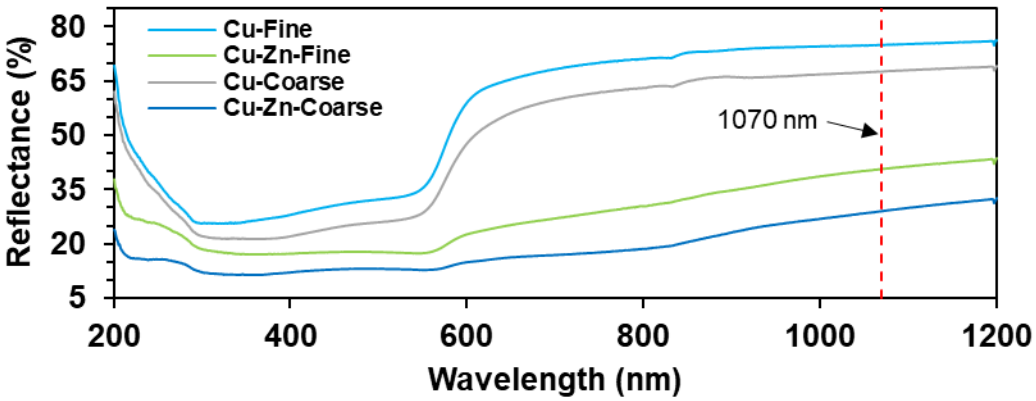

Figure 35 - UV-vis-NIR spectroscopy of the two Cu size distributions, coated and uncoated. The uncoated powders are highly reflective at > 700 nm, reflectance drops after Zn coating.

The difference between the reduced reflectance of the Cu-Zn-Fine and Cu-Zn-Coarse indicated that there may be differences in the particle surfaces and coverage. As such, imaging and elemental analysis was carried out. Powders were transferred from the coating equipment to glass vials, then a carbon adhesive tab was dipped in the powder. The population analysed represents a random sample of particles.

Figure 36 contains images of the Cu-Zn-Fine sample. From a) the contrast in the backscattered image, with brighter particles corresponding to the heavier (higher Z number) Zn indicates Zn deposition. This correlates with the bright regions in the EDX map of Zn over the same region. Given that the Zn contrast is high, with bright particles clearly visible, the coating has not been applied uniformly to the whole powder batch. Higher magnification imaging of a single powder particle is shown in Figure 36 b). These images show that the coating has been deposited relatively asymmetrically across the spherical particle. Considering the inset magnified region in b), a porous scaffold structure has formed, with epitaxial growth evident, as the thickness reduces towards the other side of the particle in b) this shifts to nodular growth. The asymmetry is an indication that the particle did not rotate during the

coating, and this coupled with the analysis from a) indicates that this particle remained at the top surface of the powder ‘bed’ during the process. A lack of particle turnover is therefore suggested. The sectioning and polishing of the coated powders is difficult, as the loosely adhered scaffold coatings are prone to smearing and material pull-out from the resin mount. Despite this the backscattered image and EDX maps in Figure 36 c) clearly distinguish the Cu powder and Zn coating, with a coating thickness ~2-3 µm.

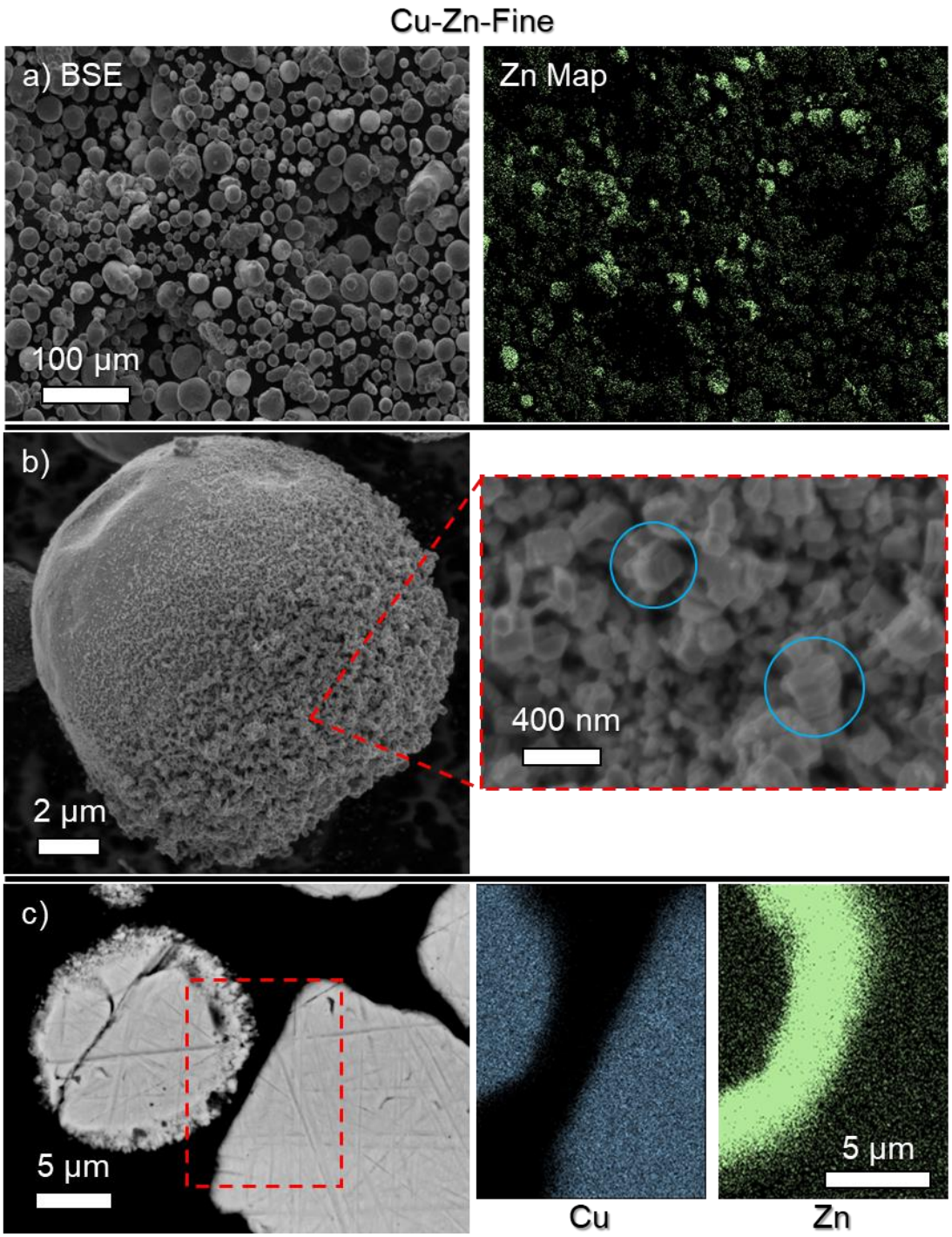

Figure 36 - Cu-Fine (lower size distribution) powder after coating with Zn at 100 W for 1 h whilst rotating, a) backscattered image of coated powder, brighter particles are visible corresponding to Zn content (higher Z number), corroborated by EDX map highlighting Zn, b) higher magnification secondary image of single particle showing coating growth, inset shows epitaxial growth of plates, c) backscattered image of sectioned powder particle, EDX maps indicate the coating, porous structure consistant with surface image.

Figure 37 contains the imaging and EDX of the larger size distribution Cu-Zn-Coarse. The difference in the contrast of the Zn map in a), when compared to Figure 36 a) is immediately recognisable. The bright patches corresponding to Zn are more uniform across the imaged population for the Cu-Zn-Coarse, indicating more uniform coating of the powder, though there are still brighter particles. Considering the single powder particle in Figure 37 b), the growth of the Zn coatings is thinner, the growth is more nodular across the surface as seen in the inset, with a qualitatively higher density through the thickness. The asymmetry across the powder surface is still evident however, as the nodules are more densely populated on the particle at the top of the image than the bottom. This indicates once again that one side of the particle has been exposed to Zn flux to a greater degree than the other. The section EDX maps in c) correlate with the surface imaging, showing a thinner Zn coating ~1 µm, still appearing relatively porous in the backscattered image.

Inductively Coupled Plasma Optical Emission Spectroscopy (ICP-OES) and X-ray Photoelectron Spectroscopy (XPS) were used to analyse the bulk and surface element compositions of the powders respectively. The ICP-OES data, Table 15, indicates that the uncoated powders contained negligible Zn, of the same order as error, whereas the coated powders had 0.69 ± 0.04 and 0.61 ± 0.03 at% for the Cu-Zn-Fine and Coarse respectively. These values are similar, as expected, due to the same process parameters, with the same quantity of material flux from the sputter target. However, as discussed above the uniformity of the coverage of all the powder population is different. Note that here at% has been used as the signals corresponding to different elements were not analysed, and as such wt% could not be calculated.

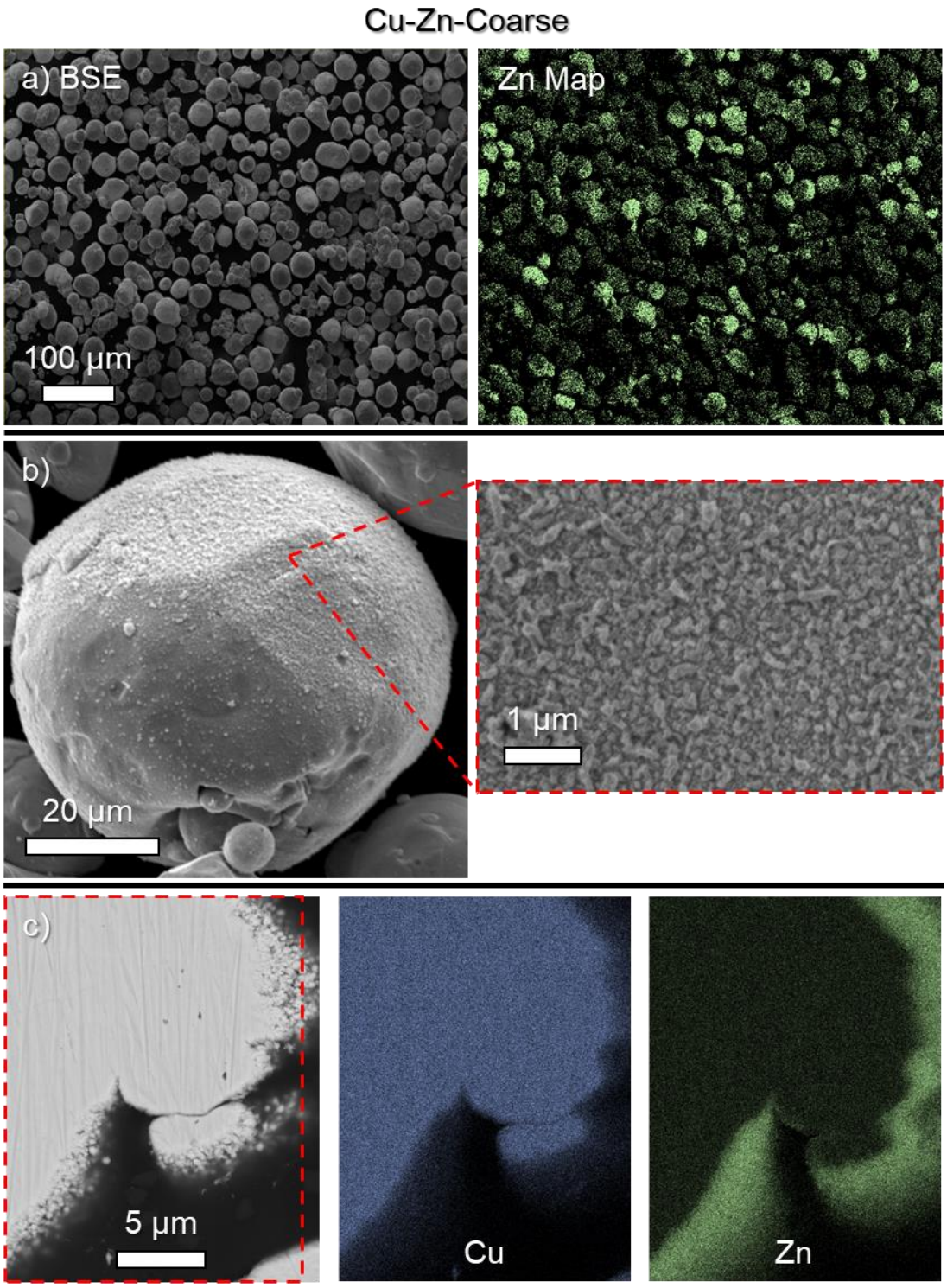

Figure 37 - Cu-Coarse (higher size distribution) powder after coating with Zn at 100 W for 1 h whilst rotating. A) Backscattered image of coated powder, brighter particles are visible corresponding to Zn content (higher Z number), corroborated by EDX map highlighting Zn, b) higher magnification secondary image of single coated particle, inset shows disrupted growth across the surface of the sphere with nodules ≤ 100 nm, c) backscattered image of sectioned powder particle, with EDX maps indicating Zn coating.

The XPS data was gathered from powder attached to carbon sticky tabs on stubs. The survey spectra are shown in Figure 38, separated by size distribution. After coating the Cu 2p and Cu LMM (Auger) peaks reduced in intensity for both size distributions, with the Zn 2p and Zn LMM peaks appearing. For all samples the composition, summarised in Figure 38 contains O and C, given the limited change across samples the latter is attributed to adventitious C. The O content is higher for the uncoated powders than the coated, this is attributed to a thin (< 5 nm) layer of oxide on the surface. Given the apparent thickness of the Zn deposits in Figure 36 and Figure 37 the reduction in Cu signal is consistent as the sampling depth of XPS is low (< 10 nm). As this depth penetration is low, it is logical to assume therefore that the remaining Cu signal comes from uncoated powder surfaces, this is the reason for using at% rather than wt% here. The Zn and Cu concentrations correlate with the degrees of coating uniformity seen in SEM/EDX with the amount of Cu detected on the Cu-Zn-Fine being higher than the Cu-Zn-Coarse, 3.7 ± 1.7 and 1.5 ± 0.5 at% respectively and the Zn concentrations 35.1 ± 1.1 and 40.4 ± 0.8 at% flipped respectively.

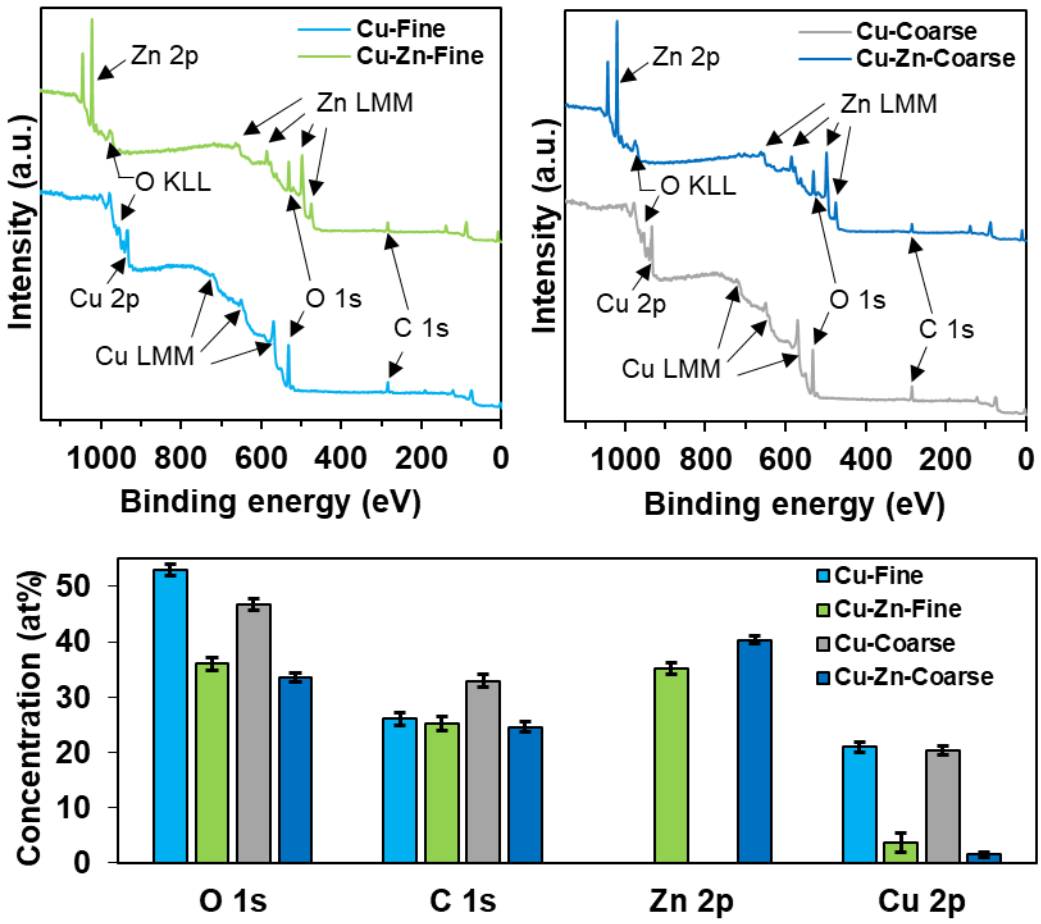

Figure 38 - Top: XPS survey spectra for the two powder size distributions (Cu-Fine and Cu-Coarse), comparing uncoated to coated with Zn, binding energies corresponding to Zn are present after coating, with Cu peaks reduced, bottom: summary of elemental concentrations in the aforementioned powder samples, full data in Table 33.

Table 15 - Zn concentrations present in the powder before and after coating, as measured by ICP-OES (Inductively Coupled Plasma Optical Emission Spectroscopy), the Zn addition is clear in both samples.

Size	Zn Concentration (at%)	
	Uncoated	Coated-Zn
Cu-Fine	0.01 ± 0.01	0.69 ± 0.04
Cu-Coarse	0.02 ± 0.01	0.61 ± 0.03

4.2.2 Ti coated Ag powder (Ag-Ti)

Similar to the previous section, the investigation of the Ag-Ti material combination was focused on the reduction of reflectivity of Ag powders in LPBF, however the coating highlighted different phenomena that led to a more in depth study of the coating process. In this study a single powder size distribution of D10: 17.4 µm, D50: 28.7 µm, D90: 45.3 µm, see Figure 39 c), was used.

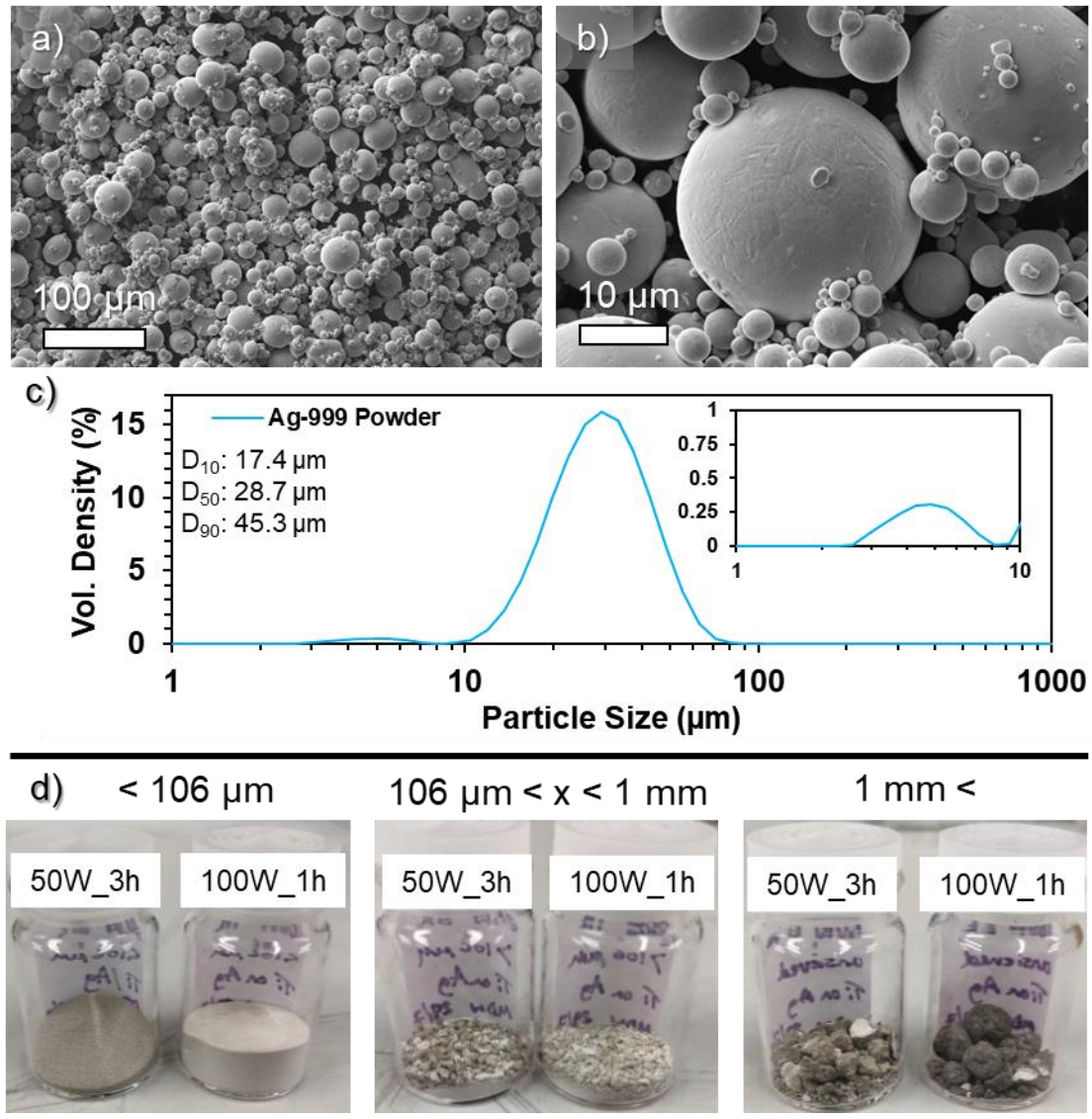

Figure 39 - a) Low magnification secondary electron image of Ag-999 powder, the powder is densely packed and spherical, b) higher magnification image of particles, the larger (20-45 µm) particles are decorated with satellite particles (< 5 µm), c) powder size distribution, d) photos of the three sieved distributions (multiple batches combined) of the Ag-Ti_50W_3h and Ag-Ti_100W_1h powders. The < 106 µm 50W_3h sample is noticeably darker.

The variables changed were the power applied to the sputtering target and the duration of the coating process. Uncoated powder was named Ag-999, powder coated at a power of 50 W for 3 h was named Ag-Ti_50W_3h and powder coated at a power of 100 W for 1 h was called Ag-Ti_100W_1h. The powder was rotated at 24 RPM during coating.

Figure 39 a) and b) contain low and high magnification images of the as received Ag-999 powder. The former shows a densely packed spherical powder with potential agglomeration, the latter shows that the larger powder particles (20-45 µm) are decorated with smaller (< 5 µm) satellite particles, consistent with the minor second peak (1-10 µm) in the distribution Figure 39 c) inset. The powder showed poor flowability from the outset of the study, consequently preliminary testing was carried out. The two coating parameter sets were run without the power applied to the magnetron, essentially rotating the powder for 3 h and 1 h in a low vacuum ($8x10^{-3}$ Torr) Ar (17 sccm) environment. The images in Figure 40 show the results of this testing. These demonstrate that for both durations, the rotation of the barrel caused 'clumps' to form. These were easily broken up with a spatula, but without intervention (viewing after venting the chamber to atmosphere) tended to roll at the front of the bulk, breaking into smaller pieces and reforming periodically.

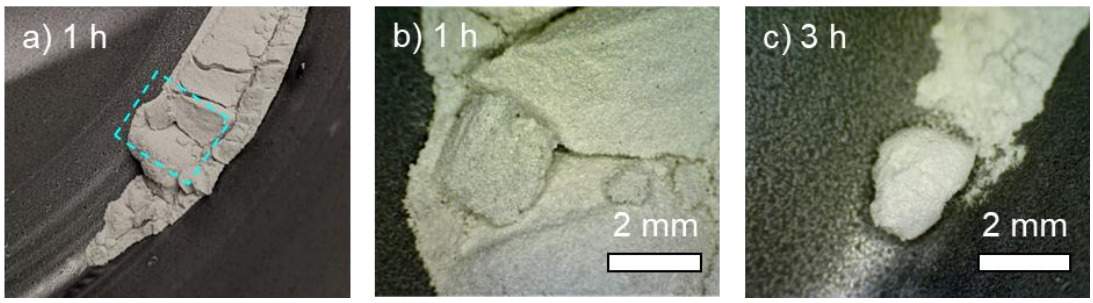

Figure 40 - Photo a) and optical micrographs b) and c) of Ag-999 powder after rotating under vacuum with Ar flow for the corrsponding 1 h and 3 h durations without power applied to the magnetron.

The powder ‘bulk’ slid and maintained a position ~20-40° from the centre-bottom of the barrel. As the barrel rotated this was carried up the edge following the direction of rotation, with the front edge reaching ~40° before friction was overcome and the bulk slid back to ~20°. In addition to this, the top surface of the powder could be seen ‘folding’ under the front edge of the bulk. Isolated powder particles were also carried up to the top of the barrel and dropped onto the retaining screw and base of the barrel.

Visual inspection of the powders coated with both parameter sets indicated agglomeration. As the end goal of the study was to produce powders suitable for use in LPBF, the powders were sieved to remove larger particles, first with a 1 mm, followed by 106 µm sieve. Photos of the upper, mid and lower ranges are shown in Figure 39 d). The mid-range (106 µm < x < 1 mm) particles were flake-like and irregular, appearing to be coated predominantly on one side. In contrast the upper range (1 mm <) particles were generally spherical, indicating rolling, and were relatively hard, once broken open they revealed uncoated powder, encased in a Ti coated shell. Both coated powders (< 106 µm) were visibly darker than the Ag-999, indicating successful deposition, with the Ag-Ti_50W_3h sample obviously darker. Improved flowability and agitation was also observed for the lower size range (< 106 µm) coated powders. It should be noted that agglomeration varied batch to batch for both parameter sets, leading to a varied yield of < 106 µm powder of 0.5-2 g from 5 g input.

As seen previously for the Cu-Zn powders, after Ti coating the reflectivity of the powders decreased, see Figure 43 a). The reflectivity at 1070 nm reduced from 59.8 % (Ag-999) to 46.8 % for the Ag-Ti_100W_1h, and further to 34.1 % for the Ag-Ti_50_3h.

Figure 41 contains the imaging and EDX maps taken from the Ag-Ti_50W_3h (< 106 µm) sample. The image in a) indicates that despite appearing fine, the powder has formed loose agglomerates ~100 µm in size, with uniform contrast in the

backscattered half of the image, showing that there are no large concentrated deposits of Ti. Figure 41 b) shows a larger agglomerate (taken from the > 106 µm sieved range) which has an irregular shape and is formed of a densely packed arrangement of particles. Considering a single non-agglomerated particle, see backscattered images in Figure 41 c) and d), with closer inspection contrast across the surface can be seen. From the EDX maps this is confirmed to be Ti content, deposited/grown as nodules (≤ 200 nm) scattered across the particle. EDX point analysis of multiple particles (n = 10), taken at the centre of the imaged surface, gives a Ti content of 1.3 ± 1.2 wt%, indicating non uniform deposition of Ti across the powder population.

The particle size distribution of the Ag-Ti_50W_3h, measured by laser particle size analysis, was D10: 20.8 µm, D50: 37.4 µm; D90: 72.9 µm, a further indication of agglomeration when compared to the Ag-999 distribution, Figure 39 c).

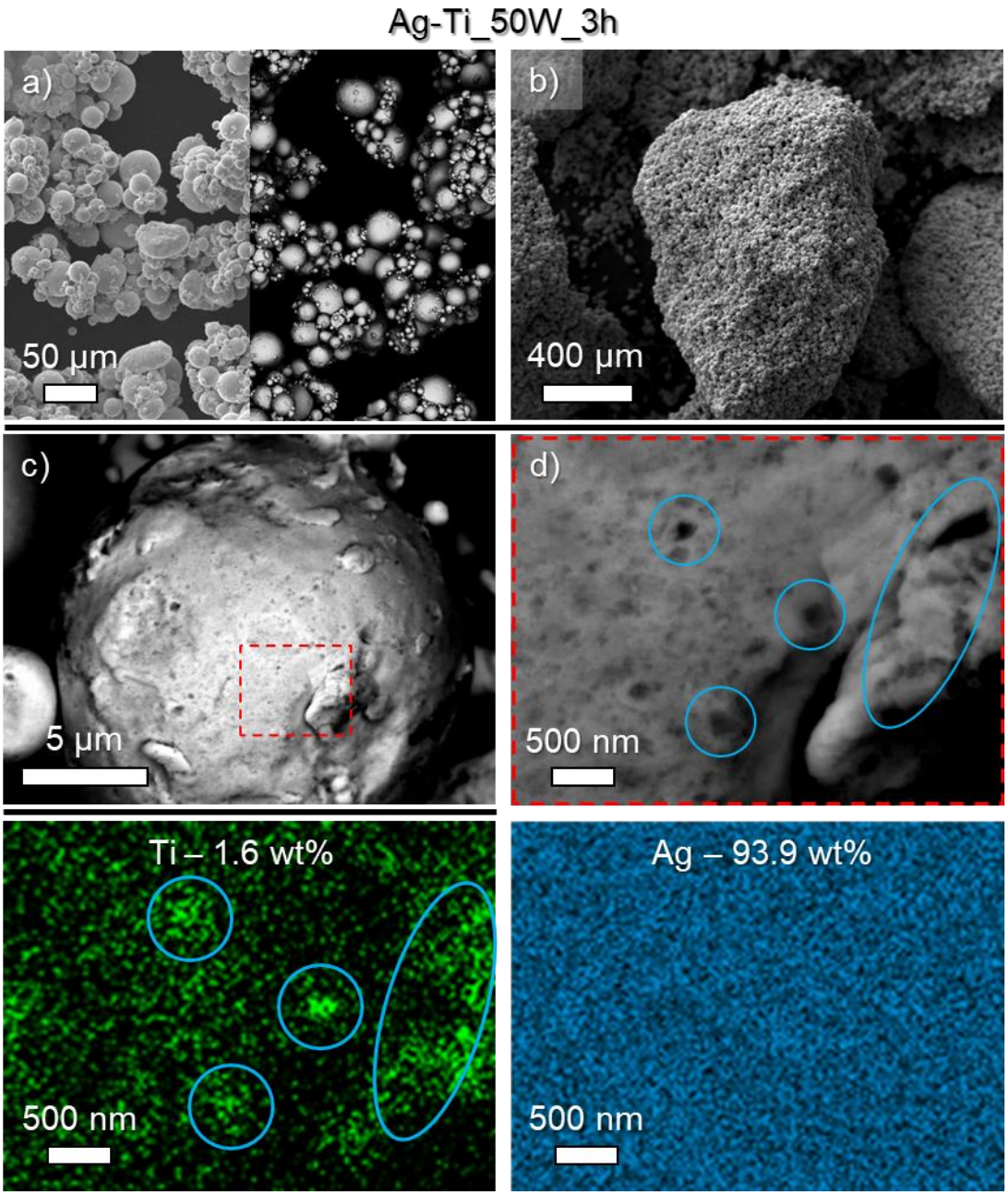

Figure 41 - SEM imaging and EDX maps of coated powder, Ag-Ti_50W_3h, a) low magnification split secondary and backscattered image of loose clumps of powder, b) secondary image of large dense agglomerate, c) backscattered image of single particle showing scattered dark spots, d) higher magnification backscattered image with Ti and Ag EDX maps, Ti nodules are highlighted on the image and corresponding map.

The EDX data (Figure 43 b)) for the Ag-Ti_100W_1h is similarly scattered, lower than the 50 W sample at 0.3 ± 0.3 wt%, indicating that particles with no titanium deposited are in this distribution. Considering the images in Figure 42 the particles appear to be closely packed in a), and conversely the large agglomerate b), of similar size to the

50 W agglomerate in Figure 41 b), has a porous lower density structure. No particles viewed and imaged showed clear deformation from the as-received gas atomised morphology. The Ag-Ti_100W_1h parameter set produced a lower yield of fine, non-agglomerated powder than the 50W parameter set per batch. Figure 42 d) shows a photo of the result of the 100 W parameter set directly after the chamber was opened, the majority of the 5 g batch had agglomerated into pebbles (~1-4 mm), with the lower size (< 1mm) powder obscured underneath.

Unexpectedly, as is shown in secondary and backscattered images in Figure 42 d), there appeared to be large (2-4 µm across) islands of fractured coating with columnar growth structure on this particle. The EDX maps indicate that the flakes to the right of the image are solely Ti, and the flakes on the left are Ti and Ti-Cr, with a multilayer structure highlighted in the blue circle. Given the difference in morphology to the previously seen nodular and porous growth, it is suggested that this material has transferred to the particle from the barrel wall, flaking from previously applied coatings. These flakes appear to have deformed to the morphology of the surface. It should be noted that throughout the study no macroscopic flaking of coating was seen on the barrel.

XPS was carried out to assess the near surface bonding and composition of the Ag-999, Ag-Ti_50W_3h and Ag-Ti_100W_1h powders, see Figure 43 c). The unaltered Ag powder survey spectrum was as expected, containing the peaks corresponding to binding energies for Ag, O, and C. For all samples the C content was assumed to be adventitious. Considering the high resolution scan of the Ag-999 O 1s peak in c), two components have been fitted, the lower component (531.7 eV / 48.1%) corresponds to either lattice bound O, indicative of a Ag oxide, or residual surface oxygen, the upper component (534.1 eV / 51.9%) corresponds to polar covalent bonded oxygen, suggested in this instance to be adsorbed residual moisture [267]. Subsequent to

coating, the Ag peaks reduce, Ti 2p and LMM peaks present, and O1s and KLL peaks increase for both parameter sets.

The surface composition, summarised in Figure 43 c), gathered from the survey spectra indicates that the 50 W sample has higher levels of surface Ti, at 11.0 ± 0.5 at%, than the 100 W sample, 9.1 ± 1.6 at%. The amounts of Ag and O correspond to this, with less Ag and more O detected on the 50 W sample than the 100W sample, 14.8 ± 0.4 compared to 19.9 ± 1.2 at% Ag and 37.4 ± 1.0 compared to 29.0 ± 2.5 at% O respectively. This indicates that the 50 W parameter set has a more uniform coverage of the powder, as Ti content is increased, Ag is reduced (due to being covered by Ti) and O is increased, as the Ti readily forms a passive oxide film. at% has been used here rather than wt% to aid the reader in understanding the values in terms of the arriving flux and subsequent oxidation of the surface.

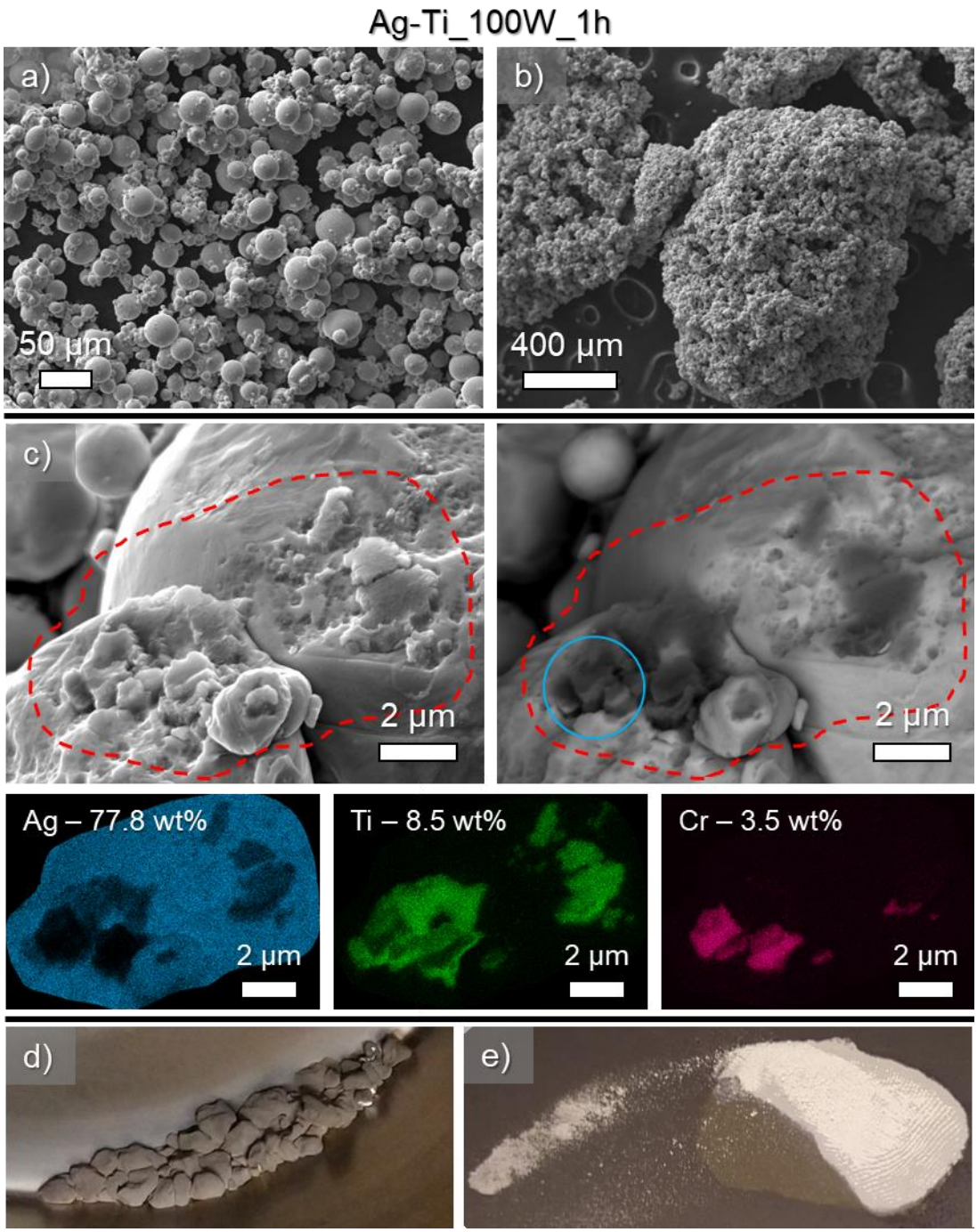

Figure 42 - SEM imaging, EDX maps and photos of Ag-Ti_100W_1h, a) low magnification secondary image of densely clumped powder, b) secondary image of large powder agglomerate, c) high mag. Secondary/backscattered images and EDX maps of powder particles, indicating Ti and Cr, potentially transferred to the powder from the barrel surface, note the multilayer highlighted by the blue circle, d) extreame agglomeration in one of the coating batches, e) example of barrel surface adhering powder to an area during processing.

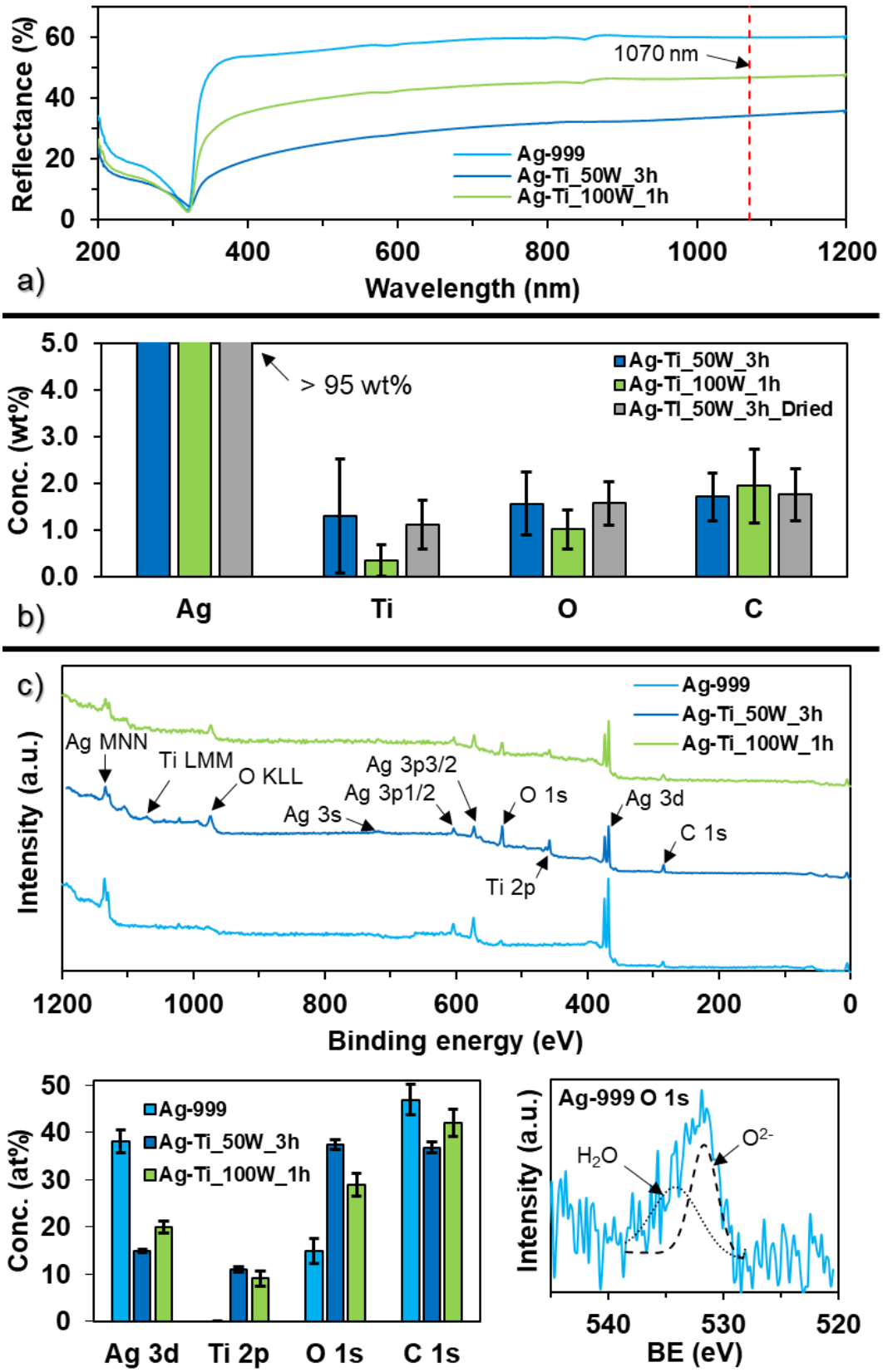

Figure 43 - a) Reflectance in the UV-vis-NIR range, a reduction is seen for the coated powders, b) EDX surface concentrations for the 3 coated powders (n = 10), full data in Table 34, c) XPS survey spectra of the Ag-999 and two coated powders with O 1s high resolution scan of the Ag-999 (two components at 531.7 and 534.1 eV respectively) and summarised elemental concentrations, full data in Table 35.

Subsequent to the characterisation of the Ag-999, Ag-Ti_50W_3h and Ag-Ti_100W_1h, an additional parameter set was investigated. This, named Ag-Ti_50W_3h_Dried, included a drying step, carried out in-situ under low vacuum (~ $3x10^{-3}$ Torr) at ~50°C (measured via adhesive temperature label) for 24 h, prior to the 50W_3h parameter set. This was achieved by wrapping a silicon heating mat around the outer surface of the barrel Figure 44 a), with power supplied through an electrical feedthrough in the chamber wall. To allow drying and subsequent coating without venting the chamber to detach the power wires, a slip ring (Moflon MT1233-S06-VC) was integrated into the rotating shaft assembly, see Figure 44 b).

Following coating of the dried powder, the appearance of the powder was distinct from that seen previously. Figure 45 a) shows this, the volume of 'loose' coated powder is increased over the non-dried results and is subjectively as dark as the sieved (< 106 µm) 50W_3h powder in Figure 39 d). Post sieving, the mass of < 106 µm powder was 3.57 g, from an input of 5 g. Furthermore, the agglomerates, highlighted in the blue circle in a), separated with a spatula in the inset, are elongated and plate-like. This indicates that a different agitation mechanism has occurred.

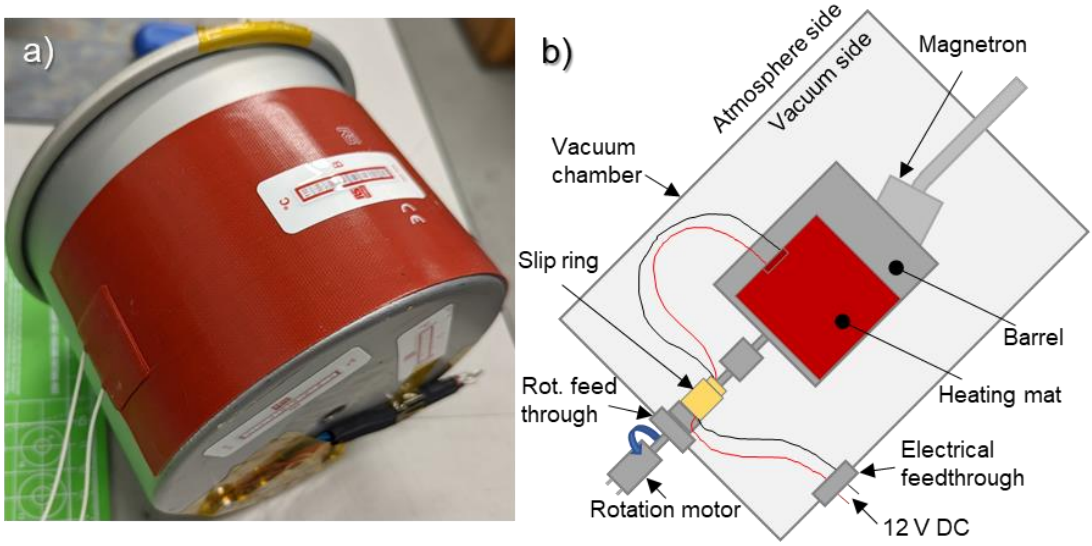

Figure 44 – Addition of in-situ heating, a) rear-side view of powder barrel, an adhesive backed heating mat has been applied, partially covering the outer surface, b) simplified schematic showing side view of setup, the power is supplied to the heater through an electrical feedthrough in the wall of the vacuum chamber, connected to a slip ring, allowing the barrel to rotate whilst power is applied to the heater.

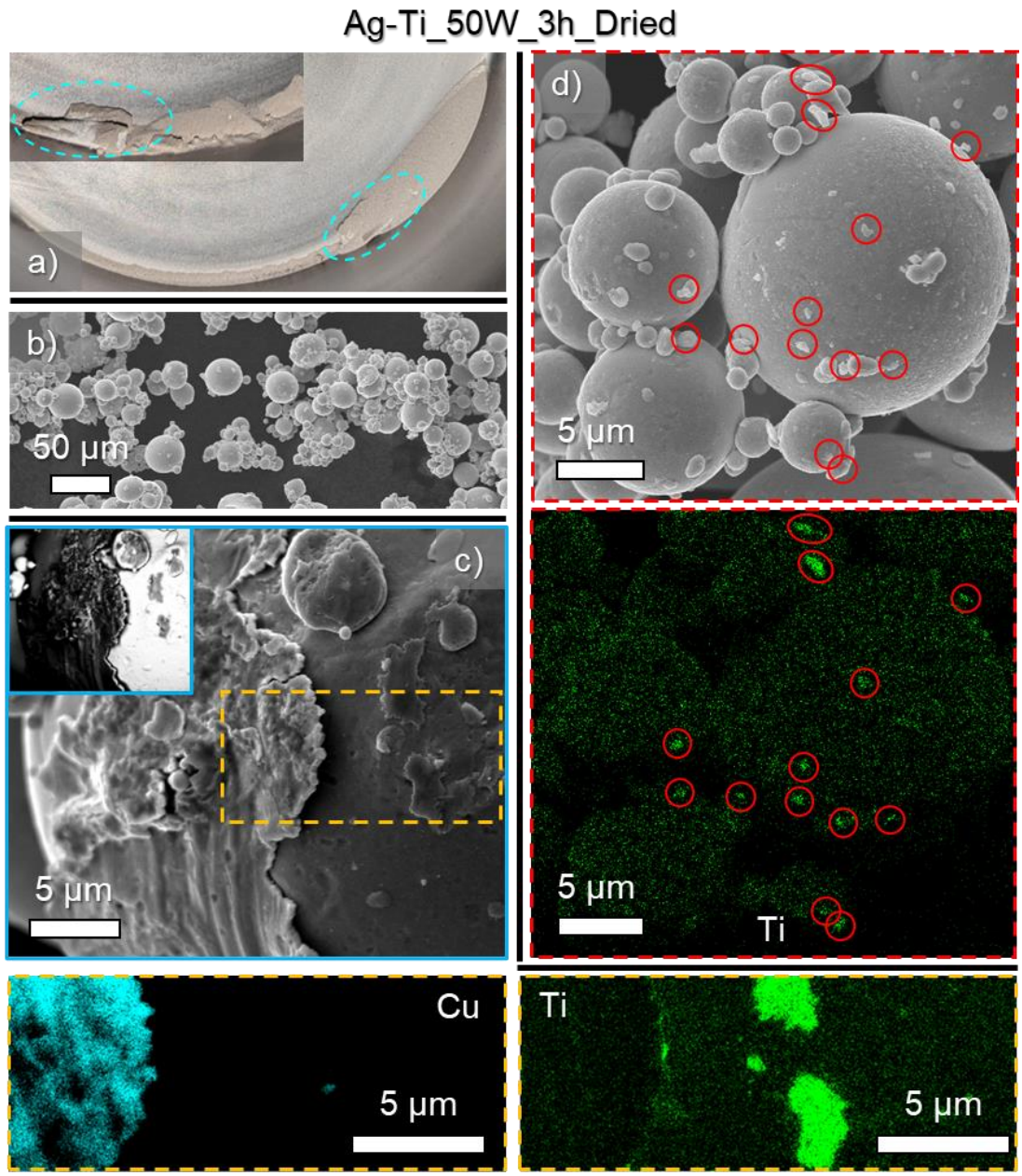

Figure 45 - Images and EDX maps of Ag-Ti_50W_3h_Dried, a) photo of as-coated powder in the barrel, inset shows plate like agglomerate separated from the powder with a spatula, b) secondary image of loosely clumped powder, c) high mag. secondary image of particle (with backscattered inset), Cu and Ti maps indicate contamination from previous coatings, d) secondary image of particles, with Ti map indicating nodular growth.

Figure 45 b) contains a low magnification secondary image of the loose powder, showing that the there was still agglomeration occurring in the < 106 µm range. Figure 45 c) and d) contain indications of coating via different mechanisms. The former, c), shows that again there has been transfer of previously deposited coating material to

the powder particles. In this case there is a large (> 35 µm measured vertically on the image) skin conformed around the surface of the particle, found to be Cu via the EDX map. In proximity to this Cu there are also smaller (in area and thickness) Ti island deposits. Figure 45 d) contains an image and EDX map showing scattered nodular growth across the surface of clustered particles, which has been observed previously.

EDX point scans of multiple individual particles were carried out as with the previous parameter sets, see Figure 43 b). For the Ag-Ti_50W-3h_Dried sample, Ti content was 1.1 ± 0.5 wt%, slightly lower than the Ag-Ti_50W_3h and higher than the Ag-Ti_100W_1h, but with a much reduced error. This indicates (though the small sample size of n = 10 should be weighed carefully) that the drying of the powder has increased agitation/flowability of the powder, allowing particles to be coated more uniformly than the previous two parameter sets.

4.2.3 Cu Coated 316L powder (316L-Cu)

As the previous two studies had highlighted phenomena associated with powder sizes, the rationale for this next study was to investigate this in more depth. In contrast to the previous studies, a powder with size distribution designed (or specified as) for LPBF was chosen (CT PowderRange 316L F, Carpenter Additive). The secondary focus of this study was to investigate the possibility of introducing BN to the surfaces of powders, in order to dope steel (in this case 316L) during LBPF.

The 316L was sieved into two size distributions (with a 25 µm sieve) to assess how the behaviour of the coarse and fine distributions differed when agitating and coating. The two distributions, 316L-Coarse and 316L-Fine are shown in Figure 46, with the upper having a slightly larger FWHM.

As Cu is readily sputtered at manageable deposition rates, it was chosen as the coating material for this study. The samples coated with Cu are therefore named 316-Cu-Coarse_X and 316L-Cu-Fine_X, with the X dependent on the agitation mechanism, rotation (rot) or vibration (vib). The duration, power and gas flows were set at 1 h, 100W and 17 sccm Ar ($8.5x10^{-3}$ Torr chamber pressure) for all the 316L-Cu samples. Powder sub-samples were taken from different regions of the as-coated powder 'bed', detailed in the appropriate figures, 'mixed' samples were shaken in sample bags and then powder was stuck to a carbon tab.

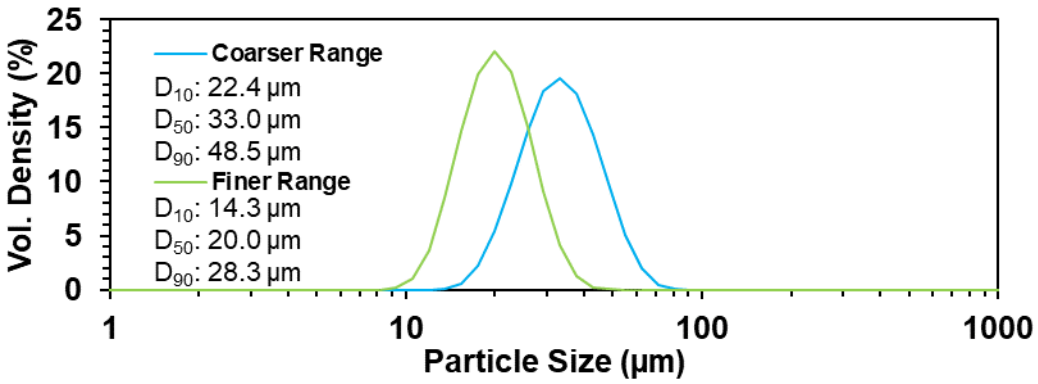

Figure 46 - Powder size distributions of the two 316L powders sieved from the as-received CT PowderRange 316L F, the upper range is named 316L-Coarse, the lower is named 316L-Fine.

4.2.3.1 Rotation trials

Figure 47 contains the images and EDX data from the 316L-Cu-Coarse_rot sample. The photo, a), shows that the powder had been partially coated with Cu, appearing dull brown in areas with grey powder still visible and some powder appearing to be adhered to the barrel surface. EDX maps, b) of the mixed sub-sample indicate uneven distribution of Cu across the particles imaged.

When considering the surface of a single particle from the Top centre sub-sample, the growth seen here, confirmed as Cu from the EDX maps in d), is consistent with nodular growth, forming islands which coalesce to form a consistent layer of columnar nanocrystals, conforming to the morphology of the particle surface. This growth indicates that this particle resided at the surface of the powder bulk for a long time.

The EDX data for point scans on multiple particles is summarised in Figure 47 e). The Cu content for the sub-sample taken from the top centre of the powder bed, indicated in a), is 37.6 ± 35.7 wt%, a large amount, however, the error is near equal to this, suggesting that there was a wide range of Cu deposited on particles. This suggests that whilst some particles were residing at the top of the powder bulk for an extended time, fresh uncoated powder was being agitated to the surface. In comparison to this, the sub-sample ‘mixed’, created by removing all the powder from the barrel and shaking in a sample bag before sampling, had a Cu content of 25.9 ± 21.8 wt%. This shows a reduction in the content, indicative of sampling of particles below the top surface which have less Cu on them, but the error is still within the mean, indicating that there are minimal particles with no Cu content.

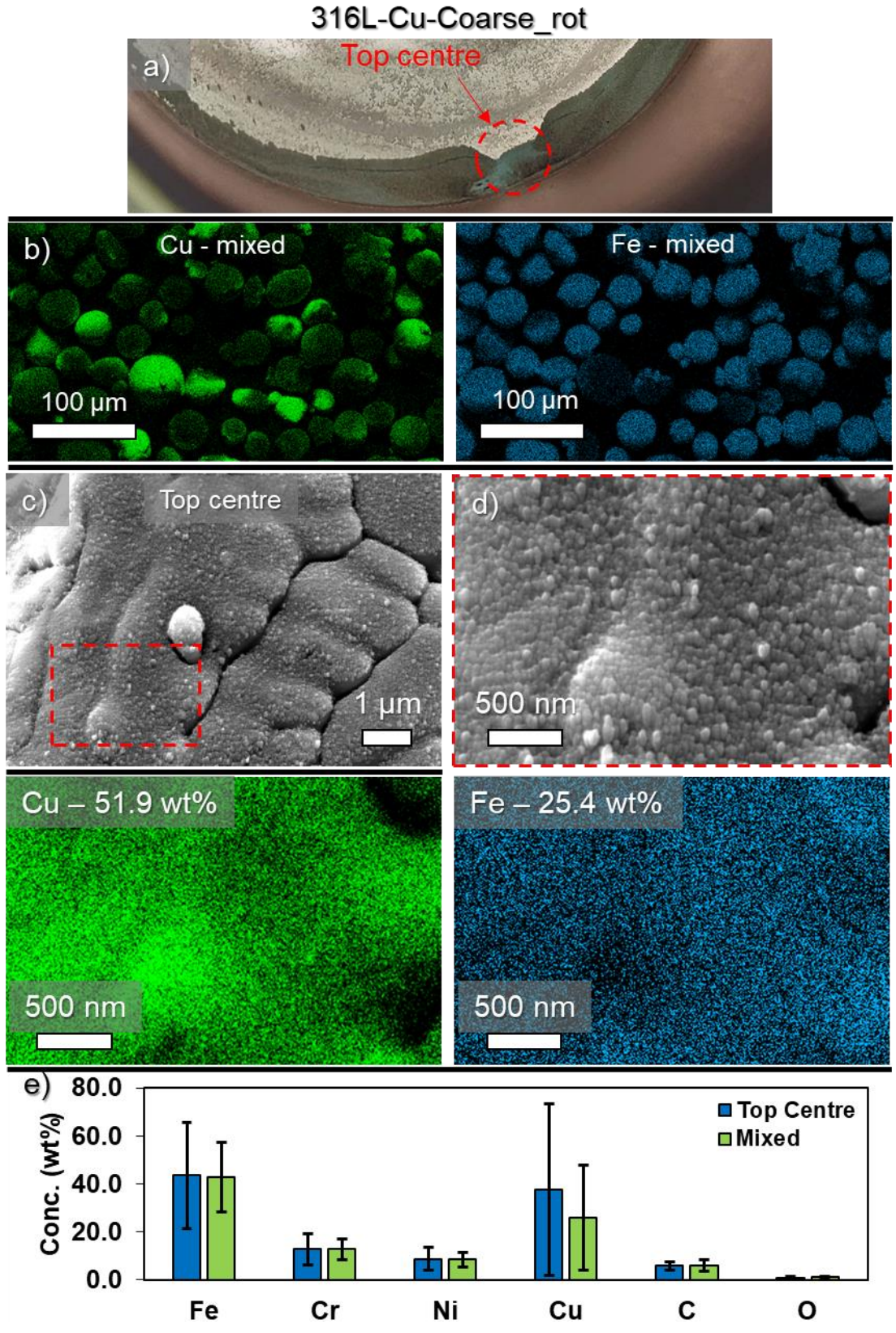

Figure 47 - Images and EDX of the coated 316L-Cu-Coarse_rot sample, a) photo of powder after opening the chamber, the depression highlighted is where the top centre sub-sample was taken, b) low mag. EDX maps of the mixed sub-sample, indicating non-uniform coating of powder, c) higher mag. secondary image of particle surface from top centre sub-sample, d) high. mag. secondary image of growth of nodules, coalescing into a uniform layer with Cu and Fe maps, e) EDX point summary of individual particles (n = 10) from the top centre and mixed sub-samples, full data in Table 36.

The data for the coated Fine distribution, 316L-Cu-Fine_rot, is presented in Figure 48. The appearance of the powder was distinct from the Coarse distribution. The powder had clearly adhered to the barrel surface, with the bright orange colour indicating that there had been minimal turnover of the powder. The streaks across the base of the barrel indicated powder had been carried up the edge of the barrel and had then dropped down, adhering to the base on the way past the retaining screw. A single tap on the barrel with a spatula dislodged the adhered powder and it cascaded to the bottom, revealing significant amounts of grey uncoated powder.

Figure 48 b) magnifies the lower part of a), showing where two sub-samples were gathered from, sub-sample 2 consisted of loose powder. The further magnification in c) similar to region 1 is an optical microscope image, showing a porous scaffold like structure of Cu coated particles atop layer of uncoated (or less coated) powder. This structure was soft and easily broken down by pressing with a spatula and from the images in d), the pressing of carbon tabs onto the surface to gather the sub-samples also broke the scaffold into loose particles. As the porous structure has formed, this suggests that agitation was successful, as the macrostructure could not form without the movement of the particles, however above a certain threshold this agitation leads to the stacking of particles. This has not dominated over the 1 h duration however, as there still remains loose powder, sub-sample 2. It is also not clear whether these structures persist and grow, or whether they periodically break and reform.

Contrast between the particles is seen in the backscattered images in Figure 48 d) for all three sub-samples, indicating non-uniform deposition as expected. The EDX data, Figure 48 d), for sub-sample 1 correlates with the observations, the average Cu content is high as expected, 29.8 ± 20.6 wt%, and whilst the error is high this is assumed to be due to asymmetrically coated particles being rotated when adhering to the carbon adhesive tab.

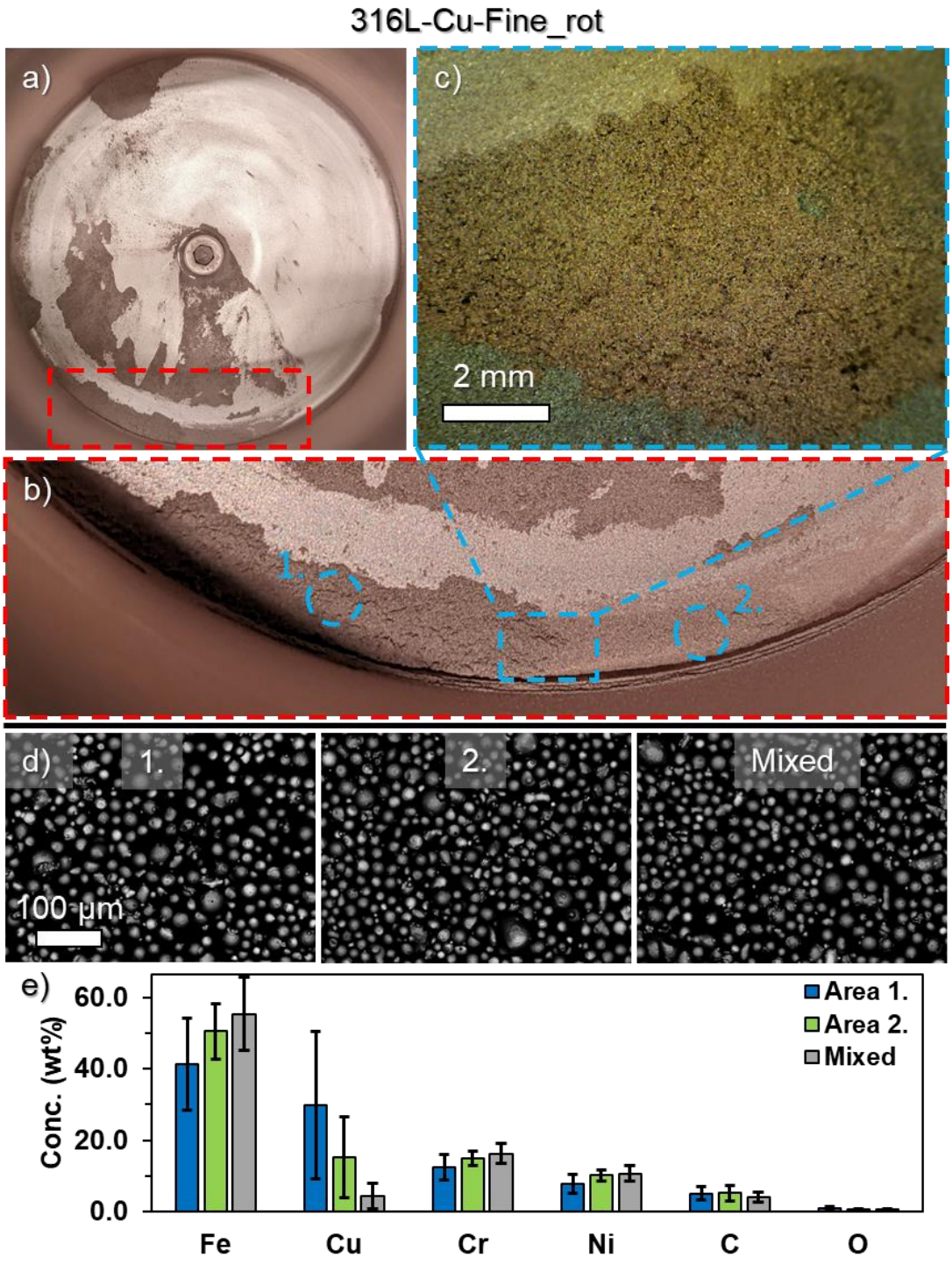

Figure 48 - Images and EDX of the coated 316L-Cu-Fine_rot, a) photo of the sample after opening the chamber, powder is loosely adhered around the barrel edge and base, magnified in b), indicating areas 1. And 2. where sub-samples were gathered from, c) optical microscope image, showing porous, 'fluffy', powder structure, d) low mag. backscattered images of the three sub-samples taken from this batch, subtle contrast is seen between coated and uncoated powders, no agglomeration is seen, c) summary of EDX point data from multiple particles, full data in Table 37.

Region 2 has a lower Cu content but a relatively higher error, 15.3 ± 11.3 wt%, again suggesting significant non-uniform deposition. The Cu content of the mixed sub-sample, 4.4 ± 3.6 wt%, confirms the poor agitation of this sample, as the mean is low, due to it containing the powder obscured by the heavily coated top powder layer.

4.2.3.2 Vibration Trials

In order to provide a different agitation mechanism, one that was less aggressive than the rotating and tumbling used previously, small unbalanced vibration motors were added to the base of the barrel, see Figure 49 a) for photo and b) for schematic. The decision to attach the motors directly to the barrel was made based on the lack of mounting points on the internal walls of the chamber for a separate mechanism. These motors were powered in parallel by 3 V DC through the electrical feedthrough/slip ring setup. After loading the 5 g powder batches, before sealing and pumping down the chamber, the voltage was raised from 0-3 V until agitation of the powder was observed. This occurred at 2.85-2.95 V, corresponding to a motor vibration frequency of ~200 Hz (read from the motor datasheet, Precision Microdrives Model: 310-113), for both 316L-Coarse and 316L-Fine powders.

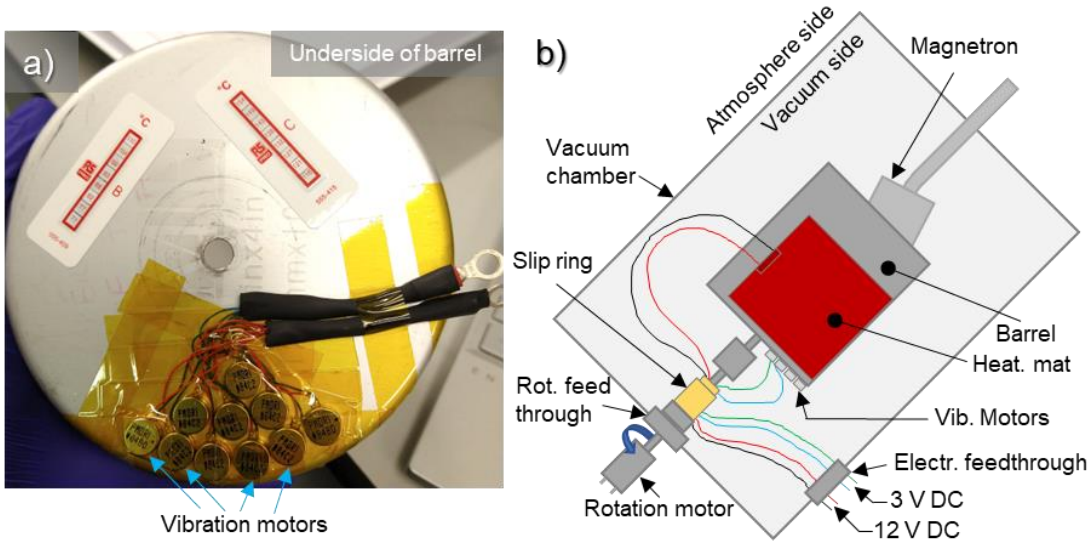

Figure 49 - Addition of vibration to the barrel, a) photo of multiple individual motors (Precision Microdrives Model: 310-113) adhered to the base of the barrel to agitate the powder, b) simplified schematic indicating motor position and power supply through the slip ring.

The powder was seen to vibrate, with the top surface moving slowly towards the edges of the powder bulk, folding under the edges, with new powder being revealed at the centre.

The results of the 316L-Cu-Coarse_vib parameter set are presented in Figure 50. The comparison between the uncoated and coated powder is shown in a) and b). The off-grey appearance of the centre portion of the powder indicates that agitation has been successful. The edges and corners, however, are bright orange, indicating that powder has been static, or agitating in place, in these regions. From the observation of the agitation prior to coating, it is therefore suggested that whilst the majority of powder passes through the corners and edges whilst flowing, there are vortices present that trap a small amount of powder.

The backscattered images of four sub-samples in Figure 50 c) show that there was no agglomeration present, and also that little contrast can be seen between the individual particles. When considering the EDX point data, the disparity between the Top Left and the other three sub-samples is clear, as the Cu content was much higher at 20.3 ± 14.4 wt%. The Top Middle and Middle Bulk (gathered by splitting the centre of the powder with a razor blade) are similar to each other, 7.6 ± 4.3 and 6.3 ± 4.2 wt% respectively, indicating that the powder was consistently folding over itself. The Mixed sub-sample Cu content further agrees with the previous sub-samples as it was slightly higher in Cu content, 9.0 ± 6.6 wt%, with an increased error, as the highly coated Top Left sub-sample is mixed into the distribution.

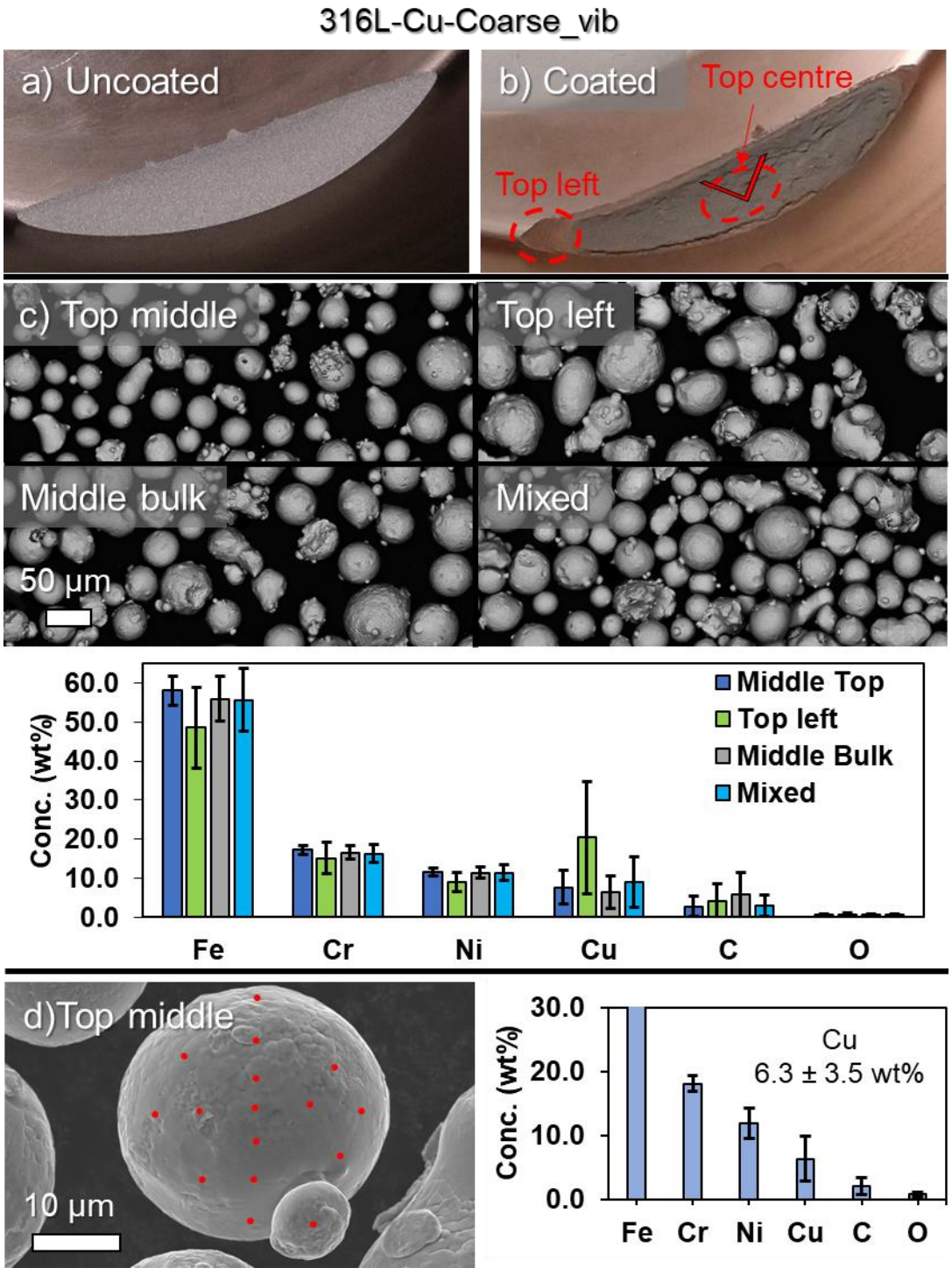

Figure 50 – a) and b) photos of uncoated 316L-Coarse and 316L-Cu-Coarse_vib, powder is dull orange with bright orange at the edges, c) backscattered SEM images of 316L-Cu-Coarse_vib powder, sub-sample positions indicated on Coated photo (the Middle bulk, indicated by a 'V' in photo was gathered by parting the powder with a razor blade) with summary of EDX point scans of multiple particles (n=10) from each sub-sample, full data in Table 38, d) secondary image of single particle with EDX point scans indicated with chart indicating Cu content and deviation.

The results for the Fine powder distribution, 316L-Cu-Fine_vib, are presented in Figure 51. The appearance, photo in a), was different to that of the Coarse distribution coated with this parameter set, in that the colour was a more uniform grey across the surface. The edges were still distinct from the rest of the powder, as with the 316L-Cu-Coarse_vib, however the difference in colour was subtle, and the width of the edge was reduced comparatively.

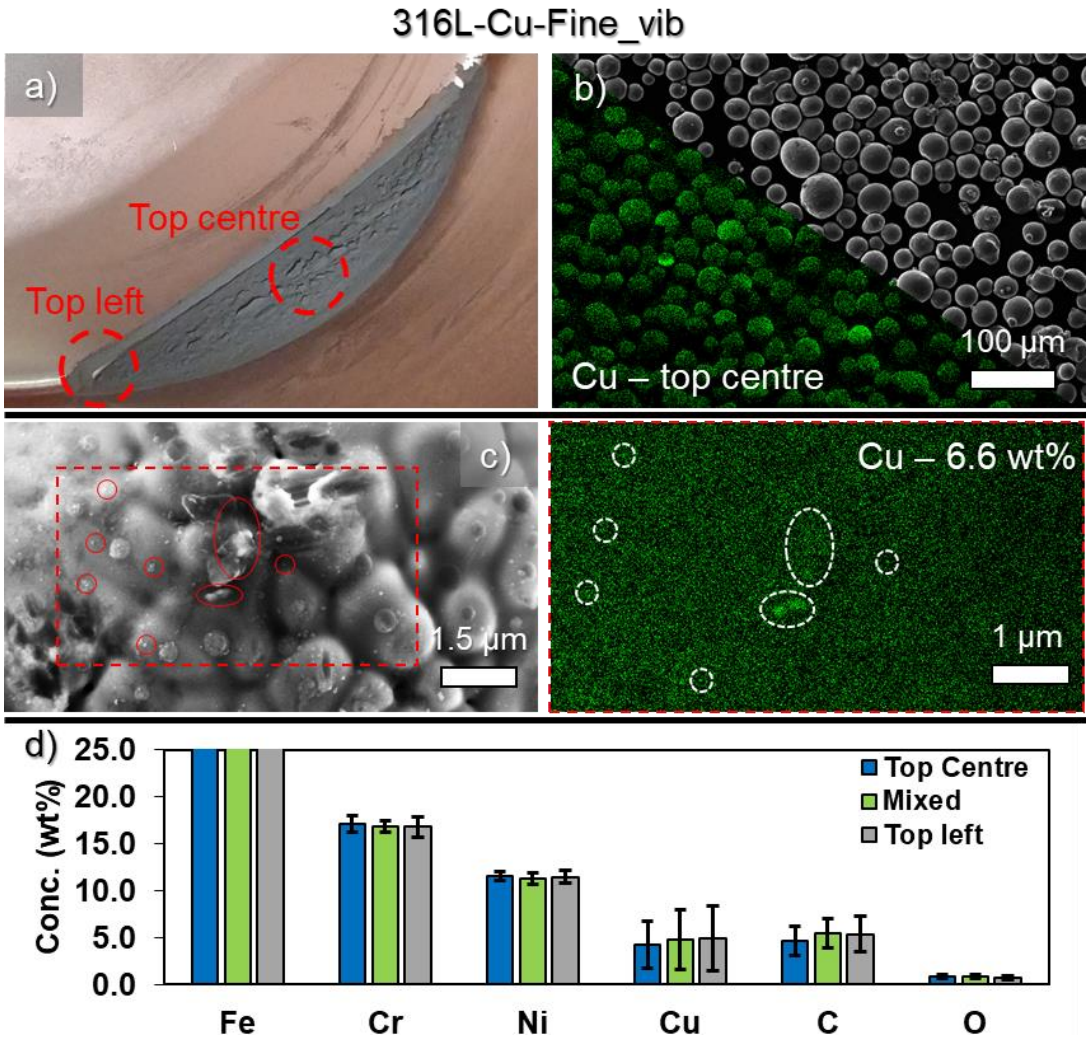

Figure 51 - Images and EDX data from the 316L-Cu-Fine_vib sample, a) photo of powder after coating, the colour is dull grey, sub-samples were gathered from the two highlighted regions, b) split Cu EDX map and secondary image of coated powder, coating is non-uniform with bright particles on the map, c) high magnification secondary image of particle surface, with corresponding Cu map highlighting nodular growth, d) summary of EDX point scans from multiple particles (n=10) from the sub-samples, full data in Table 39.

The split EDX map/backscattered image of the Top Centre sub-sample in Figure 51 b) indicates relatively consistent Cu content across the region imaged. Taking a closer look at an individual particle surface c), again nodular growth was seen as confirmed by the Cu EDX map. The Cu content across the three sub-samples, Figure 51 d), indicated on a) (as well as mixed) mirror those from the Coarse sample. The Top Left region had a content of 4.9 ± 3.4 wt%, with the Top Centre slightly lower at 4.3 ± 2.5 wt%, and the Mixed in between at 4.8 ± 3.2 wt%. Given that these values are closely grouped, it appears that this agitation via vibration leads to similar powder movement throughout the powder bulk, leading to similar amounts of uncoated and coated powders.

4.2.3.3 Dried Rotation Trials

Given the dramatic change seen when drying and coating the Ag powder in the Ag-Ti trials, pre-drying of the powder was investigated in conjunction with the rotation parameter set. Samples were heated in-situ at 50°C for 24 h under low vacuum ($3x10^{-3}$ Torr). Only the rotation parameter set was used as at this stage in the trials the vibration motors had seized before their rated lifetime had been reached. This was both due to internal wear from overheating in vacuum (these motors were designed to pulse rather than operate continuously) and because of demagnetization from being in proximity to the magnetron magnetic field. As such whilst the use of these motors provided a simple vibration solution mitigating the need to design a separate mechanism, this would not be useable for regular use.

Results for the coated coarse distribution with pre-drying are shown in Figure 52, a) and b) compare the photos after coating of the undried 316L-Cu-Coarse_rot and 316L-Cu-Coarse_rot_dried. From these images a clear improvement can be seen, as there is no powder adhered to the barrel surface and the colour (grey) is uniform across the surface of the powder. Again scattered nodular growth is seen on the surface of particles, see Figure 52 c), confirmed as Cu with EDX maps. EDX point scan data from particles from two sub-samples, Top Centre and Mixed, are summarized in d), with Cu content of 10.8 ± 3.7 and 9.4 ± 5.3 wt% respectively.

In contrast to this, the results of the coating of the fine distribution, see Figure 53, have not improved. Figure 53 a) and b) compare the previous undried result (316L-Cu-Fine_rot) with the dried powder result 316L-Cu-Fine_rot_dried. The results are similar, with the porous structure consistent between the two, and whilst the lighting conditions of the photograph are slightly different, it is clear that the visible power is heavily coated with copper.

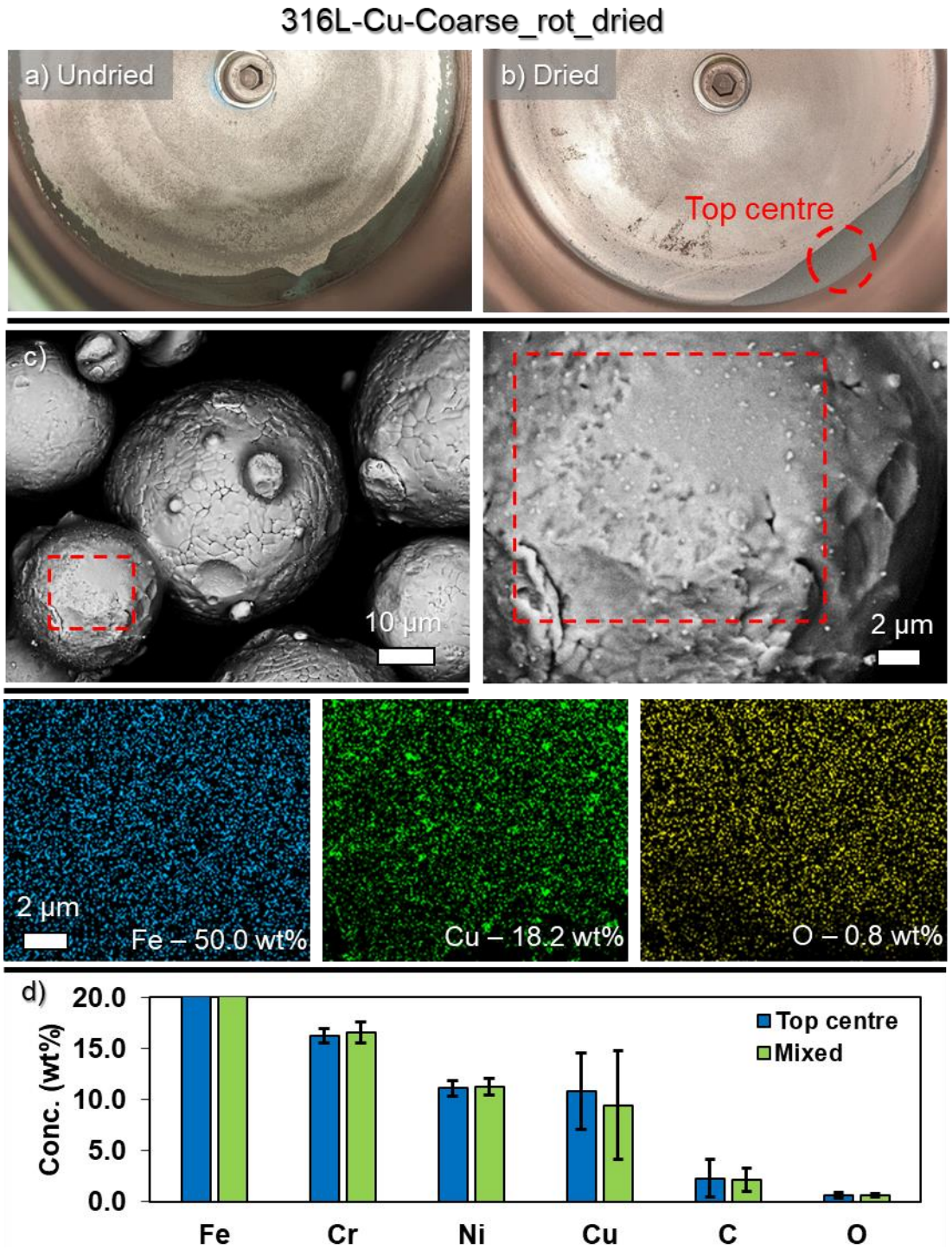

Figure 52 - Images and EDX data from the 316L-Cu-Coarse_rot_dried sample, a) repeated photo of 316L-Cu-Coarse_rot highlighting adherance to barrel, b) photo of 316L-Cu-Coarse_rot_dried showing complete lack of sticking to the barrel surface, powder is noticeably grey, c) backscattered image of a cluster of particles, highlighted region is magnified, the EDX maps for this region suggest that the nodules are Cu, d) summary of EDX point scans from multiple particles (n=10) from the sub-samples Top-Centre and Mixed, full data in Table 40.

Considering the particle surfaces from the Top Surface sub-sample, Figure 53 c) and d), the high concentration of Cu, amounts presented with the EDX maps, confirms that agitation of the powder was minimal, and particles resided at the top surface for a long time. The growth in d) is consistent with nodular growth leading to overall coverage of the surface with a columnar crystalline layer. The summary of EDX data from multiple particles confirms the observations, as the Top Surface Cu content is high, 31.7 ± 24.6 wt%, with a large error. This either suggests that particles were agitated and there is a mix of uncoated and heavily coated particles, or more likely uncoated particles, shadowed by the surrounding scaffold structure were gathered when pressing the carbon sticky tab into the sample. The Mixed sub-sample confirms the non-uniformity of the powder coating, as the mean and error are low, 3.5 ± 2.5 wt%, indicating that the heavily coated particles were such a minor part of the sample that they were not selected in the EDX point scans.

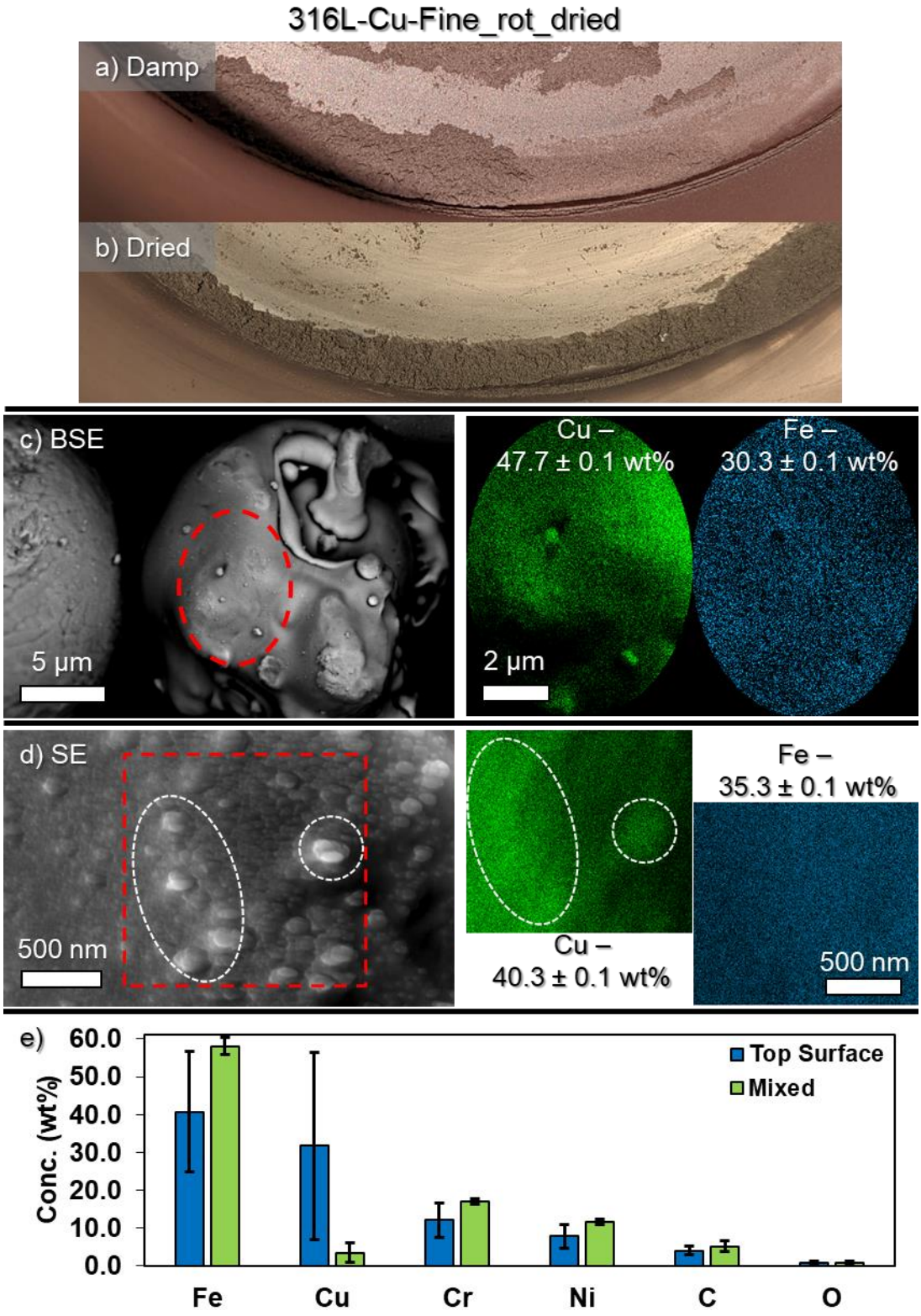

Figure 53 - Images and EDX of 316L-Cu-Fine_rot_dried, a) and b) photos of as-coated powder without drying and with drying, the powder is loosely adhered to the barrel surface with a porous structure, c) backscattered image and corresponding EDX maps of both nodular and uniform deposition/growth, d) secondary image of nodular growth coalescing to form a uniform layer, and corresponding EDX maps, e) Summary of point EDX data taken from multiple particles (n=10) from the sub-samples, full data in Table 41.

4.2.4 BN Coated 316L powder (316L-BN)

Given the mixed success of the dried parameter sets, and the issues with the vibration motors, drying with rotation was taken forward to the trials with BN coating. The as-received 316L powder size distribution was used, with a view to taking the powder for LPBF weld track testing. Due to the very low deposition rate of BN, ~16x lower than that of Cu (approximated from Semicore reference table) [268], the duration of the coating was extended. Two samples were produced, with durations of 24 h and 48 h. Both Ar and N_2 gas flow was used at 7 sccm each, with 70 W of RF power applied. Samples were again dried for 24 h at 50° under low vacuum ($3x10^{-3}$ Torr).

Results of the 316L-BN_24h_rot_dried parameter set are contained in Figure 54. Initially, from the photo in a) it appears that no powder has adhered to the barrel surface, indicating successful agitation, however, when considering the inset optical microscope image, structures similar to those seen in the just rotated Ag powder are evident. The powder had formed a loosely agglomerated island, with cracks visible. When rotation was switched on, this island was observed to shift up the barrel in the direction of rotation and then returned to the lower position as friction was overcome. No turnover of the powder was seen.

To confirm BN deposition had occurred, a strip of Cu foil was attached to the base of the barrel (not shown in Figure 54 a)) during the coating process. This was then analysed with FTIR, see Figure 54 g). The resultant spectrum was of low intensity, with characteristic B—N inter-plane bending and B—N in-plane stretching modes of h-BN visible, and potential O bonding, see Table 3 for references. From a), the coloured fringe patterns on the base of the barrel surrounding the retaining screw also indicate that a thin film has been deposited.

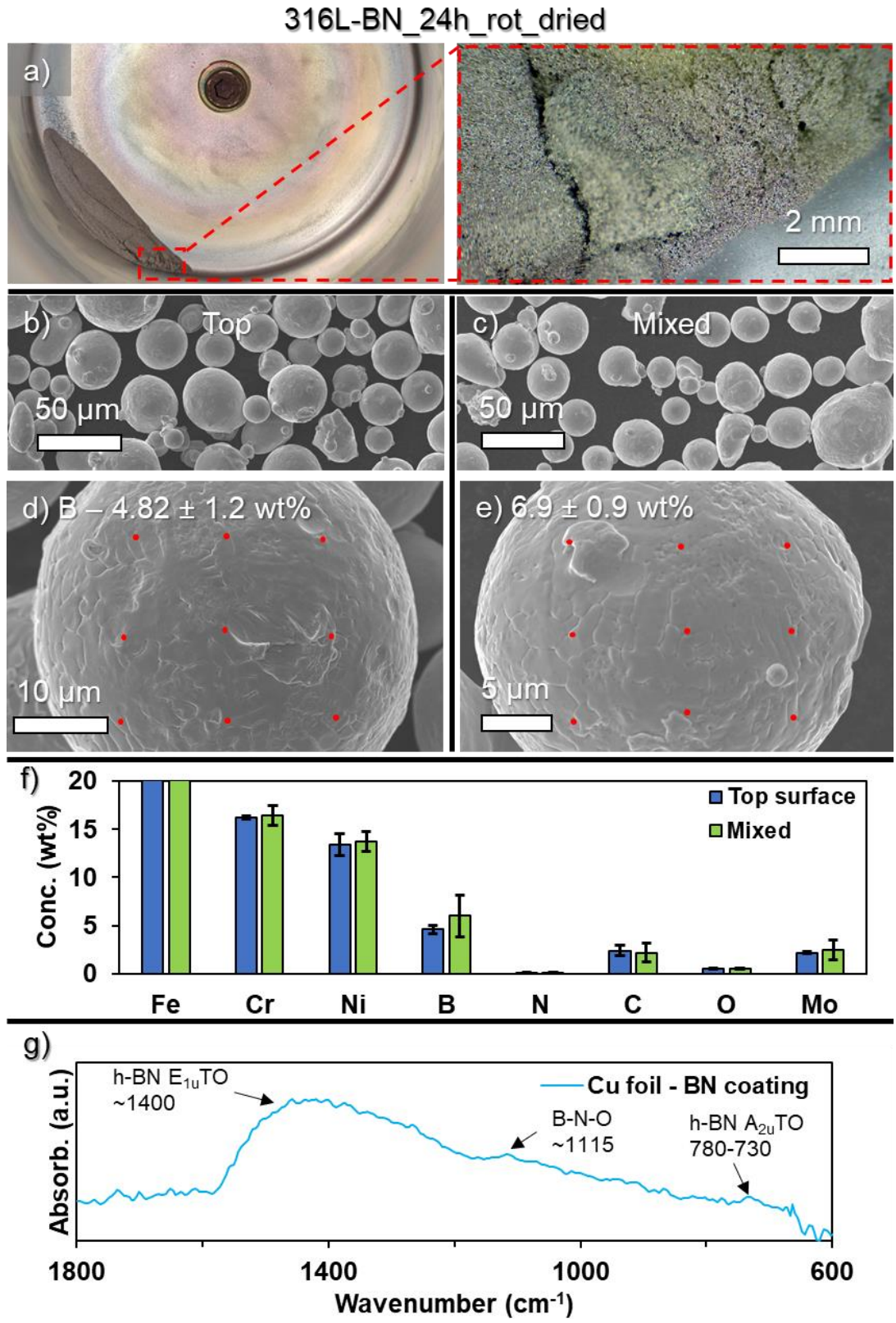

Figure 54 - Images and EDX data from the 316L-BN_24h_rot_dried sample, a) photo of the coated powder, with optical micrograph inset showing loosely agglomerated powder, b) and c) secondary images of loose powder particles from two sub-samples, d) and e) secondary images of individual particles, with dots indicating EDX point scans, with B content and error presented, f) summary of EDX data gathered from multiple particles (n=10), full data in Table 42, g) FTIR spectrum from a slip of Cu foil stuck to the inside of the barrel, indicating potential BN deposition.

Figure 55 contains the images and data from the 316L-BN_48h_rot_dried parameter set. In contrast to the 24 h sample, the powder has adhered to the barrel surface, see Figure 55 a), collecting in the corner where the walls and base meet. A colour change (h-BN is white) was not seen for either coating duration.

As previously, when collecting the sub-samples the agglomerates broke down with minimal force, as seen in the secondary electron images of loose powder in Figure 54 b) and c) for the Top surface and Mixed sub-samples of the 24 h parameter set, and the 48 h Top surface sub sample, Figure 55 b), respectively. When looking closer at the powder particle surfaces, no growth or deposition of material was observed, however, for both 24 h sub-samples B was detected by point EDX scans across individual particle surfaces, see Figure 54 d) and e). The concentration, 4.6 ± 0.4 and 6.0 ± 2.2 wt% suggests that significant material has been deposited, and as B is a low mass element, a sufficient volume of material should be present (and visible) on the powder surfaces.

Considering the EDX from multiple particles (n=10), for the 24 h sample (Figure 54 f)), the B concentration on the Mixed sub-sample was 6.0 ± 2.2 wt%, higher than the Top surface which was 4.6 ± 0.4 wt%. The B concentration on the 48 h Top surface sub-sample, Figure 55 d), was 5.6 ± 0.4 wt%. The error in these measurements is very low compared to the previous measurements of agglomerated/adhered 316L-Cu powder. There is definite evidence of B deposition, both from the FTIR (Figure 54 g)) and from the shoulder apparent in the example EDX spectrum in Figure 55 c). However, it is suggested, from comparing the relative quantities of B detected by the EDX system to the images and lack of growth features on the particles, that an overestimation of B content has occurred, and as such there is low confidence in this data. A technique such as XPS would be suited to assessing the quantity of B deposited. Due to the lack of significant deposition of B evidenced here, these powders were not taken forward for further testing via LPBF weld tracks analysis.

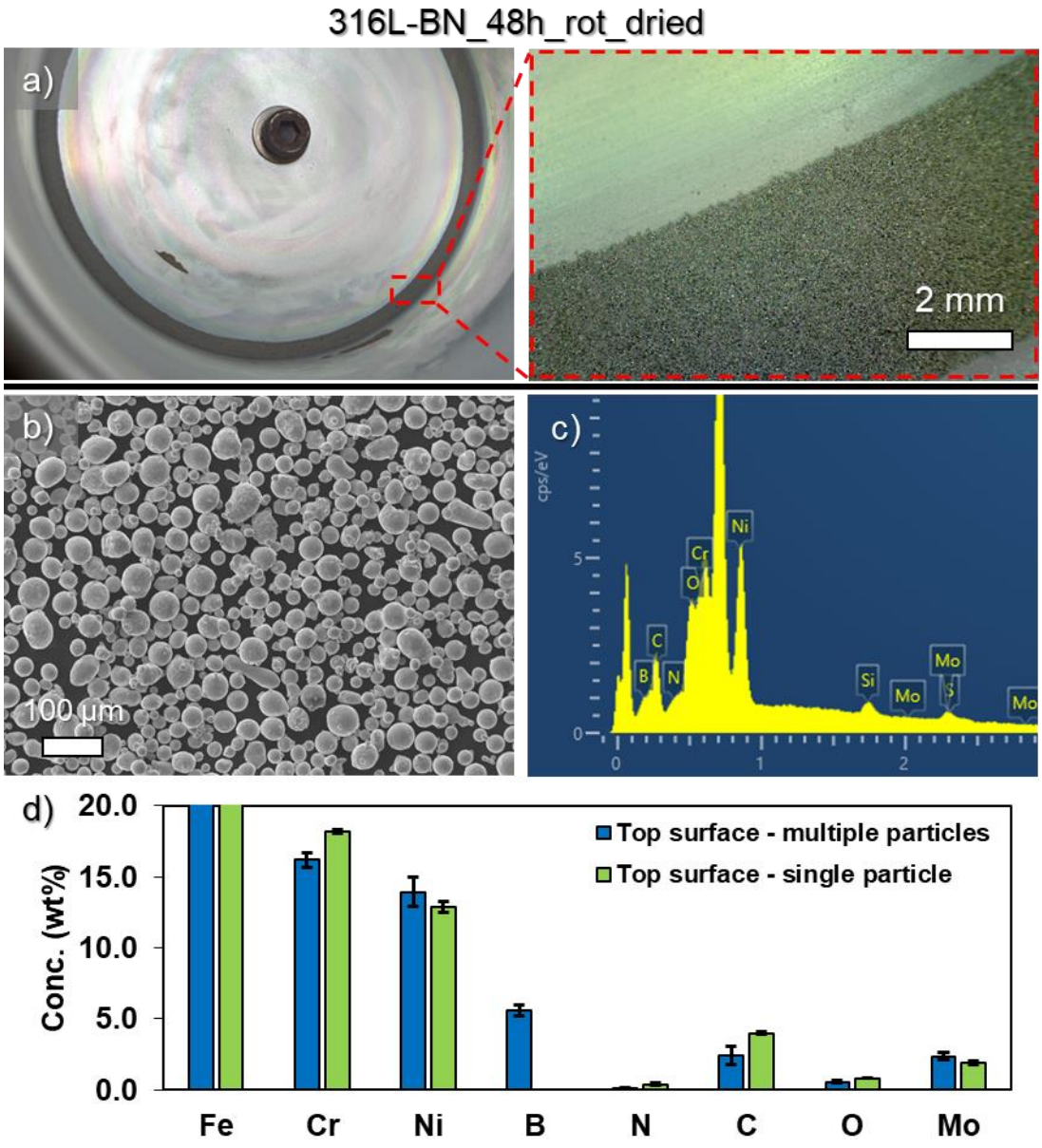

Figure 55 - Images and EDX data from the 316L-BN_48h_rot_dried sample, a) photo of coated powder with optical microscope inset showing powder adhered to the edge of the barrel, b) secondary image of loose powder from the Top surface, c) EDX point scan spectrum from a single particle surface, d) summary of EDX data from point scans of multiple particles and an area scan of single particle (not shown), full data in Table 43, note that due to the low mass of B and lack of growth features there is low confidence in this data.

4.3 Discussion

The techniques developed and descibed in this chapter offer significant scalability to generate sufficient quantities of coated powders for L-PBF [121, 131]. For the 4 studies contained in this chapter, with the parameter sets employed, a uniform coating was not applied across singular particle surfaces, or throughout the whole distribution of particles in a batch. The reason for this was due to the behaviour of the powders when agitating, since magnetron sputtering is a line of sight process. Instead, particles which had been deposited onto were partially coated.

The partially coated nature of these powders suggested both a lack of flow and turnover of the powder particles and a lack of rotation of individual powder particles about their own axis. However, the achieved partial coating of powders was sufficient to lead to significant reductions in reflectivity, critical in the use of ~1070 nm wavelength lasers in LPBF.

Figure 56 details the suggested motion of powder for the two types of agitation used in this chapter, rotation and vibration. For the former, Figure 56 a), from observations of the powder flow for all five powders (Cu-Fine, Cu-Coarse, Ag-999, 316L-Fine and 316L-Coarse) the powder bulk was seen to be relatively cohesive, holding its shape whilst it oscillated back and forth up the wall of the barrel. The top surface folded over the front edge, providing a constant supply of fresh uncoated powder exposed to sputtered material. A small quantity of powder was seen to adhere to the corner of the barrel, where the wall met the base, and was carried up to the top, either dropping down onto/past the retaining screw or remaining adhered to recombine with the bulk.

The driving force for this agitation is thought be the combination of friction between the barrel surface and the underside of the powder bulk, ‘pulling’ loose powder from the underside as the oscillations occur, and then gravitational forces cascading the drawn out powder over the top surface. Importantly, this mechanism was only

dominant during the observations prior to coating, and in the initial stages of coating, i.e. while both deposition and agitation time were low.

The increased flowability, and correspondingly more uniform coating, of the Cu-Coarse powder in the first study is likely to be due to the larger mass of the individual particles (the particles in the Cu-Coarse distribution are the largest in this chapter, D50: 39.4 µm, D90: 59.6 µm).

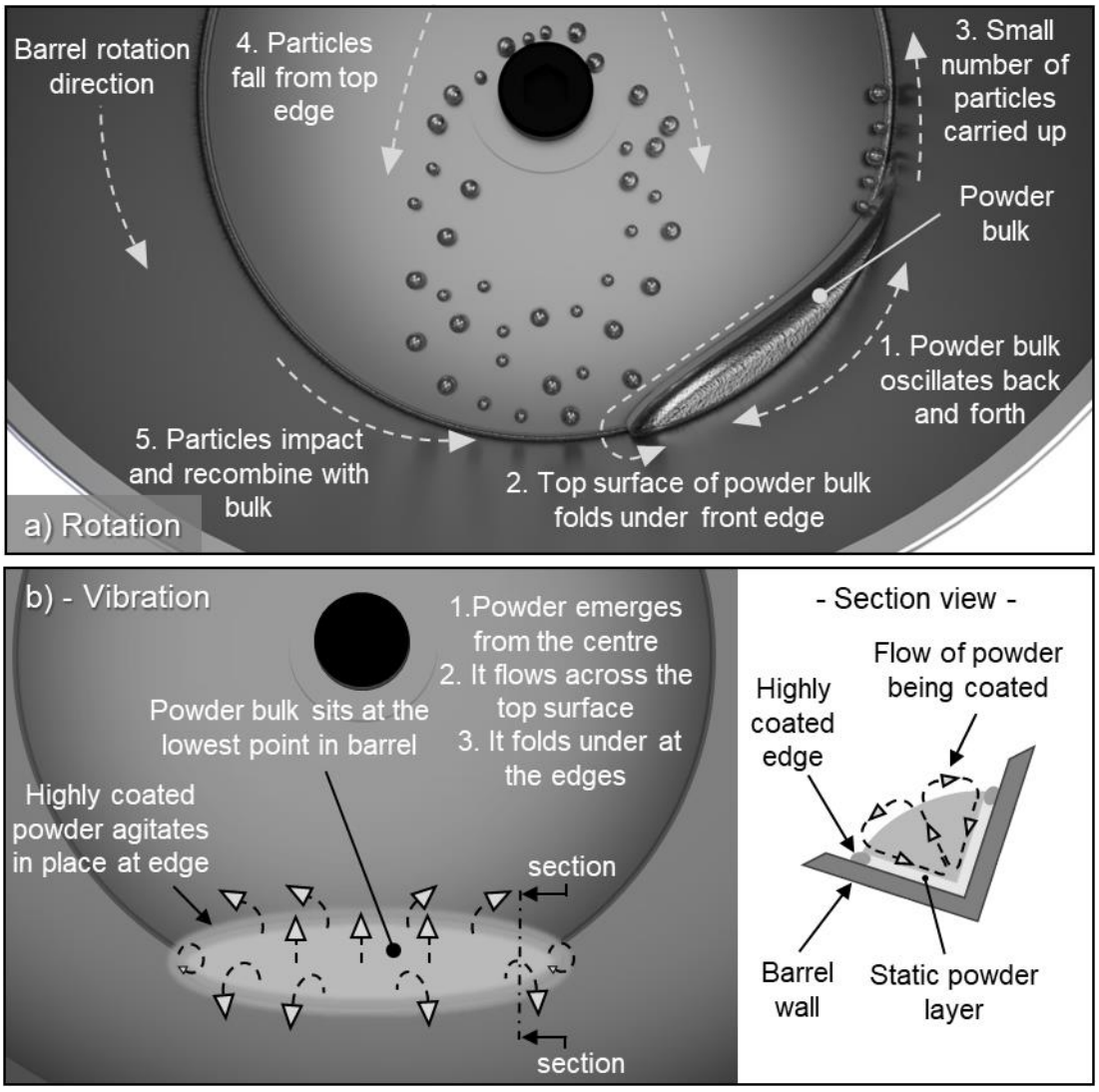

Figure 56 - Schematics demonstrating the motion of powder particles whilst being coated via magnetron sputtering, a) Rotation, powder is carried up the barrel surface, the top surface flows over, particles are carried up and fall b) Vibration, the bulk remains at the base, flowing up through the centre, flowing over at the edges, the section view shows a static powder layer in contact with the wall due to friction and cohesion. See text for details.

As these higher mass particles are affected to a greater degree by gravity, these forces could overcome the cohesive friction, van-der-waals and electrostatic forces between adjacent particles, allowing the powder to flow and cascade across the top surface of the powder bulk to a greater degree than the Cu-Fine. In contrast, the smaller particles present in the Cu-Fine distribution will have had a lower force imposed by gravity and are also likely to have had a higher packing density, leading to a higher degree of mechanical interlocking and dominant cohesive forces, preventing the motion of powder particles relative to one another [269, 270]. The lack of particle turnover was seen from the non-uniformity of Zn in the SEM image and EDX map (Figure 36) and in the higher reflectivity of the powder, indicating exposed Cu (Figure 35). These results suggest that the coated powder will absorb a greater amount of energy relative to the uncoated powder when used in LBPF processes (with the Cu-Zn-Coarse absorbing most), at least in the early stages of the melting process. It is unclear as to what effect this will have after the initial energy absorption and melt pool formation.

When considering the results of the Ag-Ti study, the immediate observation that must be considered is the agglomeration of the powder during coating. Whilst particle size is a well-established factor in powder cohesion, with the increased surface area of finer particles inducing agglomeration [119, 269], the agglomeration of the Ag-Ti cannot be solely due to the small particles and their propensity for cohesiveness. This is clear from the comparison of the size distributions of the Ag-999 and the Cu-Fine, where the D50 values are 28.7 µm and 7.3 µm respectively. In essence, why did the Ag agglomerate whilst the Cu did not? The deposition rates of Zn and Ti are different, so this could be a possible cause for agglomeration via Ti overcoating and forming bridges between particles. However, soft Ag agglomerates formed without a coating, Figure 40, and as the power applied to the magnetron, and also the duration and rotation parameters were the same, deposition cannot be the sole cause of

agglomeration as Ti deposits ~4 times slower than Zn [268]. Furthermore, as mentioned previously for the Cu powders the forces applied by gravity are key in overcoming cohesiveness. However, once again as the Ag-999 powder is larger, and of higher material density, 10.49 $g \cdot cm^{-3}$ compared to the 8.96 $g \cdot cm^{-3}$ of Cu this again cannot be solely responsible.

Alongside these bulk properties, the surface chemical state can play a significant role in agglomeration. Oxide films can act to reduce the cohesive surface energy of metal powders [271]. The results of XPS of the Ag-999 powder, Figure 43 c), showed that there was 15.0 ± 2.7 at% of O on the surface of the powders, with fitting of the O 1s peak suggesting a potential oxide layer [267]. This is not entirely conclusive however, as the peak was noisy and of low intensity and the component could also be attributed to residual surface O. Given this, there is the possibility of increased agglomeration due to a lack of an oxide film, and as Hsieh and Meyer have suggested, van der waals forces can have greater influence with noble materials [73]. The lack of a passive oxide surface film could also potentially lead to cold welding of the Ag powder. However, there was no observation of this in images and the comparatively low vacuum used during sputtering (8×10^{-3} Torr) is unlikely to support this process [272, 273].

Looking further at the XPS data, the second component fitted to the Ag-999 peak was attributed to residual surface moisture. More conclusively, the Ag-Ti_50W_3h_dried parameter set outperformed (produced a higher yield of loose powder) the previous undried parameter sets, with different agglomerate geometry. This is a strong indication that residual moisture increases the cohesiveness of the powder. This is a complex factor though, as Schmid et al. [118] have previously suggested that the evaporation of moisture in vacuum leads to lack of lubricant between particles, causing agglomeration, opposite to the findings of the current study. Assuming that the drying step did indeed evaporate moisture, for this combination of materials and

equipment, the presence of moisture in the undried samples did not lead to lubrication between the particles. Furthermore Abe et al. [98] worked under the assumption that moisture was not a contribution in their study on particle size and shape effects during coating, due the vacuum conditions used in PVD. Again in this current study this has been shown to be contradictory to results.

The suggested agglomeration mechanism for the undried Ag-Ti powder samples is presented in Figure 57. Firstly Step 1., as can be seen from the initial SEM imaging of the Ag-999 in Figure 39 a) and b), the particles are loosely agglomerated and satellited with fines. As the agitation starts, Step 2., more particles combine to form larger agglomerates. The agglomeration by the end of Step 2. represents the majority of the sieved population of the 3 Ag-Ti powders as seen in the SEM images in Figures 41 a), 42 a) and 45 b) for the 50W_3h, 100_1h and 50W_3h_dried respectively. However, if the agglomerate gains enough mass, the mechanism proceeds to Step 3, where the gravitational forces dominate, and the agglomerate moves to the leading edge of the cohesive powder bulk. At this location the agglomerate is exposed to greater amounts of sputtered material, Step 4., and starts to accumulate particles that have been carried up the side of the barrel, dropped or delivered to the bottom centre of the barrel, see Figure 56.

It is suggested, from considering the onset and amount of agglomeration in the 100W_1h sample, that the higher flux from the magnetron both increases the possibility of an agglomerate proceeding to Step 3. and also reduces the possibility of the agglomerate being reabsorbed into the powder bulk, as there is a rapid increase in mass relative to the 50W_3h parameter sets.

The irregular geometry of the agglomerate promotes frictional forces with the barrel surface leading to tumbling/rotation, further increasing loose powder up take, Step 5.. As the supply of loose powder is exhausted, the agglomerate continues to rotate, densifying over time as the irregularity causes bouncing during tumbling. This can be

seen from the comparison of the agglomerates in Figure 41 b) and Figure 42 b), for the Ag-Ti_50W_3h and Ag-Ti_100W_1h parameter sets respectively. The former has a dense, closely packed structure, whereas the latter contains porosity. This indicates that the consolidation and densification of agglomerates is time dependent, increased for the 3 h duration over the 1 h duration. As relatively few particles are being added to the surface of the agglomerate, a skin forms from the sputtered material, concluding Step 6..

The raft-like morphology of the agglomerates in the Ag-Ti_50W_3h_dried sample do not follow the mechanism outlined in Figure 57. The mechanism that does form these agglomerates is unclear, however it is suggested that due to the fine particulate size of the powder, the interstitial gaps and channels betweeen powder particles is low. This would reduce the permeabilty of the powder, and could potentially reduce the effectiveness of the drying step, as moisture could be prevented from diffusing to the surface of the powder to be pumped away [270].

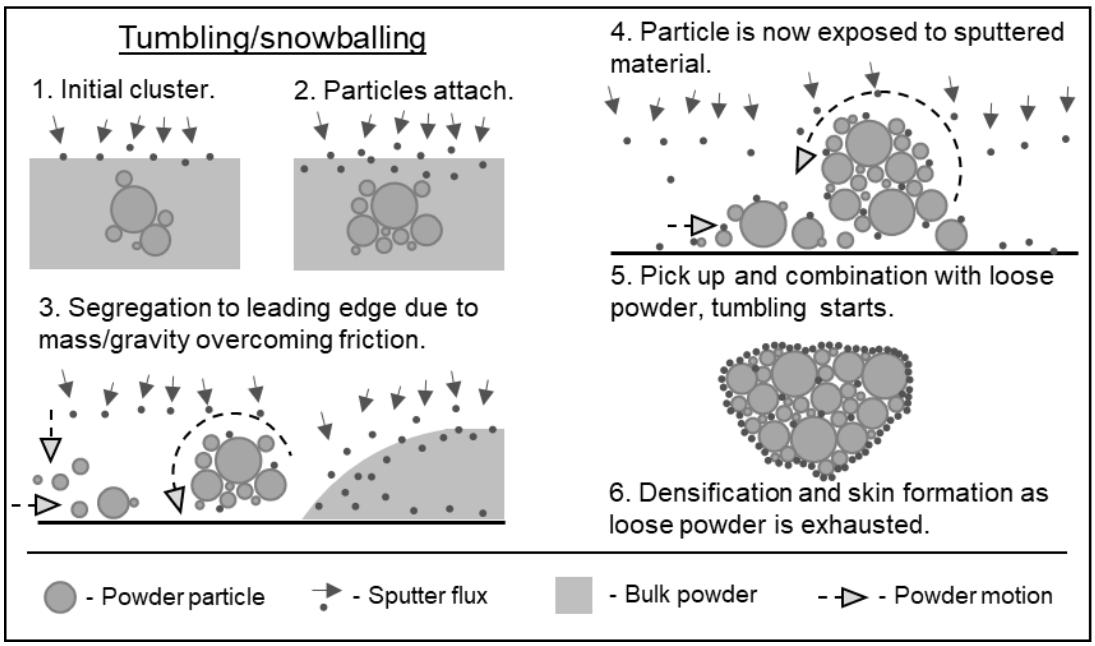

Figure 57 - Schematic detailing the suggested agglomeration mechanism for the Ag-Ti powder coating parameter sets without an added drying step prior to coating, see text for details.

This could therefore lead to a damp region, obscured by the dry powder on top. With the dried loose powder flowing around this ‘pre-agglomerate’, the gravitational forces mentioned previously would lead to separation to the leading edge, and over coating of the agglomerate. The rationale for this mechanism is taken from the shape of the agglomerates in Figure 45 a), which appear to have a geometry matching the corner radius where the barrel wall meets the base, and are elongated, so no tumbling has occured. A mid-drying agitation step could prevent this by turning over the powder to allow thorough removal of moisture.

For the vibrational agitation (used with the 316L-Fine and 316L-Coarse), detailed in Figure 56 b), the powder bulk was stationary at the bottom of the barrel, with visible flow of powder emerging from the centre and moving across the top surface towards the edges. From the images/EDX in Figure 50 a)/c) and Figure 51 a)/d), for the 316L-Cu-Coarse_vib and 316L-Cu-Fine_vib respectively, a static edge can be seen around the powder bulk, with increased levels of Cu in the Top Left edge sub-samples relative to the Mixed sub-samples. It is proposed, see section view in Figure 56 b), that due to the gentler agitation provided by the vibration motors, that a thin layer of powder remains adhered to the wall of the barrel, supporting and preventing the surface edges from flowing into the bulk powder. This then leads to the edges of the powder bulk being highly coated relative to the inner region, which flow as shown in the schematic. It was noted that for all powders coated in this chapter, that flowability (subjectively) increased subsequent to coating, and therefore this increased flowability would improve the flow of the centre region relative to the obscured adhered layer in contact with the wall in Figure 56 b).

The soft agglomeration seen in the 316L-BN_24h_rot_dried, Figure 54 a), where a cohesive cracked island has formed, with minimal cascading of powder over the top surface, is thought be due to rearrangement of the particles over time. The long

duration of the coating, 24 h, allows time for the particles to find low energy sites to sit, interlocking with one another until the whole bulk of powder is held together.

The adhesion to the barrel corner and morphology of the agglomerates in the 316L-Cu-Coarse_rot, 316L-Cu-Fine_rot, 316L-Cu-Fine_rot_dried and the 316L-BN_48h_rot_dried samples, is also thought to be due to the rearrangement of powder particles into stable positions as the coating progresses. The geometry of the 45° angled barrel in the area where the powder sits, is a corner, as illustrated in the section view in Figure 56 b). Therefore, at all times the powder, via the agitation, is being funnelled from a larger volume into a smaller volume. This provides an impetus for the compaction of powder, with the agitation providing the energy for particles to rearrange and find energetically favourable resting points. This eventually leads to a fully static powder bulk, surrounding the barrel as seen in the 316L-BN_48h_rot_dried (Figure 55 a)). The difference between this and the macroscopic porous scaffolds seen in the 316L-Cu-Fine_rot and 316L-Cu-Fine_rot_dried parameter sets (Figures 48 c) and 53 b) respectively) are due to the deposition rate and duration. As the Cu deposits at a higher rate than the BN, it is proposed that this inhibits the rearrangement of powder particles into low energy sites, and the duration of 1 h does not allow sufficient time for full densification. Also, the 316L-Fine distribution will have a greater influence from cohesive forces than the as-received distribution used for the BN_48h sample, and as such will agitate and rearrange at a reduced rate.

From these observations and suggestions, the barrel angle of 45° is shown to be a negative factor, due to the agitation of the powder into the corner of the barrel, similar to the collection of powder into crevices at the base of fins in the study by Schmid et al. [118]. This means that the majority of the powder surface is obscured below the surface at any one time. The funneling of the powder also leads to greater adherance and therefore travel up the surface leading to tumbling and impacts, potentially increasing agglomeration. The horizontal hexagonal barrel used by Abe.T et al. [98]

appears to have partially solved this issue as the powder is carried up by the edges but then falls on a flat surface, leading to powder spreading, whereas the angled cylinder in this study carries powder up and then drops it onto a converging surface. This is not ubiquotous however as unocated powder is still present with their hexagonal barrel setup [108].

The three coating morphologies observed on the coated powders in this chapter are summarised in the schematic in Figure 58. Prior to discussing these, it should be noted that whilst not all have been observed in every study contained in this chapter, given the large populations of particles in each batch it is highly likely that all three mechanisms are present in every sample, as well as additional mechanisms that have not been observed at all.

Figure 58 a) shows the first coating mechanism, seen in Figure 36 b) for the Cu-Zn-Fine sample. This mechanism occurs when there is insufficient agitation and a cohesive powder, such that particles present on the top surface dwell there for extended periods of time. The particles are coated with thick (~3 µm, see Figure 36 c)) coating, with columnar structure consistent with Zone 1 growth of tapered crystallites, due to low temperature and low energy flux to the deposited coating [29, 32]. This was seen for the Cu-Zn-Fine powder in Figure 36 b), where the structure produced is porous and scaffold-like with layered epitaxy evident. This structure is distinct from the growth of the 316L-Cu in Figure 47 c) where the coating is more dense. It is suggested therefore that the slightly higher deposition rate of Zn (~1.1x) [274] causes a more rapid vertical growth such that there is not enough time for lateral diffusion, and the island/scaffold does not coalesce as in the case of the 316L-Cu, also seen in Zn deposition previously [275]. This is also indicative of low temperature deposition, as it is more thermodynamically favourable for the sputtered adatoms to attach to previously deposited coating rather than the powder surface. Once the

scaffolds have begun to form, the particle surface is also shadowed, accelerating vertical growth of the structure [8].

The second coating morphology, nodular growth, is seen when there is a low particle dwell time at the surface, due to increased agitation, and with less cohesive powder. This in and of itself is not actually coating, and should really be classified as decorating the surface with material, as a uniform layer is not formed. This type of morphology has been seen previously by Inoue et al. [107, 115, 276] and Yu et al. [277]. The fact that nodules have grown, indicates that there has been some movement of coating adatoms across the surface, as the nanosize of these nodules (~100 nm, Figures 37 b), 41 d), 45 d) and 52 c)) will only form either if there is highly localised growth, which is not the case for the arrival of magnetron sputtered flux, especially to the surface of an agitated particle [92], or the adatoms must be coalescing due to surface energy, in Volmer-Weber type growth.

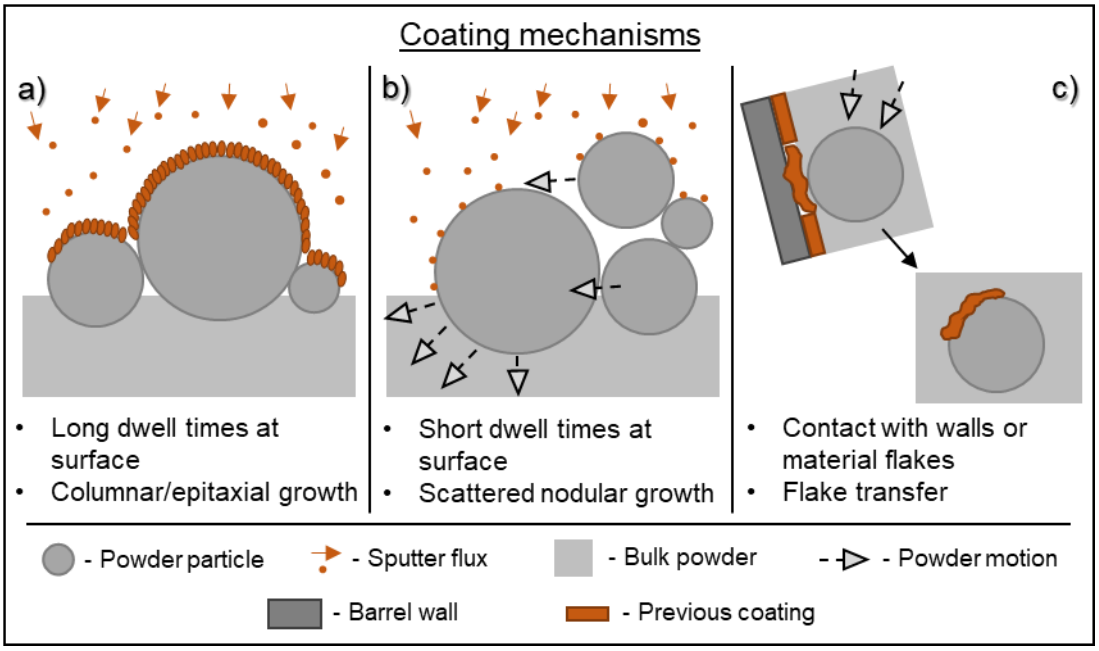

Figure 58 - Schematic detailing the 3 coating morphologies seen in the powder coating studies, characteristic of different times spent exposed to sputtered material flux, and interactions with existing material adhered to the container surface, see text for details.

This coalescence is driven either from energy input from temperature or ion interaction from the unbalanced magnetron, where field lines extend to the substrate, increasing ion bombardment [2, 9, 14].

The third coating mechanism observed in this chapter is the transfer of previously deposited material from the walls of the barrel to the powder particles, Figure 58 c). The internal stress of thin films, deposited by PVD, is generally known to be dependent on thickness, with an increase in thickness leading to increased stress [278]. This combined with the repeated vacuum and thermal cycling leads to delamination of flakes from fixtures [35]. As is shown in schematically in Figure 58 c), loosely adhered material will transfer from the wall of the barrel and come into contact with agitating powder particles. The diagram depicts the particle interacting with the flake whilst is is still partially adhered to the wall, with the particle agitation contributing to the removal of the flake, however this may not necessarily be true, the flake may delaminate independently and subsequently come into contact with a powder particle. Regardless, once contact has occurred, from the images in Figures 42 c) and 45 c), the flake adheres to the particle surface, conforming to the shape. This shape modification is due to the agitation causing interaction and impacts with adjacent particles.

4.4 Conclusions

The deposition of single layer coatings onto the surfaces of powders has been carried out by magnetron sputtering whilst agitating powder using rotation and vibration. Issues with agitation of powder, essential to achieve uniform coatings across the powder population were met, as seen previously in literature, and the reason for these have been discussed. Furthermore, several different coating morphologies and mechanisms have been observed, these have been categorized into 3 distinct growth types. The aims of this chapter (see pg 11 and pg 98) were to investigate and clarify the mechanisms occurring during deposition onto powders, and identify the

influences on the coating morphology. Furthermore, they were to pursue the potential for deposition of ceramic materials via RF sputtering. The key conclusions are contained in bullet points below:

- Reductions in the reflectivity at the ~1070 nm wavelength used in LPBF have been achieved for Cu by applying a Zn coating. This reduction was measured as 34.5 and 38.4 % for the Cu_Fine and Cu_coarse powders respectively. The dependence of coating morphology and coverage on the size distribution of powders was discussed. It was suggested that the agitation of the finer distribution was affected primarily by cohesive forces, leading to reduced turnover, and contrastingly gravitational forces dominated in the coarser distribution, increasing the flowability and therefore coating uniformity.
- When coating Ag powder with Ti, similar difficulties with agitation and uniformity were experienced, however, with yield limiting agglomeration dominating. Reflectance reduction was still seen for sieved populations, with powder coated for 3 h at 50 W target power having a reduction of 25.7 %.
- The agglomeration mechanisms have been discussed, and it is suggested that initial agglomeration of the Ag powder prior to coating, due to residual moisture, fine particle content, and potential lack of oxide layer leads to an increase in agglomerate mass as the particles are agitated. This is exacerbated by the deposition of coating, segregation to the edge of the powder bulk, and subsequent snowballing.
- In determining this mechanism, the presence of moisture on the surface of powders has been categorically identified, through the use of XPS and in the investigation of in-situ drying for Ag powders and 316L powders. This has not been carried out in literature published previously. The removal of this moisture has been shown to modify the behavior of the powder during agitation and coating via magnetron sputtering, leading to different agglomerate shape.

- The change in agglomerate shape was suggested to be due to a lack of diffusion of moisture through the powder from deep regions during drying. Furthermore, it has been concluded that the shape and angle (45°) of the barrel used in this chapter is sub-optimal. This is due to both a funneling effect, which is suggested to increase the adhesion of powder to the corner of the barrel through rearrangement of particles to lower energy sites, and due to a low proportion of powder surface area exposed to the coating flux at any one time.
- Three different coating mechanisms have been identified. The first two, thick columnar epitaxial growth and scattered nano scale (~100 nm) particle growth are highly dependent on residence time at the surface of the powder. If the particles remain in the coating flux for a long duration, they will form thick coatings.
- The third mechanism has not been seen in published literature before, and is significant as it was observed across multiple batches of different material combinations. Images of intact islands of intended coating material and foreign coating material are suggested to transfer from the barrel surface.
- BN coating of 316L powder has been attempted, in order to investigate the deposition of ceramics onto powders via RF sputtering, however the large surface area to volume ratio in powders coupled with the low deposition rate of BN has prevented thorough investigation in these initial trials. Therefore, this objective has not been completed.

5. BN Coating Development – Blended interfaces

Introduction

The majority of published literature on the deposition of Boron Nitride coatings involves the use of Si substrates, see 2.4.2.5. Therefore, there exists a gap in the knowledge of deposition onto different substrate materials, and the need for investigation into coatings deposited onto steel substrates, for the use in tooling applications is apparent. Investigating the deposition onto alternative substrates is one aim of this thesis.

The deposition of BN onto any substrate has been seen to be plagued with numerous adhesion issues, and therefore adhesion interlayers are needed to combat these. The moderate success of Boron/Carbon containing interlayers made by a number of authors [151, 163, 174, 175, 219, 231, 249] in accommodating residual stress and preventing delamination has been utilised in this chapter. Given that this BC interlayer was developed using the aforementioned Si substrates, methodology developed for the improvement of the adhesion of amorphous Graphit-iC DLC coatings [279-282] to steel has been combined. Put simply, a multilayer approach where Cr is used to adhere C, and C used to adhere BN has been attempted, for the first time. The decision to use BN targets rather than B_4C targets was in order to avoid C contamination of the top layer BN.

Furthermore, as the use of steel substrates for tooling, in their hardened and tempered state, requires coating temperatures below the tempering temperature (~480° for H13 hot work tool steel [283]), there is the opportunity to investigate low temperature deposition of c-BN. This is another aim of this thesis. As is outlined in Sections 2.1.3, 2.1.5 and 2.1.6 the increased bombardment of ions by the use of CFUBMS and PDC bias allows higher temperature structures to be formed at lower temperature, potentially advantages for c-BN formation.

5.1 Results

This results section is split into two subsections, each containing the results of different approaches to forming boron nitride coatings. Section 5.2.1 contains results of the initial trials of depositing BN directly onto substrates, with coatings deposited with constant parameters, and coatings formed using a two step methodology adapted from literature. The results in Section 5.2.2 are for coatings which are deposited with a multilayer adhesion coating applied prior to the top layer BN stages reported in Section 5.2.1. Due to the complexity of the coating recipes, each coating has been labelled chronologically with a number, with parameters summarised in tables in each subsection, and master tables, Table 8 and Table 9, containing all numbered coatings is detailed in Section 3.3.1.1.

5.1.1 Static direct deposition onto substrates (Coatings 1, 2, 3 and 4)

Initial coatings runs focused on depositing BN films directly onto static substrates, firstly forming single layer coatings using constant deposition parameters throughout. Coating recipes were then modified to include a varied substrate bias in two steps, attempting to nucleate and grow the cubic phase following methodology published previously in literature [3, 170]. Parameters for both are detailed in the master table in Section 3.2.1.1, which is repeated in Table 16 for the benefit of the reader, proposed coating structures are schematically represented in Figure 59.

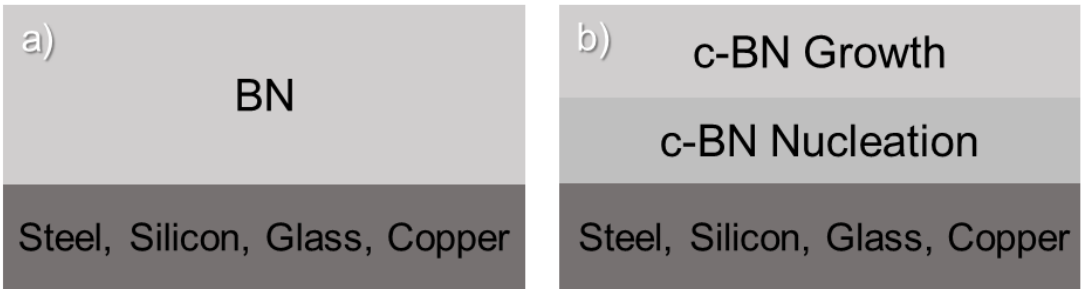

Figure 59 - Schematics illustrating two approaches to forming BN directly on substrates, a) BN coating deposited with constant parameters, b) BN coating deposited in two steps with varying substrate bias to encourage formation of cubic phase. Layer thicknesses not to scale.

Table 16 - Summarised parameters for the BN coatings deposited directly onto static substrates, all coatings except 4 were deposited in a single step, coating 4 was deposited in 2 steps, both parameter sets are shown.

Coating Number	Target Power (W)	Bias Voltage (V)	Ar Flow (sccm)	N_2 Flow (sccm)	Duration
Coating 1	175	60	50	12	6 h
Coating 2	175	60	50	0	24 h
Coating 3	175	60	50	12	6 h
Coating 4 - nuc	175	150	50	12	2 min
Coating 4 - growth	175	120	50	12	4 h

These initial parameters were chosen based on previous use of the equipment, where 60 V bias provides a high current, low energy bombardment, 50/12 sccm of gas gives a sputtering pressure in the range of 10^{-3} to 10^{-2} Torr, commonly used, and the power and duration were selected based upon the low deposition rate of BN.

Visual inspection of the initial coatings deposited with the different parameters listed in Table 16 are shown in Figure 60. Coatings 1 and 2 explored the requirement for additional nitrogen gas during the deposition, to supplement the nitrogen present in the BN target, since target decomposition during sputtering is common for BN. Figure 60 a) and b) show Coating 1, deposited with a 60 V substrate bias, and gas flows of 50 and 12 sccm of Ar and N_2 respectively on glass and copper foil. Figure 60 c) is Coating 2, similar to Coating 1 but without additional N_2 flow, for a duration of 24 h onto grit blasted stainless steel and silicon wafer substrates. Despite the different substrates and durations used, comparison of EDX data, see Figure 62 and Figure 63, shows that nitrogen is not detected in Coating 2, whereas Coating 1 has 44.2 at% nitrogen.

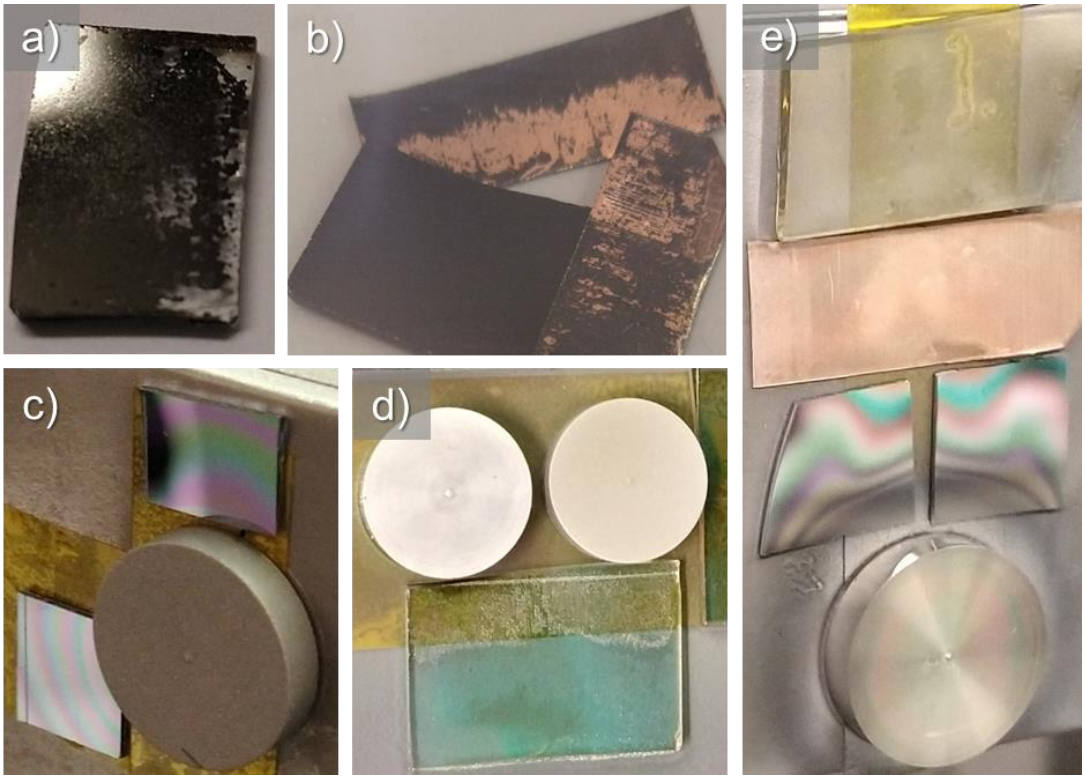

Figure 60 - Photos of initial substrates coated with Boron Nitride directly onto surfaces a) glass slide with Coating 1, b) copper foil with Coating 1, c) grit blasted stainless steel and silicon wafer with Coating 2, d) BN coating 3 deposited using magnetron attachment described in Section 3.2.1, Figure 26, substrates from top left clockwise, machined stainless steel, grit blast stainless steel, glass slide, e) Coating 4 deposited onto, from top, glass slide, copper foil, silicon wafer and machined stainless steel.

Boron was detected in both cases, 42.2 at% and 38.0 at% for the imaged regions of Coating 1 and 2 respectively, indicating that low mass elements are being detected by the EDX system. Coating 2 contains an abundance of oxygen rather than nitrogen, 60.3 at% in the region in Figure 63 a), and also a small amount of aluminium, 1.3 at % in Area c) which is likely contamination from grit blasting. From the SEM imaging, the roughened grit blast texture is apparent, with plate-like growth at the surface. The EDX confirms that both the plate growth and the surface consist of B and O, with minimal substrate material detected, suggesting relatively uniform coverage and scattered oriented overgrowth.

The colouring of Coatings 1 and 2, black and dark grey, indicate contamination of the coating with unwanted material. This was confirmed via the SEM/EDX, see Figure 62,

where 8.3 at% of iron, Fe, was detected from the coating on a glass substrate. The source of this contamination was found to be material sputtered from the stainless steel target clamping ring, see Figure 61 a). To combat this an attachment was developed, detailed in Section 3.2.1, shown in Figure 26, which prevented the Fe from reaching the substrates. All subsequent coatings were deposited with this attachment in place. Furthermore, as shown in Figure 61 b), the magnetron was found to be eroding due to plasma formation behind the magnetron sheath, reducing power directed to the target surface.

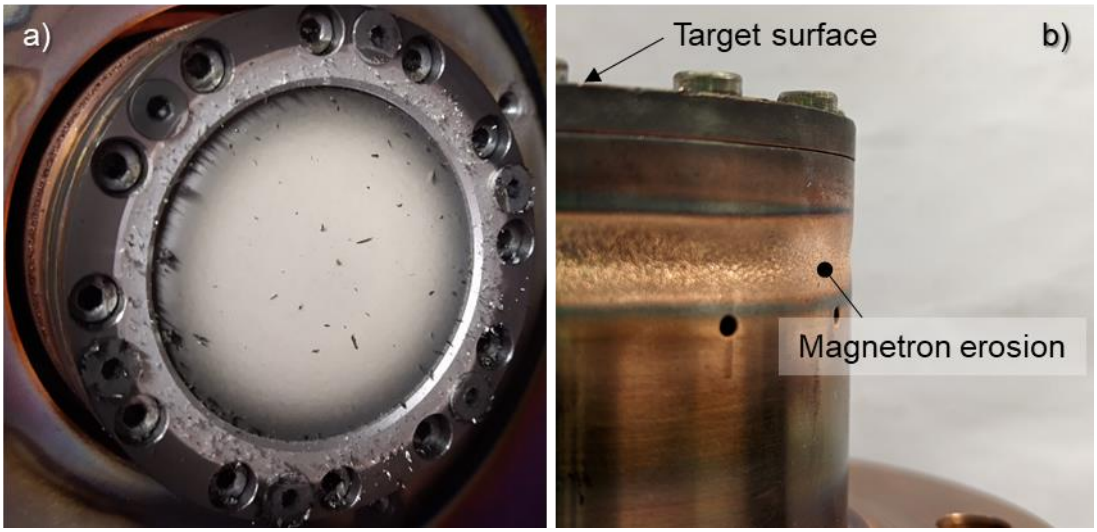

Figure 61 – a) Photo of the front of Mag 2 with BN target and stainless steel clamp ring, subsequent to sputtering at high power, steel filings are evident, b) photo of the side of Mag 2 (no target or clamp in place), highlighting the erosion from plasma formation behind the sheath, note that this ring is just visible to the left of a).

The change in coating appearance from the prevention of contamination can seen in Figure 60 d), which shows Coating 3, deposited on steel and glass substrates coated for 6 h with a pale white/off white colour. SEM imaging, Figure 64, shows that the coating growth on both machined and grit blasted substrates is non-uniform, with a topography containing ‘curls’ of material. The substrate surface is visible on the machined sample, which is indicated in the more ‘shiny’ appearance in Figure 60 d)

relative to the matte finish of the grit blasted sample where no substrate was revealed in the SEM imaging.

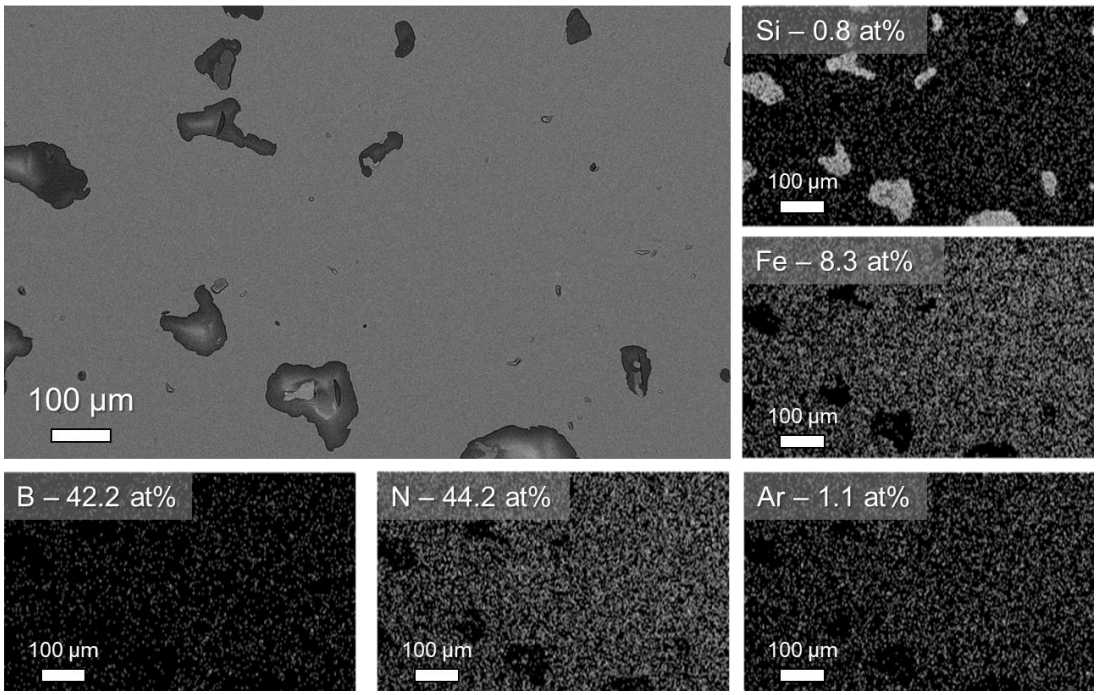

Figure 62 - Secondary electron image of glass with single step BN (Coating 1) applied at 175 W target power for 6 h, with EDX maps highlighting flaked coating with silicon content revealed, significant Fe contamination and minor Ar contamination, photo of sample shown in Figure 60 a).

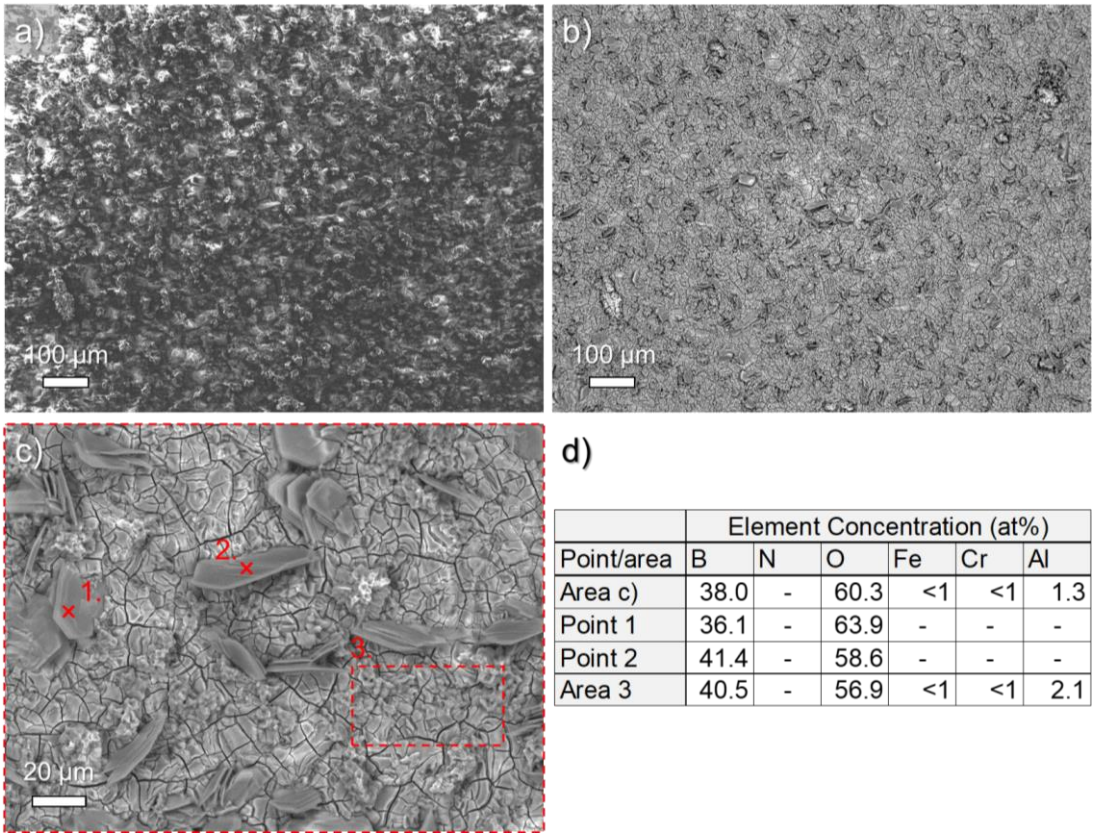

	Element Concentration (at%)					
Point/area	B	N	O	Fe	Cr	Al
Area c)	38.0	-	60.3	<1	<1	1.3
Point 1	36.1	-	63.9	-	-	-
Point 2	41.4	-	58.6	-	-	-
Area 3	40.5	-	56.9	<1	<1	2.1

Figure 63 - SEM imaging of single layer BN (Coating 2) deposited for 24 h without additional N_2 flow, on grit blasted stainless steel, sample photo in Figure 60 c), a) secondary electron imaging, b) backscattered electron contrast, c) higher magnification backscattered image with red points and boxes indicating EDX data collection, d) EDX data for regions in c), highlighting absence of N and abundance of O.

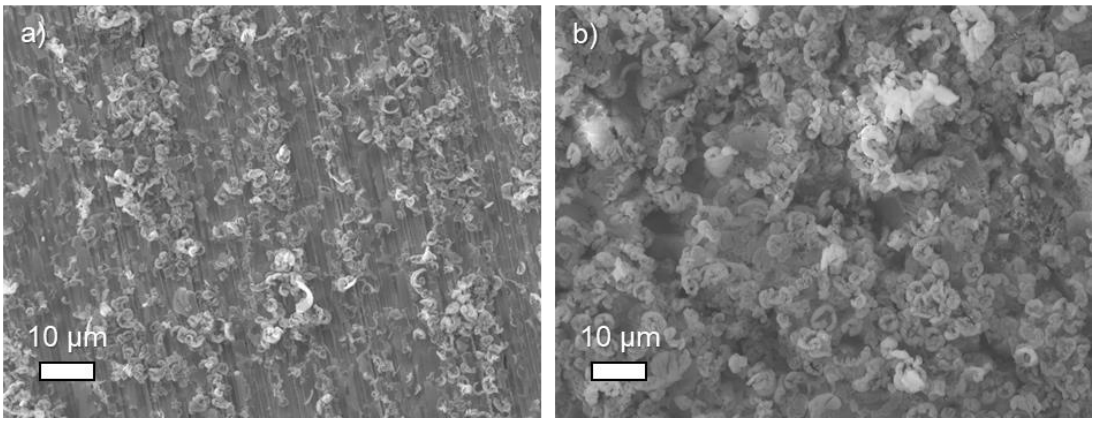

Figure 64 – Secondary electron images of a) machined and b) grit blast stainless steel with Coating 3 applied, distinct non uniform growth is apparent, with curls of material formed on the surface. The machined substrate is visible whereas the grit blast substrate is not.

Table 17 - EDX composition of grit blasted 316L with Coating 3 deposited, data collected from 750x750 µm area, image not shown, error ± 0.2 at%.

Element Concentration (at%)						
B	N	O	Fe	Cr	Al	Ni
50.7	26.5	13.1	5.0	1.7	2.5	0.5

EDX of a magnified region of the grit blasted sample is presented in Figure 65, highlighting the presence of large quantities of B, 50.7 at%, N, 26.5 at%, substrate signal Fe, 4.9 at%, and contamination from Al and O, 2.4 at % and 13.3 at% respectively. The area contained by the yellow circle in Figure 65 highlights the absence of Al and substrate signal where B, N and O are present, indicating that contamination from Oxygen is from atmospheric interaction with the deposited coating rather than solely embedding of alumina (Al_2O_3) grit. This correlates with the composition data from a larger scan area, see Table 17.

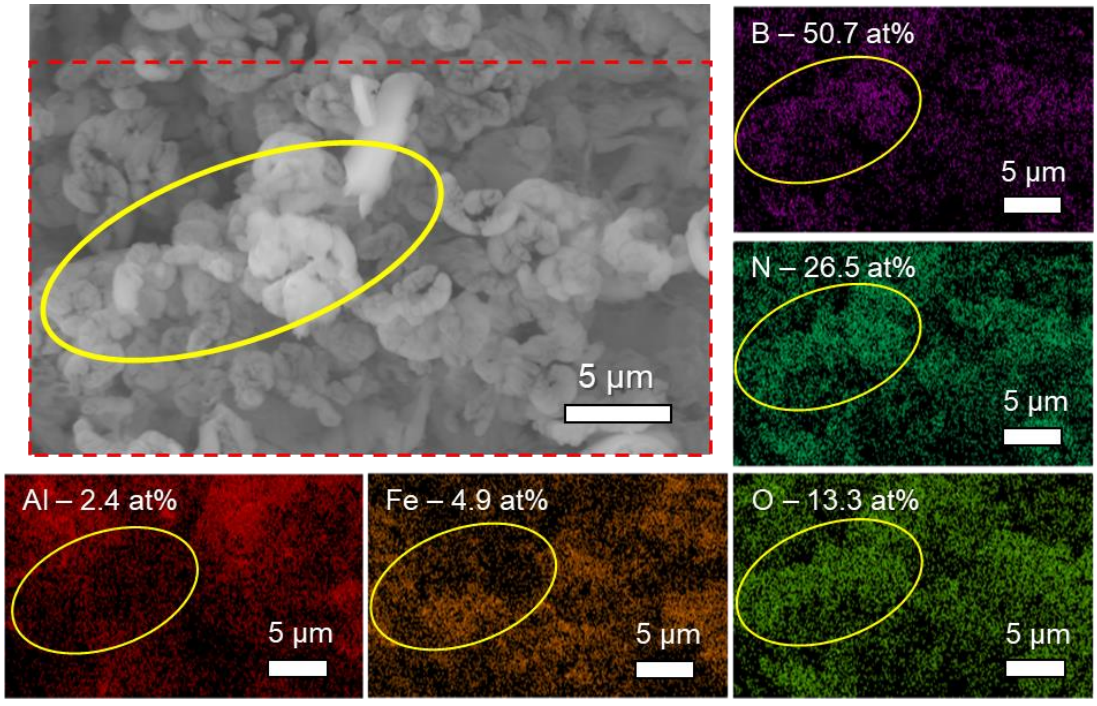

Figure 65 – High magnification secondary electron image of the texture of the growing coating (Coating 3) on grit blasted stainless steel substrate, with EDX maps showing distribution and quantity of elements, data was gathered from the region in the red box, a high proportion of B is present with intended N, O contamination from both atmosphere and grit, Fe substrate signal and Al grit contamination. The yellow circle indicates region where B, N and O are present with relative absence of Fe and Al.

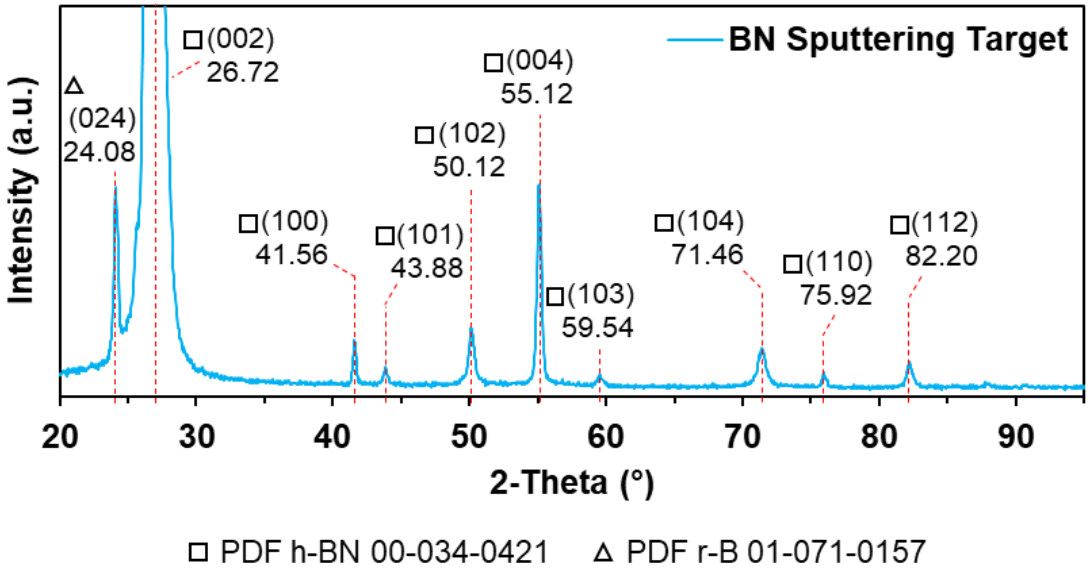

Figure 66 - Glancing angle XRD pattern of the surface of a Boron Nitride sputtering target used for deposition of coatings, the material is hexagonal phase BN primarily in (002) orientation, with some material in (004) orientation, and small quantity of rhombohedral Boron (024).

The XRD pattern for the BN sputtering target is shown in Figure 66, indicating the majority is a hexagonal BN phase with some rhombohedral B phase present. The major peak dominating the pattern is the (002) plane of hexagonal phase BN at 26.72° with minor peaks of h-BN present. The (024) plane of rhombohedral Boron is present at 24.08°.

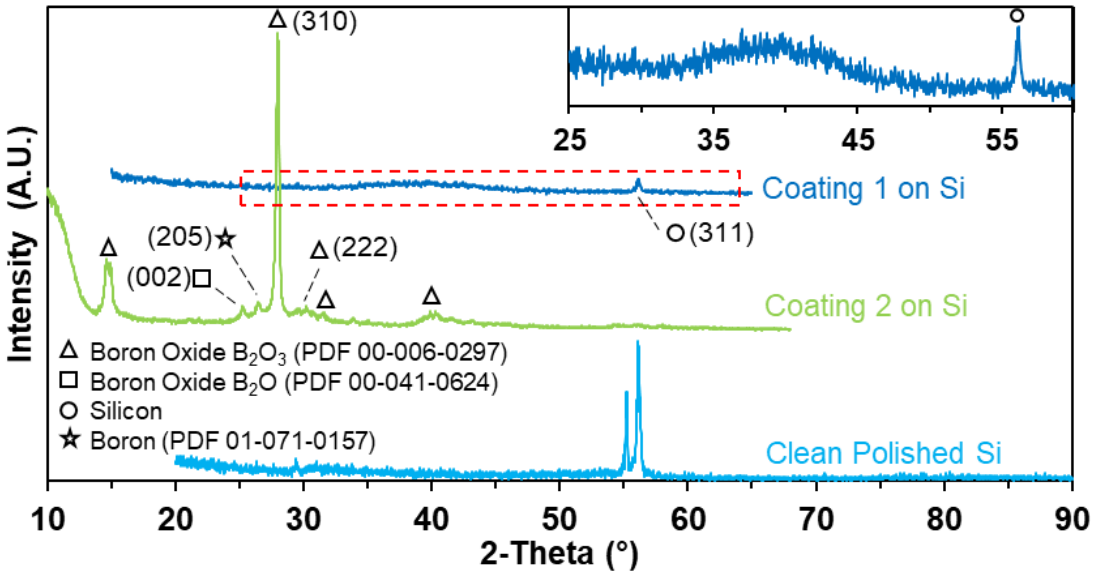

Figure 67 – Comparison of XRD patterns of coatings deposited onto silicon wafer with uncoated wafer for comparison. The substrate is highly crystalline, with Coating 2 containing crystalline oxides, and Coating 1, zoomed portion in inset, showing amorphous/nanocrystalline hump, PDFs used for identification are shown on the figure, B_2O_3 was also identified from Tran et al. [284].

Figure 67 contains the XRD patterns for the coatings deposited on silicon wafer, with the crystalline substrate signal from the (311) included for comparison. This substrate peak is present in the pattern of Coating 1 (6 h), and the inset showing the pattern in the 25-60° range highlights an amorphous/nanocrystalline hump centred around ~39°. The relative reduction in the substrate signal indicates a coating, however given the contamination, no further details can be drawn. The substrate signal is not seen in the pattern for Coating 2 (24 h), indicating that the coating is sufficiently thick that x-rays do not penetrate the substrate. The most prominent peak is for the (310) plane of B_2O_3 at 27.9° [284] correlating with the large proportion of oxygen detected via EDX (Figure 63). Less intense peaks for B_2O_3, B_2O and B are also present.

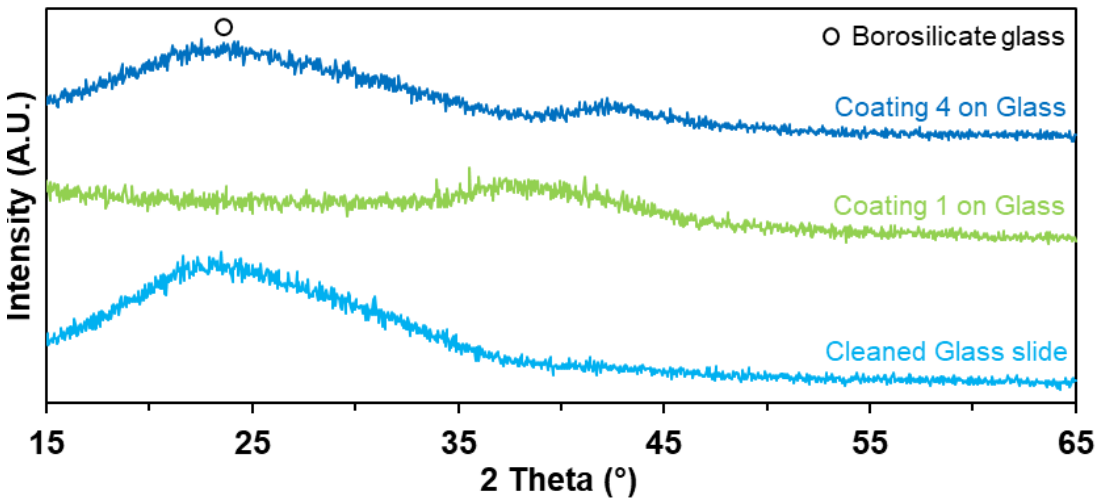

Figure 68 – Comparison of XRD patterns of BN coatings directly deposited onto borosilicate glass microscope slides, substrate shows amorphous hump characteristic of glasses, relative substrate intensity is reduced for coated samples with amorphous/nanocrystalline humps present.

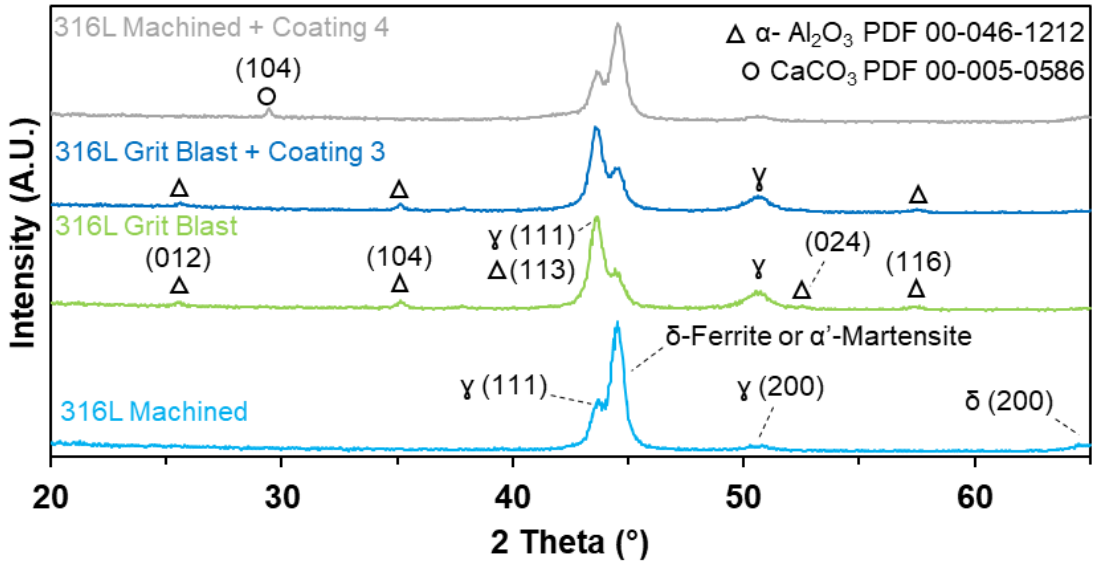

Figure 69 - XRD patterns of 316L machined and grit blast steel substrates showing characteristic peaks for austenitic stainless steels, with contamination from grit evident in substrate pattern and pattern with Coating 3 applied, machined substrate with Coating 4 applied indicates contamination with plasticine.

The pattern of Coating 1 deposited on a glass substrate, Figure 68, agrees with the same on silicon substrate, an amorphous hump centred around 38-39°, with a minimal signal from the substrate. Coating 4 (4 h) on glass shows a strong amorphous substrate signal, with a lower intensity amorphous hump centred around 42°,

potentially corresponding to the (100) peak of h-BN (41.5°), where the (002) peak (26.7°) is obscured by the substrate intensity.

From the patterns of the uncoated machined and grit blasted steel substrates, Figure 69, it is evident that there are peak overlaps with the substrate material in the ~42-46° 2θ range, and the potential c-BN (111) and h-BN (100) peaks at 43.1° and 41.5° respectively (PDFs 01-071-5052 and 00-034-0421). It is also clear that contamination of the steel surface has occurred during grit-blasting, with alumina (Al_2O_3) peaks present post blasting, potentially overlapping the austenite (111) at 43.7°. The pattern for Coating 3 deposited on grit blasted steel does not seem to indicate any additional material phases, despite 50.7, 26.5, and 13.1 at% of boron, nitrogen and oxygen detected by EDX respectively (Table 17). None of the peaks for the boron oxide detected in Coating 2, Figure 67, are present, and the characteristic h-BN (002) peak at 26.8° is missing.

The as machined surface has an intense peak for α'-martensite (or δ-ferrite). This is not expected from the austenitic stainless 316L however could potentially have arisen from deformation induced transformation of the surface material during machining. The pattern for Coating 4 on the machined surface is consistent and also contains this intense peak. The peak intensity of the austenite (111) dominates in the grit blasted patterns after removal/disruption of the machined surface layer. The only further distinguishing peak in Coating 4 is a low intensity peak centred at 29.44° 2θ. This could correspond to a shifted h-BN (002) peak at 26.8° (PDF 00-034-0421) however is more likely to be from contamination with plasticine (Calcite $CaCO_3$) used for fixing the substrates during analysis.

5.1.2 Multilayer Coatings characterisation

As introduced in Section 3.2.1.1 a multilayer approach with blended interfaces was implemented to increase adhesion of the BN to the substrate material, see proposed structure in Figure 70. The choice of this structure was based on the combination of established adhesion layers for carbon based coatings [279, 282] (Cr interlayers blended to a pure C top layer) and the promising research published on the use of Boron Carbon Nitride adhesion layers for BN [3, 163, 175], with the goal of adhering BN to steel substrates.

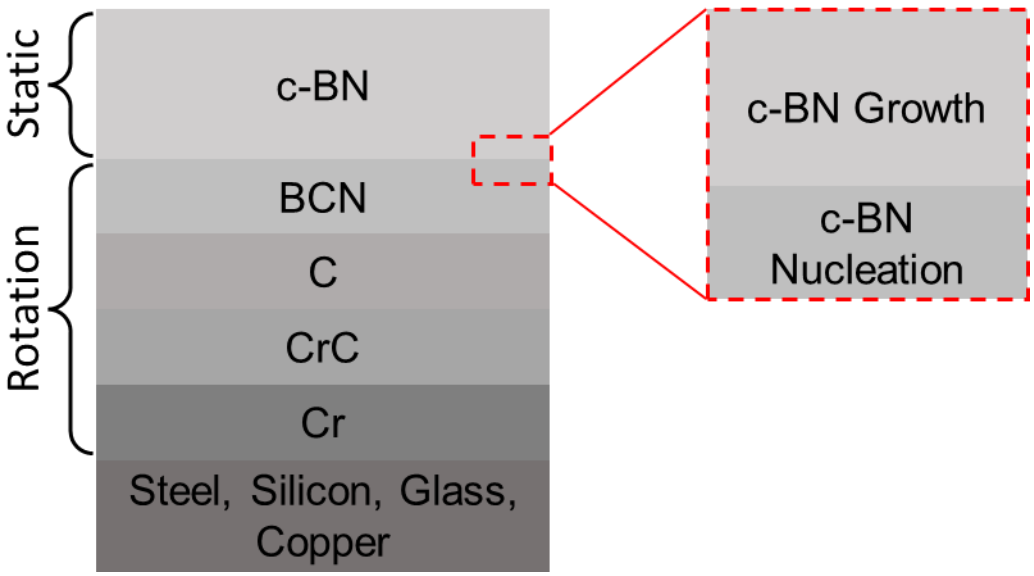

Figure 70 - Proposed structure of the multilayer BN coating applied to substrates, with inset showing the growth and nucleation layers for cubic top layer. Layer thicknesses are not to scale, however the top c-BN layer is intended to be thicker than the adhesion interlayers.

5.1.2.1 Multilayer Adhesion Coating (Rotation) – individual layer contributions

In order to fully understand the contributions of each interlayer to the overall coating structure and performance, isolated analysis was carried out at each stage of the coating, starting from the 1st Cr layer up until the end of the 4th BCN layer, the parameters are summarised in Section 3.2.1.1. Figure 71 shows the calibration data obtained to allow specified thicknesses to be deposited.

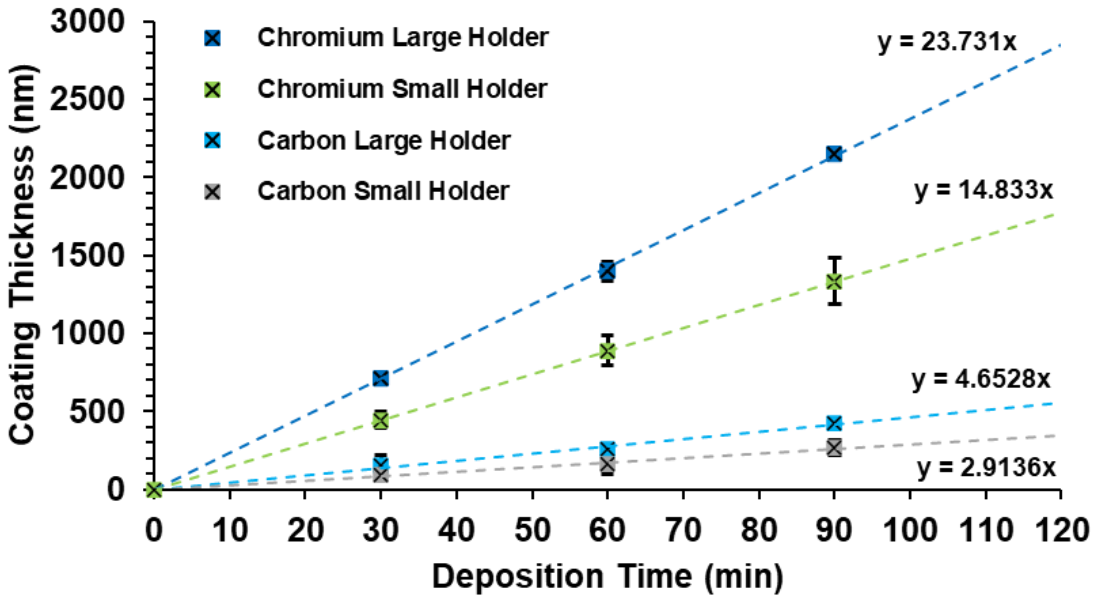

Figure 71 - Measured and forecasted coating thicknesses for Cr and C sputtering at 4 A (2.06 W/cm^2) and 3.5 A (3.21 W/cm^2) respectively with sustrates rotated at 5 RPM for two substrate holders. The large substrate holder has a target to substrate distance of ~55 mm, and the smaller ~117 mm.

Table 18 - Summary of the coating parameters for the adhesion interlayers.

Coating Layer	Target Setpoint	Bias Voltage (V)	Ar Flow (sccm)	N_2 Flow (sccm)	Duration
Chromium	Cr (4 A)	120	23	0	900 s
Chromium Carbide	Ramp Cr (4-0 A), Ramp C (0-3.5 A)	60	23	0	1200 s
Carbon	C (3.5 A)	60	23	0	1200 s
Boron Carbon Nitride	Ramp C (3.5-0 A), BN (175 W)	60	30	15	2400 s

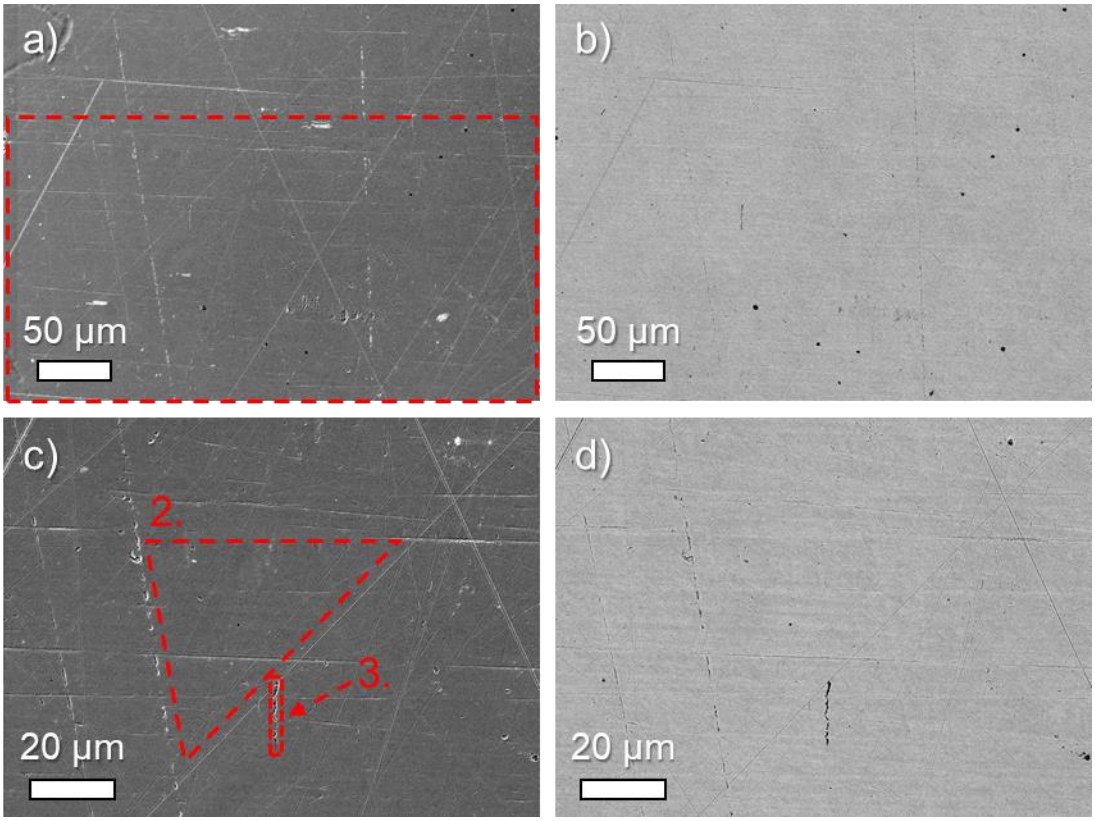

Figure 72 - SEM images, secondary a) and c), backscattered b) and d), of a 316L substrate with Cr interlayer applied, red areas indicate where EDX data was gathered from, shown in Figure 73. The substrate is poorly polished but backscattered contrast indicates uniform composition.

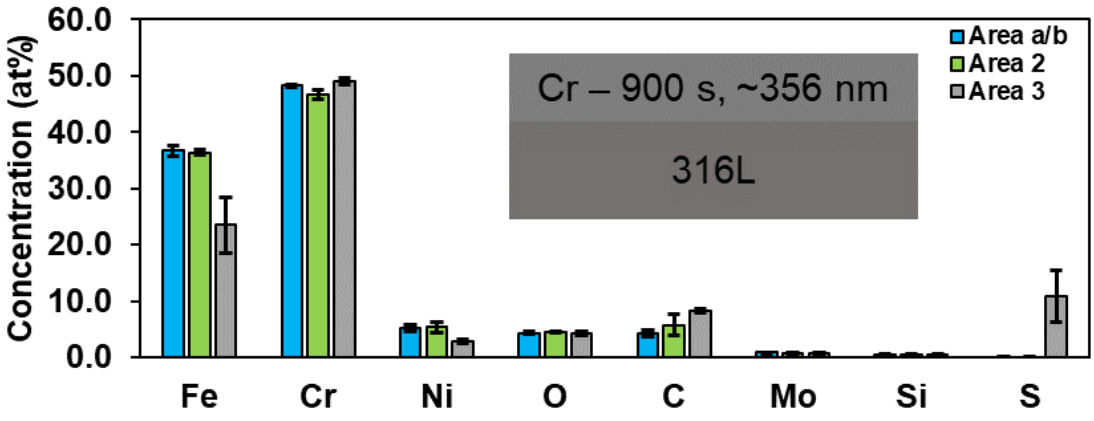

Figure 73 - EDX data from the regions highlighted in Figure 72, Cr content is consistent in all areas with variations in substrate (Fe, Ni), C and S in defect area 3. Full data presented in Table 44. 3 scans were taken per region, with mean and standard deviation shown.

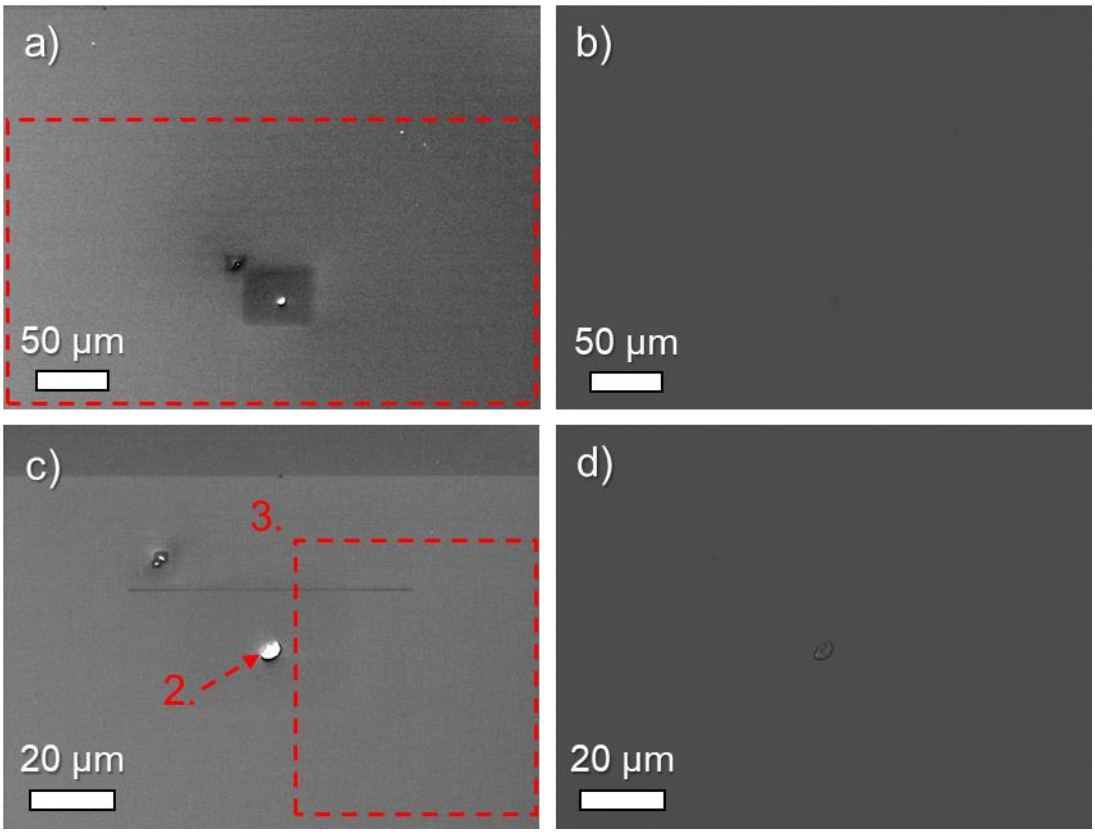

Figure 74 - SEM imaging of the Cr interlayer deposited on Si substrate, secondary a) and c), backscattered b) and d), red highlighted areas are regions which EDX data was gathered from, see Figure 75, coating is uniform across the smooth substrate surface, with minimal surface contamination. Note that the darker grey square surrounding the defect in a) is due to damage from the electron beam whilst setting focus.

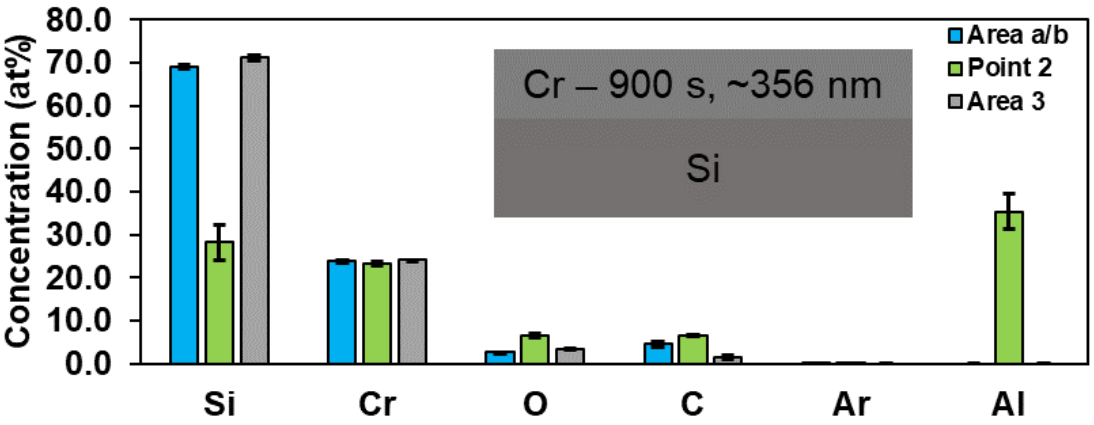

Figure 75 - EDX compositions of the regions highlighted in Figure 74, high proportion of Si substrate is detected, with Cr consistent across all 3 regions and Al deposit from foil the sample was wrapped in. Full data in Table 45. 3 scans were taken per region with mean and standard deviation shown.

Figure 72 and Figure 73 contain the SEM and EDX data for the initial metallic Cr layer applied to 316L substrates, with corresponding data for Si substrates in Figure 74 and Figure 75. This was with a coating time of 900 s corresponding to a calculated thickness of ~356 ± 0.2 nm. As is to be expected from PVD coatings, the coating follows the substrate morphology, conforming to the scratches present on the steel substrate from polishing, and the pre polished Si wafer appearing smooth. The electrons penetrate the coating and x-rays from typical elements in the stainless steel (Figure 73) or silicon substrates (Figure 75) are detected, with additional Cr content from the coating shown in the data. Backscattered imaging indicates a uniform element distribution.

The defect ‘Area 3’ highlighted in Figure 72 c), contains a relatively high at% of sulfur, 10.9 ± 4.6 at%, and whilst 316L can contain small quantities of S, this amount is indicative of a surface contamination or defect. Both substrates show small amounts of C on the surface, ~4-7 at% for both substrate types, as no carbon was intentionally deposited for these samples, the C is assumed to be adventitious from the environment, sample storage and vacuum chamber venting. Note that the small dark grey box surrounding the bright protrusion in Figure 74 a) is due to sputtering of this carbon contamination during focusing of the microscope. The EDX data for the protrusion also indicates that it is contamination, with a high level of Aluminium content, suggesting particle transfer from the foil the sample was wrapped in during storage.

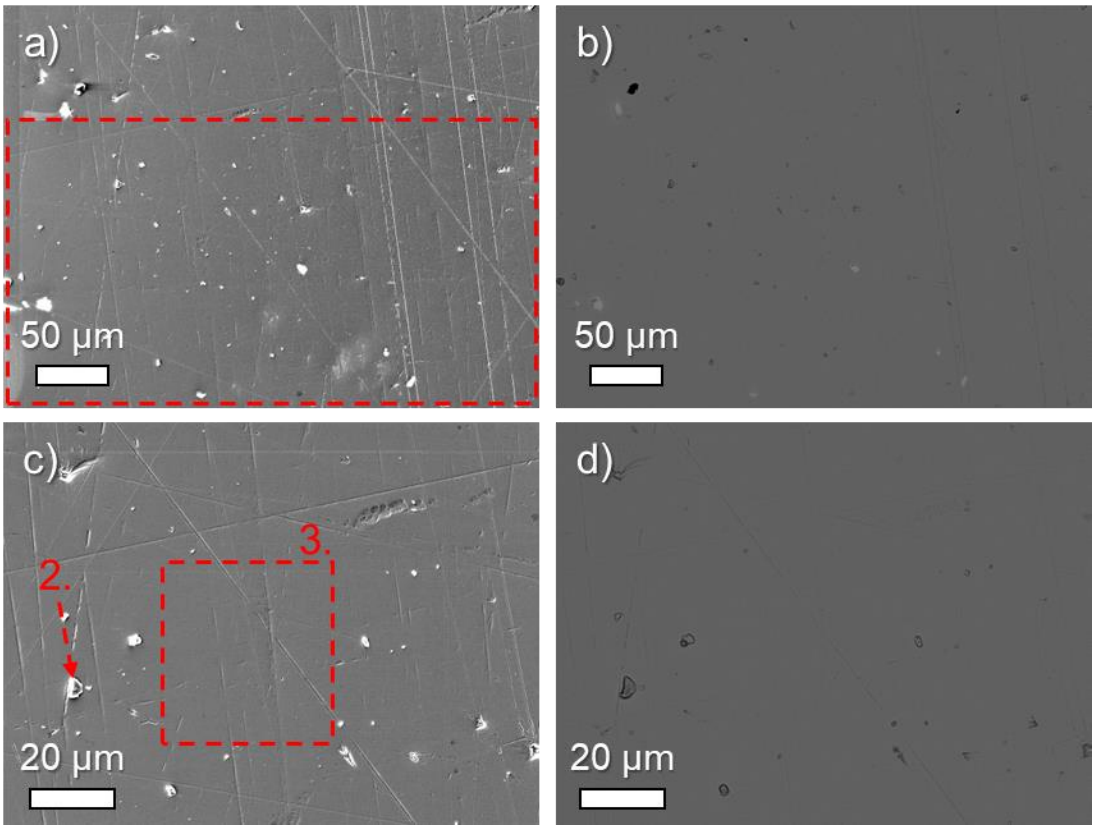

Figure 76 - SEM imaging, a) and c) secondary, b) and d) backscattered of the Cr-CrC-C interlayer deposited on 316L, the images show a poorly polished surface, with consistent composition indicated by backscattered imaging. There are some surface protrusions/contaminated particles, EDX regions are highlighted in red, summarised in Figure 77.

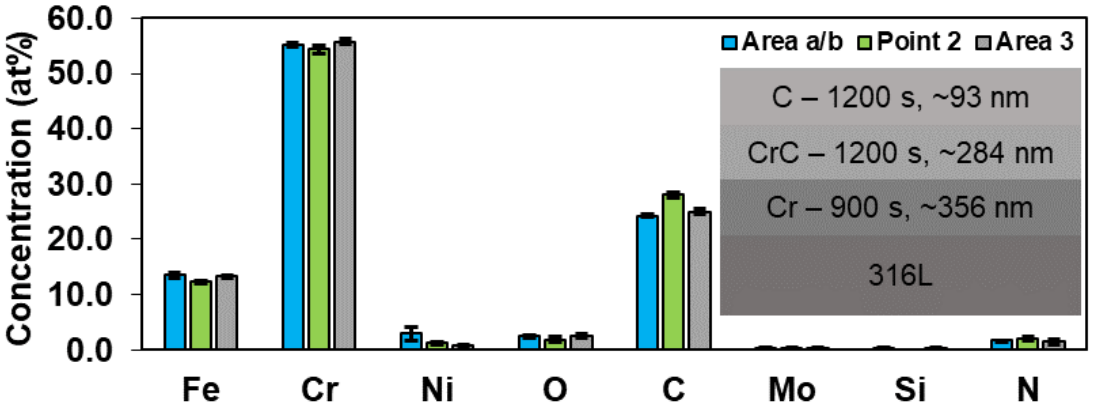

Figure 77 - EDX composition data for the regions of Cr-CrC-C coating deposited on 316L highlighted in Figure 76, majority Cr, with strong carbon intensity/content, contamination of N is of note. Full data in Table 46. 3 scans were taken per region, with mean and standard deviation shown.

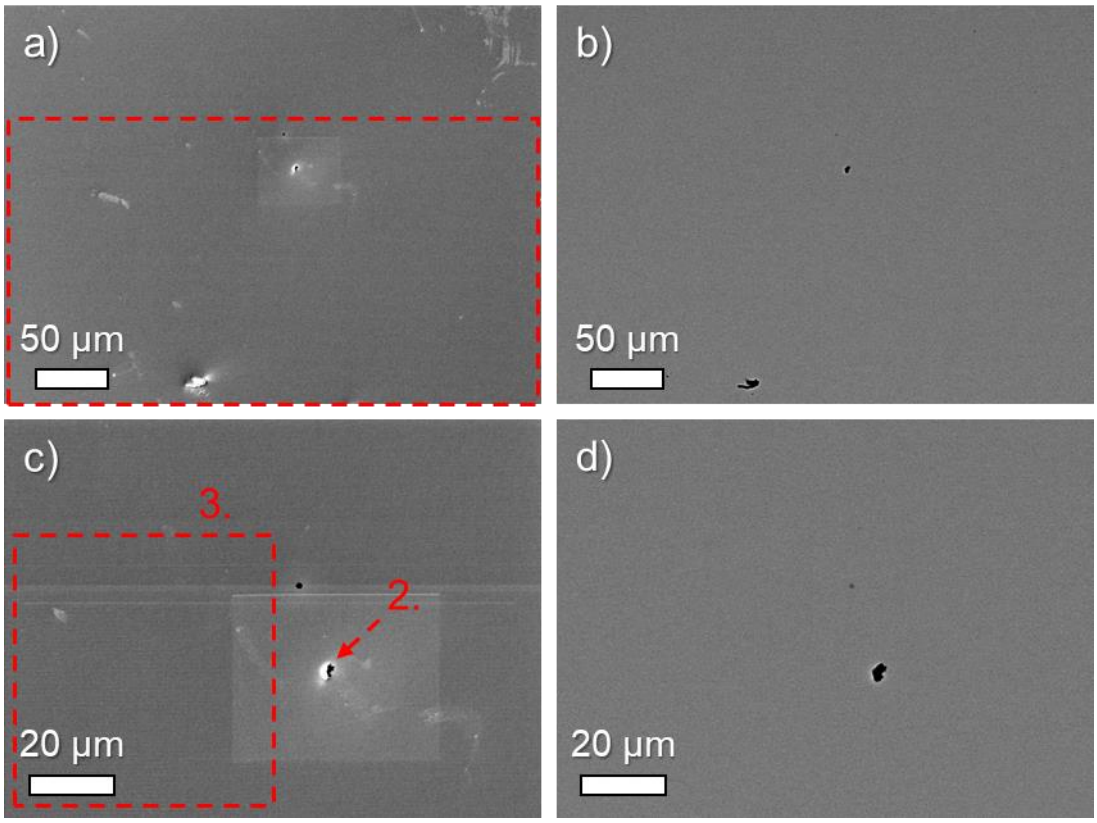

Figure 78 - SEM imaging a) and c) secondary, b) and d) backscattered of the Cr-CrC-C interlayer deposited on Si, surface is smooth, with consistent composition across the surface and a small number of surface defects. EDX regions are highlighted in red, data summarised in Figure 79. Note that the paler box in a) and c) is due to electron beam damage whilst setting focus.

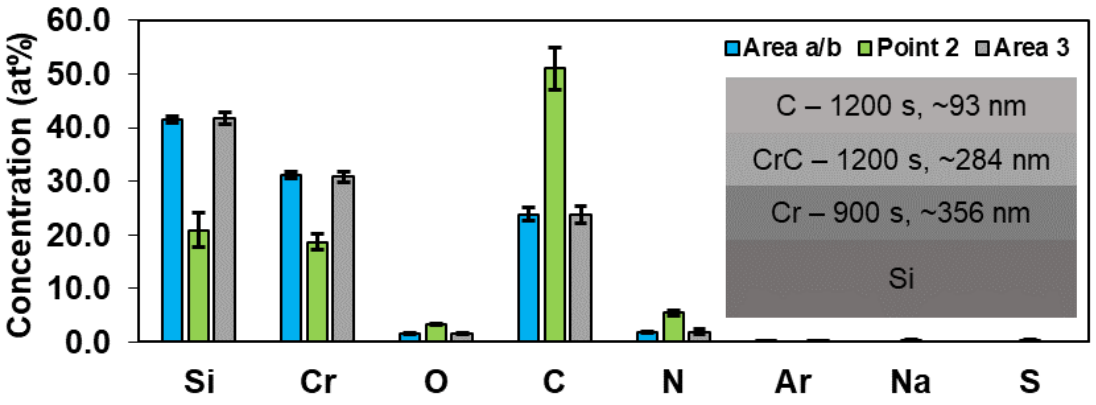

Figure 79 - EDX data for the regions of Cr-CrC-C coating deposited on Si highlighted in Figure 78. The two areas have consistent compositions, with more error in the low magnification, the point has higher C content. Again, N content should be noted. Full data in Table 47. 3 scans were taken per region, with mean and standard deviation shown.

The surfaces of the next step of the interlayer, Cr-CrC-C, again show a uniform elemental distrubution, with surface scratches on the 316L, and smooth planar surface on the Si, see Figure 78 and Figure 79 for the SEM imaging. These layers were deposited for 900 and 1200 s respectively, calculated as 284 and 93 nm, on top of the preceding Cr layer. Both surfaces contain defects/contamination. Considering the EDX data the carbon content is elevated as intended, in both surfaces. On the 316L substrate, the C content is consistant across the three regions data was gathered from, with the point defect showing a slightly higher value of 28 ± 0.5 at% compared to 25 ± 0.6 at% for Area 3. Given similarity between the composition of the defect and the surface, this is likely to be a protrusion carried over from the polishing of the substrate. Similarly for the Si substrate the composition is consistant for the two areas selected, with minimal error, 23.8 ± 1.2 at% for Area a/b. The defect at Point 2 has a higher carbon content, suggesting either a large particle ejected from the C target or contamination on the surface, the trace amounts of Na and S determine that this is contamination.

In both samples there are indications of small quantities of nitrogen, < 2 at%, which should be taken note of as there is not any N_2 gas flowing in the chamber during this deposition step. The source could potentially be nitrogen from the C target, implanted during a previous coating run, that was not sputter cleaned sufficiently to prepare a pure C target surface for this coating.

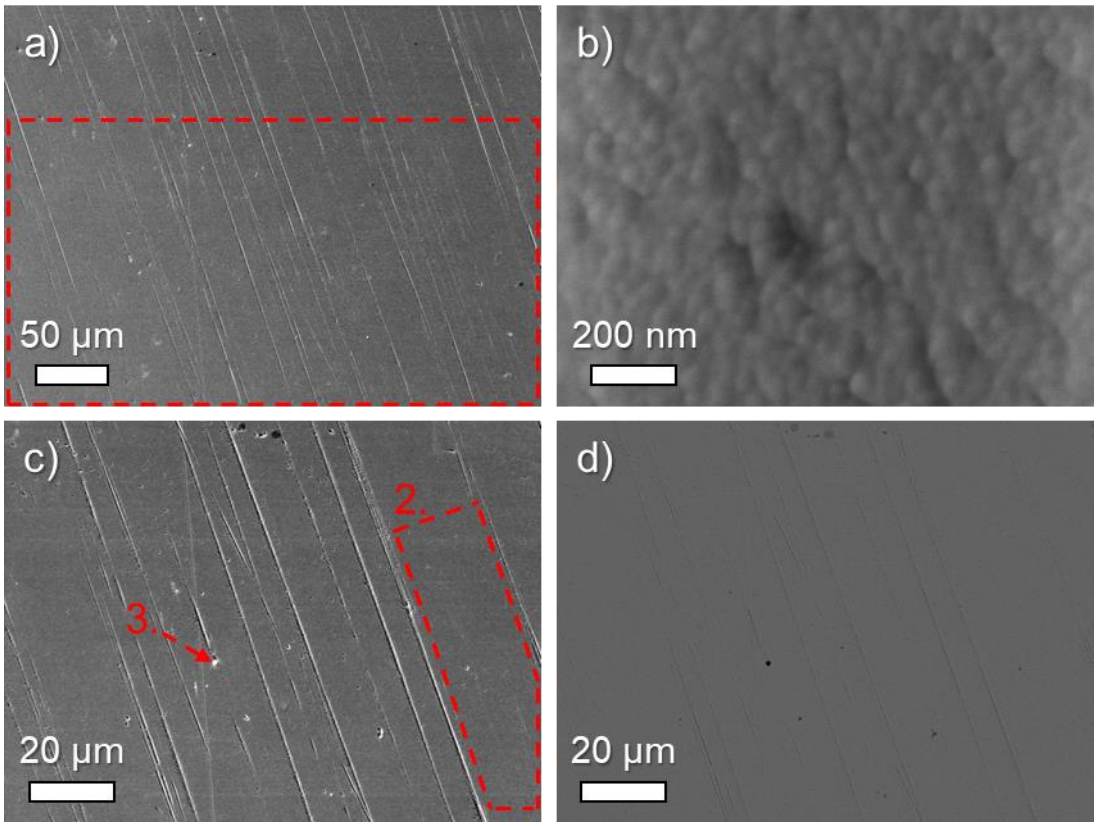

Figure 80 - SEM images, secondary a) b) and c), backscattered d), of the Cr-CrC-C-BCN interlayer deposited on 316L substrate, surface scratches are evident, with a uniform element distribution according to the backscattered contrast, scattered surface defects are present. High magnification shows the tops of grains < 100 nm. EDX data was gathered from regions highlighted in red, summarised in Figure 81.

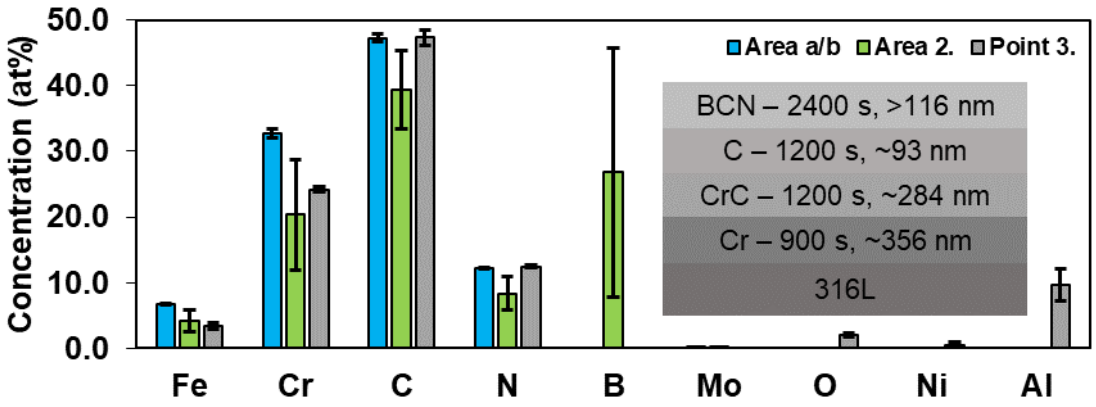

Figure 81 - Summarised EDX data for the Cr-CrC-C-BCN interlayer, substrate and previous interlayer elements, Fe, Cr and C, are present. B is only identified in Area 2, with large error. Defect at Point 3 is from aluminium foil used for sample storage. Full data in Table 48.

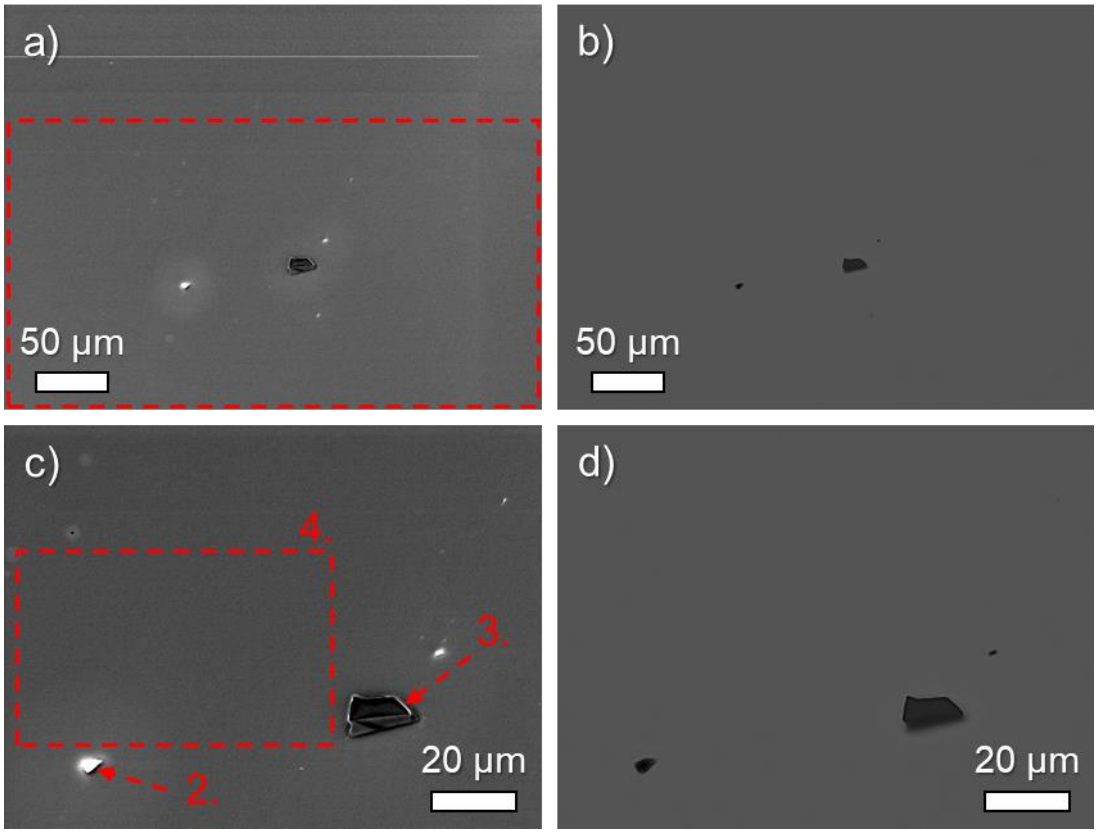

Figure 82 - SEM images, a) and c) secondary, b) and d) backscattered of the Cr-CrC-C-BCN adhesion interlayer, images show smooth surface, with uniform element distribution and isolated defects. Red highlighted areas indicate where EDX data was gathered from, see Figure 83.

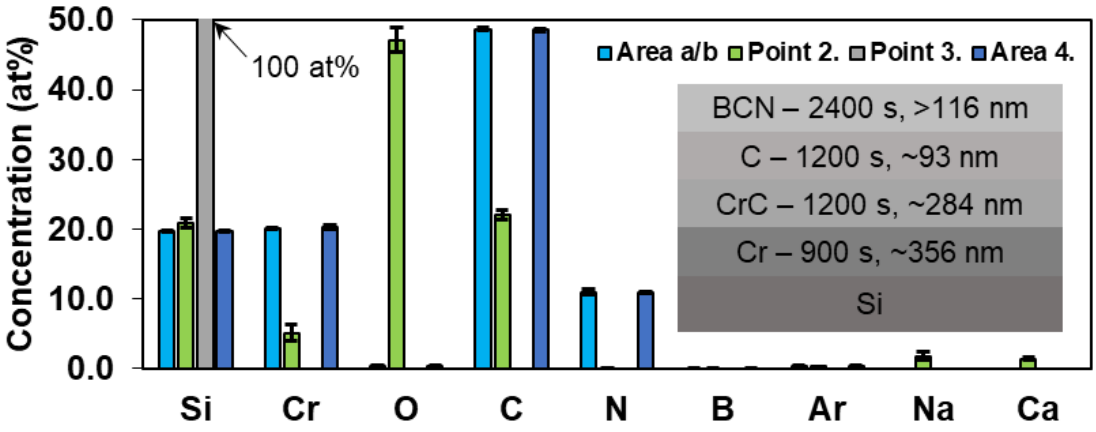

Figure 83 - Summarised EDX data for the Cr-CrC-C-BCN interlayer, regions shown in Figure 82. The two area scans corrolate with respect to interlayer element content. No B is detected. Points 2 and 3 are a coating peel and surface dirt/contamination respectively. Full data in Table 49.

The surface morphology for the final interlayer (Cr-CrC-C-BCN) is consistent with the previous layers according to each substrate type, see Figure 80 and Figure 82. The C content in both samples increases to 47.3 ± 0.5 at% and 48.7 ± 0.2 at% from 24.3 ± 0.2 at% and 23.8 ± 1.2 at% for the 316L and Si respectively, indicating C deposition. However B is absent from the spectra gathered from all regions except Area 2 on 316L, see Figure 81. In this region the B content was 26.8 ± 19.0 at%, note the large error, the B was only detected in 2 out of 3 scans carried out. Given the 2400 s (40 min) deposition time for this layer, and the low deposition rate for the BN, with thickness calculated at ≥116 nm, the quantity can be considered to be below the amount detectable by EDX on a SEM. Furthermore, the nitrogen content of both samples cannot be used to gauge deposition from the BN target, as additional nitrogen gas is added to the chamber. A critical point from this EDX data is that, excluding the contamination at Point 2 on the silicon substrate, the Oxygen content is low, 0.2 ± 0.2 at% for both Area 2 and Area 4 in Figure 81 c) and Figure 82 c) respectively. The high magnification image in Figure 80 d) shows a rough cauliflower surface, indicative of the tops of columnar grains, < 100 nm in size. The total thickness of the interlayer is calculated to be ~850 nm.

The FTIR spectra for two stages of the interlayer, deposited on 316L and Si is presented in Figure 84. The signal collected from the Cr-CrC-C first stage is weak, and is multiplied by a factor of 10 to show in comparison to the second stage. The spectra for the second stage of the interlayer (Cr-CrC-C-BCN) is more intense than the previous stage, and is relatively broad and smooth, with only a single peak being identified. The breadth of peaks is indicative of nanocrystallinity or amorphous structure. This peak potentially relates to C=N bonds, expected near 1637 cm^{-1} and 1540 cm^{-1} [205, 285], with overlap from C=C bonds in the region of ~1600 cm^{-1} [286]. There is also the potential for C-N bond vibrations at 1280 cm^{-1} [221], B-C at 1180

cm^{-1} and 1250 cm^{-1} [205], and C≡N bonding at higher wavenumber, 2264 cm^{-1} [285], though the latter is occluded by C=O=C vibrations at ~2400 cm^{-1}.

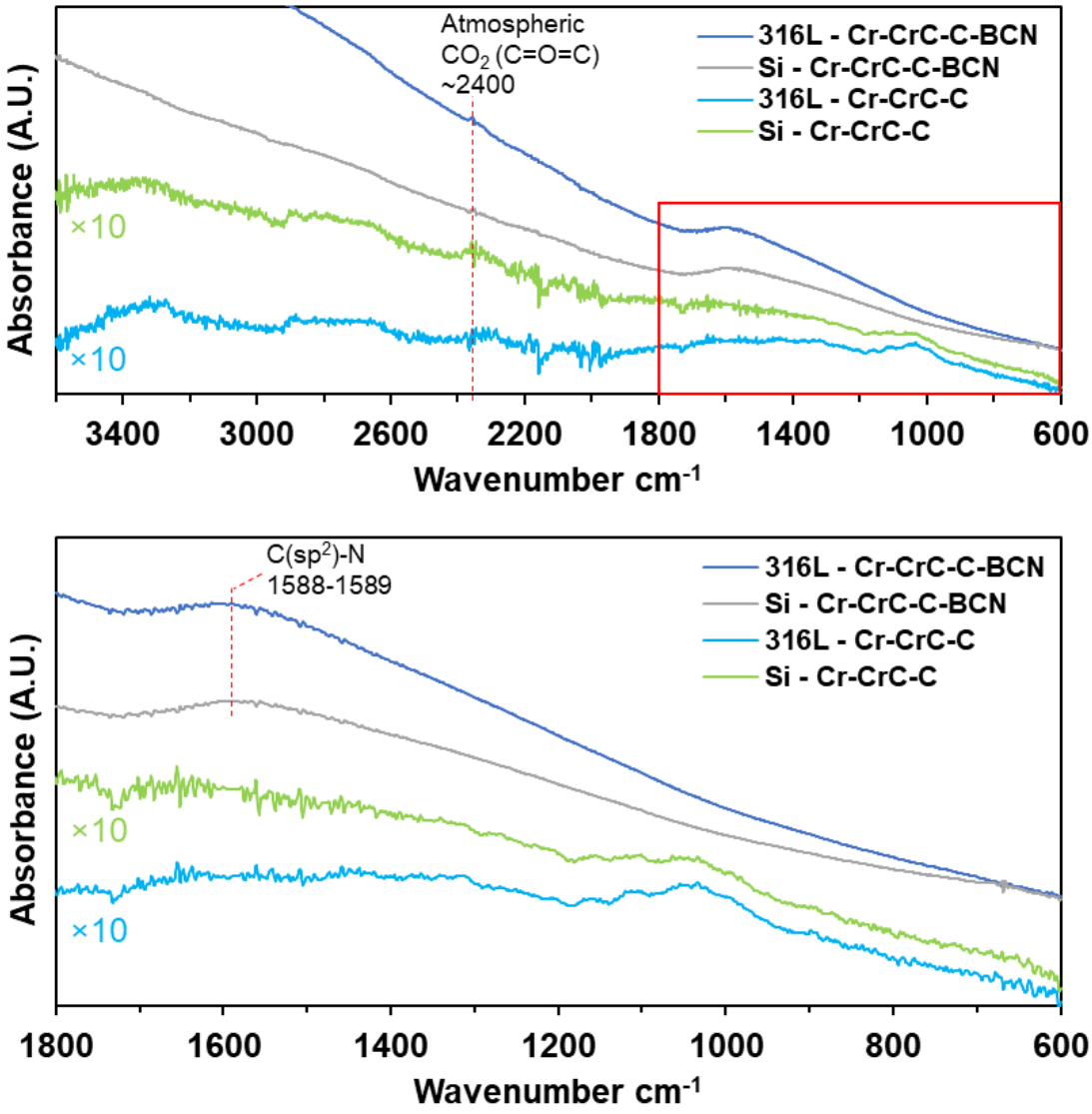

Figure 84 - FTIR spectra for two stages of interlayers, applied to 316L and Si substrates, spectra for the Cr-CrC-C interlayer had low intensity, so has been increased in magnitude to elucidate peaks. Note Cr only films have been omitted as they produce no waveforms using this technique.

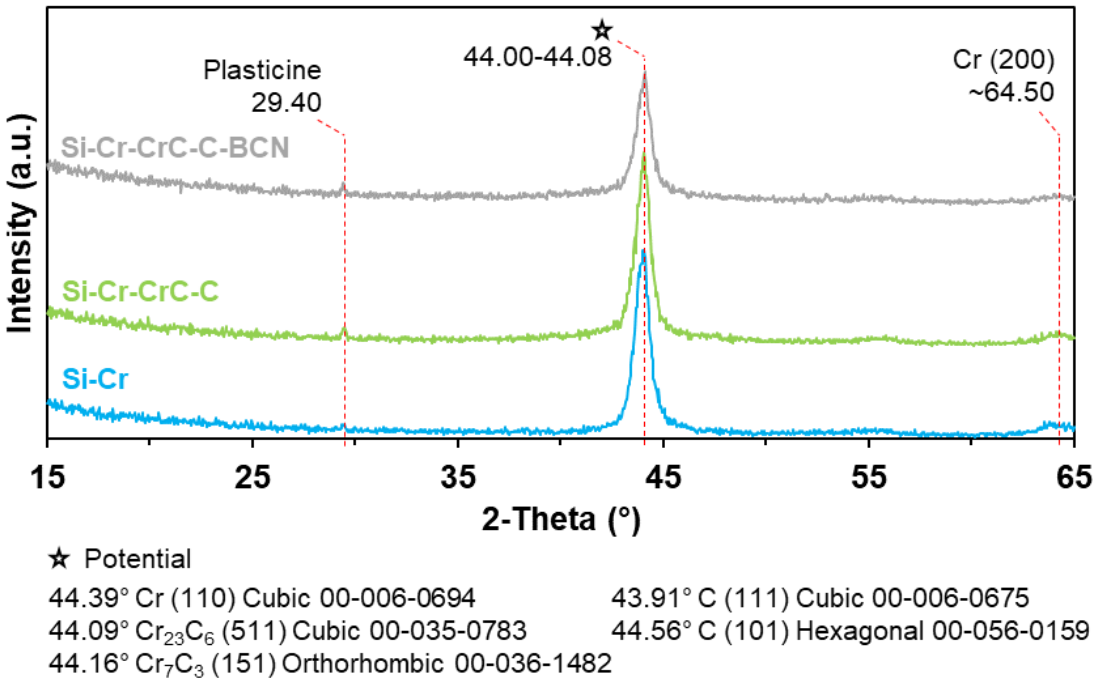

Figure 85 - XRD patterns for the different stages of the multilayer adhesion coating, applied to Si substrate, patterns are consistent with each other, a prominant broad peak is present on all three patterns, with potential materials and corresponding planes listed, plasticine contamination is evident, as is a low intensity broad peak of Cr at higher angle.

Figure 85 presents the XRD patterns for stages of the multilayer adhesion coating applied to Si substrate. For all three there is plasticine contamination from the mounting. The dominant peak at ~44° is consistent for all three stages and is primarily Cr (110), with a minor peak from the (200) plane at ~65°. The FWHM is similar for all three patterns for the Cr(110) peak and relatively broad corresponding to a nano-crystallite size of approximately 11.8 ± 0.6 nm as determined by the Scherrer equation. No observable crystallinity from the subsequent layers, distinct from the Cr, is observed on these patterns.

The temperature of the substrates varied throughout the interlayer deposition, with the cleaning, Cr, CrC and C steps approximately 200°C, ramping down through the BCN layer to ~100°C.

5.1.2.2 Multilayer coating with BN layer deposited statically (Coatings 5, 6 and 7)

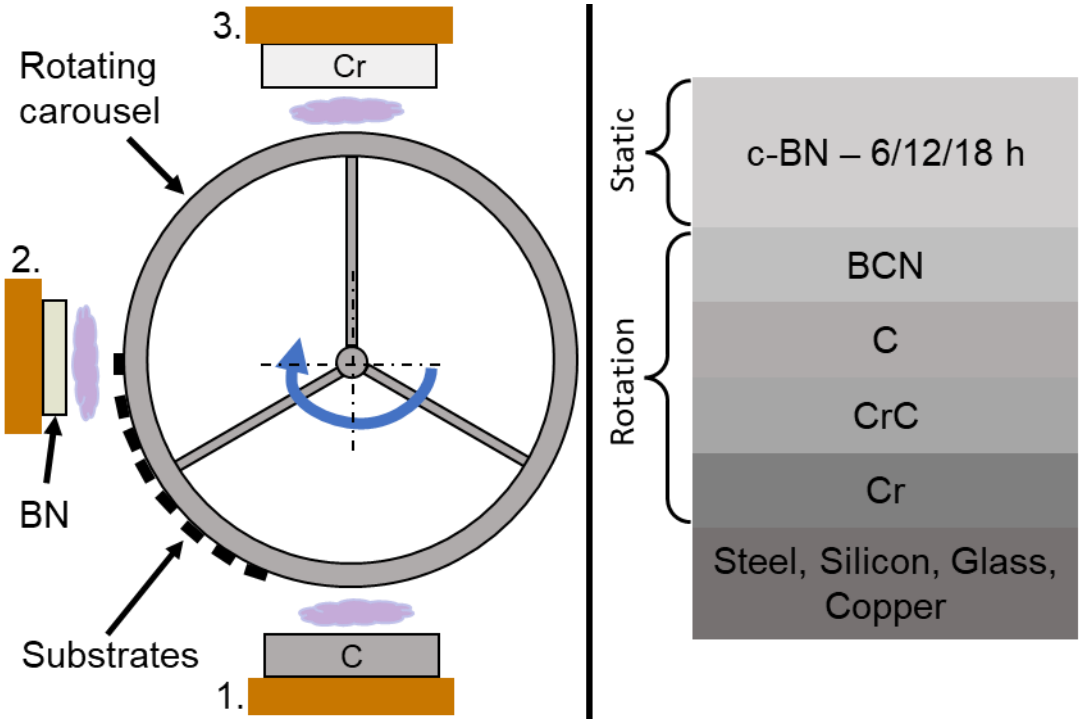

Figure 86 – Top-down schematic view of the PVD coating equipment, showing the three magnetrons (orange) used for these coatings, samples were attached to a rotating carousel, depositing interlayers by passing samples in front of the corresponding magnetrons, for the top BN layer substrates were held statically in front of the target. Note plasma is only shown in front of each magnetron in this figure, however in reality due to the closed field setup plasma was dispersed throughout the chamber with varying intensity.

Multilayer coatings were deposited in a single process using a rotating substrate holder, with substrates passing by the magnetrons to produce the individual layers and blends. Due to the low deposition rate, and long lead times when procuring BN targets, the top layer BN was initially deposited statically, with the carousel moving the substrates directly in front of Mag 2, see Figure 86, once the multilayers were deposited. The results of this are presented in this section, with full rotational coating results in Chapter 6.

The parameters for the coatings deposited in this section are summarised in 3.2.1.1 and repeated in Table 19 below. The two-step bias nucleation and growth technique for the final BN layer was utilised in these recipes as detailed in section 2.4.2.1. Three coatings were deposited with this setup, by varying the deposition time of the final BN layer, 6 h, 12 h and 18 h, named Coatings 5, 6 and 7. Over the duration of the top BN

layer, at constant set power, the RF PSU front panel voltage reading reduced from ~650 V to ~400 V.

Profilometry measurements of the thickness of Coatings 5 and 6, using partially masked and revealed edges were 1183 ± 158 nm and 1590 ± 24 nm respectively. Using these measurements, the approximate BN deposition rate can be calculated as 68 ± 30 nm/h for a single BN target depositing onto substrates held statically at 150 V bias.

Table 19 – Summarised parameters for the deposition of the multilayer adhesion coating and boron nitride nucleation and growth top layers, substrates were held statically for the BN layers. 3 coatings were deposited with this parameter set, with durations of 6 h, 12 h, and 18 h, named Coatings 5, 6 and 7.

Coating Layer	Target Setpoint	Bias Voltage (V)	Ar Flow (sccm)	N_2 Flow (sccm)	Duration
Chromium	Cr (4 A)	120	23	0	900 s
Chromium Carbide	Ramp Cr (4-0 A), Ramp C (0-3.5 A)	60	23	0	1200 s
Carbon	C (3.5 A)	60	23	0	1200 s
Boron Carbon Nitride	Ramp C (3.5-0 A), BN (175 W)	60	30	15	2400 s
Boron Nitride - nucleation	BN (175 W)	180	30	15	900 s
Boron Nitride - growth	BN (175 W)	150	30	15	6/12/18 h

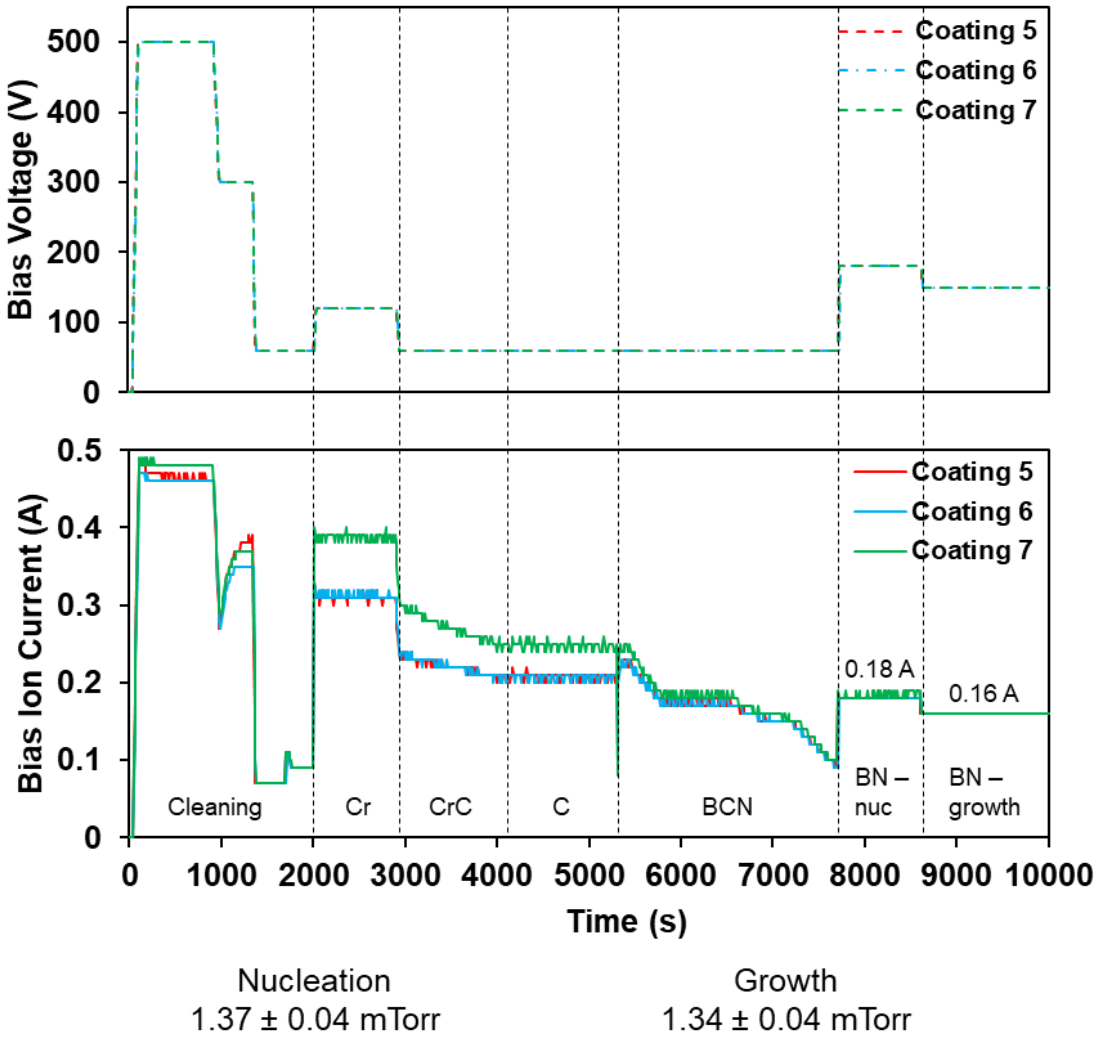

Figure 87 - Variation in Substrate Bias voltage and Bias Ion current (250 kHz/500 ns) during the different stages of Coatings 5, 6 and 7, note the extended durations of the BN top layer have not been shown on this figure as neither the voltage or current differed from the values set/recorded in the first few seconds of this stage. Voltage setpoints were consistant in all 3 coatings, data was logged in 10 s intervals.

The substrate bias setpoint, and corresponding current values, are displayed in Figure 87. The values are logged through the PC interface with the power supply, and are indicative of the average values applied/drawn from the supply during the forward (negative) pulse. As reported by Kelly at.al. [37], this current value can be used as an approximate for the ion current, suitable for relative comparison between these coatings. The ion current fluctuates according to both the bias voltage applied and also the different parameters applied to the different components of the system. As the bias voltage is increased, the ion current increases, visible in the transitions from ‘Cleaning to Cr’ and ‘BCN to BN-Nuc’.

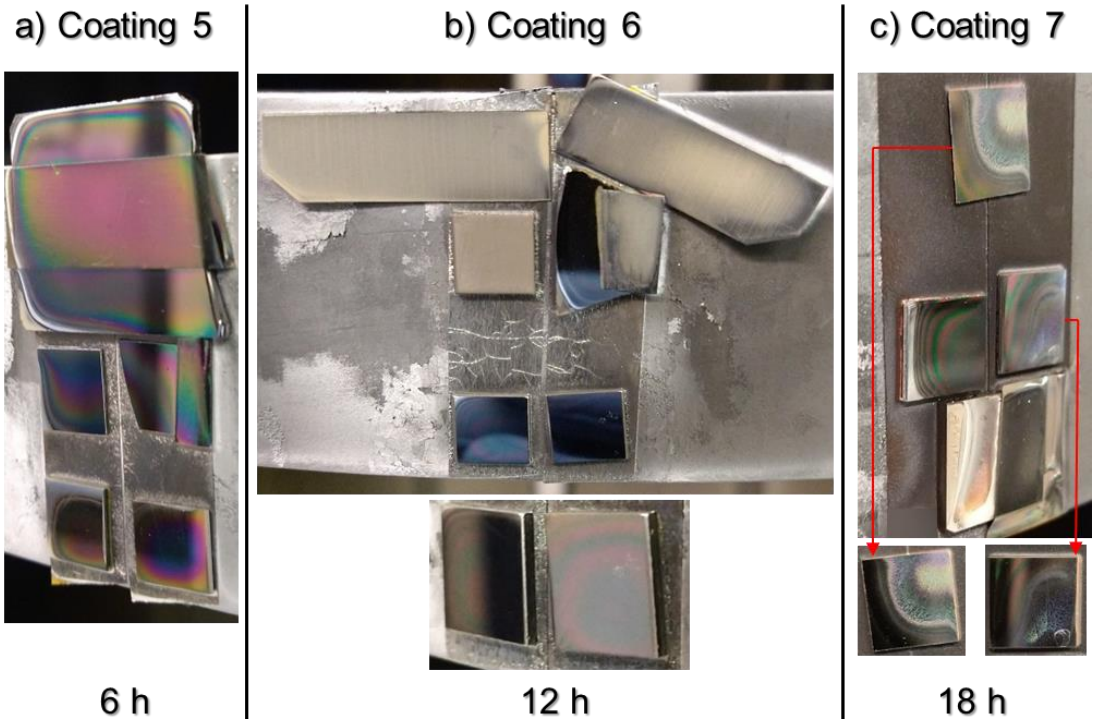

Figure 88 - Photos of substrates coated with multilayer BN coatings, using static two-step nucleation and growth for the top layer at 180 V and 150 V respectively a) 6 h top layer deposition time, substrates from top to bottom, 1x glass with tape mask, 2x polished Si squares, 2x polished 316L squares, b) 12 h top layer deposition time, substrates top to bottom, left to right, 2x as rolled Cu foil, as rolled Cu plate, polished Si with tape mask, 2x polished 316L, inset highlights fringe patterns on steel, c) 18 h top layer deposition time, polished Si, 2x polished 316L, glass with tape mask, inset shows direct on view of the Si and 2nd steel samples respectively.

As the power to the magnetrons increases the ion current increases and vice-versa, visible in the rise at the start of the Cr layer, and in the reduction as the C target power ramps down in the graded BCN layer. The pressure/gas composition has an impact on the ion current, as is seen from the sharp and momentary drop in the current at the start of the BCN layer, when the N_2 valve is opened, before the flow controller responds to the setpoint signal.

Table 20 - The three coating runs depositing the adhesion multilayer coating separated by duration of the final static BN top layer step, substrates included in each run, photos in Figure 88, with comments on appearance when removing from the chamber. Comments are highlighted in orange to indicate poor adhesion, and yellow to indicate good adhesion but with visible inhomogeneities.

Multilayer coatings with static BN top layer		
Duration	Substrates	Visual inspection
6 h	Glass masked with tape	Dark coloured, mirrored, fringe patterns around edge, patterns continuous across tape boundary
	Silicon Wafer	Dark coloured, mirrored, fringe patterns around edge
	Silicon Wafer masked with tape	Dark coloured, mirrored, fringe patterns around edge
	Polished Steel	Dark coloured, mirrored, fringe patterns around edge
	Polished Steel	Dark coloured, mirrored, fringe patterns around edge, metallic region present on one corner
12 h	Copper Foil	Pale beige/grey colour, powdery
	Copper Foil	Pale beige/grey colour, powdery, metallic around edge
	Copper Plate	Pale beige/grey colour, thick and powdery
	Silicon Wafer masked with tape	Dark coloured, mirrored, fringe patterns around edge, metallic region on one corner, tape is distinct beige/grey and powdery
	Polished Steel	Dark coloured, mirrored, fringe patterns around edge but not centered on substrate centre, metallic region at corner
	Polished Steel	Dark coloured, mirrored, fringe patterns around edge but not centered on substrate centre
18 h	Silicon Wafer	Sample has distinct halves, one is dark, mirrored with fringes, the other is pale powdery/flakey with fringes
	Polished Steel	Dark coloured, mirrored, fringe patterns around edge but not centered on substrate centre, metallic region along edge
	Polished Steel	Sample has distinct halves, one is dark, mirrored with fringes, the other is dark powdery/flakey with fringes
	Glass masked with tape	White/pale coating on glass, very powdery, tape is distinct with darker coloured metallic coating

Figure 88 contains photos of the 3 coatings deposited. There are significant variations in the appearance of the coatings when modifying the coating duration and when depositing onto different substrates. Notes on each substrate photographed in Figure 88 are in Table 20. The general trend when observing these coatings is that when increasing the duration of the top layer BN the coatings become less adherent and more powdery in appearance. Fringe patterns are present on the polished samples, indicating varying coating thickness across the surface.

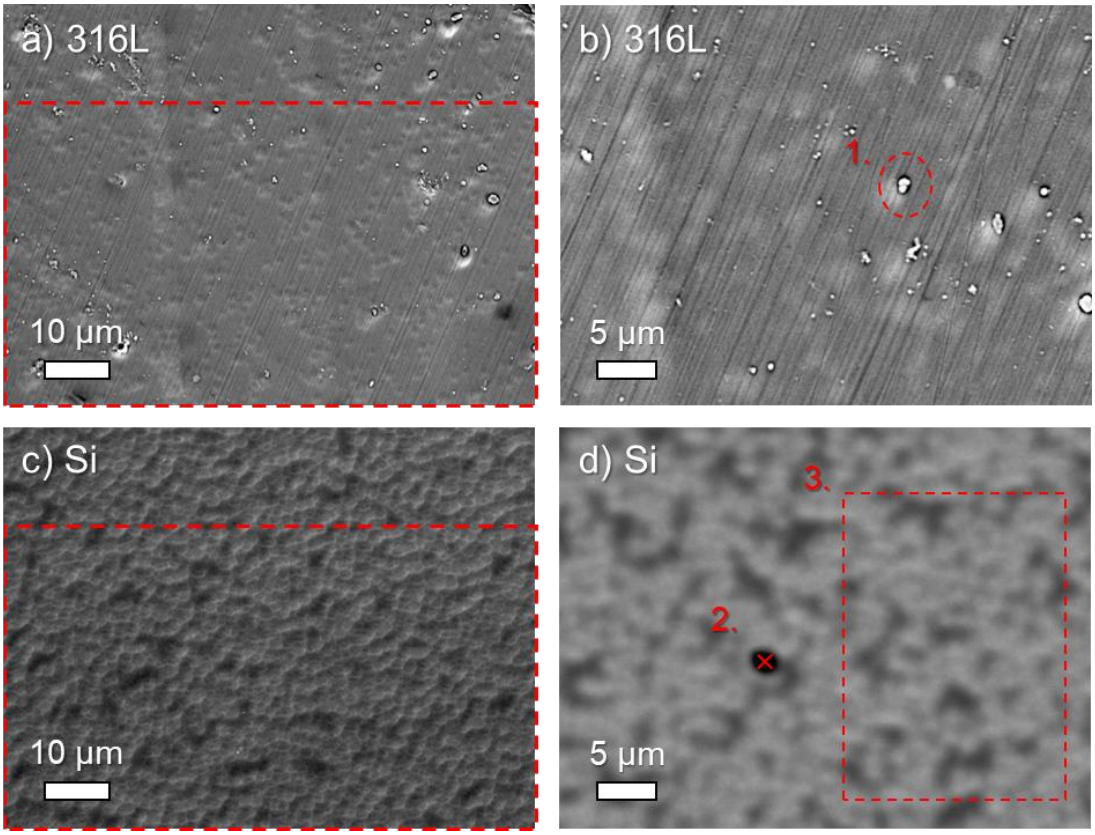

Figure 89 – Surface SEM imaging of Coating 5 (6 h), deposited on 316L a) and b) and silicon c) and d), secondary images in a) and c), higher magnification backscattered images in b) and d). EDX data was collected from the regions highlighted in red, with compositions presented in Figure 90, photo in Figure 88a).

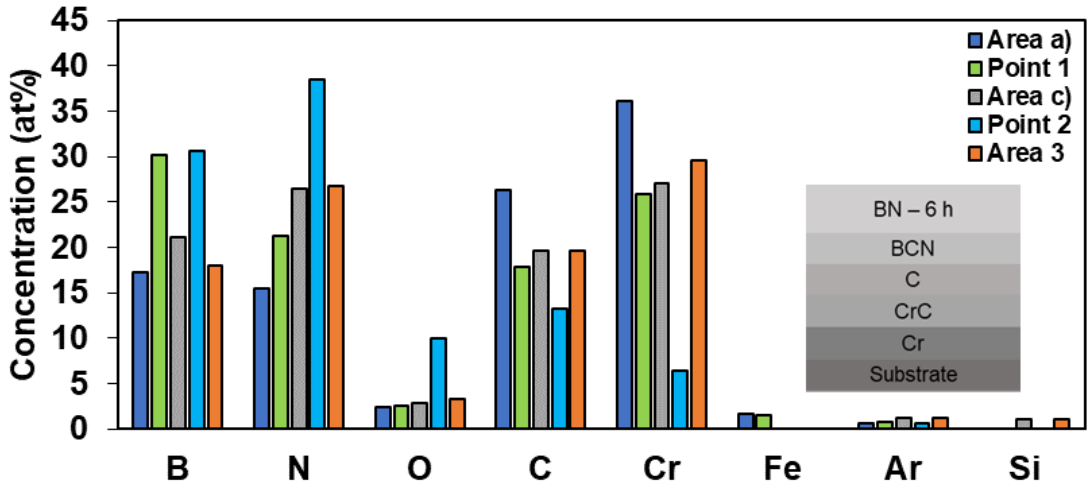

Figure 90 - EDX elemental concentrations gathered from the surface of the sample shown in Figure 89, Coating 5 (6 h) on 316L and Si, in at%, all data points show B and N with varied O and Ar contamination, different contributions from the adhesion layers can be identified. Full data shown in 10. Appendix in Table 50.

Figure 89 contains surface imaging of the initial 6 h duration multilayer on steel and silicon substrates, Coating 5. From these images and corresponding EDX, Figure 90, it is clear that there is coverage of the surface with coating material, however the texture and composition vary dramatically. Figure 89 a) and c) show that there is a ‘dimpled’ or ‘orange peel’ surface texture on both the substrate types, with the lighter and darker patches present in the backscattered images in b) and d) indicating corresponding differences in element distribution. The larger area EDX scans in a) and c) show different compositions of the coating, with B differing by 3.6 at%, between 17.5 and 21.1 at%, for the steel and silicon respectively. Much larger disparities are seen with the quantity of N, Cr and C; with N content, similarly to B content, lower in the coating on steel substrate 16.1 at% compared to 26.4 at% on the Si. The Cr and C are correspondingly higher in the coating on the steel substrate. The area EDX (Area 3.) of the coating on silicon in the higher magnification Figure 89 d) shows, again, a different composition, lower B content compared to the larger scan in c), a similar N content and increased Cr and C and O content. The B/N ratio of the coating

is 1.09 and 0.80 for the 316L and Si substrates respectively, using data collected from a) and c).

When examining defects on the surface of both coatings the proportion of B increases, to 30.1 and 30.5 at% for point 1 and 2 on the steel and silicon substrate respectively. The nodule on the silicon substrate also has a larger amount of nitrogen, and a relatively high proportion of O, at 10.0 at%. Furthermore, point 1 also contains higher proportions of Cr and C though it should be noted that for the defect on the steel substrate, data was gathered from the region circled in Figure 89 b) however the data from the point in d) was from a single point. Figure 90 summarises the EDX gathered for this sample.

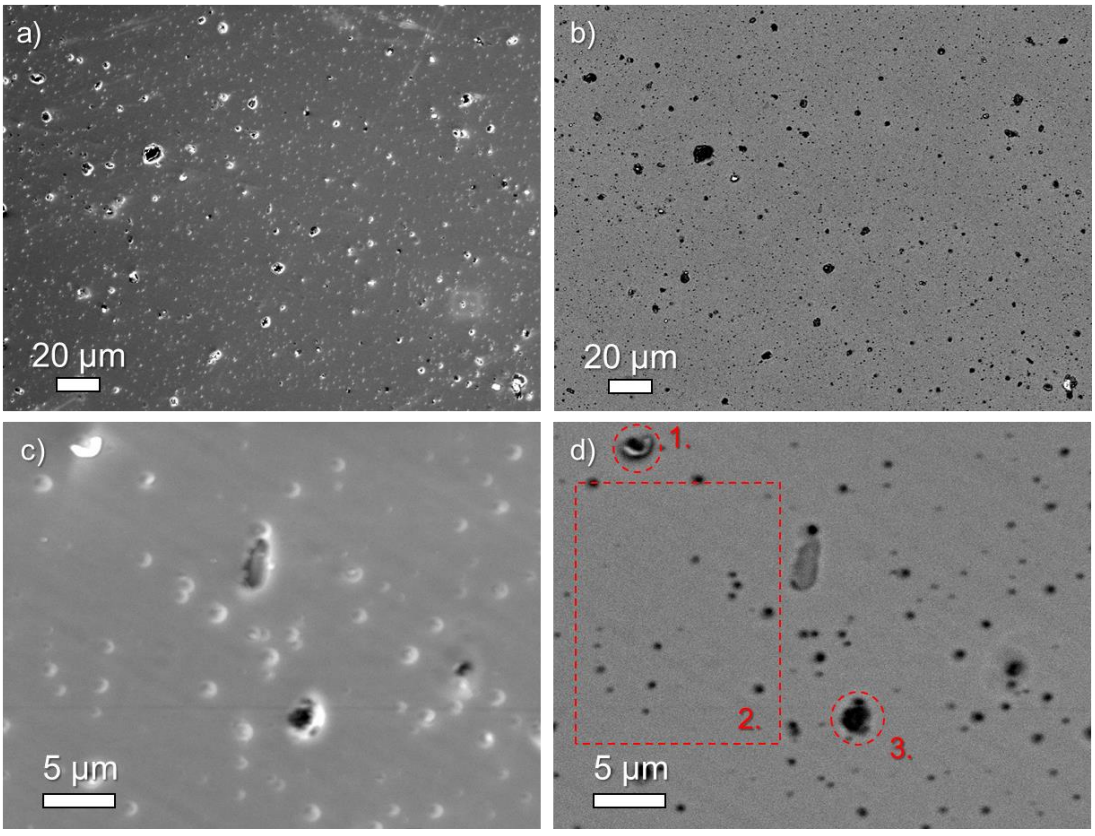

Figure 91 - SEM imaging of 316L substrate with Coating 6 (12 h), a) and b) low magnification images of the sample surface showing a wide distribution of surface defects, secondary and backscattered electron respectively, c) and d) higher magnification images of coating surface, d) selected points and regions are highlighted, composition gathered via EDX in Figure 92.

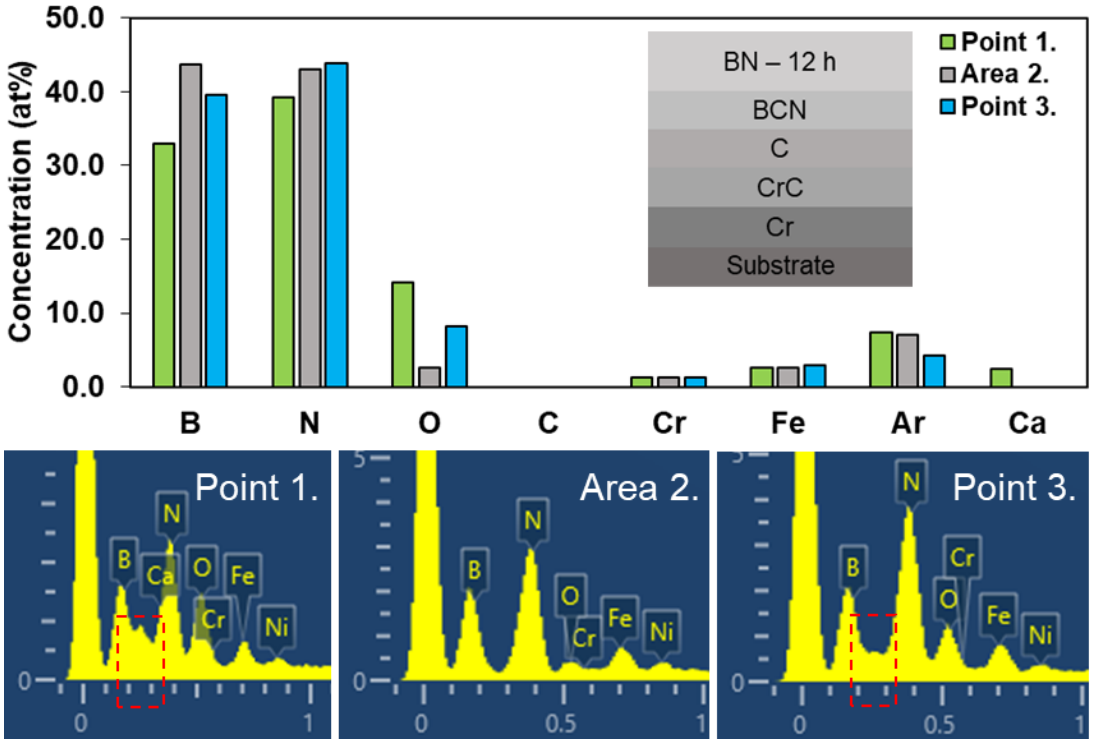

Figure 92 - Surface EDX composition of Coating 6 (12 h) with BN top applied to 316L substrate, B and N are close to a 1:1 stoichiometry, with defects showing O and Ca components, minimal detection of interlayers and substrate materials. Full data presented in 10. Appendix in Table 51.

Figure 91 shows the imaging of the 316L sample with Coating 6 applied. There is consistent disruption over the surface area comprising defects such as pinholes and surface protrusions or nodules. The EDX data, gathered from the highlighted regions in Figure 91 d) and shown in Figure 92, establishes that the boron content in Area 2, consisting of a smooth surface dotted with pinholes, is 43.7 at%, with a corresponding N content of 43.0 at%. This is close to the 1:1 stoichiometry required for c-BN formation (1.02). A low amount of O contamination, 2.5 at% is detected from this area. Similar to Coating 5, the defects contain higher levels of O, 14.1 and 8.2 at% for points 1 and 3 respectively, with the surface protrusion at Point 1 containing a small concentration of calcium, 2.4 at%. It is essential to note that there is no indication of C content from the quantitative data, however the spectra in Figure 92 show peaks in the C position (Kα 0.2774 keV) at Point 1 and 3. When manually selecting the element

in the EDX software, this causes a negative value of C content to be reported. Imaging of Coating 7 applied to 316L is presented in Figure 93.

The surface appearance contrasts with the previous coatings deposited on 316L in that in some regions the coating has delaminated into flakes on the surface, Figure 93 b), imaged from the 2nd steel sample in Figure 88 c).

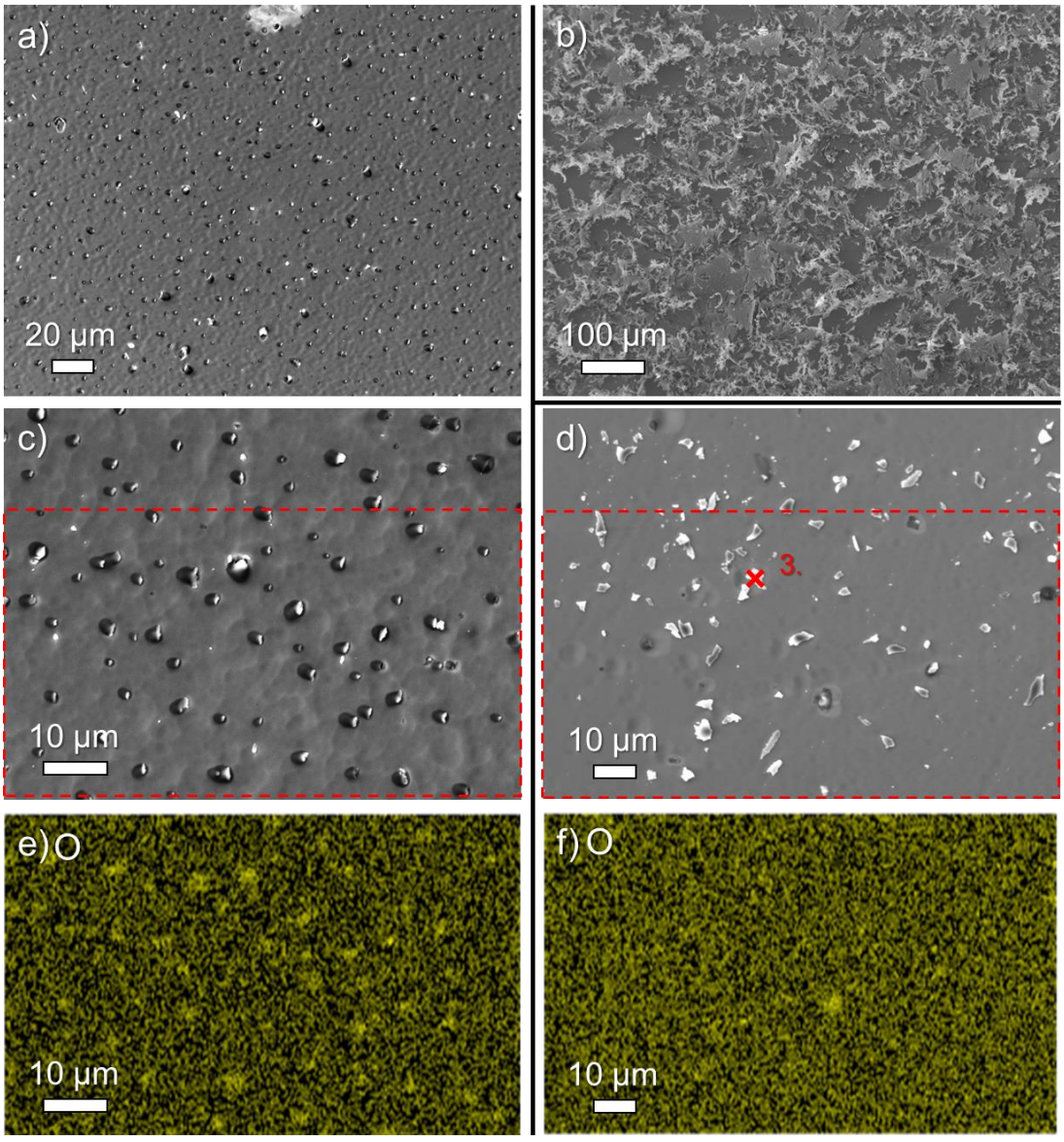

Figure 93 – Secondary electron imaging and EDX maps of Coating 7 (18 h) deposited on 316L, two regions a) and c) are smooth with nodular surface defects at different magnifications, b) and d) show flaked defects, e) and f) EDX maps of O in c) and d), the EDX data is summarised in Figure 94.

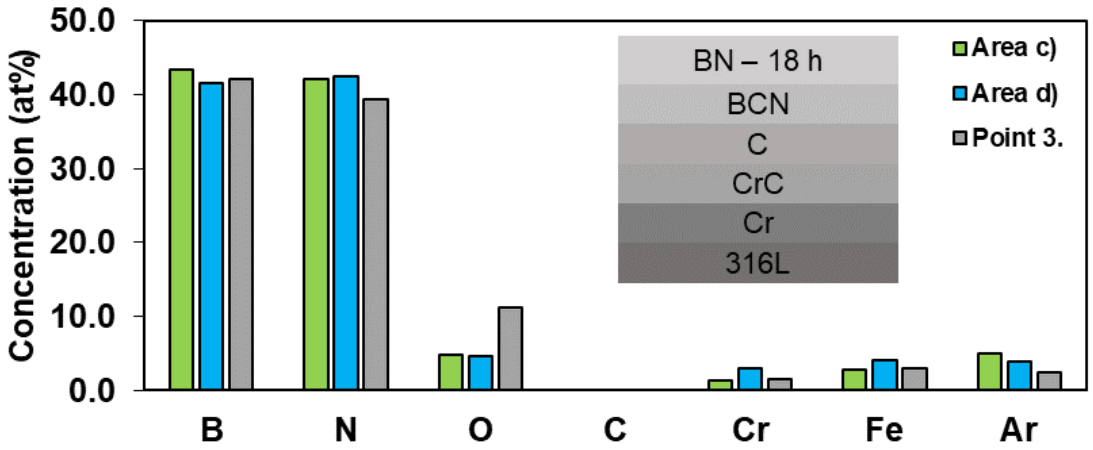

Figure 94 - Element content for the two different regions mapped in Figure 93, predominantly composing of B and N in close to 1:1 stoichiometry, O contamination is detected primarily in surface particles, it is of note that C is not detected, full data in Table 52.

In areas where the coating has remained adhered to the surface there are again surface defects. These are shown in Figure 93 c) and d), which correspond to two regions of well adhered coating, showing surface protrusions or nodules, and surface flakes respectively. The former image, Figure 93 c) shows a surface with a disrupted pattern with separations of ~1 µm, potentially corresponding to the tops of grains. The EDX maps Figure 93 e) and f) indicate both types of defects are high in O, all other element maps show uniform colour across the scanned area (not shown). When considering the EDX data, Figure 94, no C content from the CrC or C interlayers was detected, as with Coating 6 (12 h), despite the Fe and the Cr in the substrate and first layer being detected in small quantities. The surface composition indicates approximately 1:1 stoichiometry of B and N at 1.03, 0.98 and 1.07 for the three scans respectively. Nanoindentation of an adhered region of Coating 7 was carried out to a depth of 152 ± 2 nm (9 indents), giving a hardness of 6.98 ± 0.66 GPa, with 316L substrate hardness at 4.15 ± 0.67 GPa.

All three coating durations (for the samples imaged here with smooth intact coatings) were stable in atmosphere and showed no cracking, delamination or composition change after ~22 months stored in ambient conditions.

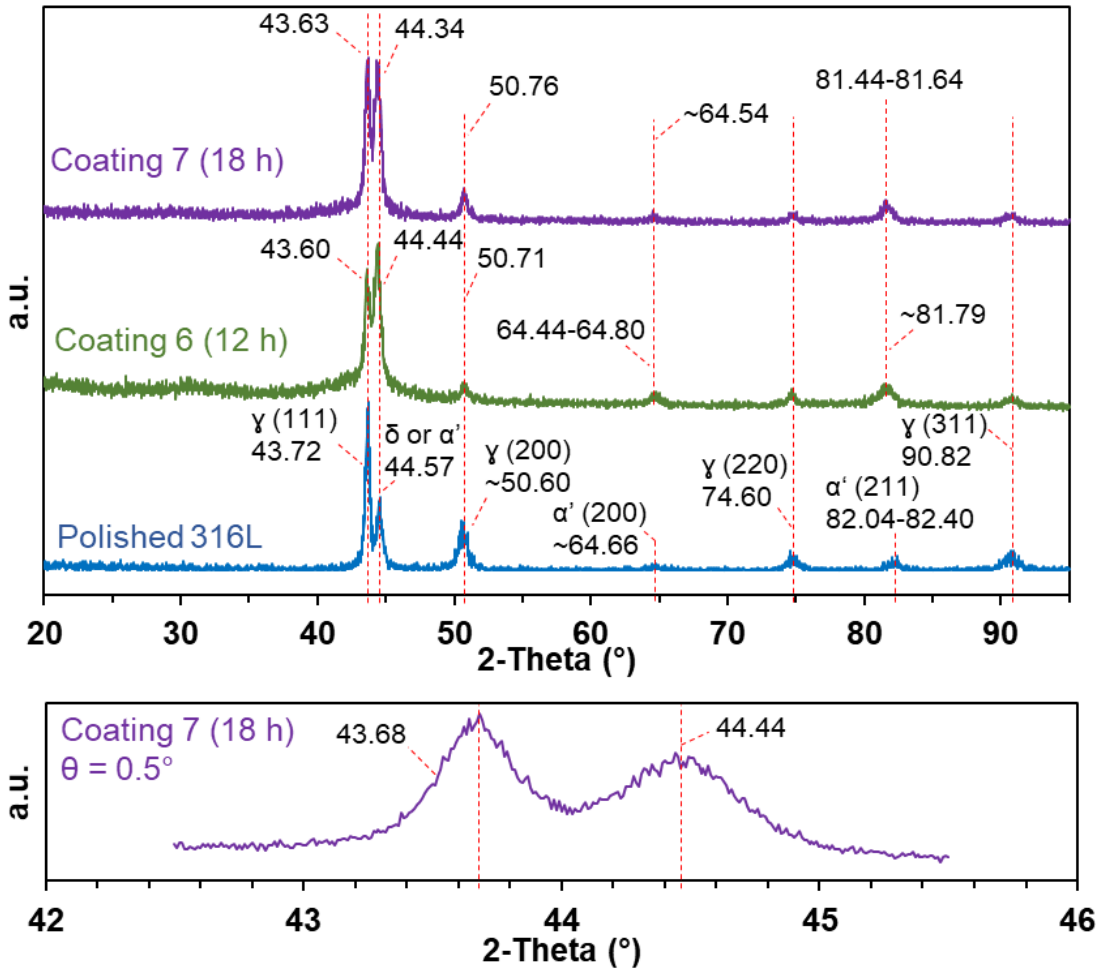

Figure 95 – Glancing angle XRD patterns of 316L steel substrates uncoated and with coatings 6 (12 h) and 7 (18 h), significant peak overlap is evident with no clear indication of BN phase, all peaks are broad suggesting amorphous or nanocrystalline phases. The lower pattern is a repeat scan of the double peak in Coating 7 with θ = 0.5°.

Table 21 - Relative peak intensities for the patterns shown in Figure 95, 316L substrate and Coatings 6 and 7 on 316L. The peak at ~43.6° is normalised to 1 for all four patterns.

Sample	Relative peak intensities						
	43<2θ<44°	44°<2θ<45	51°	65°	75°	82°	91°
Coating 7	1.000	1.000	0.620	0.556	0.550	0.583	0.548
Coating 6	1.000	1.185	0.187	0.133	0.156	0.187	0.109
316L	1.000	0.433	0.287	0.037	0.112	0.078	0.112
Coating 7 (θ = 0.5°)	1.000	0.770	N/A	N/A	N/A	N/A	N/A

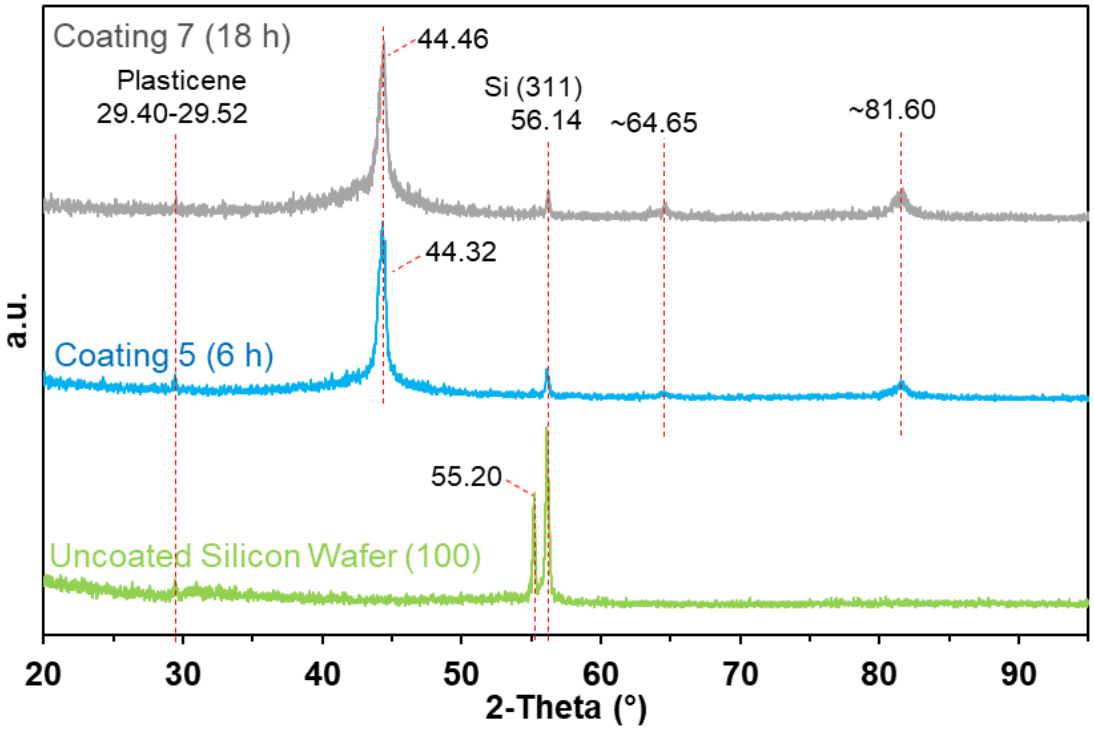

Figure 96 – Glancing angle XRD patterns of silicon substrates uncoated and with multilayer coatings composed of adhesion interlayers with 6 h (Coating 5) and 18 h (Coating 7) BN top layer deposition durations. Si substrate peaks are narrow, coating peaks are broad, suggesting amorphous or nanocrystalline structure.

Table 22 - Relative peak intensities for the XRD patterns presented in Figure 96, for Coatings 5 and 7 on Si substrate, the first peak at ~44.4° has been normalised to 1.

Sample	Relative peak intensities			
	44.4°	56°	65°	82°
Coating 7	1.000	0.161	0.101	0.184
Coating 5	1.000	0.175	0.047	0.109

Table 23 - 2-Theta values for different elements and compounds that have the potential to be present in the multilayer, with the values corresponding to peaks in Figure 95 and Figure 96 and the Powder Diffraction File No. they were sourced from.

Material (structure)	2-Theta (hkl)	PDF No.
Cr (Cubic)	44.39° (110), 64.58° (200), 81.72° (211)	00-006-0694
$Cr_{23}C_6$ (Cubic)	44.09° (511), 50.62° (531)	00-035-0783
Cr_7C_3 (Orthorhombic)	44.16° (151), 50.19° (222), 64.66° (081)	00-036-1482
C (Diamond)	43.91° (111), 75.30° (220)	00-006-0675
C (Graphite)	44.56° (101), 50.69° (102)	00-056-0159
$C_{11}N_4$ (Tetragonal)	44.44° (112), 64.52° (212), 81.45° (300), 81.58° (222), 81.97° (214)	01-081-8115 (Hypothetical)
B_2O_3 (Orthorhombic)	43.81° (002), 44.98° (201), 45.64° (131)	01-076-0781
B_2O (Hexagonal)	44.42° (102), 64.64° (110), 81.81° (202)	00-041-0624
BN (Hexagonal)	26.76° (002), 41.59° (100), 43.87° (101) 40.82° (100), 42.86° (002), 46.37° (101), 74.33° (110)	00-034-0421 00-049-1327
BN (Cubic)	43.19° (111), 50.29° (200), 73.89° (220) 43.31° (111), 50.43° (200), 74.09° (220), 89.93° (311)	01-071-5052 00-035-1365
Si (Cubic)	56.10° (311)	00-005-0565
$CaCO_3$	29.40° (104)	00-005-0586

Glancing angle XRD was carried out for Coatings 6 and 7 deposited on 316L, and for 5 and 7 deposited on Si, see Figure 95 and Figure 96 respectively. The glancing angle, θ, was set at 1° for all scans except for the repeat pattern in Figure 95, which was 0.5°. As with previous XRD patterns, there is initially no clear indication of the presence of a BN phase. The peaks in all 4 coating patterns are broad, potentially due to nanocrystallinity and microstrain [287]. As seen previously, the 316L substrate

consists primarily of austenite (γ), with some delta ferrite (δ) or martensite (α') present. The patterns for Coatings 6 and 7 on 316L mimic the peak positions from the pattern of the uncoated substrate, with a dominant double peak in the 43-45° range, followed by minor peaks around 51°, 65°, 75°, 82° and 91°.

Following coating it is expected that contributions from the substrate diminish, due to a reduced penetration of x-rays to the substrate depth. The ratio of the intensities of the double peak changes, with the peak at 44.4° increasing relative to the peak at ~43.6°. Table 21 contains relative peak intensities calculated by normalising the intensity of the peak at ~43.6° to 1 for each of the patterns and multiplying the other peaks by the corresponding factor. From these values, at first the peak at ~44.4° becomes dominant after Coating 6, then equals the first peak after Coating 7. This suggests that in the thinner of the two coatings (Coating 6), the increase in intensity of the ~44.4° peak is due to one or more of the interlayer phases, Cr (110), C-graphite (101), $Cr_{23}C_6$ (511), Cr_7C_3 (151), or an oxidised top layer, B_2O_3 (201) or B_2O (102). As well as the contribution from the substrate austenite (γ) diminishing.

As the duration of the top BN layer, and correspondingly the thickness, increases in Coating 7 the relative intensity of the first peak (~43.6°) increases once more, indicating that there is contribution from the BN layer to this peak. The potential phases are h-BN (101) and c-BN (111), see Table 23. A repeat scan using a theta value of 0.5° was carried out, to reduce the substrate and interlayer contributions to the pattern. The relative intensity of the peaks at this reduced penetration depth confirms the increased contribution to the ~43.6° peak from the top layer.

The minor peak at ~51° in Coating 6 has a lower relative intensity than that of the 316L substrate, suggesting that it is solely a contribution from the substrate material, however the relative intensity of this peak in Coating 7 is higher than both the substrate and Coating 6 patterns. Given the drop and then rise in relative intensity with the two coatings respectively, it is possible that again this peak has contributions

from the BN layer (c-BN (200)), with film thickness dependence. Similarly, the peak at ~91° shows this drop and then increase in relative intensity in Coating 6 and 7 respectively. This peak does not match closely with any of the potential compounds in Table 23, with c-BN (311) being the closest match at 89.93°.

The peaks at ~65°, ~75° and ~82° all increase in relative intensity in Coating 6 and then Coating 7. For Coating 6 the peak at ~65° can be attributed to Cr (200), Cr_7C_3 (081), $C_{11}N_4$ (212) and B_2O (110), in Coating 7 the further increase can only be attributed to B_2O (110). For ~75°, the contributions in Coating 6 are potentially from C-diamond (220), h-BN (110) and c-BN (220), with increase in the BN contributions in Coating 7. At ~82°, Cr (211), $C_{11}N_4$ (300), (222) or (214), and B_2O (202), again with B_2O being the only component that can be attributed to the rise in intensity in Coating 7.

In contrast to Figure 95, Figure 96 contains simpler patterns of the multilayer on Si substrates. For the uncoated silicon wafer, as with previous patterns, the peaks corresponding to the (311) plane and the forbidden peak associated with misalignment are present. After Coating 5, this substrate contribution reduces, and 3 other peaks are present (discounting the peak at 29.4° attributed to plasticene contamination). The most intense peak is at ~44°, as with this coating on 316L, this can be attributed to many compounds, including the Cr (110), C-graphite (101), $Cr_{23}C_6$ (511), Cr_7C_3 (151) peaks, but not contribution from the substrate material. The small peak at ~65° appears after coating, and increases in intensity relative to the peak at ~44° in Coating 7, see Table 22. Initially this peak could be attributed to Cr (200), Cr_7C_3 (081) or $C_{11}N_4$ (212) however given the increase with longer BN deposition, B_2O (110) could also be contributing. Finally, the peak at ~82° has contributions from Cr (211), $C_{11}N_4$ (300), (222) or (214), and B_2O (202).

Figure 97 contains the FTIR spectra for Coatings 5, 6 and 7, deposited onto 316L. The higher wavenumber regions, 3800-2200 cm^{-1}, for all spectra are relatively

featureless, with a very broad (~1000 cm^{-1}) peak in Coatings 5 and 7, and a rise beyond 3800 cm^{-1} in Coating 6 with a shoulder near ~3400 cm^{-1}. This region is associated with bonding with hydrogen, and has potential contributions from the stretching of N—H bonds in B—NH_2/B_2—NH [160, 206, 211, 212], and O—H stretching in B—OH/B—OH_2 [206, 211-214].

When considering the BN fingerprint region in the bottom of Figure 97, 1800-600 cm^{-1}, the three coating durations clearly produce different spectra. All three contain the vibration associated with h-BN/t-BN bond stretching mode in the ~780 cm^{-1} region, with the 6 h duration having a relatively low intensity, increasing relative for 12 h, and then decreasing for the 18 h duration. This is similar to the corresponding h-BN/t-BN bending vibration near 1370 cm^{-1}, where the intensity is higher than the latter vibration across all 3 spectra, increasing for 12 h duration, and reducing for 18 h duration. The spectrum for Coating 5 resembles the shape of the interlayer spectrum (Figure 84), and given that this is the thinnest (6 h deposition) of the coatings, this indicates a contribution from the interlayer material, with the main peak shifting down due to the BN contribution. It should be noted that the peak for 12 h duration, identified as the h-BN E_{1u}TO mode, is centred at 1307 cm^{-1}, a large shift to lower wavenumber, so identification is not conclusive and could be instead identified as a w-BN or E-BN peak.

The broad peaks in the region 1500-1400 cm^{-1} have been assigned to E-BN [160, 181, 209] for all spectra, reduced in Coating 6, with the peak at ~945 cm^{-1} for Coating 6 also identified as an E-BN contribution [180, 181, 209], absent from the other 2 spectra. In Coating 7 (18 h) there is a peak at 1141 cm^{-1}, attributed to the sp3 bonded w-BN phase [181, 200, 202] absent in the other spectra. There are also potential contributions from B—O bond stretching (BO_3, BO_4) and B—O—B bending in the 1550-1200, 1100-850 and 690-770 cm^{-1} regions respectively.

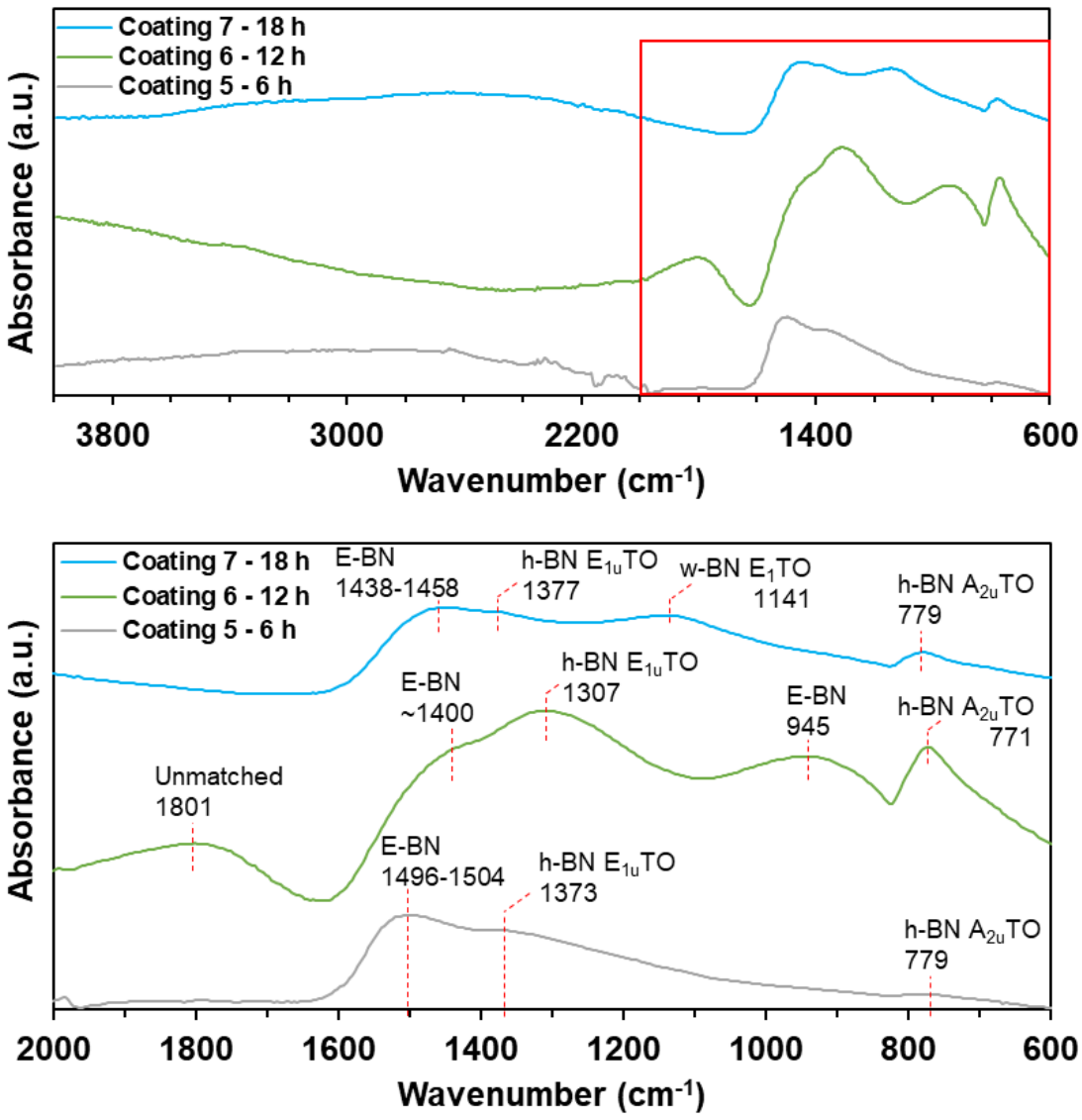

Figure 97 - FTIR spectra of multilayer coatings with varied deposition duration of BN top layer deposited on 316L substrate. Top, full spectra, bottom zoomed 'fingerprint' region with potential assignments.

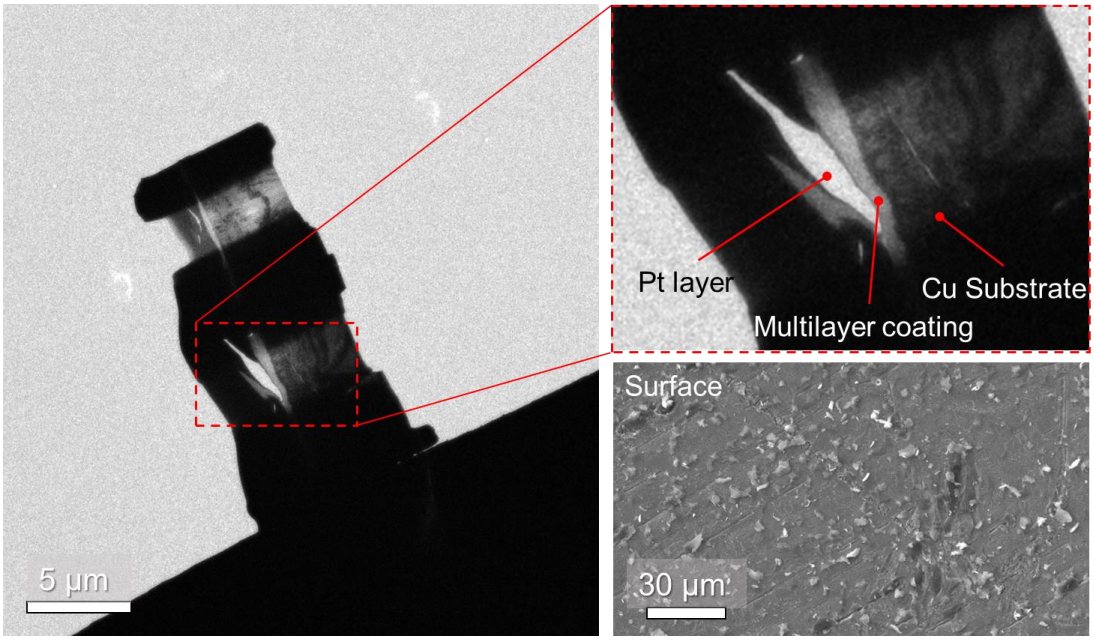

Figure 98 - Low magnification TEM image of a FIB milled lamellae from a multilayer coating with 12 h static top layer deposited on copper substrate, two adjacent regions have been thinned to electron transparency, with the lower of the two selected for analysis, as indicated. The magnified inset highlights the contrast between the protective platinum layer, multilayer coating and substrate, no scale has been applied to the inset as it is only intended to convey contrast. Bottom right, image of surface of sample prior to milling.

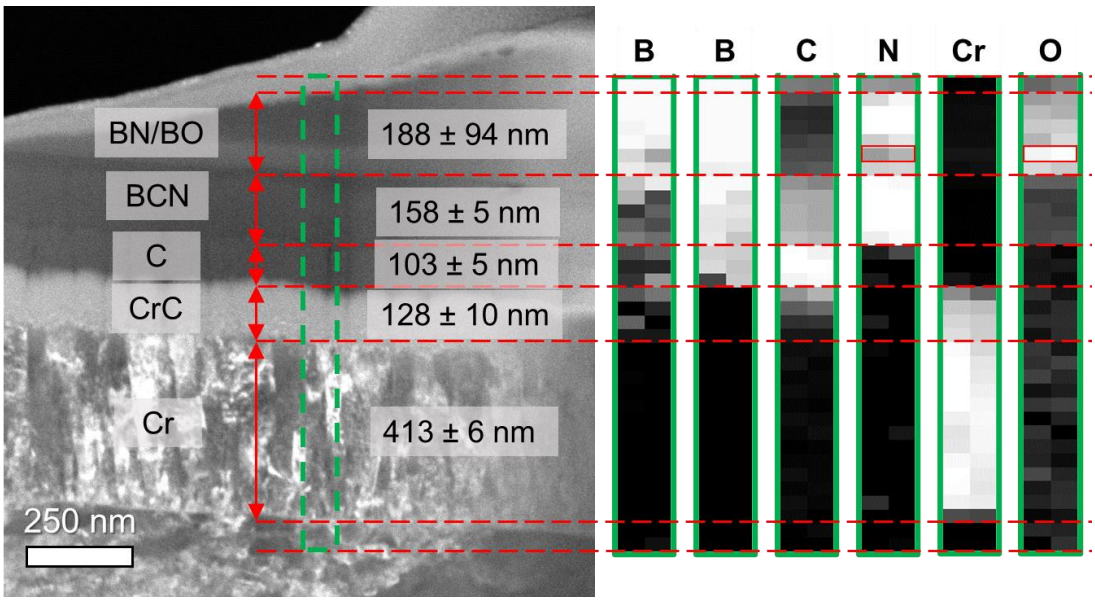

Figure 99 - Cross-sectional TEM micrograph of the multilayer coating structure with 12 h BN top layer deposited statically, qualitative EELS bars aligned with coating structure indicate the composition of the layers and blends at the interfaces. Thickness values were measured using ImageJ software (n=10).

Table 24 - Energy loss fit ranges for each element of the qualitative EELS bars aligned to the image in Figure 99, indicating the composition change through Coating 6

Element	**B**	**B**	**C**	**N**	**Cr**	**O**
Energy Range (eV)	189.9-197.1	190.6-197.1	291.4-297.9	403.9-423.6	569.4-586.1	529.9-550.4

Further identification of the multilayer structure was performed using cross section TEM on a sample from Coating 6 (12 h). Figure 98 shows a low magnification TEM image of a FIB milled lamella with two regions ion thinned to electron transparency, consisting of Cu substrate material with Coating 6 (12 h) applied, photo of sample in Figure 88 b) top left. A higher magnification image, showing the cross-section of the coating is presented in Figure 99, with layer identification, thickness and qualitative EELS bars alongside. Table 24 contains the energy ranges chosen for detecting the different elements. The thickness of the interlayers is uniform. In contrast to this, and agreement with the observations in Table 20, the final BN layer varies across the area imaged, with a thickness 188 ± 94 nm, indicative of the flaked/powdery appearance of the surface, see Figure 98 for the surface image.

Considering the image and EELS bars in Figure 99, the Cr layer is evident both from the intense signal, and from the crystalline, columnar growth. At the interface of the Cr and CrC layer the C signal is faint, and moving further outwards in the coating, the increase in signal, and corresponding decrease in the Cr signal is apparent confirming the blend from Cr to C through CrC, as per the recipe. This image also indicates that as the carbon is introduced the growth changes from the relatively large columnar (Zone 2 growth [29]) structure into smaller crystallites, and then amorphous growth as the C deposition dominates.

The sharp onset of the N signal indicates the start of the BCN layer, corresponding with the reduction in the C signal, note that the N content should not ramp up as the gas flow was constant in this step. The C signal does reduce, indicating an end to the

BCN layer, however some brightness remains, potentially attributed to either contamination from the vacuum chamber during coating, from the microscope during milling, sample transfer, or as a noise level signal.

Two energy ranges, starting at different edge energy values, were used to fit the B energy loss (Table 24). The range including the low component 189.9-190.6 eV indicated low concentrations of Boron starting at the Cr-CrC interface, and both ranges indicating B content in the C layer upwards. Both ranges also confirm B content in the expected BCN and BN layers. The indication of Boron in lower layers than those intended could be due to sputtering of the top and penultimate layers whilst ion milling and thinning, however the lack of N deeper into the coating contradicts this. Finally, the O bar indicates oxygen content in the final BN layer, with a bright pixel at the onset of the final layer, corresponding to a darker pixel on the N bar, both highlighted in red, suggesting a larger concentration of O in this spot.

Figure 100 contains HRTEM images of the coating, taken after further ion beam thinning of the lamella. These indicate that the coating initially grows in columnar grains, with the Cr crystallites of the order of 20 nm visible in the first layer. Layer thicknesses are consistent with the image in Figure 99, with the exception of the final layer, which is thin in this region.

As the coating grows and the C is blended with the Cr; less crystallites are visible and by the midpoint of the CrC/C layer the coating appears to be fully amorphous. Epitaxy from the columnar grains remains through to the end of the C layer, evident in the bright contrasted lines extending from the Cr layer. The contrast between the C and BCN layers is subtle, but can be distinguished in a) and conveyed to b). The structure does not appear to differ between these layers, remaining amorphous. The final BN/O layer is thin in this region, magnified image of the BCN-BN/O interface in Figure 101.

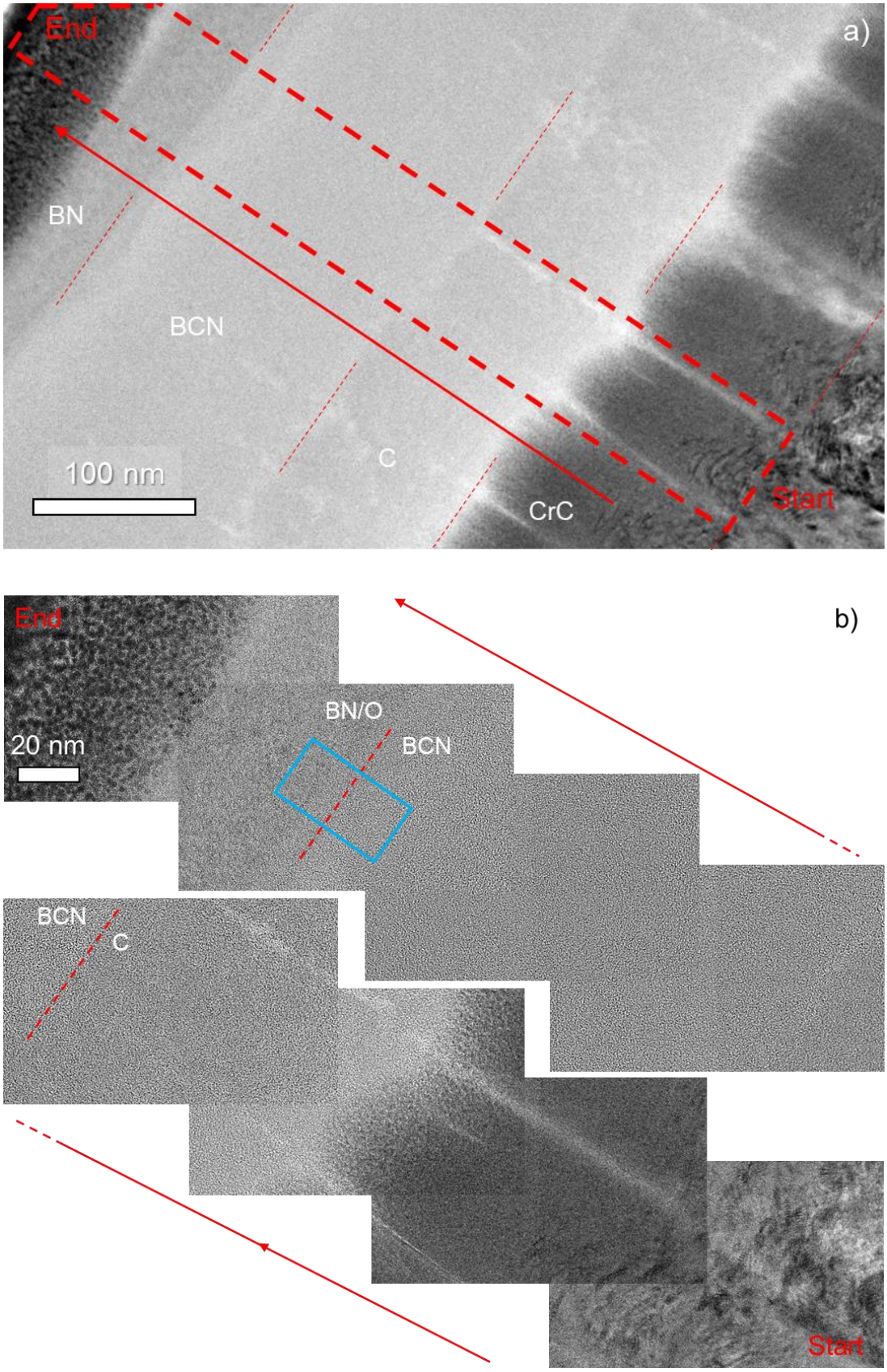

Figure 100 - High Resolution TEM (HRTEM) images of the cross-section of BN multilayer coating, a) low magnification, b) higher magnification overlayed series of images starting at the Cr to CrC interface and ending at the protective platinum layer. Polycrystallinity is evident in the Cr/CrC layers, trending towards amorphous higher in the coating. Blue region is magnified in Figure 101.

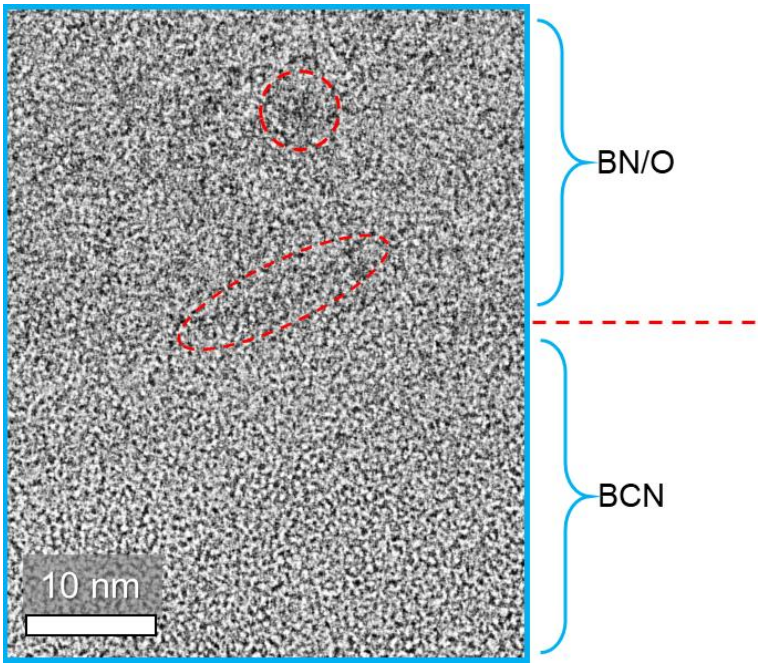

Figure 101 - High magnification HRTEM image of the interface between the interlayer and the top layer (BCN-BN/O), from the region in Figure 100 b), transition point indicated, there is a subtle change in contrast, with darker 'patches' in the top layer.

There is a subtle change in contrast at the interface, with darker patches in the top layer, which could be indicative of a shift to nanocrystalline texture [288], similar to Lattemann et al. (2-5 nm crystallites) [250], Yamamoto et al. (5-10 nm crystallites) [163], or Gimeno et al. (5-15 nm crystallites) [186], however at this resolution this is not conclusive. There is also the possibility of alteration of the structure via damage during FIB milling [289-291], TEM imaging [243], oxidation, and also the lamellae could be too thick for HRTEM imaging.

5.2 Discussion

The aim of the Cr-CrC-C-BCN-BN interlayer design was to assess whether the use of fully blended interfaces (concurrent deposition ramping up/down) improved the adhesion and reduced degradation of c-BN coatings, as an alternative to sharp (instant changeover of material deposition) layer boundaries, with a specific focus on the use of steel substrates.

For the benefit of the reader summaries of the top layer coating parameters and interlayer parameters are repeated and shown in Table 25 and Table 26 respectively.

Table 25 - Summary of the top layer BN deposition parameters for coatings deposited onto planar substrates whilst held statically, repeated from Table 10.

No	Multi-layer	Top layer motion	BN Targets (Duration)	Ar:N_2 (sccm)	Bias Voltage (V)	Pulse Frequency (kHz)	Reverse time (ns)
1	N	Static	1 (6 h)	50:12	60	250	500
2	N	Static	1 (24 h)	50:0	60	250	500
3	N	Static	1 (6 h)	50:12	60	250	500
4	N	Static	1 (4 h)	50:12	150 - 120	250	500
5	Y	Static	1 (6 h)	30:15	180 - 150	250	500
6	Y	Static	1 (12 h)	30:15	180 - 150	250	500
7	Y	Static	1 (18 h)	30:15	180 - 150	250	500

Table 26 - Summary of the Cr-CrC-C-BCN adhesion interlayer coating parameters used for Coatings 5, 6 and 7, repeated from Table 11.

Layer	Target Setpoint	Substrate Bias (V)	Ar:N_2 (sccm)	Layer duration
Chromium	Cr (4 A)	120	23:0	900 s
Chromium Carbide	Ramp Cr (4-0 A) Ramp C (0-3.5 A)	60	23:0	1200 s
Carbon	C (3.5 A)	60	23:0	1200 s
Boron Carbon Nitride	Ramp C (3.5-0 A) BN (175 W)	60	30:15	2400 s

As is presented in Section 5.1.1, the design of the magnetron(s) and the target clamping system used for BN meant that Fe contamination was present in the initial coating (1, static, single-layer, 60 V bias, 6 h), measured at 8.32 at% by EDX, Figure 62. This issue occurred with the BN coatings due to the need for higher power densities than had previously been used with this magnetron and target fixing arrangement. The stainless steel clamping ring overlapped the edge of the sputtering racetrack and at the higher power densities required for depositing BN the plasma intensity at the edge was sufficient for sputtering. This would have been advantageous, if the clamping ring was not present, as a wider racetrack would increase target utilization, as a higher target surface area would contribute to deposition, maximizing material efficiency.

In order to reduce this Fe contamination an attachment was developed and implemented, Figure 26, which blocked the sputtered Fe. This reduced the contamination, a change seen in the different appearance and EDX results from Coating 2 onwards. A negative consequence of the attachment was a reduction of the aperture of the target, leading to sputtered BN being blocked from reaching the substrates at high angle, see Figure 102 a) and b).

This, however, did not prevent sputtering of the clamping ring, it only prevented the Fe from reaching the substrates. For further optimisation of this solution, the attachment should be redesigned such that the lip which blocks unwanted sputtered material, see Figure 102 b), is in closer proximity to the ring surface. This would reduce the distance between the cathode (clamping ring) and anode (attachment lip) to less than the minimum cathode dark space distance, preventing electrons from being accelerated, and therefore from ionising atoms, and therefore preventing plasma discharge [1, 9, 26].

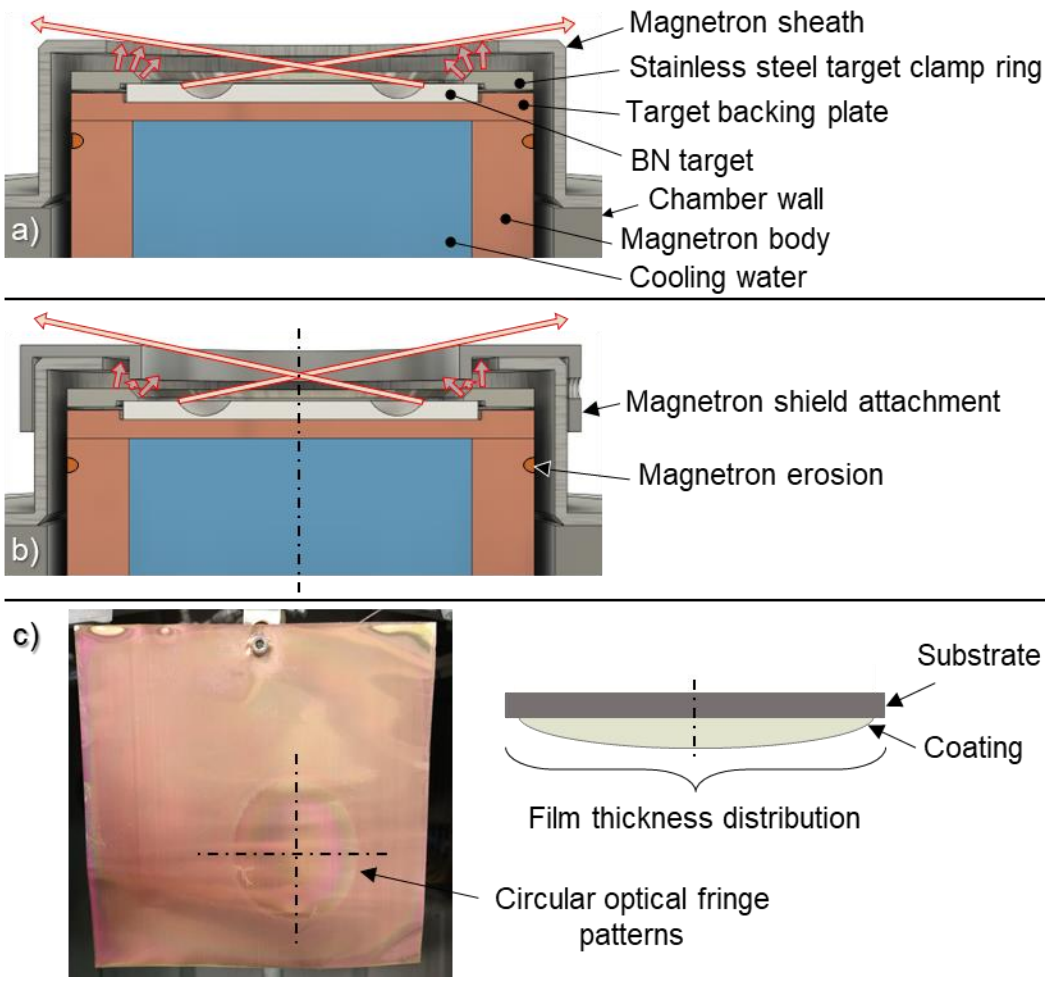

Figure 102 - Schematics showing the cross-section of the magnetron with labels identifying each component, a) in standard setup and b) with attachment in place to reduce contamination. Arrows extending from the outer edge of the target racetrack indicate the field of view of the magnetron, narrowed when using the attachment. Arrows extending from the target clamp ring indicate sputtered stainless steel contamination, partially blocked by the attachment. Note the permanent magnets have been omitted from this schematic as they are sealed and the exact arrangement is not known, c) an example of the inhomogeneity of deposition from the BN target with static samples.

The material sputtered from a target on a magnetron predominantly comes from the racetrack, and this is reflected in the deposition, as thicker coating regions will be present directly opposite this. The deposition can in effect be considered as a ring source. Optimisation of the target size and source to substrate distance can lead to uniform deposition across the surface area of substrates held in front of the magnetron, the reader is directed to the review by Swann et al. [1] which contains a diagram showing this. At a too close target to substrate distance, the material deposited will be thickest at a point on the substrate in line with the central axis of the

target aperture, with deposition/thickness tailing off further from the centre [1, 292]. Figure 102 c) shows a schematic of this, and a photo of a large coated foil sheet, taken subsequent to the coating trials in this chapter. The photo clearly indicates, from the different colours present in the fringe patterns, that coating thickness varies significantly. Therefore, it is proposed that in this current study the inhomogeneity of the statically deposited samples (Coatings 1-7, Table 25), was at least partially due to a too small target to substrate distance, combined with small target dimensions and reduced aperture. The reduced aperture, as mentioned previously, blocked BN material sputtered at high angles from reaching the substrate. If not occluded, this material would have worked to minimise the thickness reduction at the edges.

Considering the single layer static BN Coatings (1-4), from the outset there was a need for consistent surface preparation, as the topography and morphology of deposited material was dependent on the substrate surface, as has been seen before [293]. This was seen from the comparison of non-uniform coatings on different substrates, glass (white powder deposits), grit blasted 316L (epitaxial plate growth) and machined 316L (preferential growth of curled material), see Figure 60. The machined and grit-blasted surfaces, due to the mechanically disrupted morphology of their surfaces, contained a high amount of macroscopic defect sites. This led to growth of material at oblique angles, which then shadowed the substrate surface, leading to preferential growth on top of previously deposited material, and porous scaffold structures [35]. The decision to move to polished substrates was motivated by the removal of these substrate effects as they could obscure material mechanisms.

Furthermore, due to the N contents of 0 and 26.5 at% in Coatings 2 and 3, where N_2 gas input was 0 and 12 sccm respectively, the need for additional N_2 gas flow was confirmed due to dissociation of the BN in the target, as expected from literature [39].

The interlayer structure, based on an amalgamation of existing adhesion layers proven in DLC coatings on tool steel [279, 282], and BC interlayers for BN adhesion

[163, 174, 175, 219, 231, 249] was analysed in stages to understand individual layer contributions. The deposition of Cr-CrC-C produced visually uniform smooth layers with morphology and composition only altered from expectations by surface preparation and environmental/handling contamination. The expectations were that coatings would appear smooth, conforming to the substrate surface, due to the good step coverage of sputtered material, as such scratches remaining from surface polishing were visible, but were overcoated [1]. The Cr layer was predominantly oriented (110), confirmed by XRD, as seen in literature [279] with dense columnar structure visible in XTEM (Figure 99) similar to Yang et al. [282]. This is indicative of Zone 2 growth, when referring to the modified structure zone models by Kelly and Arnell [2, 31] and Anders [32]. These models describe this growth as being present under conditions of low homologous temperature (ratio of substrate temperature/coating melting temperature) and in the presence of low energy ion bombardment. The subsequent blend from pure Cr to CrC formed a layer gradually increasing in amorphous content as the layer increased to pure C, confirmed by cross-section TEM (Figure 100), with some epitaxy evident up to the end of the C layer.

From the surface EDX results gathered from the final interlayer stage (Cr-CrC-C-BCN), B was only detected in either small concentrations or not at all, see Figure 81 and Figure 83. In contrast to this, the EELS data gathered from X-TEM (varying with fit range) indicates B content gradually increasing from the start of the pure C layer. For Coatings 5, 6 and 7 (multilayer, static BN, deposition time 6 h, 12 h and 18 h respectively) the deposition rate of C was found to be much higher than BN in this stage. This was due to the difficulty of sputtering ceramic materials with RF power [24], as an alternating current is needed to remove residual charge from the non-conductive target surface. The deposition time is therefore reduced by the reverse cycle. The relative size difference of the BN (57 mm) and C (380 x 175 mm) targets,

and the aforementioned reduction in aperture also contributed to this. The power density used on the BN target was set higher than the C, 6.86 and 3.21 W/cm^2 respectively, but this still led a lower deposition rate for BN, meaning that the deposition rates were only equivalent at the end of this step.

Therefore, the final layer can, in reality, be defined as a CN layer instead of a BCN layer, blended to a thin BCN layer at the top, with a total thickness of 158 ± 5 nm, see Figure 99, as the B component will have a low ratio in the majority of the layer. The deposition rate of C during this step equates to a thickness of 93 ± 17 nm, though the addition of N_2 in this step will alter the C deposition rate, due to target poisoning [24]. This allows estimation of the thicknesses of the CN/BCN sublayers by calculating the crossover point when the C deposition rate is equal to the BN deposition rate. This point is at the C target current of 1.17 ± 0.04 A, corresponding to a remaining layer deposition time of 700 ± 20 s, and therefore true BCN→BN gradient thickness of 28 ± 11 nm, see Figure 103. Further study using XPS depth profiling or Secondary Ion Mass Spectroscopy (SIMS) could be carried out to understand the exact blending of this gradient layer.

This is distinct from previous attempts in literature, where Yamamoto et al. [163] have deposited 250/100 nm B_4C/BCN, and Wang et al. [175] ~170/250 nm BC/BCN adhesion interlayers, with the current coatings presented here closer to the ‘few tens of nm’ of B_4C deposited Mirkarimi et al. [151]. Thus when comparing to literature it is clear then that the gradient transition from interlayer to BN in the current work is thinner. The intended interlayer transition thickness of 100-300 nm has been reached, in accordance with general practice in PVD adhesion layers [2, 282, 294], though the composition is altered from intentions. This has the potential to influence the adhesion and stability of the top layer, as a thinner layer may not be able to accommodate residual stress mismatches , due to deposition, material and thermal effects, between the layers [27, 33].

As detailed in Section 2.4.2.3, a 1:1 ratio of Boron and Nitrogen is an essential starting requirement for cubic phase nucleation and growth in thin films. The combination of sputtering parameters (primarily a gas ratio of 2:1 $Ar:N_2$) for Coatings 5, 6, and 7 (multilayer, static BN, deposition time 6 h, 12 h and 18 h respectively) produced coatings with B/N atomic ratios of 1.09, 1.02 and 1.03 from EDX, for the 3 durations tested. This indicates that the growth time/thickness does not alter the elemental composition of the coating, with only small changes in N deficiency, sub-stoichiometric N content is commonly reported in literature [43].

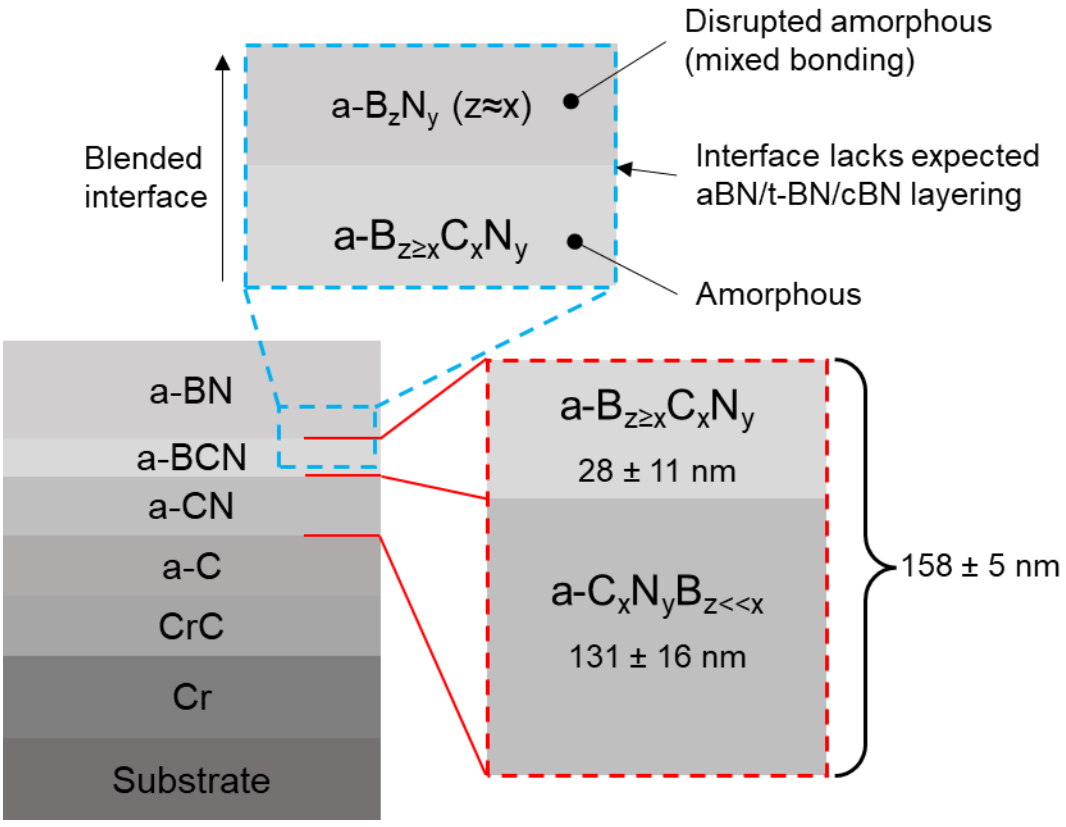

Figure 103 - Schematic of the multilayer coating indicating the separate definition of the CN and BCN layers, with the calculated thicknesses and change in composition in these sublayers, 'a-' indicates amorphous structure.

XRD, FTIR and TEM analyses indicated that, with the exception of the Cr and CrC interlayers, there was a lack of crystallinity in the coating. Glancing angle XRD

patterns (Figure 95 and Figure 96) of 316L substrate with Coatings 6 (12 h) and 7 (18 h), and Si substrate with Coatings 5 (6 h) and 7 (18 h) showed broad peaks, indicating nanocrystallinity (Cr layer crystallite size of 11.8 ± 0.6 nm) with little difference when compared to interlayer patterns, Figure 85. Relative peak heights indicated that there was no contribution to the patterns from crystalline BN phases, but the interlayer and substrate intensities reduced with increased coating time, indicating that material was deposited and interfered with diffracted X-rays. The HRTEM images in Figure 100 supported this, showing that there was no visible long-range order beyond the CrC layer.

The broad and overlapping peaks in the FTIR spectra (Figure 97) also indicated bond length and angle disorder due to a lack of crystallinity [210]. Further to the lack of crystallinity, it is clear that despite following the general methodology in literature for nucleating and growing a cubic phase film (bombarding the growing film with energetic ions, and using a 2-step varied bias methodology [170] (in the current work 180 V nucleation reduced to 150 V for growth)) that crystalline cubic phase BN has not formed, see Figure 103. The characteristic cubic nucleation steps, a-BN followed by t-BN followed by c-BN [3, 234] have therefore not occurred, as these distinct structures are not seen by HRTEM. Kulisch et al. [43] wrote in their review that the thickness of these nucleation layers varies with parameters, and consequently the thin BN/O layer imaged by HRTEM in Figure 57 could be too thin to capture the transition, however the FTIR and XRD data, showing amorphousity/nanocrystallinity, was gathered from uniform regions of coating (≥ 282 nm thickness, Figure 56) so the lack of nucleation structures is confirmed.

FTIR analysis does however give an additional indication of the bonding within the film, Figure 97. Corroborating with EDX, only minor concentrations, ~2.9, ~2.5 and 4.8 at% (see Appendix for tabulated data), of O are present in Coatings 5, 6 and 7 respectively. From this the spectra can be assumed to be dominated by BN bonding

contributions. The films are mixed sp2 and sp3 bonded, as all contain E-BN (sp2/sp3 [243]) and h-BN/t-BN (sp2), with Coating 7 (18 h) showing w-BN content. The appearance of the w-BN mode in Coating 7 (18 h) could suggest that increased sp3 content forms with increasing coating thickness. This could potentially be explained by a mechanism reported previously in literature [3, 43 McKenzie, 1993 #725], related to the Stress model. As named, the model links the internal stress of the growing coating to the formation of c-BN structures, and as the residual stresses in thin films tend to increase as the thickness increases, this has been observed to correlate with higher cubic content fraction. However, this is not conclusive with the current data as the definition of sp3 bonding in w-BN and E-BN is distinct from that in cubic structures. Furthermore, when considering peak shifts in FTIR, with a rise or fall in wavenumber known to indicate compressive or tensile stress respectively, the peaks for h-BN present in Coating 7, at 779 and 1377 cm^{-2}, differ only slightly from the values for single crystal BN, 783 and 1367 cm^{-2} reported in Table 3. This points to the possibility of similar structures to those seen in amorphous mixed sp2/sp3 bonded Diamond-like-Carbon films [295].

Whilst the O contents are minor components in the coating, this could be a potential reason that the cubic phase has not nucleated. This has been reported by Lüthje et al. [245] who found contamination, thought to be from outgassing jigging, present in their coatings, which reduced but did not eliminate cubic content, the authors gave no mechanism for this reduction. However as is the case with the current study, the O content cannot be linked conclusively to either incorporation during coating or on exposure to the environment. The X-TEM/EELS data is not of use here either as the lamellae was exposed between milling and imaging. In contrast to this, publications by Lattemann et al. [250], Choi et al. [296] and Ulrich et al. [252] report stable BN films with cubic content when intentionally introducing small quantities of oxygen, 4.6 at% for the latter. Given that in these publications cubic phase was nucleated, and

only reduced with O contamination, this cannot be the sole cause for lack of cubic phase in this current work. c-BN has also been shown to nucleate on top of amorphous interlayers [163], and therefore the lack of nucleation also cannot be solely attributed to the structure of the CN/BCN interlayers used. There could potentially be, however, a dependence on the hardness of the interlayers, as found by Mirkarimi [3, 297]. The authors deposited BN onto metal and Si substrates, and found that the harder (higher strength) Si substrates produced films with higher cubic content, with the suggested mechanism being the related to the capacity of the substrate to contain the stresses imposed on the growing film during deposition. Therefore, in the current work, during the nucleation of the BN layer, the stress in the film could have caused a yielding at the interface with the BCN layer, reducing the stress, preventing the cubic phase from forming. However, this is unlikely, as if this had occurred, the aforementioned characteristic a-BN followed by t-BN layer structure would be visible in the X-TEM images, with only the c-BN missing. Though again this could be disguised by oxidation of the lamella prior to TEM imaging.

The key parameter differences between the current coatings and those referenced previously are the bias parameters and the temperature. The parameters that nucleated cubic phase top layers with BC interlayers 200 V/600°C [163], 200-350 V/not stated [175] and 100 V/1000°C [151], and the aforementioned oxygen containing films 250 V/400°C [250] and 350 V/350°C [252] are higher than those used in the current work (180/150 V and ~100°C). Note that here the 100 V/1000°C parameter set used by Mirkarimi et al. [151] will not be considered because of the extreme difference in temperature. No additional heating was applied to the substrates in this study, for Coatings 5, 6 and 7, relying solely on plasma heating, from both the target plasma and substrate bias plasma. This temperature (~100°C, via temperature labels) was lower than expected, with assumptions based upon the temperatures reached during the interlayer stages (~200°C), which used DC power

on large (380x175 mm) targets. The limiting factor in the heat transferred to the substrates is the total power applied to the magnetron whilst depositing. This is because plasma processes are inherently inefficient, with ~80% energy lost to heat [1]. During the interlayer stages 1.4 kW and 2.2 kW were applied to the Cr and C targets respectively, heating the substrates significantly. When compared to the lower 175 W applied to the BN target during the final layer, as the target is smaller (57 mm diameter), the disparity is clear, there was less energy transferred to the coating as heat (1120 W and 1760 W compared to 140 W). This temperature is also below the minimum threshold, 120°C, reviewed by Kulisch et al. [43] for cubic nucleation and the authors also suggest that the temperature threshold rises when impurities are present in the coating, such as O. It should be mentioned however that cubic phase has been proven to nucleate even at room temperature [298].

As mentioned, the substrate bias (180/150 V) was also lower than studies in literature. This parameter influences the energy of bombarding ions, and the ion/sputtered atom ratio, which is critical when depositing cubic phase films [3]. Measuring ion energies and ion to sputtered atom ratios in plasma based processes is non-trivial, as there can be a wide range in both metrics, differing with measurement position and interdependent parameters, [41-43, 164] and has not been carried out in this study. Furthermore, as opposed to IBAD (Ion Beam Assisted Deposition) processes where the ion energy and current can be fully independently controlled, substrate biasing resolves these into a single user variable parameter, the bias voltage [19]. As such, only suggestions can be made as to the mechanisms present in the coating formation, relating the observed coating to the bias voltage applied and the front panel bias current (analogous to total ion current [37]). As a top BN layer was deposited (≥ 282 nm thickness, Figure 56), the resputter region as reported by Mirkarimi et al. [3] and thoroughly reviewed by Kulisch et al. [43, 169] has not been reached, which suggests that the bias parameters have headroom for further studies with increased

bombardment, considered in Chapter 6. However, in assuming that either one or both the ion current/ion energy is below the threshold for cubic nucleation, the coating environment should reside in the h-BN nucleation (lower left, Figure 18, pg 13) of the parameter spaces from both reviews. Here it is important to emphasise that the data used to compile these spaces is from FTIR, and as such does not necessarily take into account crystallinity. The amorphous, mixed BN bonding Coatings 5, 6, and 7 can therefore be tentatively placed in this region despite not presenting crystalline h-BN.

However, Ar contamination could give an additional indication of the formation mechanism of the amorphous coating. Residual Ar content was measured by EDX in the coatings and whilst the B/N ratio was not altered by the coating duration, the Ar varied, with 0.6, 7.0 and 5.0 at% in Coatings 5 (6 h), 6 (12 h) and 7 (18 h) respectively (Figures 90, 92 and 94 corresponding to Tables 50, 51 and 52). This indicates that there is trapped Ar in the coating through implantation or adsorption and overcoating [9]. As to the reason for the decrease in the longer duration, it is not clear at this time, though this could be due to Ar diffusion to the surface over time [33]. Lehtinen et al. [299] simulated ion irradiation of h-BN monolayers, analogous to the BN nucleation stage in the current work, and found that when at low to medium ion energies (< 10 eV), there was the possibility of amorphous structure formation. They suggested this was due to constant displacement of deposited atoms via ions, leading to adatom motion, but with minimal energy, leading to short range structures. In the current work this could be a reason for the lack of crystalline structure, as either the low energy bombardment constantly displaces bonded atoms, disrupting the growth of long range order, or contrasting to this, the bombardment creates an abundance of defects, and therefore nucleation sites, creating competition between regions of short range order [29, 300, 301]. Additionally, due to the high energy needed to disrupt the

covalently bonded material and to nucleate crystalline cubic BN, short range order remains [8].

As is covered in Section 2.4.2.3, there are multiple suggested mechanisms for the cubic phase formation or transformation in thin films, none which can fully explain the nucleation and/or growth of cubic films. Given that Coatings 5, 6 and 7 are all amorphous, it is difficult to suggest a formation mechanism without a trend to highlight differences or a threshold. When compared to the Sputter [164, 236], Thermal spike [238] and Stress (Static and Dynamic) [239, 240] mechanisms [3] it is proposed that the critical thresholds of temperature and ion bombardment (ion energy or flux) have not been reached. In attempting to relate this to more general PVD structure growth zone models, see Anders [32] and Kelly and Arnell [2, 31], the parameters sets used in the current work are present in Zone 1 of the former and Zone 2 of the latter. Neither of these sufficiently fit what has been observed, as the structure in Zone 1 proposed by Anders describes crystallites growing perpendicular to the substrate surface, and Zone 2 from Kelly and Arnell describes dense columnar growth. The coatings could be related to the region from Anders' diagram at the boundaries of Zone T, Zone 3 and Ion etching, where nanocrystalline growth is proposed, however this is not conclusive.

Coatings 5, 6 and 7 (multilayer, static BN, deposition time 6 h, 12 h and 18 h respectively) also showed no morphological or compositional degradation after storage in atmosphere for extended periods of time. This is an important point to emphasise, as BN films are well known to delaminate in contact with moisture [3]. This indicates that the relatively thin BCN gradient successfully adheres BN to steel, (though this has not been quantified through adhesion testing) and that the structure and composition of the top layer is stable in atmosphere as there has been no compositional change over time. The most prominent delamination mechanism in literature, proposed by Cardinale et al. [242] and supported by Möller et al. [168] and

Kim et al. [244] suggests that the delamination of BN coatings is driven by both compressive stress remaining in the coating from the deposition, coupled with a decrease in density (increase in volume) of material as the BN reacts to form higher volume oxides and hydroxides. This overcomes an adhesion threshold at the interlayer/top layer boundary, delaminating the material.

Given that both this delamination mechanism and the cubic formation mechanisms have not been observed, it can be suggested that there are minimal internal stresses present in the film, corroborated by the lack of peak shifting in the FTIR spectra. This coupled with the lack of a defined interlayer/top layer boundary, and the stability of the top layer when exposed to ambient humidity, prevents delamination. The stability of the coating could be further aided due to the amorphous structure possessing lower humidity sensitivity than crystalline phases [206, 253], but further study is needed to ascertain this.

5.3 Conclusions

This study has explored the use of a novel interlayer structure for adhering BN coatings to different substrates, focused primarily on steel, a coating-substrate combination previously underreported in literature. This was the aim of the chapter, and has been partially realised.

According to the objectives set out in the introduction (pg 10), single layer and complex multi-layered BN coatings have been deposited via substrate bias assisted magnetron sputtering. In confirmation of literature, coatings were found to be non-uniform and had low adherence to all substrate types when depositing directly onto steel and glass. The multilayer, deposited by rotating samples past multiple magnetrons, combined Cr-CrC-C layers with BCN layers to improve adhesion. The top BN layer was applied by holding substrates statically in front of a single magnetron.

The aim, to investigate BN coatings for application to tools has not been fully completed, as c-BN was not uniformly deposited with a sufficient hardness for testing. The detailed conclusions are contained in bullet points below:

- A gas flow ratio of 2:1 for $Ar:N_2$ has been shown to produce 1:1 stoichiometric BN top layers within this PVD setup, assessed via EDX, however low O content (< 5 at%) and Ar content (< 7 at%) is present in the coatings.
- The interlayer-top layer interface showed a uniform transition between the material types, as indicated by HRTEM, showing that a successful blended interface was created, as intended by the ramped deposition of coating materials.
- The previously unreported stacking of CN-BCN-BN layers combined with the well researched Cr-CrC-C layers adhered the top BN layer to the substrate, however inconsistencies in positions in front of the magnetron and sample proximities led to surface inhomogeneity and some regions delaminating.

- Nucleation and growth of crystalline c-BN on top of the interlayer was attempted, taking established methodology from literature in the form of energetic ion bombardment. However no crystallinity was seen with HRTEM, and XRD patterns and FTIR indicated amorphous material.
- The established mechanisms for c-BN formation in thin films were not observed to occur, and the coatings were not conclusively found to have followed general PVD structure zone models. It was suggested that the amorphous structure formed because the threshold for crystalline arrangement (hexagonal or cubic) was not reached for one or all of the following parameters:
    - Substrate/coating temperature
    - Energy of bombarding ions
    - Ion bombardment current (and therefore the ratio of bombarding ions to sputtered neutrals
- Furthermore, contamination from oxygen and argon was proposed to have increased these threshold parameters and disrupted the nucleation of crystalline structures at the interlayer/BN layer boundary respectively.
- The corresponding hardness of these coatings (6.98 ± 0.66 GPa) was not high enough to be suitable for tooling applications.

6. BN Coating Development - Rotational Coating (Coatings 8-12)

A key conclusion from Chapter 5 was that the use of a single magnetron with static samples for depositing the top layer led to a lack of coating homogeneity, in the thickness and morphology variation across the sample surfaces. This was due to constricted placement of samples in front of the target and in proximity to each other, which also restricted the number of samples coated per batch.

In an attempt to reduce this inhomogeneity and variation, the methodology was adapted. Rotation was used for the top BN layer as opposed to static deposition. This also facilitated the use of 2 BN targets for both the final interlayer BCN (or CN/BCN as discussed in 5.2). The potential for coating a higher number of samples per coating batch was an additional rationale for this methodology change, as it facilitated investigation into first steps towards more efficient large-batch coating, fully utilising the multi-magnetron large volume TEER UDP650 coating equipment.

This corresponds to one of the aims of this thesis, to investigate the application of these coatings to tools, which requires large batches to take advantage of economies of scale.

6.1 Results

A compromise in the use of rotation during this final step was in the deposition rate of the BN. As the samples were only in the field of view of a target for ~1/3 of each rotation this rate was reduced from 68 ± 30 nm/h to 12.8 ± 1.8 nm/h nm/h at the varied 180-150 V bias with two targets in the BN steps. The samples were placed on a ledged substrate holder, removing the need for double sided adhesive tape that had the potential to outgas contaminants. The reduction in deposition rate was anticipated, and so for Coatings 8, 9 and 10, reduced gas flows were used to reduce the pressure and increase the mean free path of sputtered material, in an attempt to increase deposition rate.

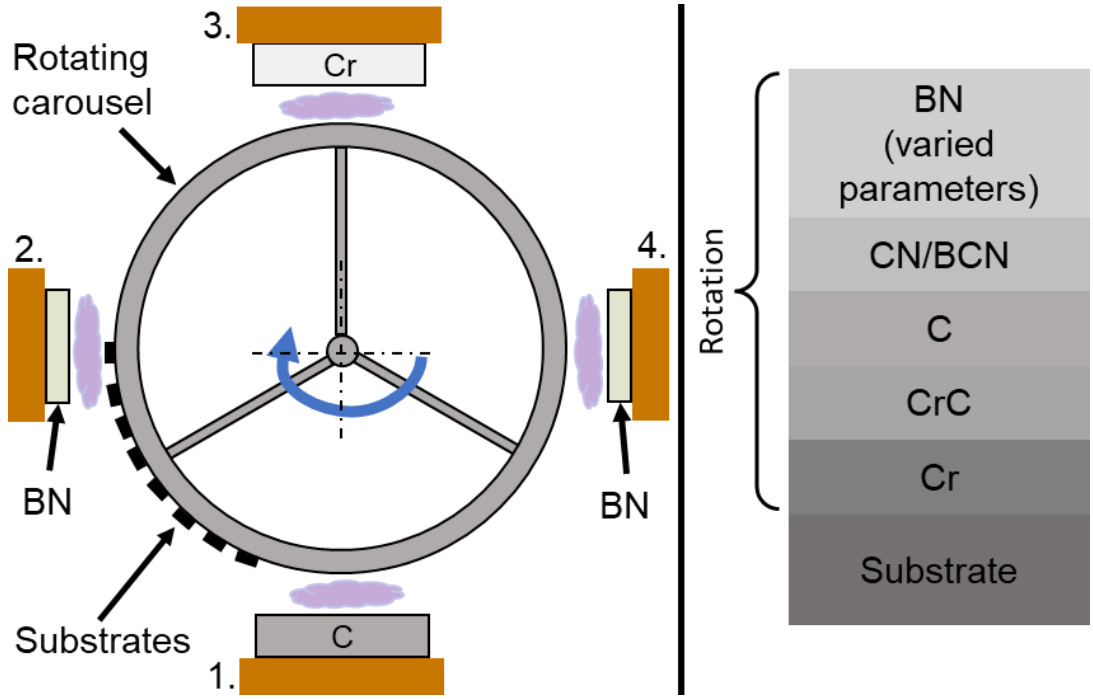

Figure 104 - Schematic showing the PVD coating equipment, with 2 BN targets, both interlayers and the top BN layer were deposited with substrates rotating past the targets. Note that whilst this schematic shows plasma in front of all the magnetrons at once, in reality this varied according to each stage of the recipe.

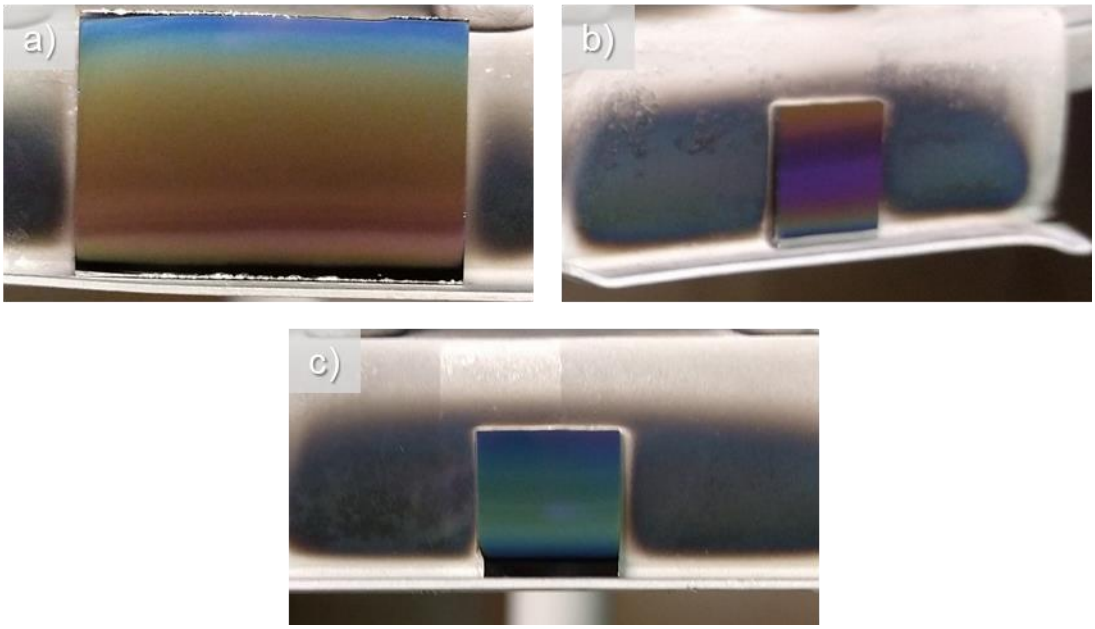

Figure 105 - Substrates, a) glass, b) 316L, and c) silicon, coated with a multilayer BN coating where all steps of the recipe were carried out with substrate rotation active at 5 rpm. The top layer BN was deposited for 6 h at 60 V bias.

Throughout all the coatings in this subsection, the temperature during the final BN layer was measured as ~100 °C using adhesive backed temperature labels attached to the substrate holder. As the parameters for the blended CN/BCN layer were unchanged except for the second BN magnetron, the calculated thickness for the total CN/BCN layer was therefore to ~221 ± 39 nm, with CN and BCN thicknesses of ~95 ± 15 and ~126 ± 54 nm respectively.

The photos in Figure 105 show the resulting surface appearance of substrates following a 6 h trial of the multilayer coating process with rotating BN layer at 60 V substrate bias. The fringe patterns on the surfaces are uniform horizontally, as this is the tangential direction of rotation, and such the samples will pass through regions of higher and lower flux of sputtered atoms leading to an average distribution of deposited material across the substrate width. However, the change in appearance when viewing from top to bottom indicates that the coating thickness is not uniform in the vertical direction. This can be attributed to the slight angle of the ledges on the substrate holder, with the top of the substrates being further away from the magnetron, and the partial masking of the substrate by the bottom lip of the ledges. Furthermore, in the case of the glass substrate in a) the material is taller than the ledge, and so will be bombarded by ions on the reverse of the substrate at the top, causing different temperatures in the vertical direction.

When using the second magnetron for BN deposition in these coatings, Mag 4, the gas flows fluctuated ~± 5 sccm, with random reductions to 0 sccm. This issue was troubleshooted and was found to be caused by RF interference from Mag 4, not present in previous coatings. Faraday cages were constructed from mesh and foil, surrounding the magnetron enclosure and gas mass flow controllers (MFCs), connected to ground, see Figure 106. This stabilised the gas flows sufficiently that compensation could be made when programming recipes for further coating.

Figure 106 - Photo of the mesh/foil Faraday cages in place covering Mag 4 (far) and the gas mass flow controllers (MFCs) (near).

6.1.1 Multilayer rotational BN – 60 V (Coating 8)

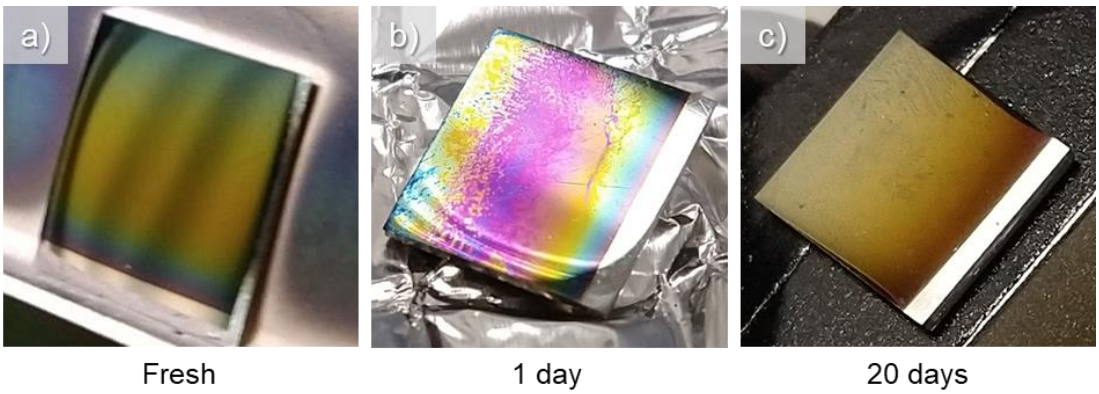

Figure 107 - Photos showing polished 316L sample coated with multilayers and BN top layer in rotation for 24 h with an applied substrate bias of 60 V for the final BN step, at a) opening of coating chamber, b) 1 day stored, c) 20 days stored, the coating appearance changes as the time in atmosphere increases.

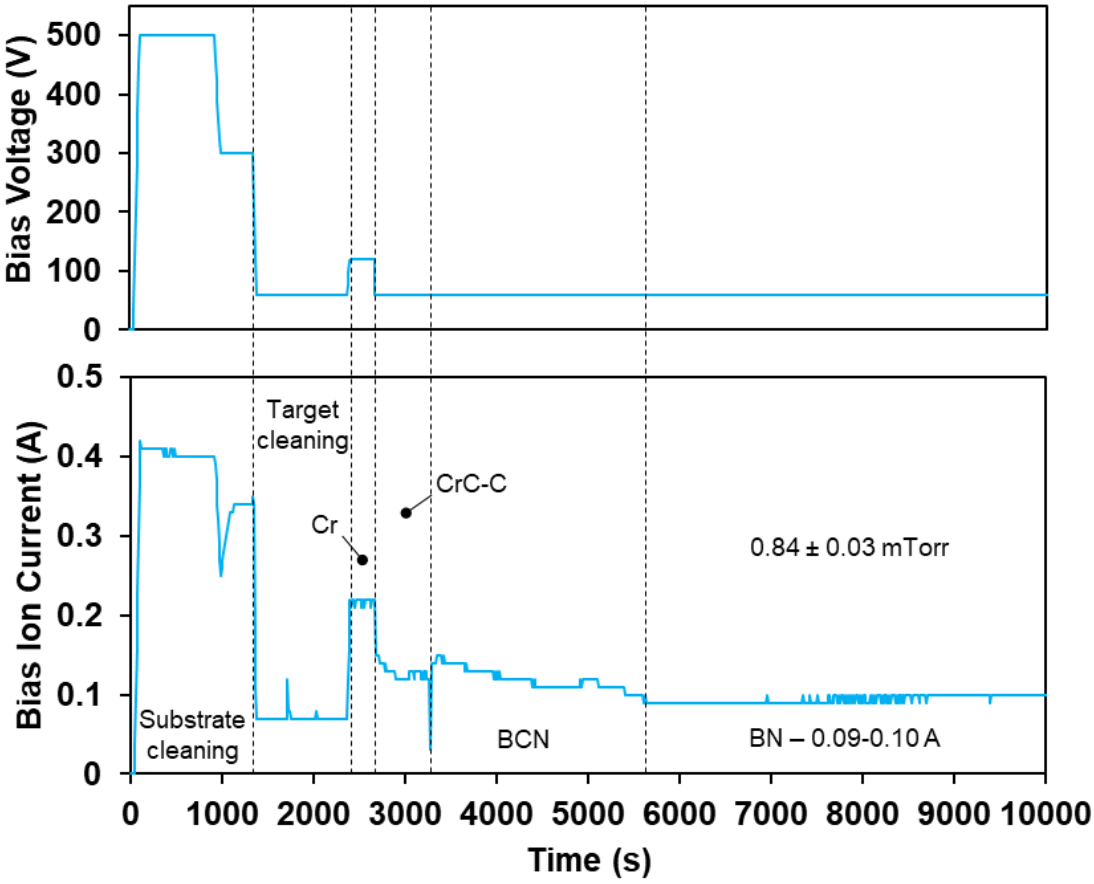

Figure 108 - Bias voltage and bias ion current for the BN multilayer deposited at 60 V bias (250 kHz/500 ns) for the top layer. The bias current for the final BN layer fluctuates 0.09-0.10 A. Note a short cleaning time was used for this recipe.

Figure 107 shows photos of a multilayer coating with 24 h full rotation BN layer when left for different durations in air. The samples were wrapped in aluminium foil and sealed in plastic bags. There is a clear change in colour and appearance of the fringes from the as coated image as the chamber was opened in a), to the following day in b) (photo was taken during FTIR measurements, shown in Figure 113, and c) taken after 20 days prior to SEM imaging.

Figure 109 shows SEM images and EDX maps for this coating deposited on 316L after 20 days in atmosphere. The coating consists of flakes upon a smooth surface, the backscattered images, b) and d), have high contrast between these flakes, indicating the flakes are composed of low mass elements. The maps, e)-h), provide

more information on the composition, showing that the smooth surface is composed of C and Cr, with small amounts of N. The flakes appear to consist of O and N. No boron was detected from these area scans. This data suggests that the flakes have separated at the C/BCN interface and have oxidised.

Figure 110 contains corresponding images and maps for this coating deposited on Si. The results are similar here, flaked coating on smooth coating. The morphology of the flakes is different to that of the 316L sample, here they have a more distinct and consistent structure suggesting that the coating has cracked and separated into ‘plates’ rather than peeling entirely from the preceding layer. Again, the backscattered images show high contrast between the flakes and surface, and the EDX indicates failure at the C/BCN interface.

When further examining a region of the Si sample, Figure 111, and in particular examining the spectra produced during EDX data gathering, it is clear that B is still present in the samples. Scans of Area 1. and at Point 3. of the flakes in Figure 111 b), see Figure 112, pick up 15 and 30 at% of B, and 4.3 and 2.2 at% N, respectively. Furthermore, the spectrum of the larger area scan a/b) has a shoulder on the C peak, indicating B content, though this is not distinct enough from the C peak for the analysis software to quantify. This therefore indicates that the BCN layer is intact, given the present but unquantified B content, and therefore the separation is at the BCN/BN interface.

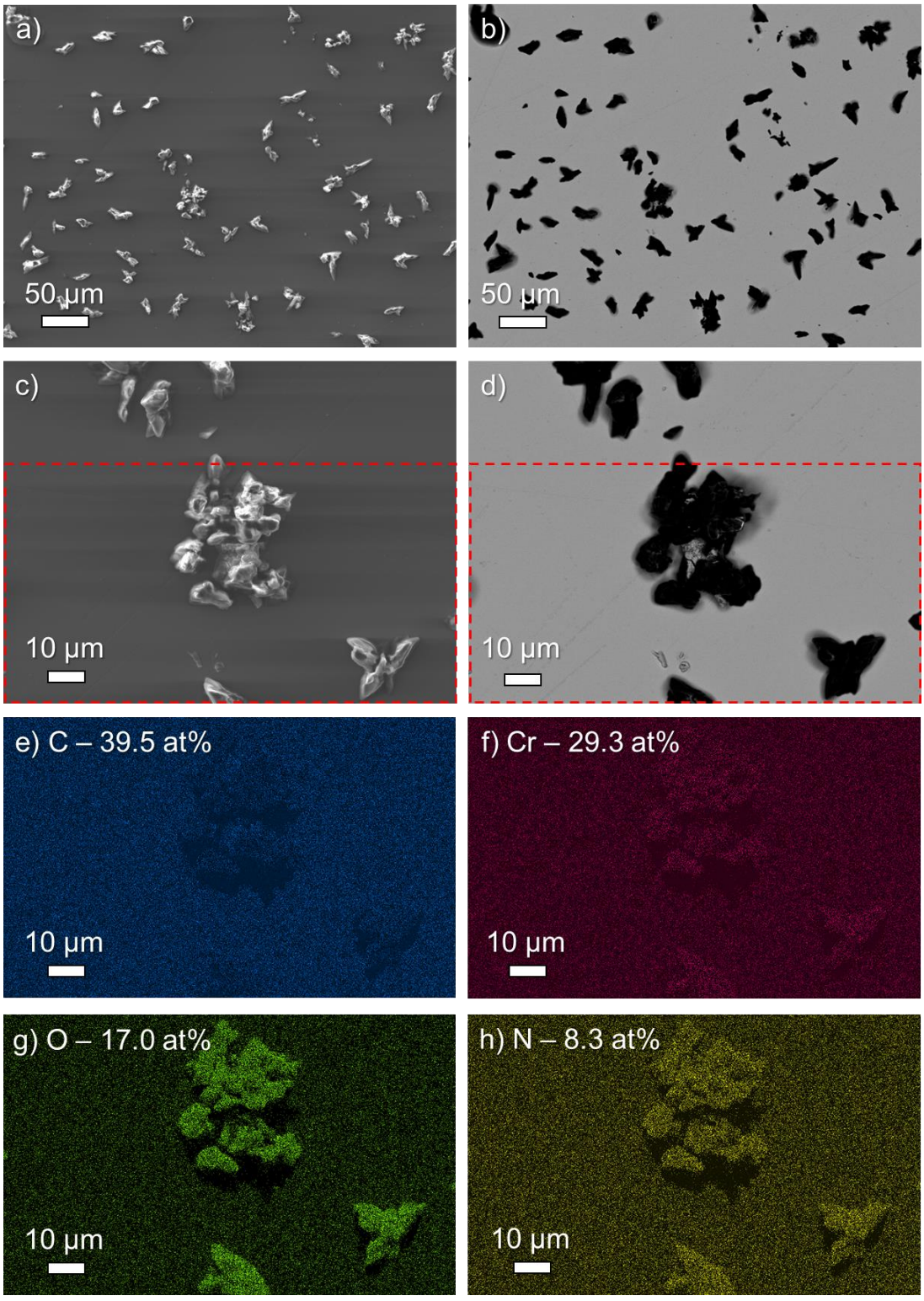

Figure 109 - SEM and EDX maps of polished steel with multilayer BN coating with 24 h top layer deposited at 60 V substrate bias, a) and b) Low magnification SEM images, SE and BSE respectively, c) and d) higher magnification images with red box indicating EDX mapping region shown in e) to h). EDX data summarised in Figure 112.

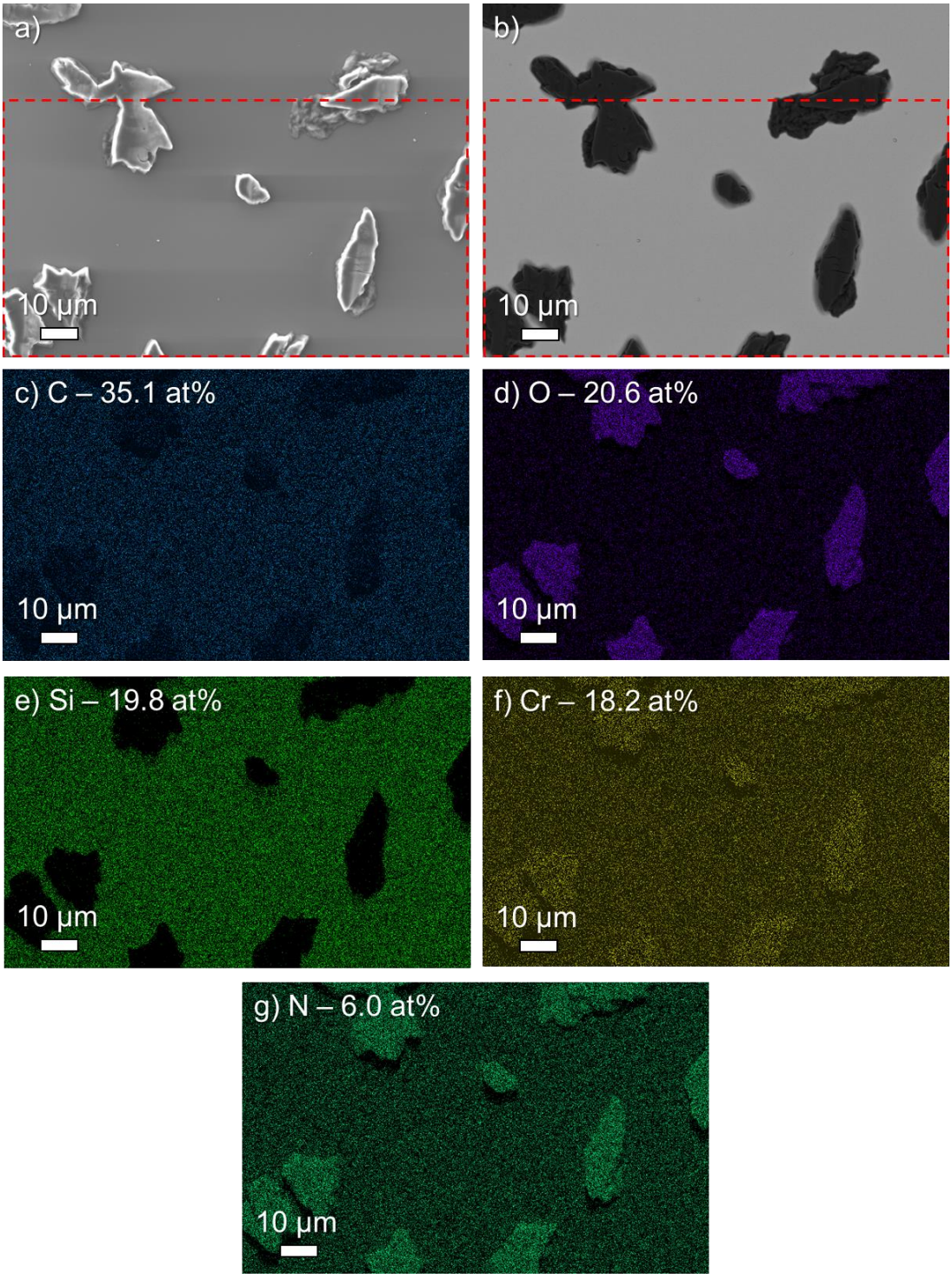

Figure 110 - SEM images and EDX maps of 24 h BN multilayer coating with 60 V bias using rotation, deposited on silicon wafer, images and data captured after 20 days in atmosphere a) Secondary electron image showing flaked coating, b) corresponding backscattered image c)-g) EDX elemental maps. EDX data summarised in Figure 112.

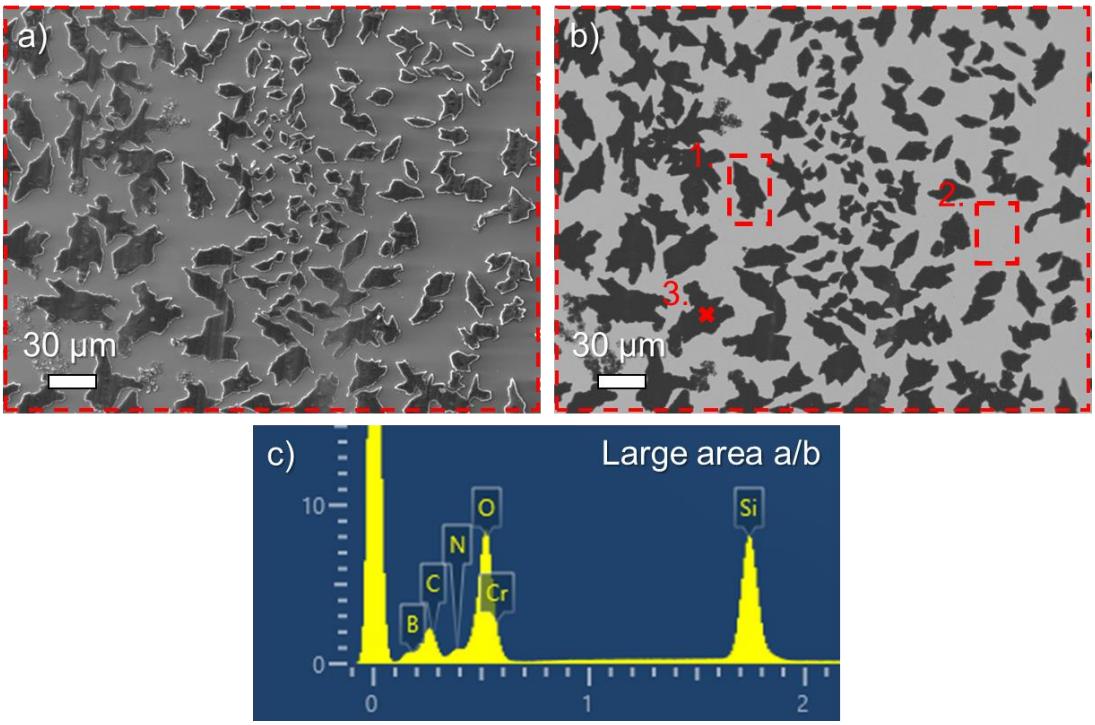

Figure 111 - Lower magnification images of second flaked region of 24 h 60 V BN multilayer coating using rotation on silicon substrate, a) secondary electron image b) backscattered electron image with numbered areas and point indicating where EDX data was gathered from, c) Snip of spectrum gathered from the large area in a/b, showing a shoulder indicating boron content, note that this was not quantified by the Aztec software. EDX data summarised in Figure 112.

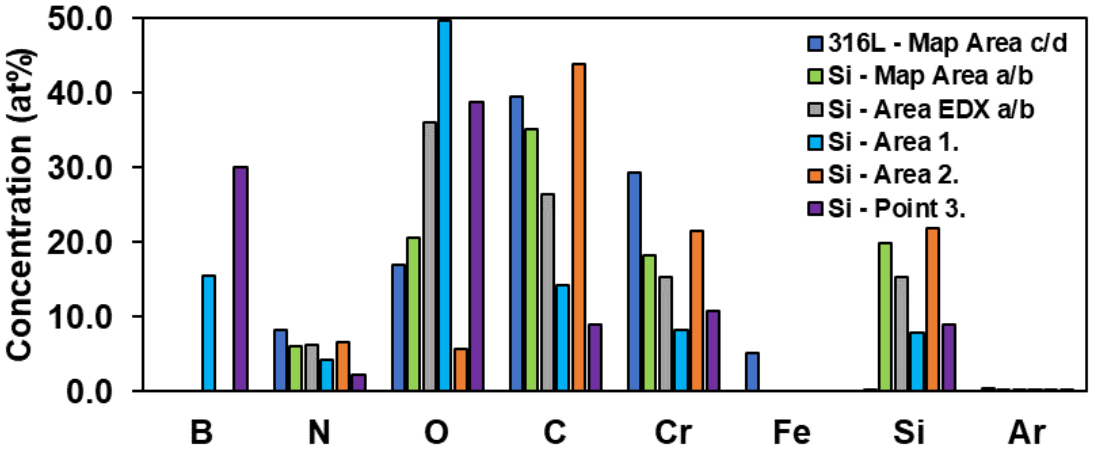

Figure 112 - Summary of EDX data gathered from the surface of multilayer BN coatings deposited at 60 V, with rotation, onto 316L and Si substrates, the areas scanned are highlighted in Figure 109, Figure 110, and Figure 111, Oxygen contamination is the dominant feature. Full data in Table 53.

Figure 113 contains the FTIR spectra of the coatings after 1 day stored in atmosphere. Initial observations of the spectra indicate that the signal collected from the Si sample is much more intense than the 316L signal, which can potentially be attributed to the surface morphology, the smooth wafer scatters less radiation than the imperfectly polished steel surface. The higher wavenumber region of the spectra contains 4 distinct components in the 3500-2900 cm^{-1} range, with the potential for more masked by the breadth. These can be attributed to the stretching of N—H bonds in B—NH_2/B_2—NH [160, 206, 211, 212], and O—H stretching in B—OH/B—OH_2 [206, 211-214]

In the lower wavenumber fingerprint region, the spectra are more complex, with many distinct components. The characteristic h-BN/t-BN bending mode is present at 783-779 cm^{-1}, and there is a broad region on both spectra, 1600-1200 cm^{-1}, with peaks near ~1348 cm^{-1}, corresponding to the h-BN/t-BN stretching and potential 2-phonon contributions in the 1600-1500 cm^{-1} range [208, 302]; or to residual moisture. There is a peak in the range 1093-1088 cm^{-1}, that matches with the characteristic transverse optical mode of c-BN in thin films. There are also components near 930 cm^{-1}, and in the range 1431-1406 cm^{-1}, that could be attributed to E-BN [160, 180, 181, 209], but also correspond to potential oxygen related components in BO_3 and BO_4 [206, 213, 215, 216].

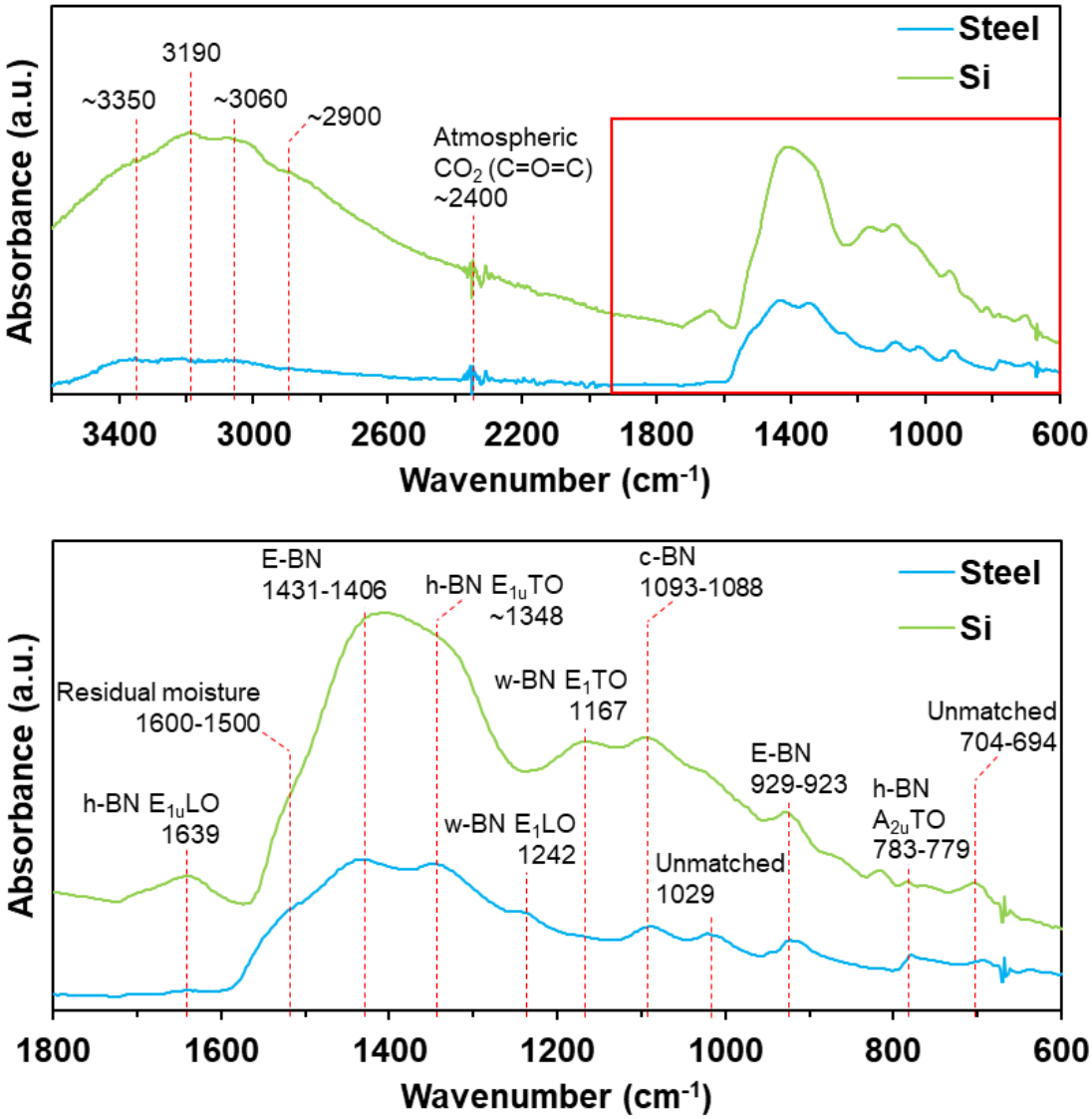

Figure 113 - FTIR measurements of the 24 h multilayer rotating BN top coating deposited with 60 V substrate bias during the final BN deposition, deposited on polished stainless steel and silicon wafer, data was gathered 1 day after the coating was deposited and samples were stored in atmosphere.

Given the difficulty in discerning the modes present in these spectra, fitting of the Si spectrum was carried out, see Figure 114. This brings unresolved peaks to light, confirming those previously assigned. However, the 4 split peaks in the 700-800 cm^{-1} range, 2 peaks in the 800-900 cm^{-1} range and 2 peaks 900-1000 cm^{-1} range have not been matched beyond components mentioned previously.

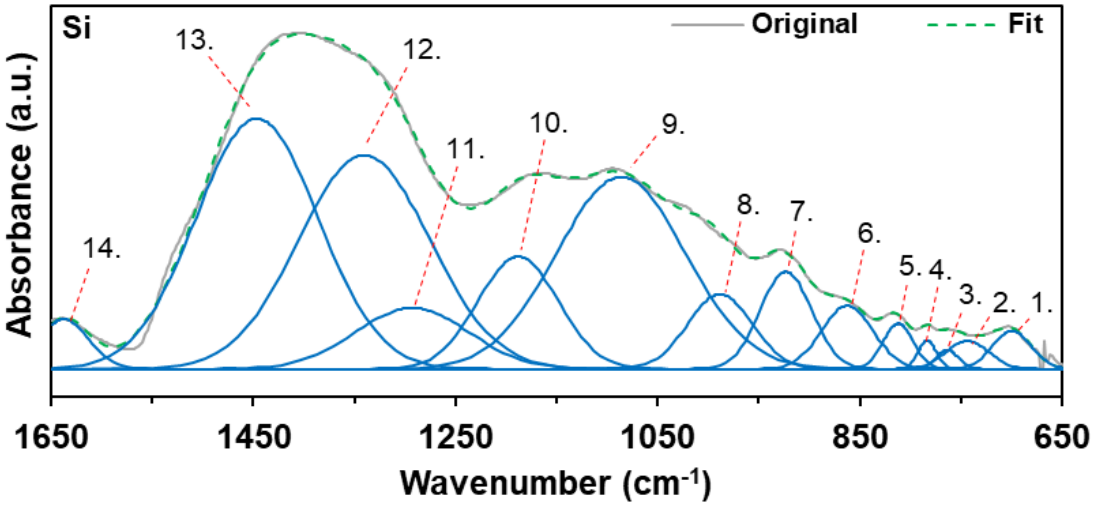

Figure 114 - Fitted FTIR spectrum from multilayer BN coating deposited with 60 V bias onto Si, all layers rotational. Origin Pro 8 software was used for Gaussian peak fitting. Peak wavenumbers are listed in Table 27.

Table 27 - Wavenumbers of peaks from the fitted spectrum of multilayer BN coating deposited at 60 V bias on Si.

Peak No	Wavenumber (cm^{-1}) (FWHM)	Peak No	Wavenumber (cm^{-1}) (FWHM)
1	700 (45)	8	988 (75)
2	743 (50)	9	1086 (150)
3	763 (25)	10	1188 (93)
4	783 (21)	11	1293 (132)
5	812 (35)	12	1340 (152)
6	862 (60)	13	1447 (142)
7	923 (60)	14	1637 (57)

6.1.2 Multilayer rotational BN – 100 V (Coating 9)

Figure 115 - a) Photo of a polished 316L substrate coated with multilayer BN deposited for 24 h at 100 V substrate bias fresh from the coating process and b) the same sample after 20 days in atmosphere, the coating appearance is unchanged by exposure relative to the 60 V coating in Figure 107.

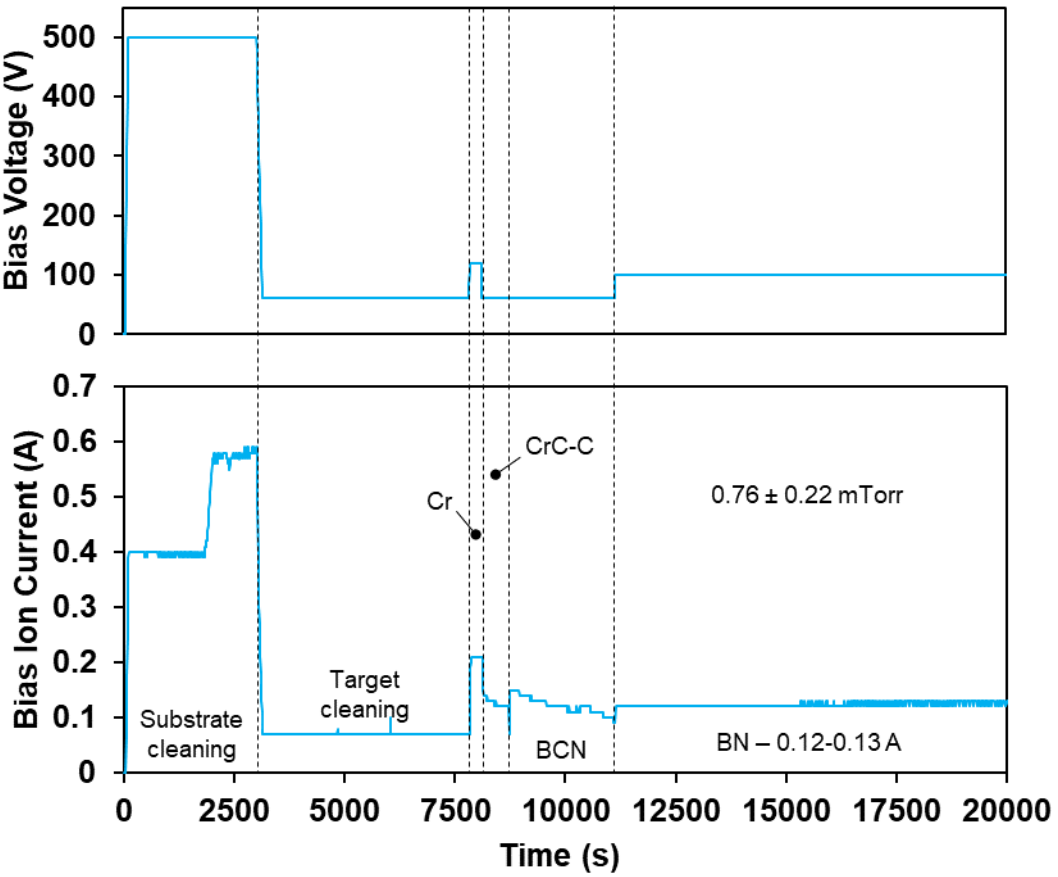

Figure 116 - Substrate bias voltage and bias ion current for the BN multilayer deposited at 100 V (250 kHz/500 ns) for the top layer. The ion current fluctuates 0.12-0.13 A for the top layer. Note that the large error in the pressure during the top layer deposition is because the pressure was close to the crossover point of the combination pirani-penning gauge.

Increasing the final layer bias voltage to 100 V changed the appearance of the coating, see Figure 115 a). The appearance is blue rather than the green of the 60 V coating (Coating 8), indicating a change in thickness from the change in wavelength of light refracted through the coating. The coating appears to have a semi-transparent layer partially covering the surface, not quite reaching the edge of the substrate.

The SEM imaging, Figure 117 a)-d), shows a relatively smooth, intact coating, with pinholes on both the 316L and Si substrates, a higher density on the former, with some surface scratches remaining from polishing. Given the same coating has been applied to both the substrates it is logical to suggest that the difference in pin hole density is due to substrate differences, either preparation or material. When examining the same 316L substrate after 20 days exposed to atmosphere, Figure 117 e)-f), the appearance (note that this is not the exact region imaged previously) is unchanged.

The EDX data for the coating is summarised in Figure 118, with the 1-day timepoint having a B and N content of 24.4 and 16.6 at % for the area on 316L in a), and 16.1 and 18.2 at% for the corresponding area on Si in c). This equates to B:N ratios of 1.47 and 0.89 respectively. The samples have comparable amounts of O and C, and the Si sample has lower Cr content, a difference of 4.2 at%. It is not clear as to why the stoichiometry of the same coating applied to 316L is nitrogen deficient, and the Si sample is conversely boron deficient. Lower boron content has been seen in previous degraded coatings, but only with a corresponding increase in O.

After 20 days the composition of the coating on 316L has altered slightly, the area in Figure 118 e) (note not the exact region captured previously) contains 27.8 and 15.1 at% of B and N respectively, a ratio of 1.84. The oxygen content is lower at 6.9 at %. This difference cannot be taken at face value as repeat measurements were not taken to calculate a standard error. It does however confirm that degradation of the coating

has not occurred, given that the O content has not increased indicating oxidation of the coating.

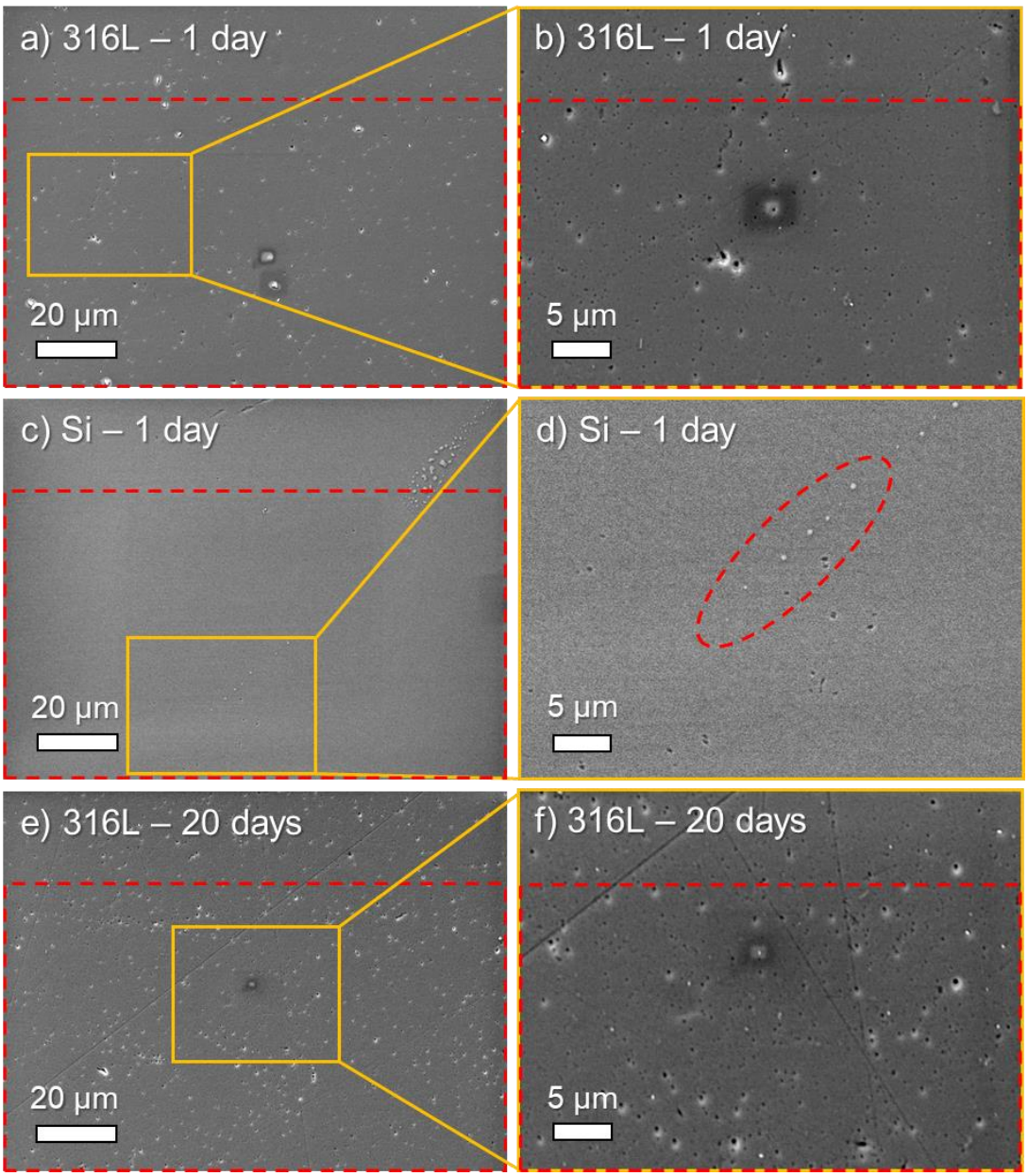

Figure 117 - Lower a), c), e) and higher b), d), f) magnification secondary electron imaging of the surface of 24 h, 100 V, BN multilayer coating showing the surface morphology and defects, a) and b) polished steel substrate after 1 day in atmosphere, c) and d) silicon substrate after 1 day, e) and f) polished steel substrate after 20 days. Red dashed lines indicate areas that EDX data was collected from, contained in Figure 118, orange solid lines indicate where higher magnification images were taken from.

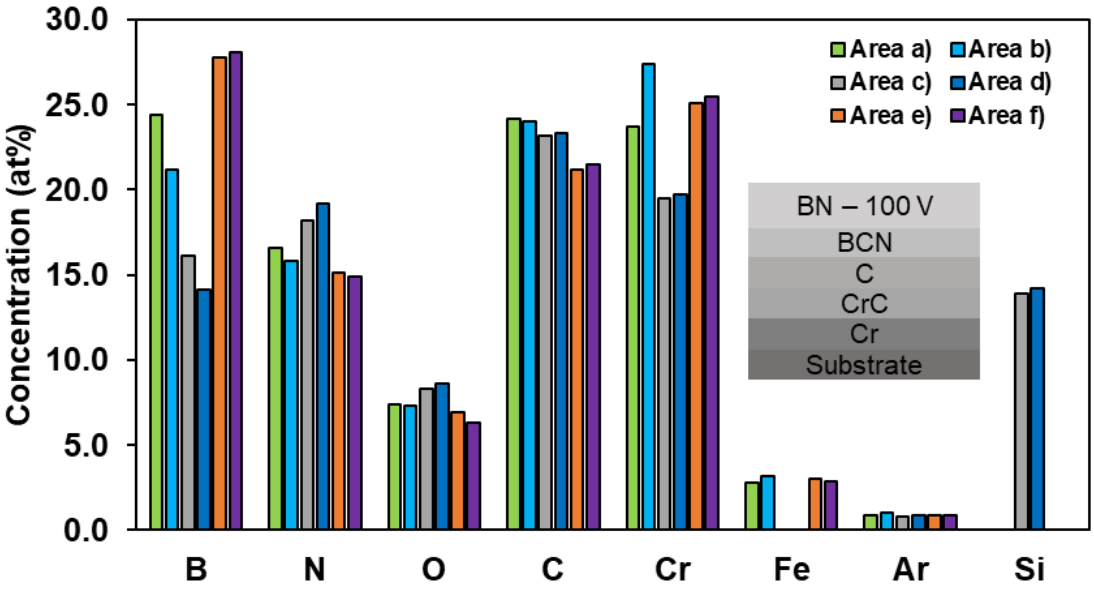

Figure 118 - Summary of EDX data gathered from surface areas of the multilayer BN coating deposited at 100 V bias, on 316L and silicon, Figure 117. B and N are present, with varying stoichiometry across the timepoints and substrate type, O contamination is present, though has not become prominent during time in atmosphere. Full data in Table 54.

The FTIR spectra of the coating on the 316L and Si substrates at two timepoints is presented in Figure 119. The spectra increase in intensity gradually in the 3900-1700 cm^{-1} range, with a single distinct peak in at ~3400 cm^{-1}, corresponding to NH/NH_2 stretching [160, 206]. Further indistinct peaks in this range could be attributed to OH stretching in B—OH [203, 213, 214], and atmospheric CO_2.

The fingerprint region 600-1800 cm^{-1} also rises gradually from a small peak at 783-767 cm^{-1}, up to an intense peak at 1554-1527 cm^{-1}. The former peak corresponds to the h-BN/t-BN bending mode, with the latter corresponding to E-BN [160, 181, 209]. The broad slope/shoulder in between can be attributed to multiple modes in BN or it's oxides, see Table 3.

Of particular note is the near identical spectra of the 316L sample and the Si sample despite the difference in surface composition from EDX. Furthermore, when rescanning the samples after 6 months, both show near identical curve shapes, with the 316L having a slightly higher intensity than previously. This difference can be

attributed to a better contact with the diamond crystal. The 6 month 316L sample also shows a shift in wavenumber for the E-BN peak, down to ~1527 cm^{-1}, potentially due to stress relaxation in the film.

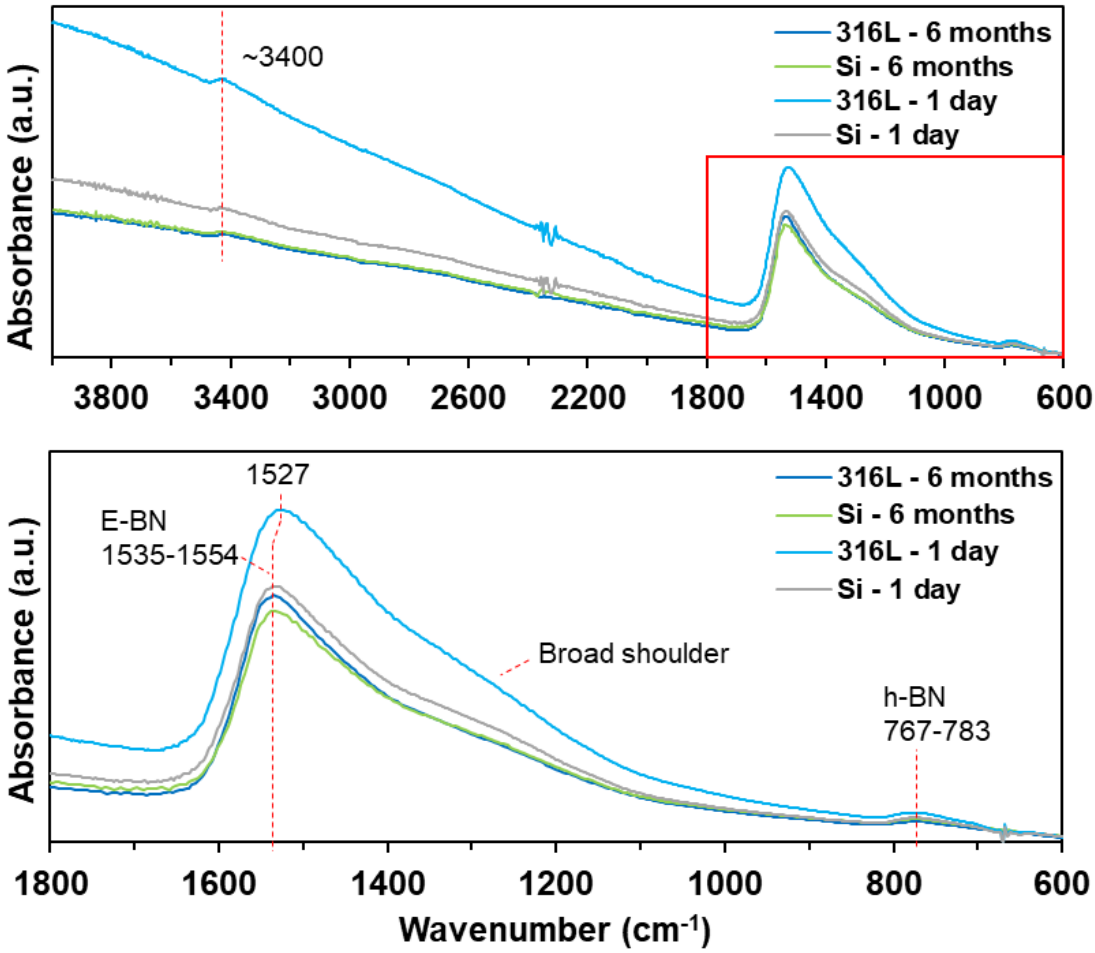

Figure 119 - FTIR spectra of the multilayer coating with BN top deposited at 100 V substrate bias, coatings applied to 2 substrates are shown, peaks indicating explosion and hexagonal phase are present, with broad shoulders inbetween. Data was gathered 1 day and 6 months after coating.

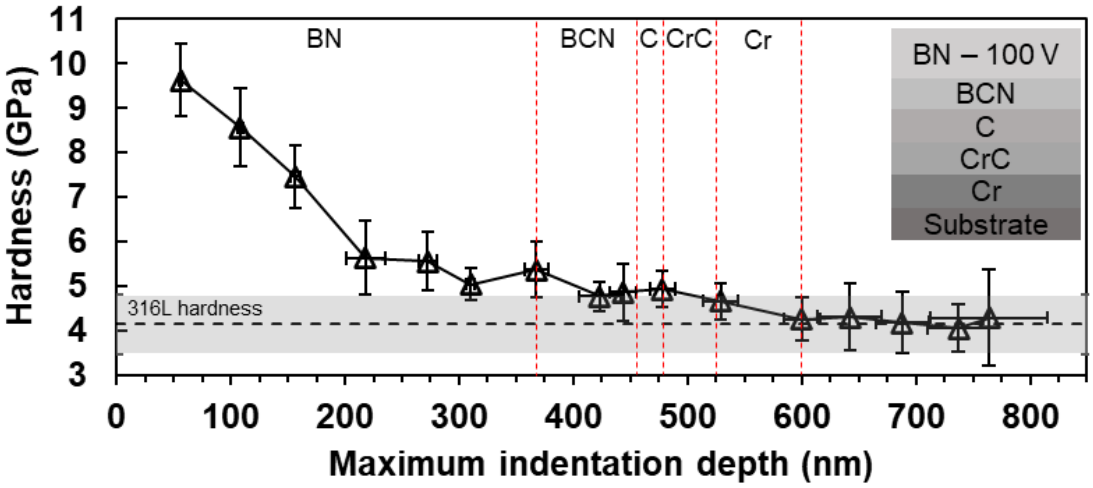

Figure 120 - Hardness versus indentation depth for the multilayer coating with full rotation BN top layer deposited for 24 h at 100 V substrate bias onto polished stainless steel, nominal indentation depths 50-800 nm in 50 nm intervals. Datapoints are the mean values with error bars applied according to the standard deviation of measurements. 9 indents were carried out at each depth. Dashed line indicates the mean hardness of 316L, with gray block showing standard deviation (13 indents). Approximate layer thicknesses are indicated.

Due to the stability of this film, nanoindentation was carried out on the surface of the coated 316L sample, at different indentation depths, see Figure 120. The hardness peaks at 9.63 ± 0.81 GPa in the near surface region (~50 nm), steadily decreasing until 5.63 ± 0.83 GPa near 200 nm. The hardness then decreases at a lower rate than the former drop, reaching a hardness comparable to the 316L substrate (4.15 ± 0.67 GPa) in the 500-600 nm depth range.

Approximate layer thicknesses are indicated on Figure 120, allowing a better understanding of what material is probed at each depth, the interlayer thicknesses are calculated from the deposition rates in Figure 71. Based on the approximate deposition rate for BN at the varied 180-150 V bias setpoint, of 12.8 ± 1.8 nm/h, the top layer thickness of this coating is at least 307 ± 43 nm, given the lower 100 V bias. Comparing this to the hardness, it appears that there is graduated hardness in the BN layer, suggesting that there is thickness dependent structure formation.

6.1.3 Multilayer rotational BN – varied 180-150 V (Coating 10)

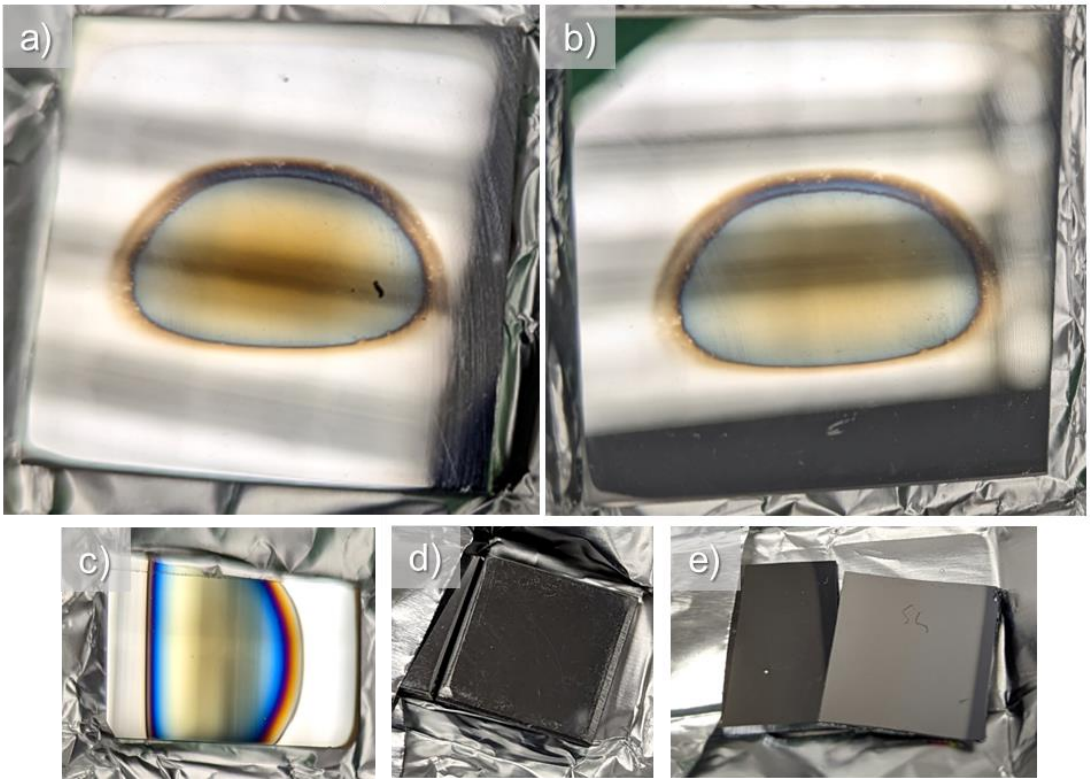

Figure 121 - Photos of substrates coated with the multilayer adhesion coating and BN top layer deposited with 180-150V bias voltage, a) 30x30 mm 316L fresh from the coating chamber, b) 30x30 mm 316L 34 days after, prior to SEM, c) ~ 25x30mm glass fresh from coating, d) 10x10 mm 316L fresh from coating, e) 10x10 mm Si wafer fresh from coating.

This coating was deposited as Coating 9 and 10 were (in rotation) but combining this with the previously trialled 180-150 V varied bias. Due to the reduced deposition rate the duration of the 180 V step was increased to 6 h.

The photos in Figure 121 indicate the difference that this change has made to the appearance and uniformity of the coating, from a) the coating does not reach the edge of the substrate (25 x 25 mm 316L), lacking uniformity in both horizontal and vertical directions. The glass fragment (25 x 15 mm, oriented portrait for coating) in c) shows some uniformity in one direction, and the 316L and Si fragments (both 10 x 10 mm) have metallic appearances. Figure 121 b) shows the large 316L substrate after 34 days, prior to SEM imaging, the centre ‘amber’ region is duller in the second image.

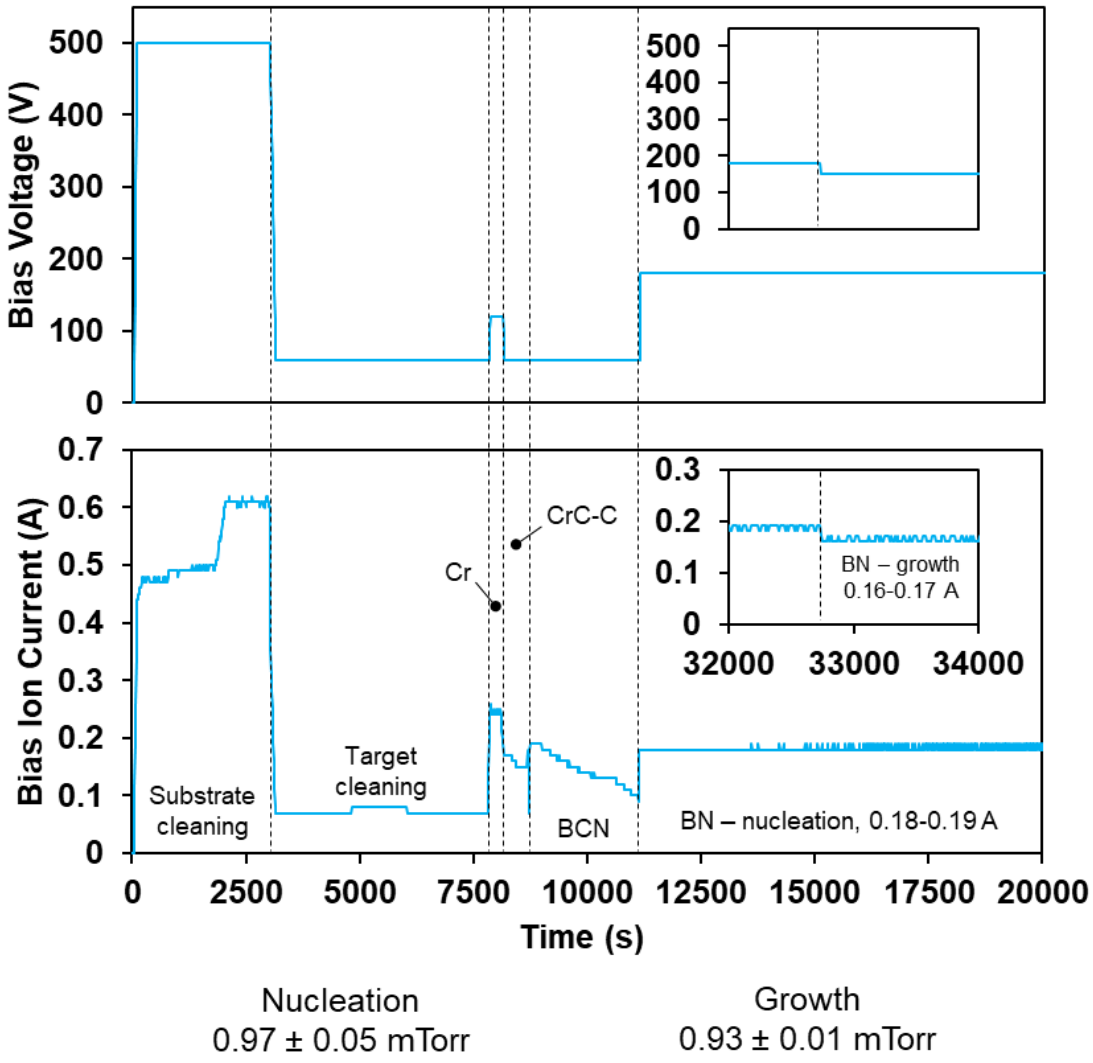

Figure 122 - Substrate bias voltage and ion current for the BN multilayer deposited at varied 180-150 V (250 kHz/500 ns). The ion current for the BN nucleation step fluctuates 0.18-0.19 A, and for the growth 0.16-0.17 A.

The reduced uniformity in these samples is due to resputtering of the film by the substrate bombardment of ions, this was seen in the statically deposited samples (Coatings 5, 6, and 7) see Figure 88, but is evident to a greater degree here. This particular pattern, where the centre of the sample remains coated whilst the edge of the coating recedes from the edge of the substrate will be discussed later. Whilst the small 316L and Si samples were not analysed further, due to the appearance it is assumed that they have been resputtered to the Cr layer.

The SEM images in Figure 123 show the coating on 316L, having degraded over time (34 days), the surface has scattered deposits, and is otherwise smooth and uniform. From the EDX gathered from Image a) and Area 2. in c) (see Figure 124), the surface is predominantly C and Cr, 44.7 ± 0.1 and 45.0 ± 0.3 at%, and 34.0 ± 0.1 and 32.5 ± 0.2 at% respectively. There are lower quantities of N at 10.7 and 10.9 at%, with no B detected.

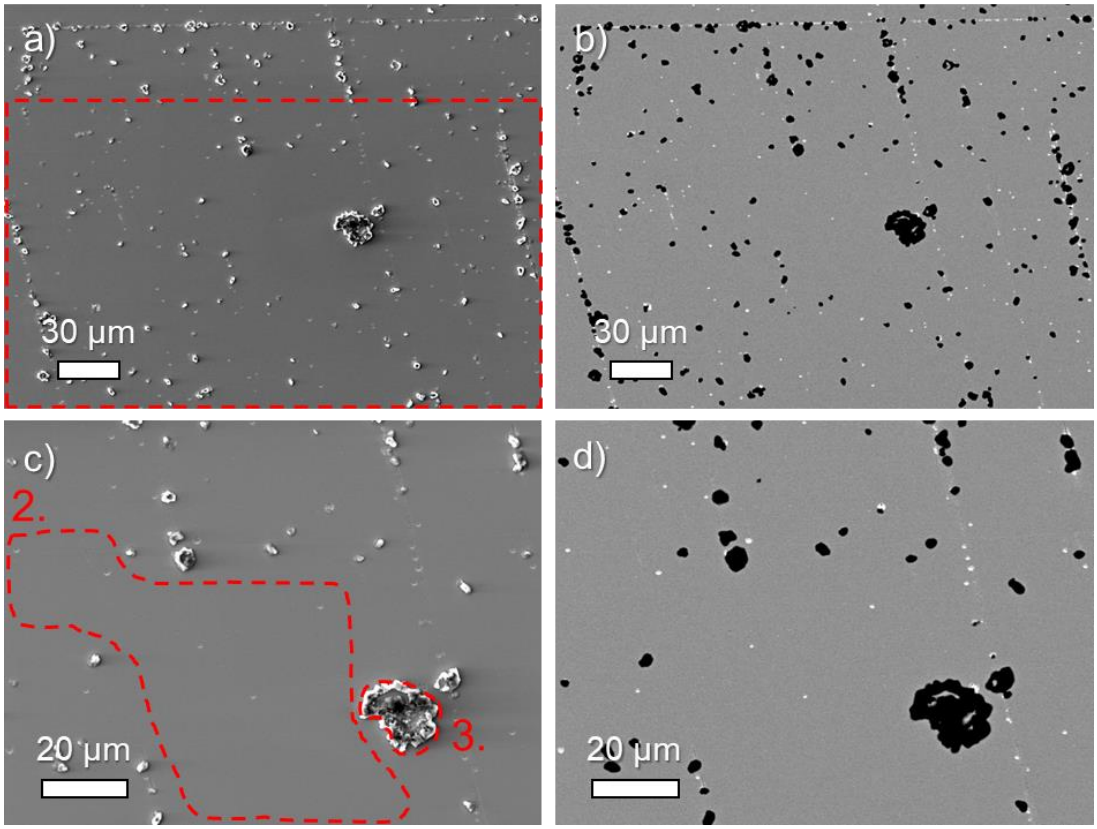

Figure 123 - Secondary a) and c), and backscattered b) and d) images of the surface of a multilayer coating with BN top layer deposited with varied 180-150 V substrate bias, after 34 days in atmosphere, areas highlighted in red are regions EDX data was gathered from, data shown in Figure 124.

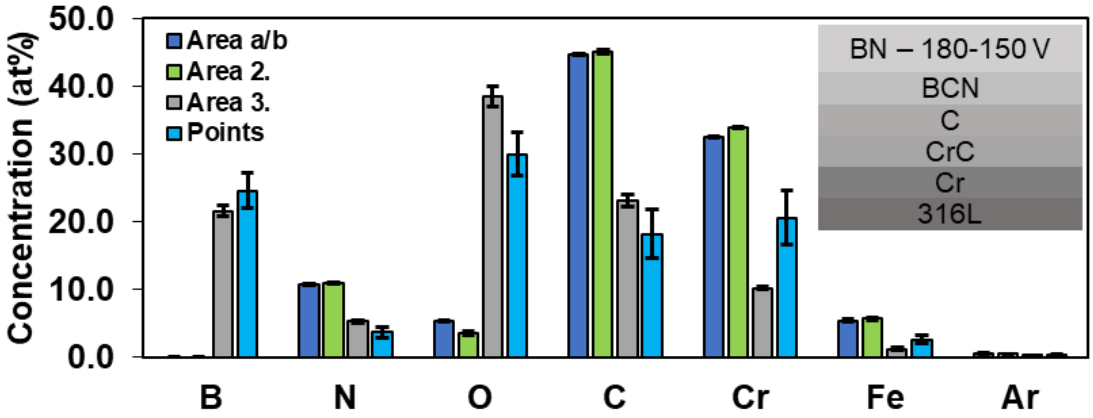

Figure 124 - Composition of regions highlighted in Figure 123, steel sample with multilayer BN at 180-150 V, after 34 days, gathered from EDX in at%, columns are mean with error bars equaling standard deviation (n = 3 for areas), 'Points' refers to point EDX data gathered from bright surface defects in Figure 123 e) (n = 10). Full data in Table 55.

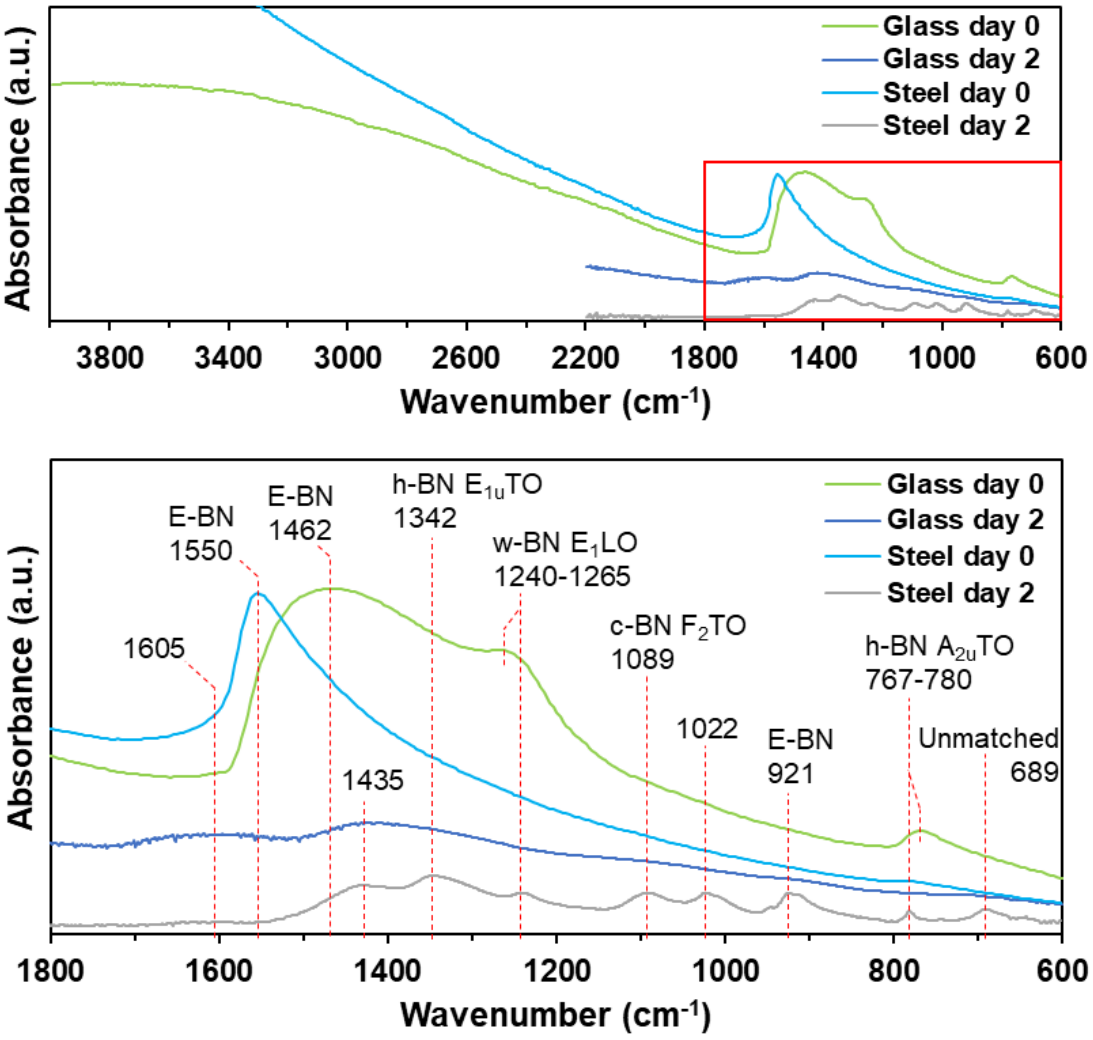

Figure 125 - FTIR spectra for the BN multilayer coating deposited with varied 180-150 V bias, spectra shown are for steel and glass substrates fresh from the chamber and rescanned after 2 days, peaks indicate mixed phases and change in intensity and peak definition over time.

Area 3. and the Points (n = 10) contain predominantly B, 21.5 ± 0.8 and 24.6 ± 2.5 at%, and O, 38.4 ± 1.5 and 30.0 ± 3.2 at% respectively. This indicates that the coating has failed at the BCN/BN interface, with the BN flaking and oxidising. The lack of B in the larger area scans is not definitive as B has been detected in low quantities from point scans in the BCN layer previously.

The FTIR data for Coating 10 is presented in Figure 125, note that due to the metallic surface of the Si sample, this was not scanned, and the glass was used instead. The samples fresh out of the coating chamber have intense broad humps extending > 2200 cm^{-1}, attributed to N—H, O—H and B—H stretching, as previously.

The 316L sample (note this was scanned at the centre of the coating), has 2 peaks centred at ~780 and 1550 cm^{-1}, the latter being much more intense. These are attributed to h-BN bending and E-BN [160] or B—O bending [215], as previously. The glass sample is distinct from the 316L in that it contains a more intense peak at 767 cm^{-1}, shifted down in wavenumber, and is also broader in the 1600-1100 cm^{-1} region, with 2 distinct peaks, ~1462 and ~1265 cm^{-1}, instead of 1. These peaks can be identified as being produced by E-BN [160, 181, 209], and w-BN [179, 200], however there is likely to be contributions from the h-BN/t-BN stretching mode (1400-1300 cm^{-1}) overlapping.

After 2 days in atmosphere, the sample spectra reduced in intensity, likely due to surface material loss and scattering, with both curve shapes changing, the glass spectrum has fewer peaks than before, and the 316L spectrum has more. These additional peaks are at 689, 921, 1022, 1089, 1240, 1342 and 1435 cm^{-1}. The peak at 689 is uncertain, potentially attributed to B—O—B bond bending [215]. The peaks at 1022 and 1089 cm^{-1} are both candidates for c-BN vibration, but given the values collated in Table 3, the higher of the two is more likely attributed to this mode, with the 1022 cm^{-1} peak potentially due to B—O stretching in BO_4 [215]. The peak at 1240 cm^{-1} corresponds to the E_1LO mode of w-BN [179, 200], but could also be due to B—

O stretching in BO_3 [215]. The peak at 1342 cm^{-1} can be attributed to the h-BN stretching mode, though the peak is shifted to the lower end of the range possible for this mode. Finally, the peak at 1435 cm^{-1} could be assigned to E-BN, though this is also lower than the peaks reported in this region for this structure, see Table 3.

6.1.4 Multilayer rotational BN – varied 180-150 V with increased gas flows (Coating 11)

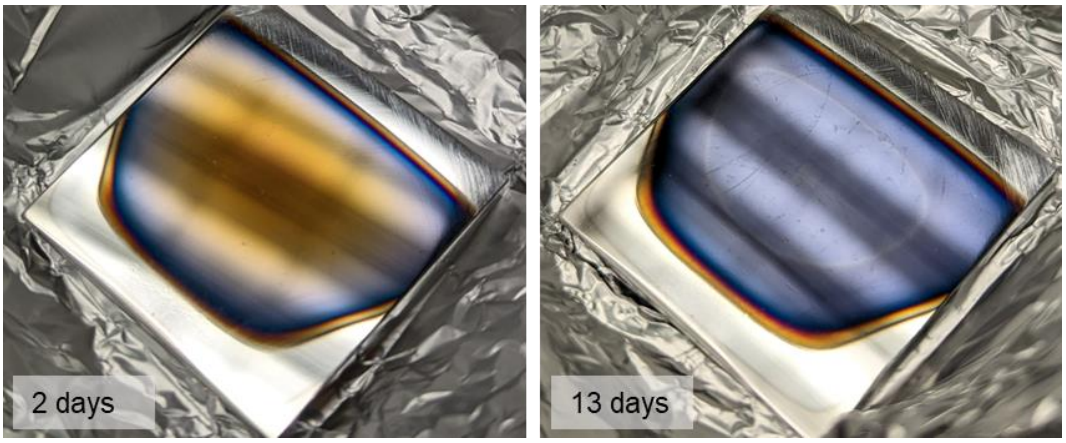

Figure 126 - Photos of the multilayer BN coating deposited on 316L (25x25 mm) at 180-150 V with increased gas flows, at two timepoints in atmosphere, 2 days and 13 days, note the change in colour of the centre portion of the coating.

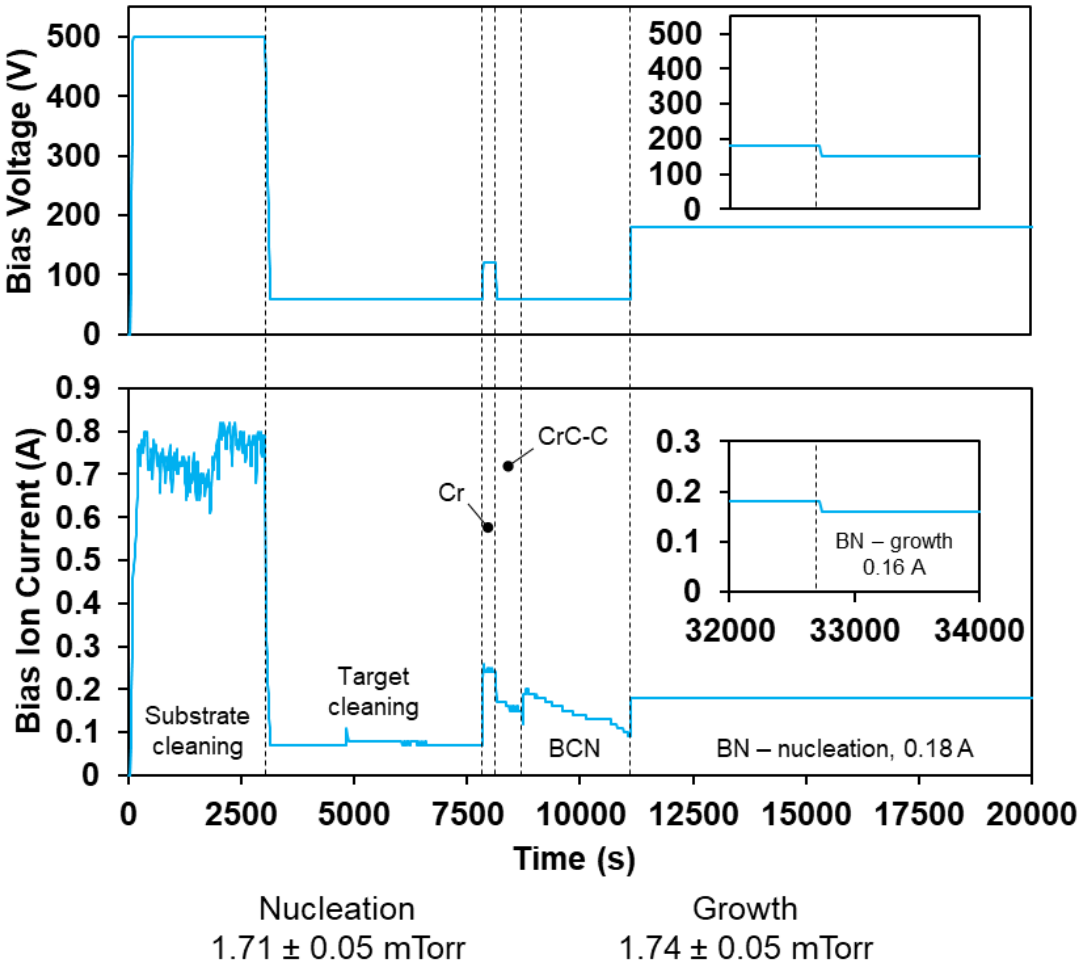

Figure 127 - Bias voltage and Bias Ion Current for the multilayer BN coating deposited at 180-150 V (250 kHz/500 ns), with increased gas flow, the current drops from 0.18 to 0.16 A transferring from the nucleation to the growth stages.

Due to the excessive resputtering of Coating 10, the gas flows were modified to attempt to increase the intensity of the plasma near the target, increasing sputtering, and therefore increasing deposition rate. This was balanced against the calculated mean free paths of elements involved, see Table 1. Furthermore, the ratio of the gases was modified due to the apparent nitrogen deficit in Coatings 8 and 9, intending to increase the N content in the coating [303]. The gas flow Ar:N_2, was modified from 15:5 to 30:25 sccm nominal.

As can be observed from Figure 126 the surface coverage is improved by this change in parameters, with increased horizontal uniformity, however the top layer is still offset from the edge of the substrate, and still degraded over time in atmosphere whilst stored waiting for SEM time.

Figure 128 contains images of the coating, with EDX identifying the content of the flake and remaining coating, Figure 129. This is as previously, where the coating has failed at the BCN/BN interface, with oxygen content increasing in the flakes. From Area 3, with B ~ 33.7 % and O ~62.3 %, a rough ratio can be calculated as $B_2O_{3.7}$, analogous to B_2O_3 as some of the oxygen will be bonded to other elements. Note that the spectra for Area a/b and Area 2. contain a shoulder indicating B content, but as previously this is not quantified with area scans.

Figure 130 contains higher magnification images of the surface surrounding the flake imaged in Figure 128. There are lines near to the edge, on the preceding BCN layer, which appear to be shallow cracks ~60 nm wide. Given that the flake has remained adhered to the surface (though this adhesion cannot be quantified) this gives an indication to the mechanism of delamination of the coating. For the cracks to form there must be a certain degree of mismatch, thermal, lattice parameter or other, which has been accommodated by the fracture of the previous layer [27].

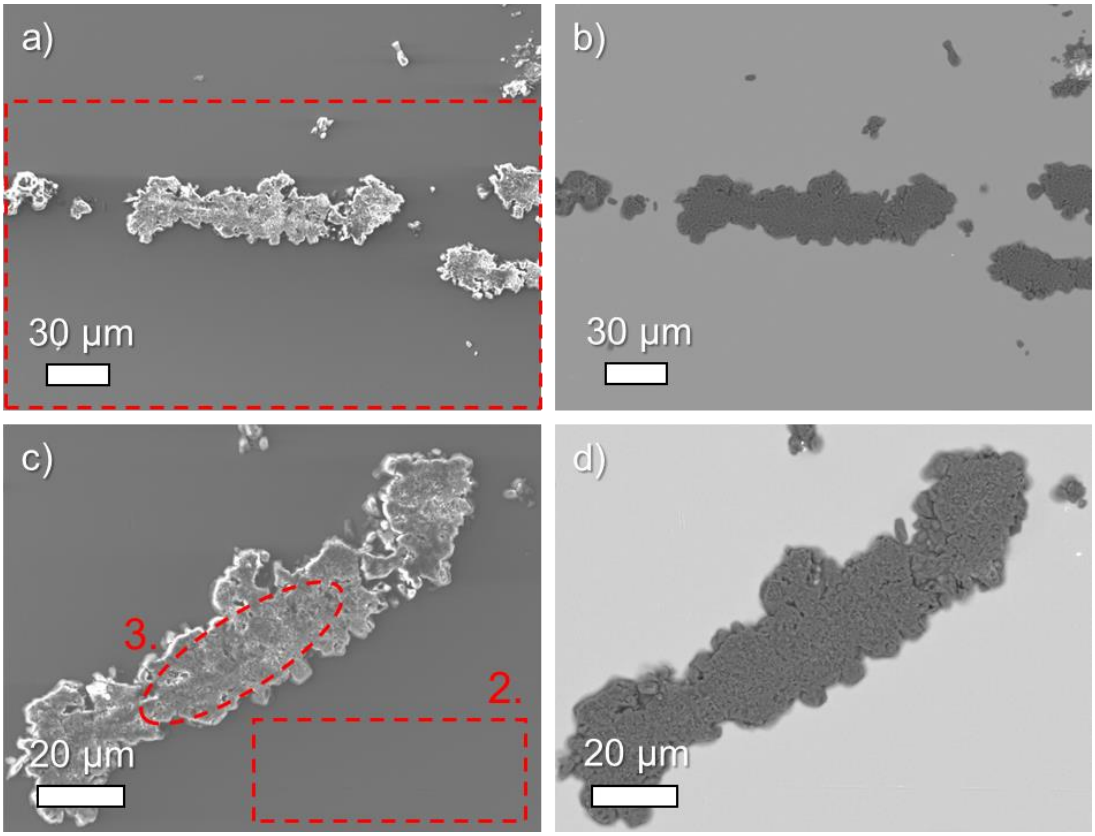

Figure 128 - SEM imaging a) and c), secondary, b) and d), backscattered, at different magnifications of the multilayer BN coating deposited at 180-150 V with increased gas flows, on polished 316L, after 13 days in atmosphere, the surface consists of flakes. Red areas indicate regions where EDX data was gathered from, summarised in Figure 129.

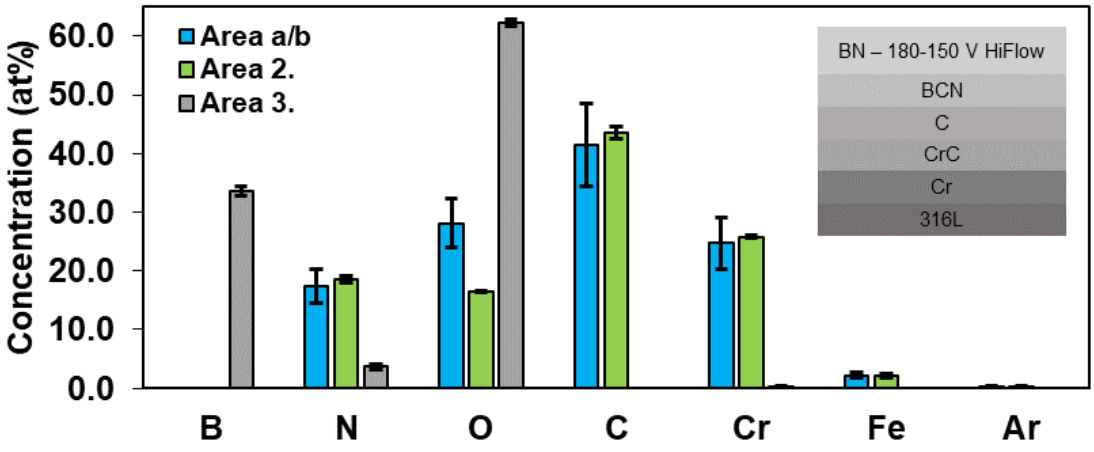

Figure 129 - Summarised EDX data from the surface of 316L coated with multilayer BN, deposited at 180-150 V with increased gas flow after 13 days in atmosphere, images in Figure 128. The coating is heavily contaminated with O, with B only present in the flakes. Full data in Table 56.

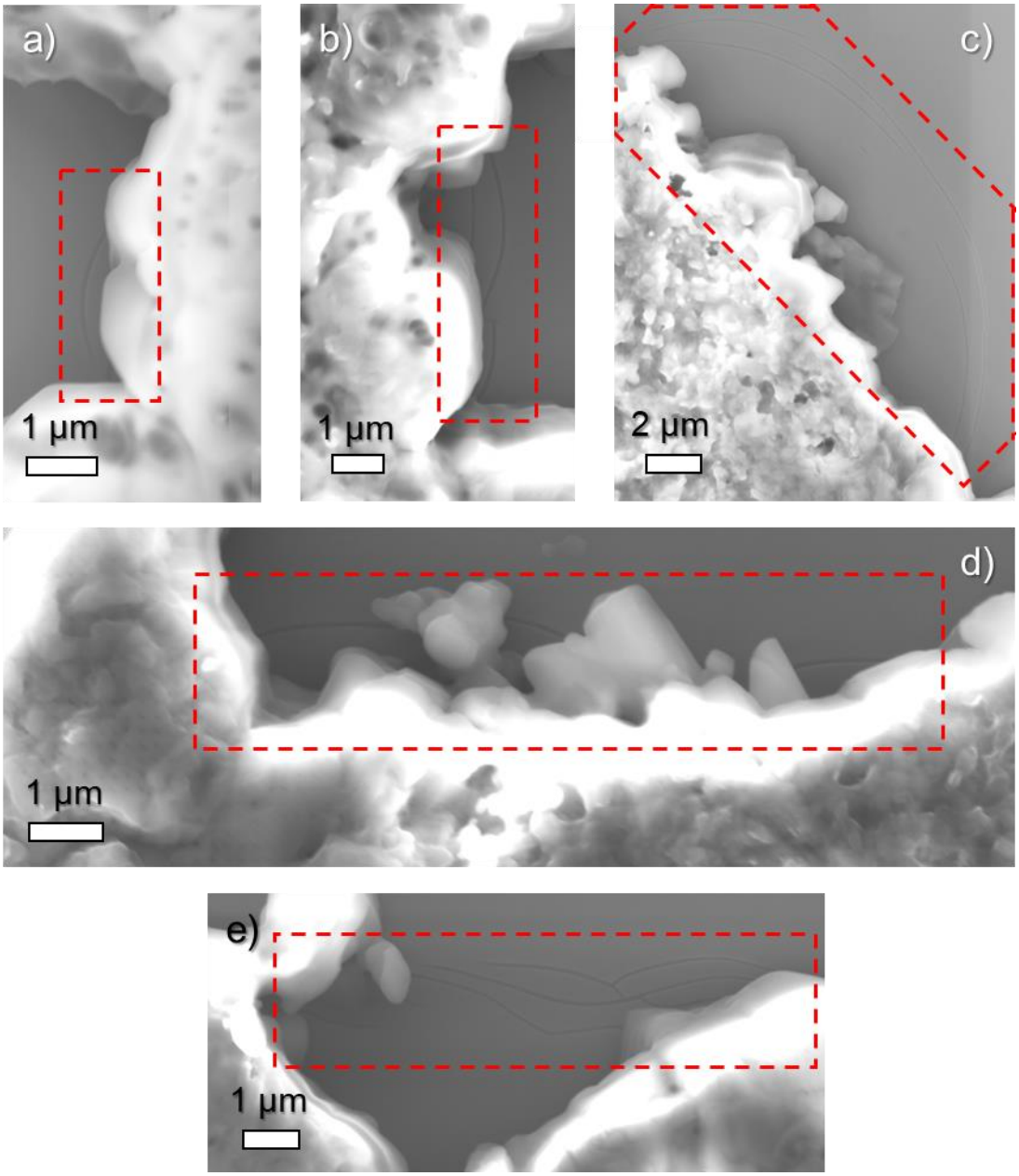

Figure 130 - High magnification secondary images of the edges of the coating flake shown in Figure 128 c), adhered to the multilayer, showing cracks surrounding the flake suggesting destructive stress relief.

The top layer has been under tension, with the BCN layer under compression. As this is an isolated case, the majority of the surface is bare, it can be suggested that it is energetically favourable for the top layer to delaminate rather than fracture the previous layer and remain adhered.

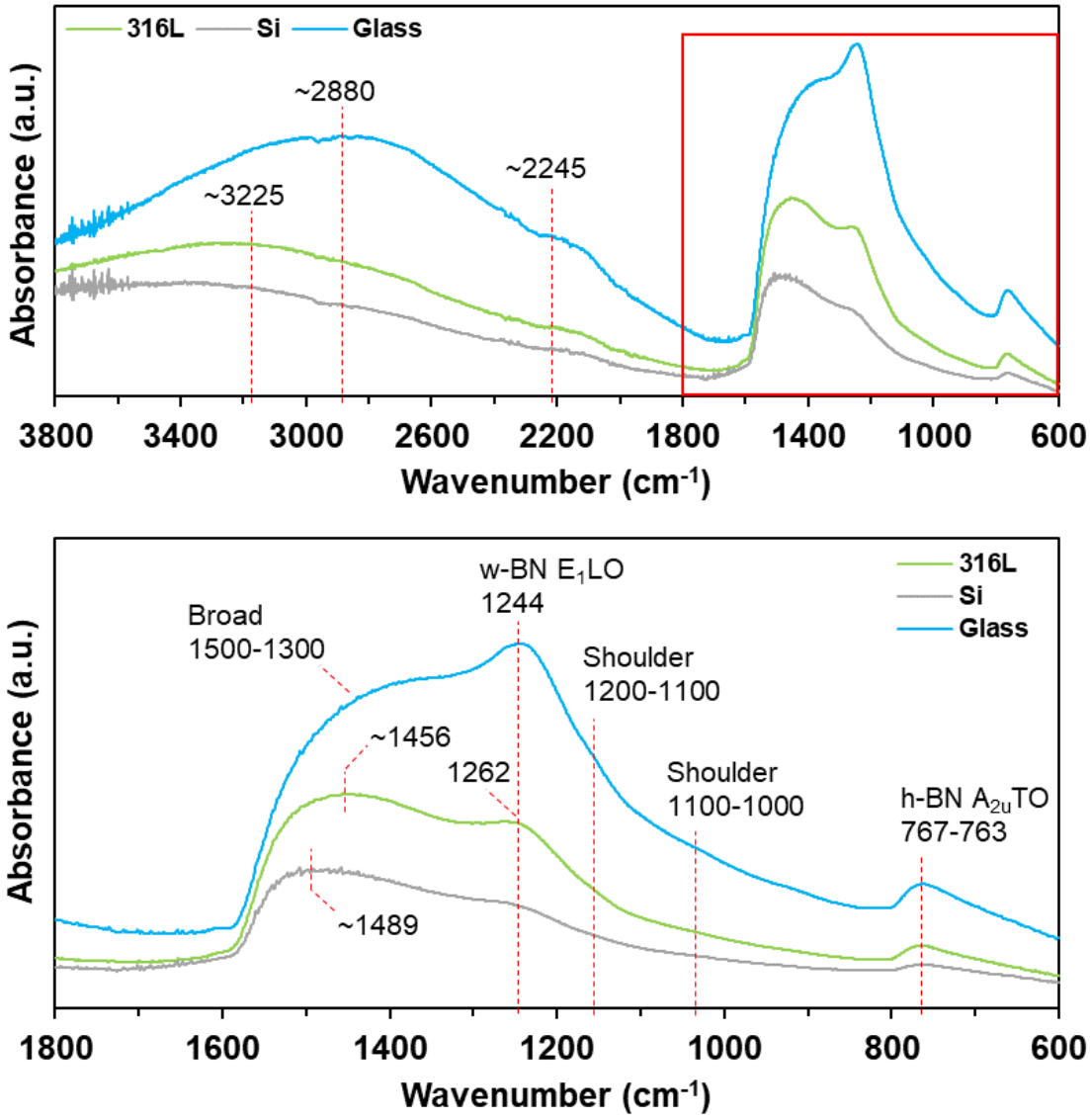

Figure 131 - FTIR spectra for Coating 11, multilayer BN deposited with varied 180-150 V and increased gas flows. Spectra show a distinct peak attributed to wurtzite phase BN, with a mixture of other phases. Scans were taken after 2 days in atmosphere.

The FTIR spectra for the coatings on different substrates are displayed in Figure 131. The general overview is similar to previous coatings, with changes in mode dominance. In the higher wavenumber range (2000 <) there are very broad regions with 3 identifiable peaks across the 316L, Si and glass substrates. The peak at ~2245 cm^{-1}, present in all spectra has not been definitively matched, the value is too low for the characteristic atmospheric CO_2 bonding, expected at ~2400 cm^{-1}, and too high for the fingerprint region of BN compounds. There has been an intermolecular E-BN

mode reported in literature for the 2500-2000 cm^{-1} range, however this is a vague identification [181]. It is likely that multiple components make up this peak. The peak at 2880 cm^{-1} in the glass spectrum is similarly unmatched, not consistent with any modes in Table 3. The final broad peak in the 316L and Si spectra can be related to B—OH stretching.

The 'fingerprint region', 1800-600 cm^{-1} is difficult to discern, with a maximum of 3 peaks, and multiple shoulders. The peak at 767-763 cm^{-1} corresponding to h-BN/t-BN bending is present in all 3 spectra, with the glass at the lower wavenumber end of the range. The mode corresponding to h-BN/t-BN stretching is not distinct, however, it is likely contributing to the hump in the 1600-1100 cm^{-1} region. The defined peaks on the glass (1244 cm^{-1}), and 316L (1262 cm^{-1}), are attributed to the longitudinal w-BN mode [179, 200]. The peaks on 316L (1456 cm^{-1}) and Si (1489 cm^{-1}) have a separation of 33 cm^{-1}, however considering the reported values in Table 3, they are in the range of an E-BN mode [160, 181, 209, 210]. As with previous coatings, and as these scans were taken after 2 days in atmosphere, there is likely to be components of oxygen or hydrogen bonding in the fingerprint region as well.

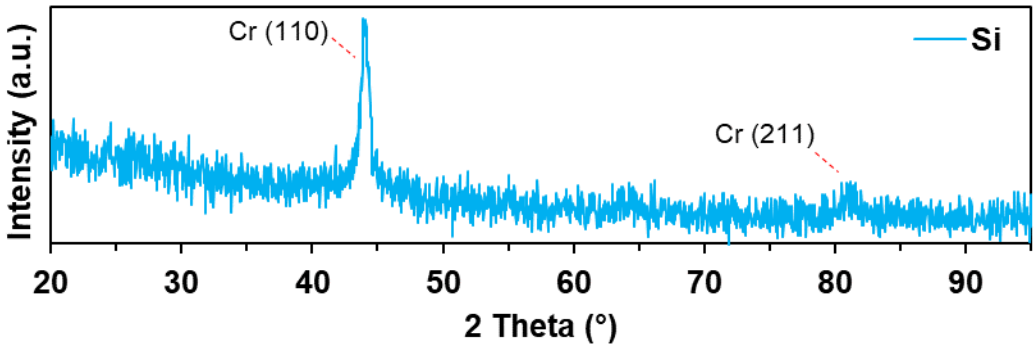

Figure 132 - Glancing angle XRD pattern of Coating 11 deposited with varied 180-150 V bias and increased gas flow on Si, no clear crystalline peaks apart from the Cr (110) and (211) peaks are observed.

6.1.5 Multilayer rotational BN – varied 180-150 V with increased gas flows and pulse modification (Coating 12)

For this coating the pulsing parameters of the pulsed DC substrate bias were changed. This was in an attempt to reduce the number of ions bombarding the samples, whilst maintaining the same voltage and same ion energy, increasing the deposition rate. The parameters, frequency (kHz) and pulse width (ns), were chosen to be widely different to the parameters used previously, see Figure 133, at 50 kHz and 1500 ns (92.5 % on duty cycle) compared to 250 kHz and 500 ns (87.5 % on duty cycle) [38].

Comparing the logged current between this coating (Coating 12, Figure 135) and the previous (Coating 11, Figure 127), identical coatings other than this change in pulsing parameters, it is apparent that this change has reduced the ion current from 0.18 to 0.06 A in the nucleation stage, and 0.16 to ~0.055 A in the growth stage.

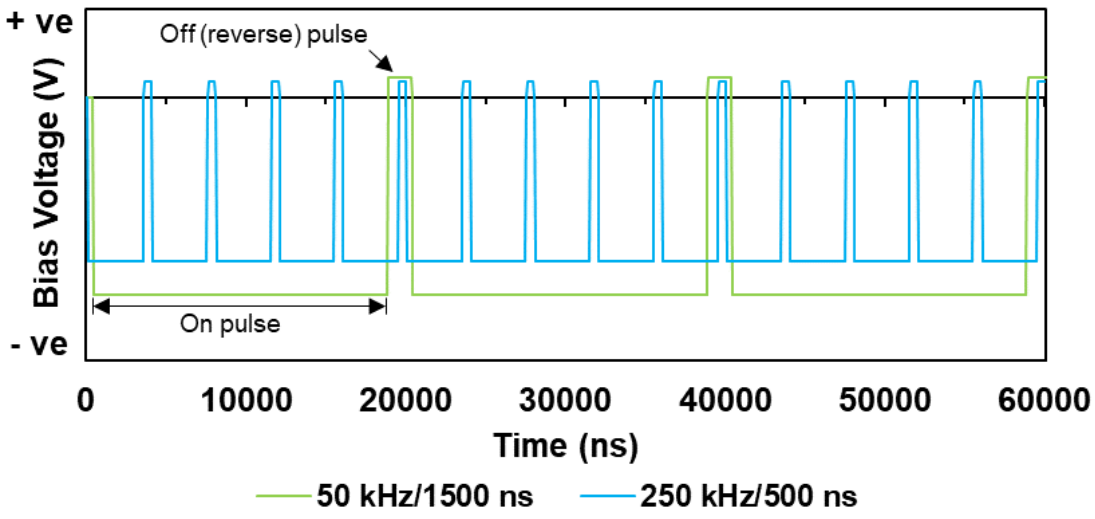

Figure 133 - Schematic demonstrating the differences between the 2 pulsing parameters used for this modified coating, one with a lower frequency and longer on pulses, and the other with a higher frequency and shorter on times. The magnitude of off pulses is generally 10% of the on setpoint. These are 'ideal', in reality the waveforms are not square. Note that whilst the schematic shows different maximum and minimum voltages, this is just to increase clarity when comparing the waveforms, the coatings produced with different pulse parameters maintained the same voltages.

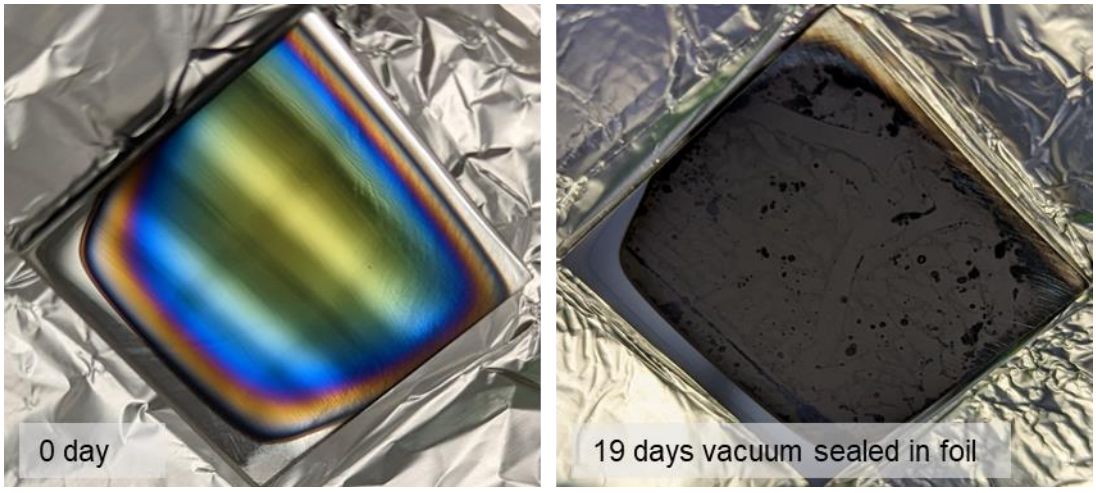

Figure 134 - Photos of the BN multilayer deposited with increased gas flow and pulse modification at 180-150V (50 kHz/1500 ns) on 316L, on removal from chamber, and after 19 days stored wrapped in foil under vacuum. A clear change of appearance and moisture attack has occurred.

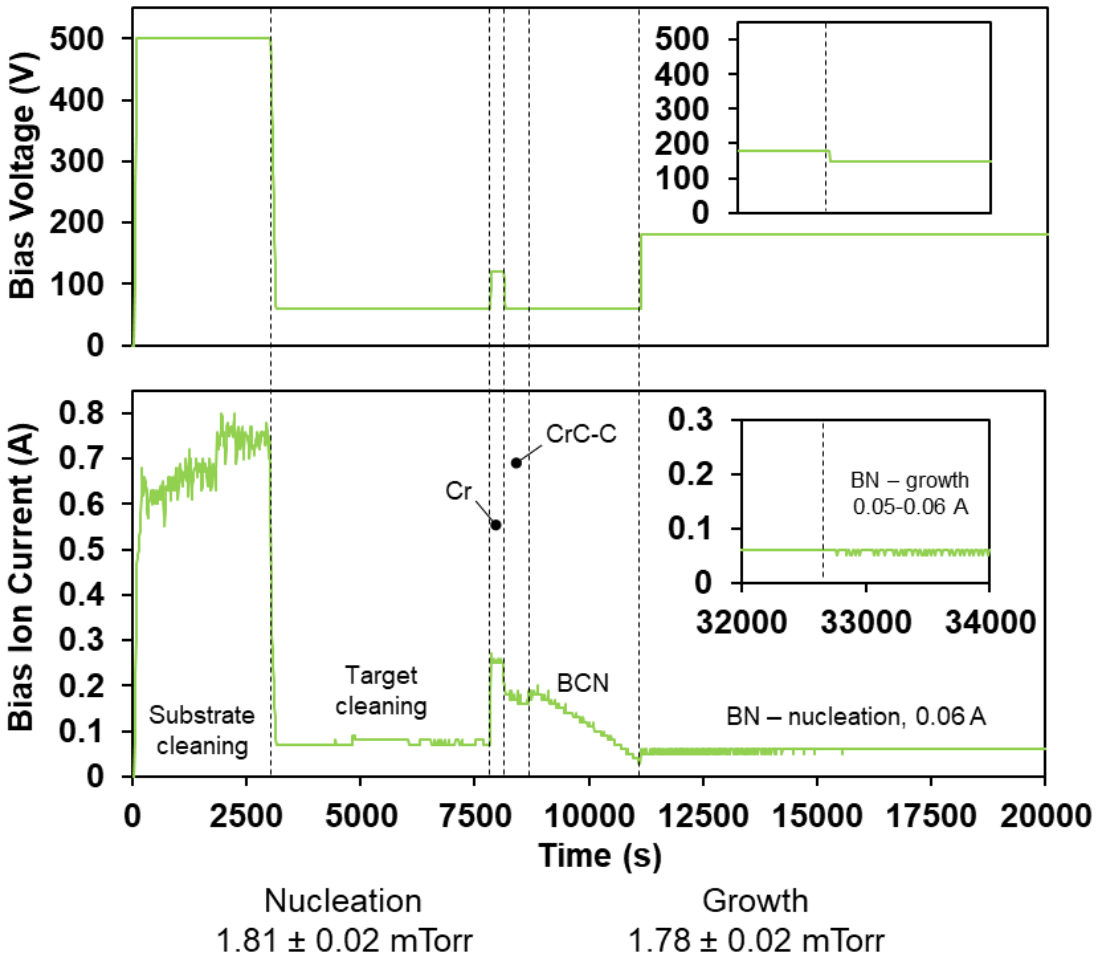

Figure 135 - Bias voltage and Bias Ion current logged for the duration of the multilayer BN coating deposited with increased gas flow and modified pulse parameters (50 kHz/1500 ns), inset is the time at which the bias voltage changed from 180V to 150V, showing a slight instability forming in the ion current.

Images of the 316L substrate (25 x 25 mm) at two timepoints, 0 and 19 days, are shown in Figure 134. At this point in the experiment series access to vacuum storage became available, and so the samples were wrapped in multiple layers of foil and held under low vacuum in the 10^{-2} to 3 x 10^{-3} Torr range. This was intended to 'hold' the samples at their just coated state, however due to the tight wrapping of the foil moisture that had adsorbed onto the surface was sealed in rather than desorbing and being pumped away as intended. As such, the samples once again degraded with time, all samples subsequent to this coating were covered loosely with foil under vacuum to allow contaminants to be pumped away.

Prior to storage, immediately after removal from the coating chamber, samples were imaged (~30 min exposure to atmosphere), see Figure 136 and Figure 138. The former, containing images of the 316L sample, shows a relatively smooth coating, uniform across the imaged region, with superficial scratches remaining from surface preparation, surface particles from sample handling, and scattered pinholes visible at the higher magnification. The EDX data, Figure 137, consistent for both the area scans, and Point 2. confirms that the surface particles are handling contamination, with Ca content and increased O Content. For Area 3. the B content is 33.2 ± 0.5 and N is 24.1 ± 0.4 at %, corresponding to a 1.38 B/N ratio, nitrogen deficient. The coating is still contaminated with O, despite the short interval exposed to atmosphere, at 18 ± 0.2 at% for both area scans.

The Si sample (Figure 138/Figure 139) is similar, a smooth uniform coating, with no pinholes seen in the imaged area. The B/N ratio is 1.34, with an oxygen content of 18.4 ± 0.2 at%, this closely agrees with the 316L sample. An attempt was made to measure the thickness of the coating on this sample using the ball crater method, see Figure 140. This was unsuccessful because the top layer of the coating peeled away from the concentric wear pattern, rather than wearing a ring that could be measured.

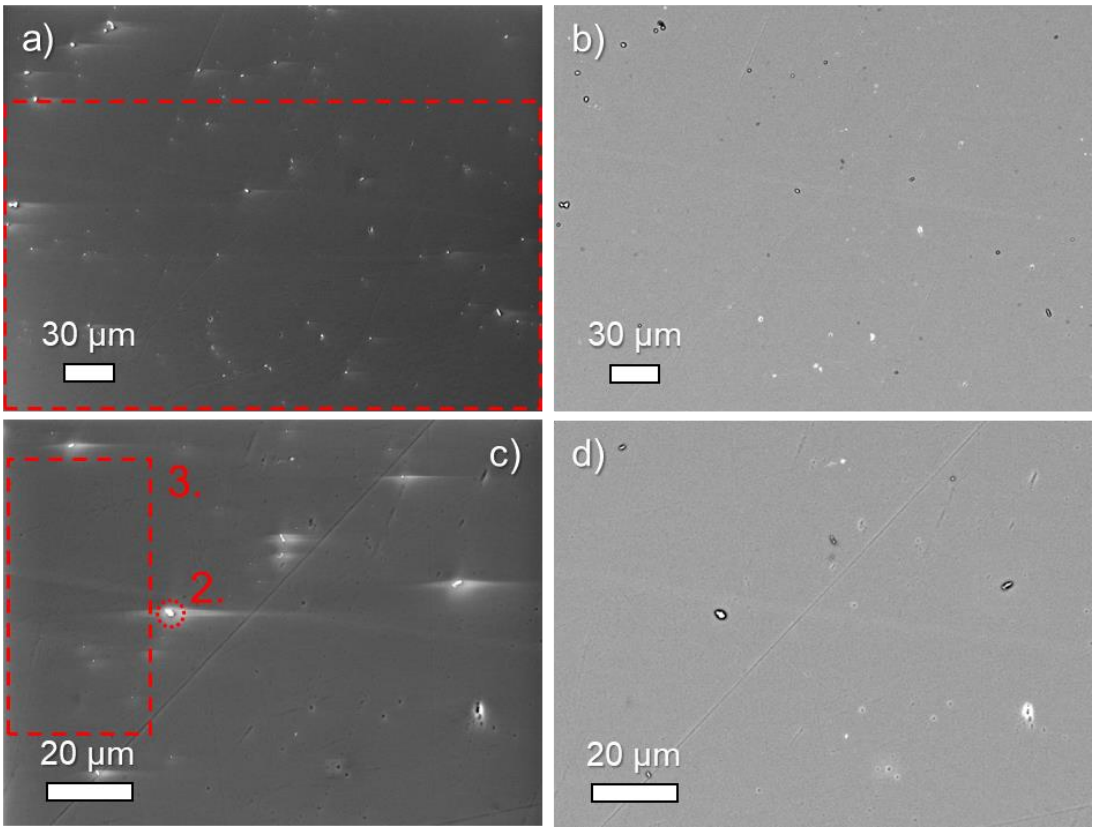

Figure 136 - Secondary a) and c) and backscattered b) and d) imaging of the surface of BN multilayer coating deposited on 316L substrate at two magnifications. The top layer was deposited at a varied 180-150V bias, with increased gas flows, and modified pulse parameters. Regions highlighted in red indicate EDX data acquisition, summarised in Figure 137.

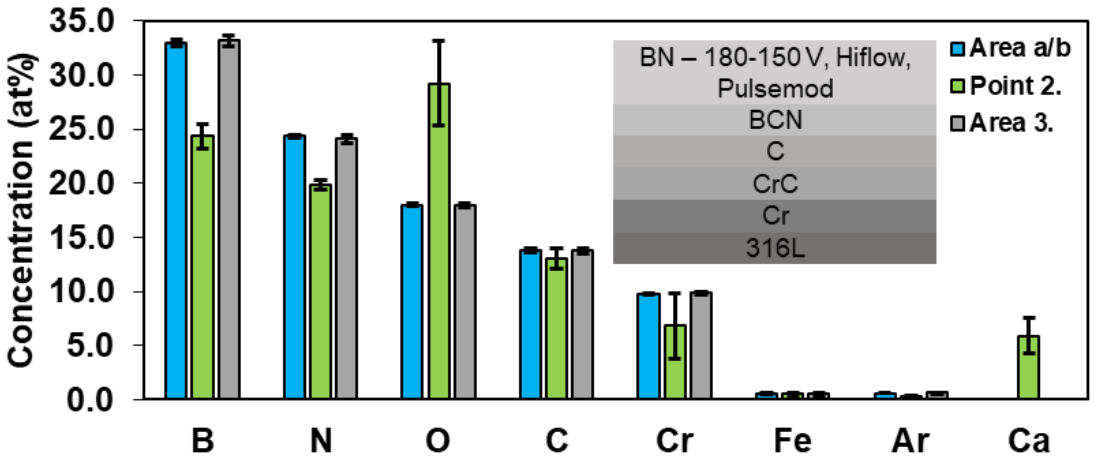

Figure 137 - Summary of EDX data gathered from the regions of BN multilayer shown in Figure 136, the surface B content is higher than the N content, the larger area scan is consistant with the higher magnification area, with defects likely to be from handling contamination. Full data in Table 57.

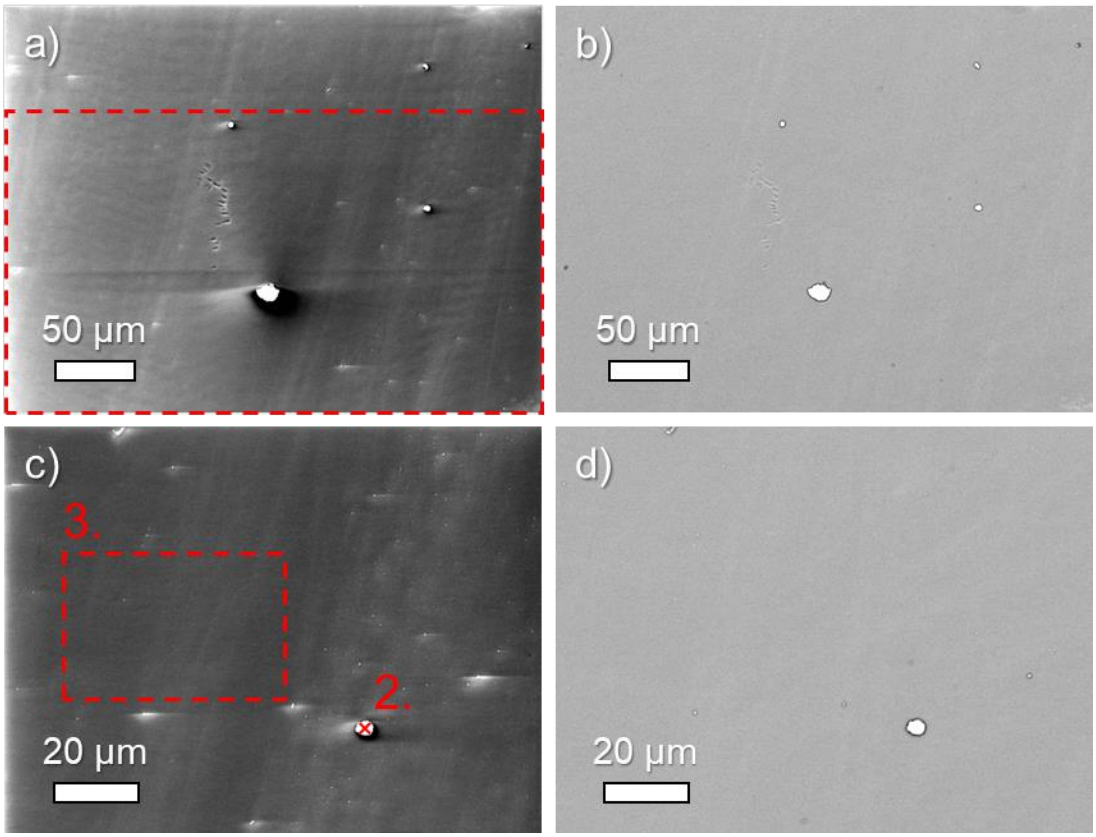

Figure 138 - Secondary a) and c), backscattered b) and d), imaging at two magnifications, of the BN multilayer coating deposited on Si, with a varied bias 180-150V and high gas flow, with pulse parameter modification. Red areas indicate where EDX data in Figure 139 was gathered from.

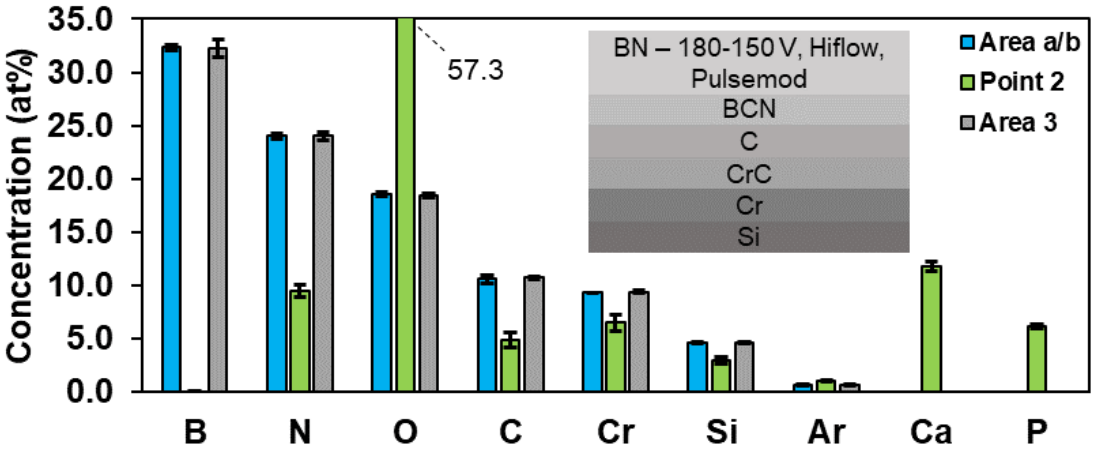

Figure 139 - Summary of the EDX data gathered from regions presented in Figure 138, B content is higher than N content, with O contamination present, surface contamination likely from sample handling is indicated. Full data in Table 58.

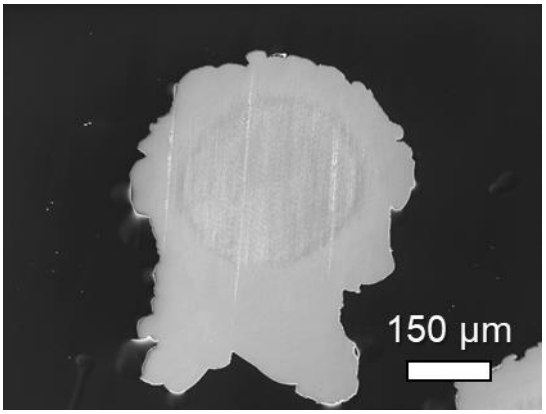

Figure 140 - Attempt at coating thickness measurement by the ball crater technique on Si substrate, the top layer has peeled from the multilayer, secondary electron image.

Figure 141 contains SEM images of Coating 12 after degradation. In contrast to previous degraded coatings, the surface contains a high density of flakes, due to the foil sealing the sample and preventing material loss. This imaging indicates that the degradation of the coating (if similar to the unsealed case) forms smaller flakes which are removed from the surface, rather than a large area peeling/delamination of the top layer. As previously the flakes are composed of mainly O and B, 56.1 ± 3.5 and 34.1 ± 4.3 at% for Point 1., Figure 142. The revealed interlayer surface contains the expected elements B, C, N, and Cr, with O contamination of 19 at% for Area 2.

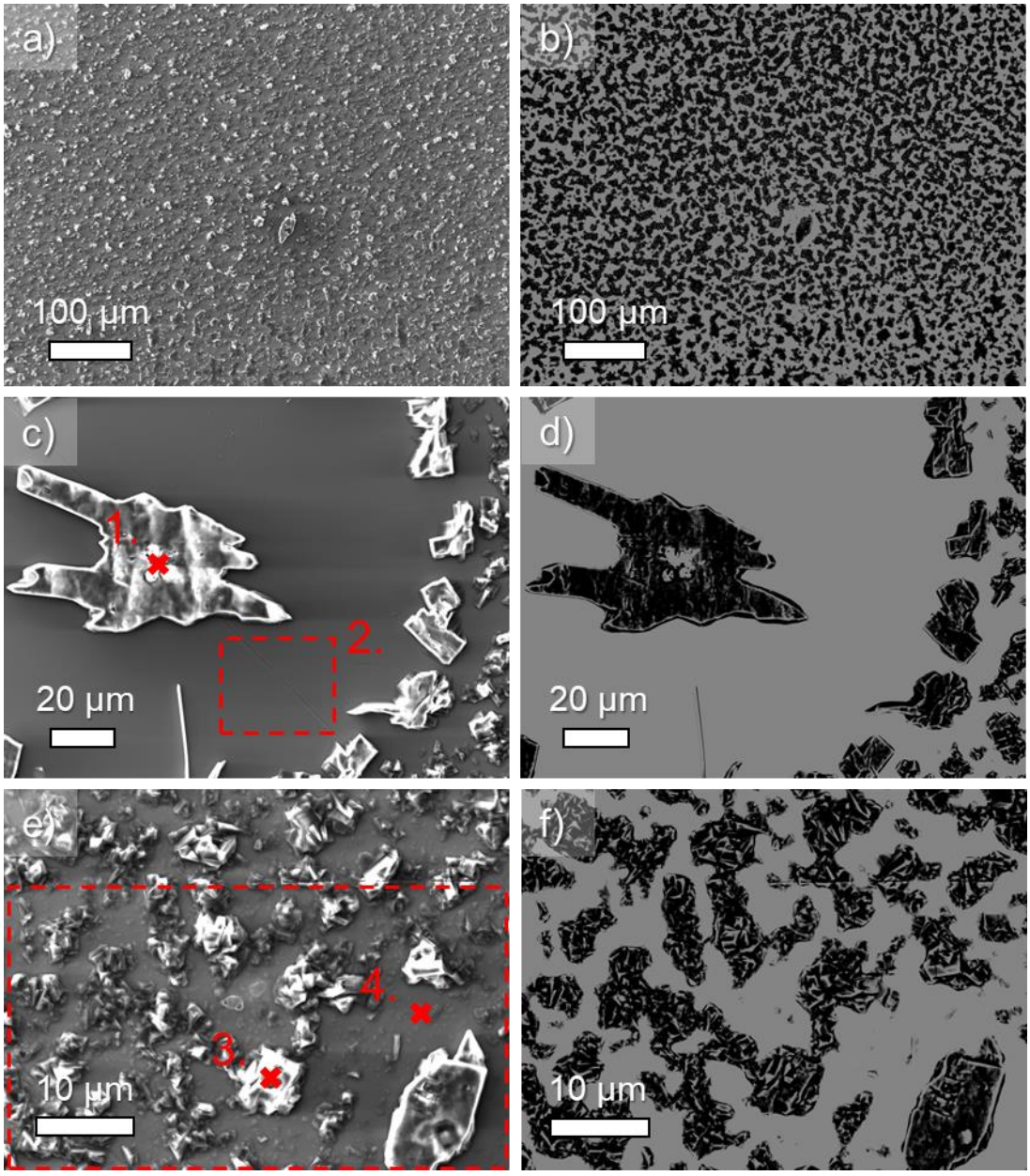

Figure 141 - Secondary a), c) and e) and backscattered b), d), and f) imaging of the multilayer BN coating with increased gas flow and pulse modification deposited on 316L after 19 days vacuum sealed in foil, the coating surface has delaminated and broken into flakes. Red areas indicate where EDX data was gathered from, summarised in Figure 142.

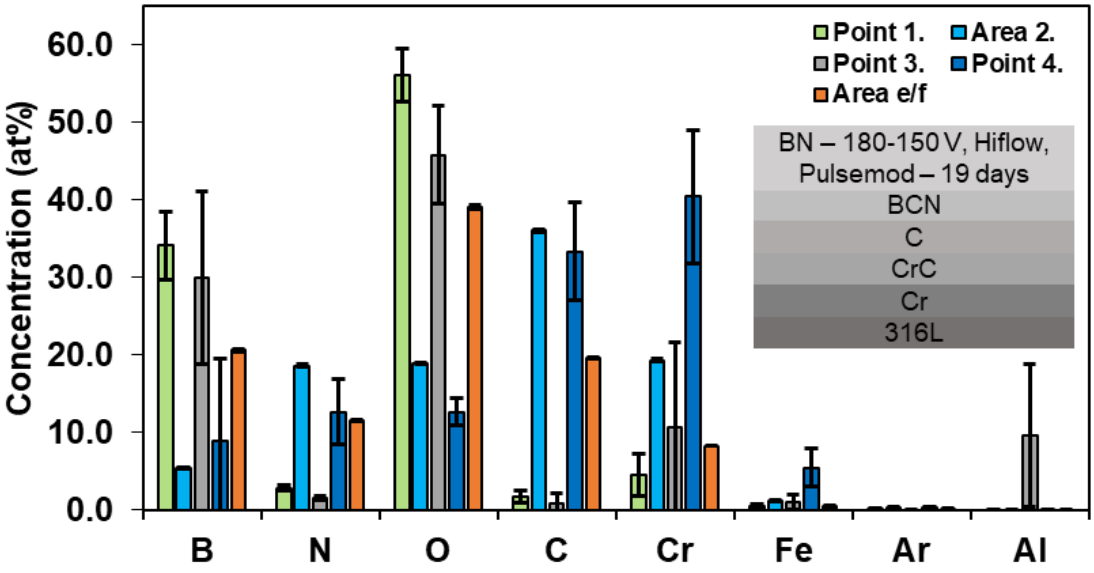

Figure 142 - Summary of EDX data for the multilayer BN coating with increased gas flow and pulse modification applied to 316L, after 19 days, see Figure 141. There is significant O contamination, with multiple regions exhibiting large error for multiple elements, Al contamination is present from foil used for storage. Full data in Table 59

The FTIR for Coating 12 is presented in Figure 143. The higher wavenumber range (3500-1800 cm^{-1}) contains a broad hump for both substrates, differing in the peak position, ~3100-3000 cm^{-1} for the Si and 3200-3050 cm^{-1} for the 316L. These humps contain components from NH and OH stretching modes with the former more likely to be responsible for the peak at 3420 cm^{1} emerging from the hump on the 316L spectrum. As previously the shoulder at 2245 cm^{-1} is not definitively matched. The h-BN/t-BN interplanar bending mode, 772-765 cm^{-1}, is present in both spectra, along with the w-BN mode at 1248-1243 cm^{-1}.

Fitting was carried out on the spectra using the Peak Fitting tool in Origin Pro 8 software, see Figure 144 and Figure 145, to further reveal the modes present. These spectra have been fit with peaks based on the shape of the original spectra, and any distinct visible peaks, and on the expectation of different components judged from previous coatings and from literature values.

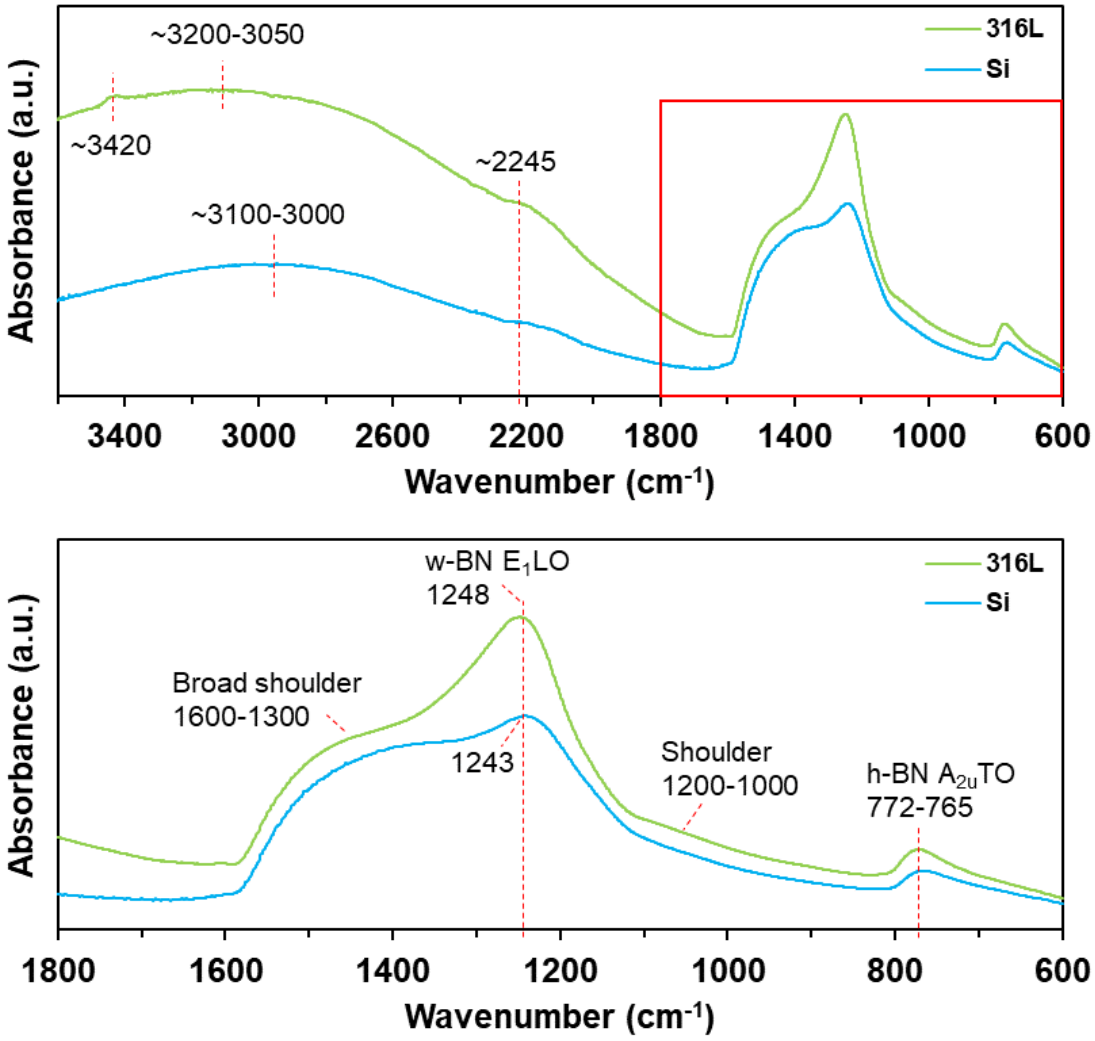

Figure 143 - FTIR spectra for the 316L and Si substrates coated with BN multilayer with increased gas flows and varied 180-150 V bias (50 kHz/1500 ns), the material is mixed phase with a prominant peak corresponding to wurtzite BN. Samples were scanned immediately after removal from the coating chamber.

Starting with the 316L spectrum, 6 peaks were fitted. The prominent peak for the w-BN LO mode is confirmed, at a slightly lower wavenumber than read from Figure 143, and lower than reported in literature [179, 200]. The corresponding TO mode for w-BN is also present at 1116 cm^{-1}, close to the values reported in literature [181, 200]. This is followed by the h-BN/t-BN stretching mode at 1357 cm^{-1}, at the lower end of the range reported for thin films, see Table 3. The final peaks realised in this spectrum correspond to two modes of E-BN, at 1486 cm^{-1} [160, 181, 209, 210], and 983 cm^{-1}, with the latter shifted higher than values reported in the literature for the 1000-900

cm^{-1} region [161, 180, 181, 209]. As with previous coatings, modes due to O and H bonds contaminating the coating could also be contributing to the spectra. As detailed in Table 3, there are B—O bond stretching modes in the 1550-1200 and 1100-850 cm^{-1} ranges for BO_3 and BO_4 respectively, though it is difficult to assign them definitively given the wide ranges reported [213, 215]. Furthermore, modes related to BNO bonding match well with the w-BN TO peak, 1116 cm^{-1}, complicating identification [206, 215]. All peaks have large FWHM suggesting only short range order.

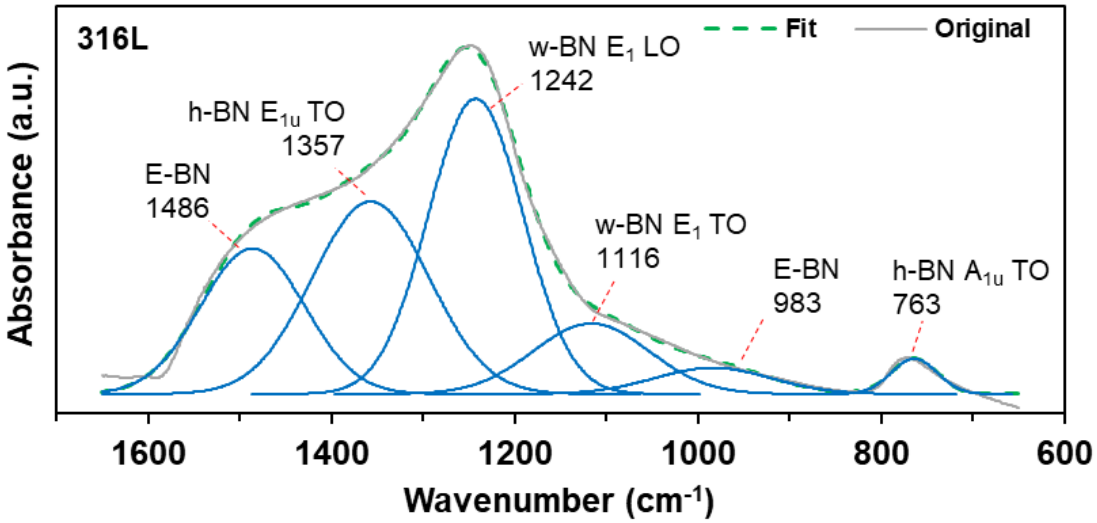

Figure 144 - Fitted FTIR spectrum for Coating 12 deposited onto 316L, original spectrum in Figure 143, Origin Pro 8 was used for peak fitting with Gaussian shape.

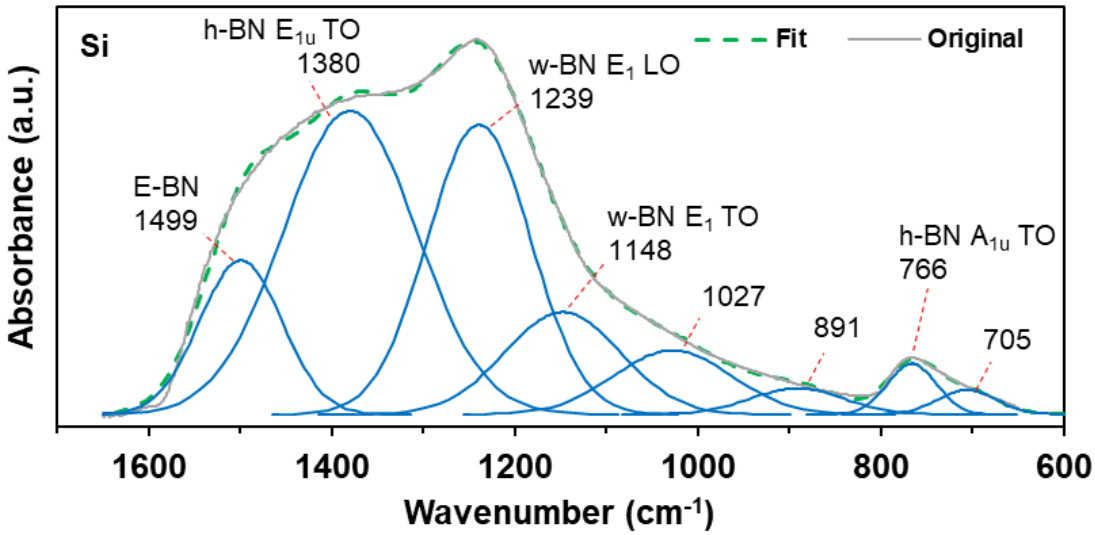

Figure 145 - Fitted FTIR spectrum for Coating 12 deposited onto Si, original spectrum in Figure 143, Origin Pro 8 software was used for peak fitting with Gaussian shape.

For the Si spectrum 8 peaks were fitted, one due to the wider peak in the spectrum at 800-650 cm^{-1}, necessitating a peak at 705 cm^{-1}, and the other in the 1100-900 cm^{-1} region. As with the 316L sample, the w-BN LO mode is present, at a slightly lower wavenumber, 1239 cm^{-1}, as well as the h-BN/t-BN bending mode at 766 cm^{-1}, slightly higher. This spectrum has a more intense shoulder between 1600-1300 cm^{-1}, and therefore the fitted h-BN/t-BN stretching mode has a higher intensity, at a higher wavenumber, 1380 cm^{-1}, than the 316L sample, more in-line with the values for this mode in literature. The fit in this region is less certain, as there is a slight deviation from the original spectrum near this peak, this may be due to the E-BN mode at 1499 cm^{-1}, as the high end of this peak does not fit with the original spectrum, a better fit would slightly reduce the width and reduce the wavenumber. The additional peak at 706 cm^{-1} could be due to either E-BN, reported at 700 cm^{-1} [161], or B—O—B bond bending reported in the 770-690 cm^{-1} range [215].

Due to the addition of a peak at 1027 cm^{-1} in this fit, the peaks identified as w-BN (1116 cm^{-1}) and E-BN (983 cm^{-1}) in the 316L spectrum have been shifted up and down respectively. These peaks are instead at 1148 and 891 cm^{-1}. The former is now

slightly above the range of values reported for the w-BN TO mode, and the latter is below the values for the E-BN mode in this region, between 800 cm^{-1} [161] and 927 cm^{-1} [180], see Table 3. The peak at 1027 cm^{-1} could potentially be due to cubic BN bond vibrations but it is at a lower wavenumber than the majority of c-BN values collated in Table 3, given this it is more appropriate to assign this peak to an E-BN mode (1030 cm^{-1}) [161] or a BO_4 stretching mode (1100-850 cm^{-1}) [215].

To provide more information about the degradation of the top layer of the BN multilayer, XPS was carried out, with samples exposed to atmosphere (loosely covered in foil) for different durations prior to analysis. To facilitate this, 10 x 10 mm 316L samples were coated and kept in the coating chamber (1 x 10^{-5} Torr), and at 0, 3 and 5 days the chamber was vented, a sample removed and the chamber reevacuated (samples referred to as 0 d, 3 d and 5 d). Note that this is not a perfect solution, as all samples were exposed to atmosphere briefly (~1 min) each time one was removed, but given that all samples would be exposed to atmosphere for transfer to the XPS chamber anyway, the adsorption/desorption of contaminants during the repeated sample removal was considered acceptable. An ideal solution would be to carry out 3 separate coating runs to produce the samples, however this is time consuming, and the samples would be from different batches, and not identical. At the end of the 5^{th} day the final sample was removed (0 days in atmosphere) and all 3 samples were transferred to the XPS instrument.

Visual inspection of the 3 samples showed a difference in appearance, the 0 d sample was smooth, similar to the photo in Figure 134, whereas the 3 d and 5 d samples were ‘glittery’ to the eye, indicating flakes from partial coating fracture and delamination. No further in-depth imaging of the surface was carried out to avoid contamination/modification.

Survey spectra for the 3 samples are presented at the top of Figure 146, with the peaks labelled with the element that the bonding energies correspond to. From the

peak areas the surface composition was extracted, see Table 28, error values were calculated by the CasaXPS software. at% has been used here to aid identification of compounds and formulae. All samples contained B, C, N, and O; the exposed samples also contained Cr. The 0 d 'as coated' sample had a B content of 32.2 ± 0.4 and a N content of 17.2 ± 0.3 at%, with a calculated B/N ratio of 1.87. The oxygen content was high at 40.3 ± 0.3 at%, with carbon content, attributed to adventitious contamination from the environment or coating chamber during venting, at 10.3 ± 0.2 at%. It should be noted that the amount of O could be over-estimated here, as no ion cleaning was carried out to remove contamination, as Wang et al. have reported [175].

As the time exposed to atmosphere increased, the B and N content reduced, with the latter decreasing substantially over the first 3 days, with less of a reduction in the following 2 days. The O content initially increases from 0 to 3 d, potentially due to integration into the top surface, then decreases from 3 to 5 d due to material loss of the top layer containing the diffused oxygen as flakes. The C content increases from 0 to 5 days, and the Cr content increases between 3 and 5 days, with both increases due to the interlayer being revealed by loss of the top layer material, and increased time exposed to environmental contamination.

Curve fitting of the high-resolution spectra was carried out to understand the bonding states of the surface elements, using procedures from Major et al. [304] and Fairley [305]. All the attributed peak components are shown in Figure 146 and Figure 147, details and references are collated in Table 29, with full details of references and ranges compiled in Table 4 and Table 5.

Starting with the 0 days sample as a baseline, the centre of the B1s peak was situated at 192.2 eV and was comprised of four components, correlating with various valence states at 187.4, 190.2, 191.3 and 192.3 eV. These states have been attributed to B—B (1.15 %), B—N sp2 (3.18 %), B—N sp3 (25.9 %) and B—O or BN_yO_x bonding (69.8

%), respectively, with the first two as minor components. It should be noted that the B—N sp3 component is at the upper limit, 191.3 eV, of the range reported in literature (Table 5). Looking at the N1s peak, located at 398.4 eV with a clear shoulder at the higher binding energy side, four components have also been fitted. Both sp2 (57.5 %) and sp3 (19.8 %) N—B bonding states are resolved at 398.1 and 399.1 eV, with N—H or N—C (16.8 %) and N—O (10.0 %) also fitted. In contrast to the B1s spectrum, the peak areas for the N—B bonding are reversed, with the majority of nitrogen sp2 bonded to B (57.5 %). From the O1s spectrum, the majority (99.3 %) of the oxygen is bonded either in ternary boron oxynitrides or hydroxyl contaminants centred at 532.4 eV. The majority of the carbon is attributed to adventitious carbon, with a minor component (286.1 eV, 12.4 %) related to bonding in C—O—C or C—N sp2 bonding or both.

As the sample is exposed to atmosphere the bonding states change. For the 3 d B1s spectrum, the peak shifted up to 192.5 eV from 192.2 eV (0 d). Furthermore, the B—N sp3 component is not present, with a minor (2.3 %) indication of B—N sp2 bonding shifted to lower eV (190.2 to 189.6 eV). The peak is dominated by the B—O/BN_yO_x component shifted up by 0.2 eV. Of note here is the subtle indication of the presence of a π plasmon loss peak approximately 9 eV above the main peak, indicative of sp2 bonding, not present in the 0 d sample. The N1s peak is similarly altered, missing the N—B sp3 bonding state, and the proportion of sp2 N—B bonding (22.4 %) is reduced compared to the N—C sp2 bonding (65.9 %). The π plasmon peak is not present. The large increase in the proportion of N—C bonding is indicative of the interlayer revealed by the loss of top layer material. This is corroborated by the C1s spectrum, which has a broadened shoulder on the higher energy side of the peak. This spectrum has been fitted with four components; the major component is the adventitious carbon peak at 284.5 eV (68.5 %). The peaks fitted to the shoulder correspond to C—N sp2 (285.6 eV/17.4 %) and sp3 (287.1 eV/7.3 %) bonding states, and C—O (289.3 eV/6.9

%) bonds. At this timepoint, it assumed that the major peak is due to both adventitious carbon and also carbon bonding in the interlayer, further scanning of the interlayer would be required to separate these contributions. The O1s spectrum is consistent, though the BN_yO_x/hydroxyl component proportion is slightly reduced (6.1 % lower) with a bonding state matching bonding in B_2O_3 appearing at 533.7 eV.

After 5 days the coating is further degraded, no B—N component is present in the B1s spectrum, and a minor component potentially matched to B—O bonding has emerged at 194.3 eV, with the B—O/BN_yO_x component once again dominating at 192.3 eV (94.3 %). This minor peak could correlate with the component in the O1s matched to B_2O_3. The N1s spectrum does still have a minor (7.1 %) N—B sp2 state at 397.5 eV, dominated by the N—C sp2 at 400.0 eV. The C1s spectrum is complex, with 5 components fitted, the major peak at 284.6 eV is again matched to carbon contamination, with suggested overlaps with C in the interlayer, and potential C—B bonding. The peaks fitted to the shoulder are consistent with the 3 d sample, matched to sp2 (shifted + 0.4 eV) and sp3 (shifted – 0.2 eV) C—N bonding, and C—O bonding. It is uncertain as to the difference between the two different C—O components, further scanning of the interlayer would elucidate this.

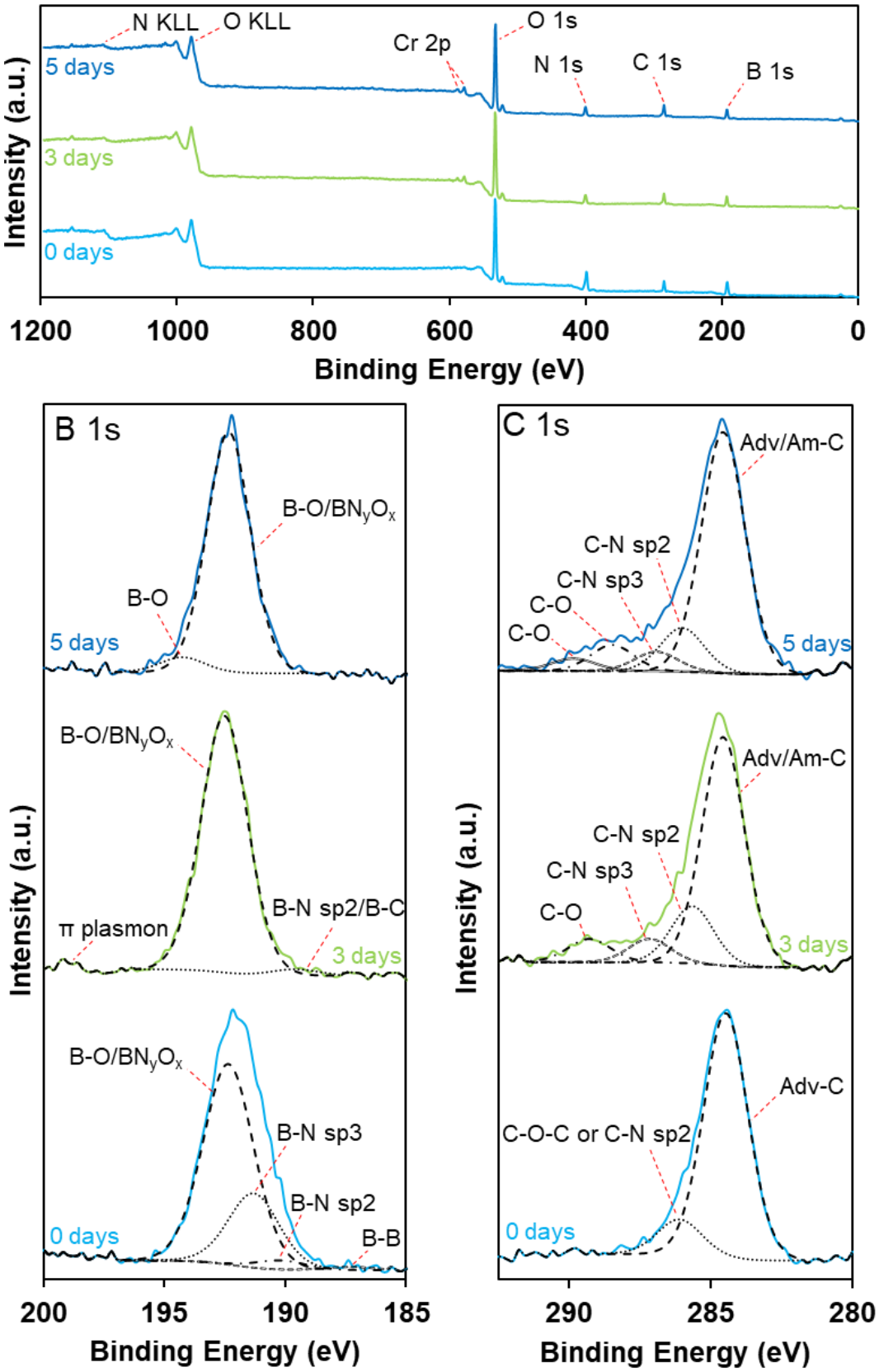

Figure 146 - Annotated survey and fitted B 1s and C 1s high resolution XPS spectra of BN multilayer film applied to 316L, exposed to atmosphere for 3 different durations, see Table 28 and Table 29 for details. All spectra have been min-max normalised. Adv-C refers to adventitious carbon, and Am to amorphous.

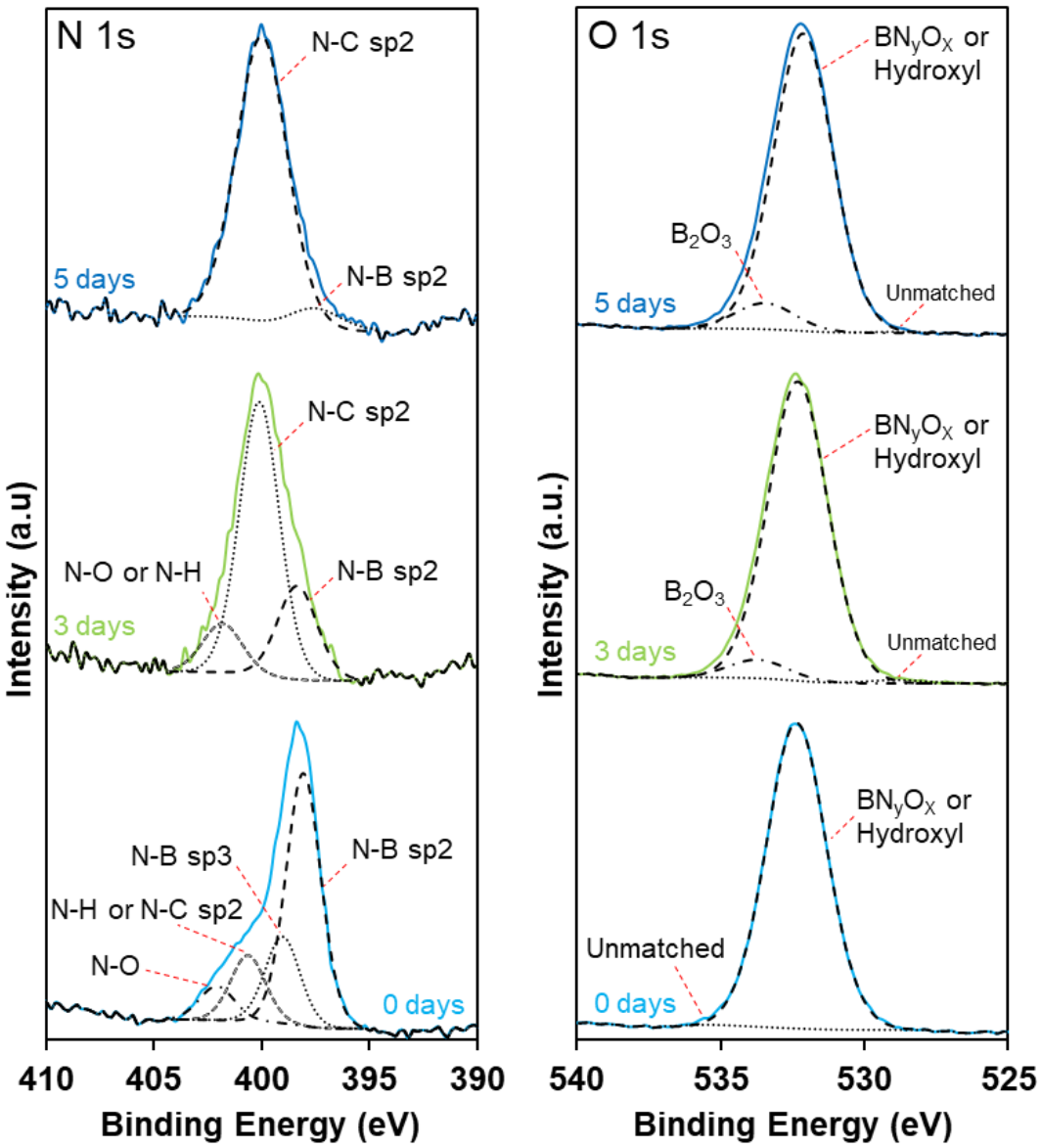

Figure 147 - Annotated fitted N 1s and O 1s high resolution XPS spectra of BN multilayer film applied to 316L, exposed to atmosphere to 3 different durations, see Table 28 and Table 29 for details. All spectra have been min-max normalised.

Table 28 - Element concentration in the near surface of BN multilayer deposited with high gas flows and pulse modification, gathered by XPS, error values are produced by CasaXPS software. Survey spectra in Figure 146.

Sample	Element Concentration (at%)				
	B	C	N	O	Cr
0 days	32.2 ± 0.4	10.3 ± 0.2	17.2 ± 0.3	40.3 ± 0.3	-
3 days	28.1 ± 0.5	14.0 ± 0.3	8.7 ± 0.3	48.2 ± 0.4	1.0 ± 0.1
5 days	27.6 ± 0.6	16.5 ± 0.4	7.9 ± 0.2	46.4 ± 0.5	1.6 ± 0.2

Table 29 - High resolution XPS raw data for the BN multilayer surface, deposited on 316L with high gas flows and modified bias pulse parameters, at three different durations exposed to atmosphere, spectra in Figure 146 and Figure 147, GL(30) line shapes were used.

Time	Element	Binding Energy / eV (FWHM)	Corresponding Bonds (Area %)	References
0 days	B1s	187.4 (2.46)	B-B (1.15)	[163, 202, 217]
		190.2 (2.46)	B-N sp2 (3.18)	[176, 202, 204, 218-220]
		191.3 (2.46)	B-N sp3 (25.9)	[163, 179, 205, 219, 227]
		192.3 (2.46)	B-O or BN_yO_x (69.8)	[202, 205, 223, 224] or [204, 218]
	C1s	284.5 (1.83)	Adventitious C (87.6)	[202, 306]
		286.1 (1.83)	C-O-C or C-N sp2 (12.4)	[307] or [202, 306, 308]
	N1s	398.1 (1.90)	N-B sp2 or N-C sp3 (57.5)	[163, 202, 205, 219] or [306, 308, 309]
		399.1 (1.90)	N-B sp3 (19.8)	[179, 219]
		400.7 (1.90)	N-H or N-C sp2 (16.8)	[224] or [219, 306, 309]
		402.1 (1.90)	N-O or trapped N^2, or N-H (10.0)	[308, 309] or [204, 222]
	O1s	532.4 (2.45)	BN_yO_x or Hydroxyl (99.3)	[226] or [224]
		535.4 (2.45)	Unmatched (0.7)	
3 days	B1s	189.6 (2.25)	B-N sp2 or B-C (2.3)	[202, 218] or [205, 219]
		192.5 (2.25)	B-O or BN_yO_x (97.7)	[202, 205, 223, 224] or [204, 218]
		+ 9 eV	π plasmon loss	[176, 217, 226, 227]
	C1s	284.5 (1.77)	Adventitious C or C-B (68.5)	[307] or [202, 219]
		285.6 (1.77)	Trigonal C-N sp2 (17.4)	[219, 306]
		287.1 (1.77)	Tetrahedral C-N sp3 (7.3)	[163, 205, 219, 306, 308]
		289.3 (1.77)	C-O (6.9)	[308]
	N1s	398.4 (2.17)	N-B sp2 or N-C sp3 (22.4)	[202, 219] or [306, 308, 309]
		400.1 (2.17)	N-C sp2 (65.9)	[219, 306, 309]
		401.8 (2.17)	N-O or trapped N^2, or N-H (11.7)	[308, 309] or [204, 222]
	O1s	528.9 (2.44)	Unmatched (1.1)	
		532.3 (2.44)	BN_yO_x or Hydroxyl (93.2)	[226] or [224]
		533.7 (2.44)	B_2O_3 (5.8)	[226]
5 days	B1s	192.3 (1.81)	B-O or BN_yO_x (94.3)	[202, 205, 223, 224] or [204, 218]
		194.3 (1.81)	B-O (5.69)	[204]
	C1s	284.6 (1.81)	Amorphous C or C-B (70.3)	[306, 308] or [202, 219]
		286.0 (1.81)	Trigonal C-N sp2 (12.9)	[202, 306, 308]
		286.9 (1.81)	Tetrahedral C-N sp3 (5.7)	

		288.5 (1.81) 289.9 (1.81)	C-O (7.7) C-O (3.5)	[163, 205, 219, 306, 308] [202, 205, 306] [308]
	N1s	397.5 (2.78) 400.0 (2.78)	N-B sp2 (7.1) N-C sp2 (92.9)	[179, 204] [219, 306, 308, 309]
	O1s	528.8 (2.42) 532.1 (2.42) 533.5 (2.42)	Unmatched (0.4) BN_yO_x (91.6) B_2O_3 (8.0)	 [226] [226]

6.2 Discussion

There is still significant research needed subsequent to this study in order to produce pure c-BN coatings, well adhered to substrates, in efficient ‘one pot’ PVD solutions combining coating adhesion techniques and BN deposition into commercial large batch coating equipment (>100 substrates).

The most adherent/stable and hard coatings to date have involved deposition of interlayers in high capacity equipment, followed by transfer of samples to research scale equipment for BN deposition [310-312], with only a single paper published using high volume equipment suitable for bulk batch manufacturing [313]. Furthermore, most coating setups used for depositing BN coatings have static sample stages, reliant on having samples smaller than the target aperture in order to deposit uniformly across the substrate surface [191]. The challenge is to identify processes suitable for scaling up to become viable for introduction into industry, a key aim of this chapter, through the use of commercially viable Closed Field Unbalanced Magnetron Sputtering (CFUBMS) equipment.

Furthermore, from the conclusions of the previous chapter, increased surface homogeneity is required, in addition to increased ion/sputtered atom arrival ratio, increased ion energy and increased substrate temperature to promote nucleation of crystalline cubic phase BN. Rotating the samples between multiple BN targets enabled investigation of the first two of these aspects, homogeneity and ion/atom ratio.

For the benefit of the reader summaries of the top layer coating parameters and interlayer parameters are repeated and contained in Table 30 and Table 31 respectively.

Table 30 - Summary of the top layer BN deposition parameters for coatings deposited onto planar substrates with full rotation, repeated from Table 10.

No	Multi-layer	Top layer motion	BN Targets (Duration)	Ar:N_2 (sccm)	Bias Voltage (V)	Pulse Frequency (kHz)	Reverse time (ns)
8	Y	Rotation	2 (24 h)	15:5	60	250	500
9	Y	Rotation	2 (24 h)	15:5	100	250	500
10	Y	Rotation	2 (24 h)	15:5	180 - 150	250	500
11	Y	Rotation	2 (24 h)	30:25	180 - 150	250	500
12	Y	Rotation	2 (24 h)	30:25	180 - 150	50	1500

Table 31 - Summary of the Cr-CrC-C-BCN adhesion interlayer coating parameters used for Coatings 5-12, repeated from Table 11.

Layer	Target Setpoint	Substrate Bias (V)	Ar:N_2 (sccm)	Layer duration
Chromium	Cr (4 A)	120	23:0	900 s
Chromium Carbide	Ramp Cr (4-0 A) Ramp C (0-3.5 A)	60	23:0	1200 s
Carbon	C (3.5 A)	60	23:0	1200 s
Boron Carbon Nitride	Ramp C (3.5-0 A) BN x 2 (175 W)	60	30:15	2400 s

Surface coverage for Coatings 8 (Ar15:N5, 60 V) and 9 (Ar15:N5, 100 V), see Figures 107 a) and 115 a) respectively, was more homogeneous than the samples deposited statically in the previous chapter (Coatings 5, 6, and 7). This shows that the use of rotation can form coatings with superior surface uniformity, as expected. In contrast to this, for Coatings 10, 11 and 12, where the substrate bias was raised to the varied 180-150 V level, surface non-uniformity was evident from the appearance of the samples, Figures 121, 126 and 134.

To understand why this change in uniformity occurred, it is necessary to examine the coating setup further. The change to rotational coating led to a change in the ratio of ions/sputtered atoms arriving at the substrate. This was intentional as a primary conclusion from the previous chapter was that the ion/sputtered atom ratio had not been high enough to overcome the energy and stress thresholds to nucleate cubic

BN, potential structure formation mechanisms will be discussed later. The change in ion/atom ratio occurred because the deposition rate of BN was reduced when rotating samples, as the substrates moved in and out of the field of view of the magnetron(s), see Figure 148, as the magnetrons were arranged opposite to one another.

In static mode, the deposition and bombardment are constant and concurrent, Figure 148 a), similar to the majority of published studies, as this reduces the setup to a single highly unbalanced magnetron. The uniformity is therefore dependent on the deposition profile across the magnetron field of view, as discussed in 5.2. In contrast to this, when using rotation, the substrates moved through different levels of sputtered flux from the target, averaging out to form a uniform distribution across the surface horizontally in the direction of rotation, as is seen for Coatings 8 (Ar15:N5, 60 V) and 9 (Ar15:N5, 100 V). The surface uniformity in this case is therefore dependent on the net deposition around the circumference of the substrate holder.

This is demonstrated more clearly by considering the appearance of Coating 10 (Figure 121), where the substrate bias was raised to the varied 180-150 V. The coating does not cover the surface of the 316L substrate, and is concentrated in the centre, fringe patterns indicative of thickness variation are evident. As the only parameter change from Coating 9 (100 V bias) to Coating 10 (180-150 V bias) was in the bias voltage, the change in surface uniformity must be due to this. Table 32 contains collated ion current values for all of the multilayer BN coatings.

Table 32 - Collated ion current and sputtering pressures for the BN nucleation and growth steps (where applicable) for the multilayer Coatings 5-12. Coatings 8-12 all had a duration of 24 h.

Coating No.	Ion Current (mA)		Pressure (mTorr)		Ar/N_2	Motion
	Nucleation	Growth	Nucleation	Growth		
5, 6, 7	180 ± 0	160 ± 0	1.37 ± 0.04	1.34 ± 0.04	2	Static
8	100 ± 2		0.84 ± 0.03		3	Rotation
9	129 ± 3		0.76 ± 0.22		3	Rotation
10	184 ± 5	166 ± 5	0.97 ± 0.05	0.93 ± 0.01	3	Rotation
11	180 ± 0	160 ± 0	1.71 ± 0.05	1.74 ± 0.05	1.2	Rotation
12	59 ± 2	58 ± 4	1.81 ± 0.02	1.78 ± 0.02	1.2	Rotation

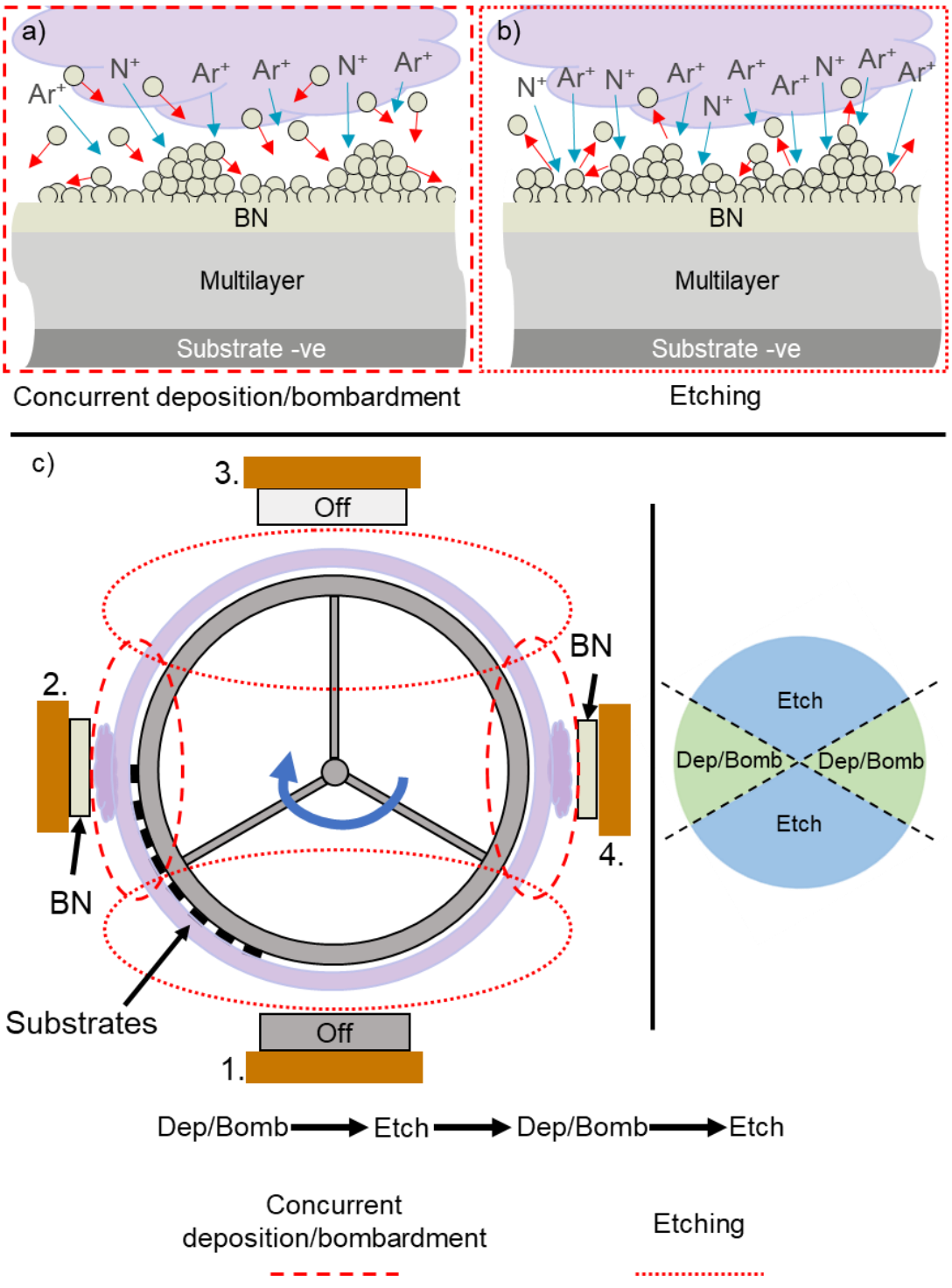

Figure 148 - Schematics illustrating the different coating environments, dependent on sample motion, and the region that the sample is in at a given time. The coating growth during static mode is illustrated in a), where the deposition of the coating material and ion bombardment happen concurrently, the growth of the coating during rotation alternates between a) and b), plasma etching and chemical reaction, according to the region that the sample is in, displayed in c).

Comparing the ion currents for Coatings 9 and 10, 129 ± 3 and 184 ± 5/166 ± 5 mA, irrespective of whether the growth or nucleation parameters in Coating 10 are considered, the current is higher than Coating 9. The increase in voltage also increases the energy of bombarding ions [38]. This is entirely expected and obvious, an increase in voltage will increase the current flowing. However, as mentioned, the substrates do not receive a constant supply of sputtered material throughout the full rotation. Therefore, it is necessary to define further distinct process steps. These consist of alternating deposition-bombardment and plasma etching periods per rotation, Figure 148 a/b). These are distinct steps, as the ion bombardment is consistent around the circumference of the holder, whereas the deposition happens only in the field of view of the magnetron(s). Therefore the substrates pass through these different regions in the chamber as demonstrated in Figure 148 c). Figure 148 b) shows etching/resputtering, as there is no fresh material arriving at the surface, the ions bombarding the surface are modifying and removing material that has been previously deposited. This is in contrast to Figure 148 a), where fresh material is supplied to the surface from the BN target. As an aside, comparing the ion current (Table 32) from Coatings 5, 6 and 7 (Static) to the current for Coating 10 (rotation), 180 ± 0 and 184 ± 5 mA (nucleation) respectively, similarity is evident. Both have the same applied voltage (180 V), but the ion bombardment is different. Therefore, the ion current alone cannot be used in isolation to explain phenomena.

The consistent ion bombardment across the substrate holder is due to the use of a Closed Field Unbalanced Magnetron System (CFUMBS). The key benefit, as detailed in Section 2.1.3 and repeated here, of using a CFUBMS setup is that the magnetic field lines extend between and connect the magnetrons, meaning that the plasma species are not lost to thermalisation at distance from the magnetron. Instead, the ionisation is sustained along and across the field lines, even when no power is applied to alternate magnetrons (as is the case in this current study with Mag 1 and Mag 3),

increasing ion current to the substrate in regions away from the magnetrons [2, 14, 22]. The bombardment is more uniform across the sample surface, allowing energy input at increased ion current 'per' voltage applied over open field systems, advantageous for producing high quality thin films on complex geometry [20].

An important point to emphasise is that the regions depicted in Figure 148 c), for the Concurrent deposition/bombardment and the Etching, are not equal in size (or more specifically angle). This region imbalance was due to the small size of the targets (57 mm) compared to the diameter of the substrate holder (365 mm), meaning there was a large substrate area/target area ratio. Furthermore, the issues with the design of the magnetron(s) used for BN, discussed previously in 5.2, also contribute to this. The reduced aperture led to blocking of material sputtered at high angle and when rotating substrates, Figure 148 c); the time per rotation that BN was being deposited onto substrates from the BN targets was therefore reduced.

Simply put, for the bias parameters used in Coating 10 onwards, the net deposition averaged across the sample surfaces was negative due to a greater etching rate than deposition rate.

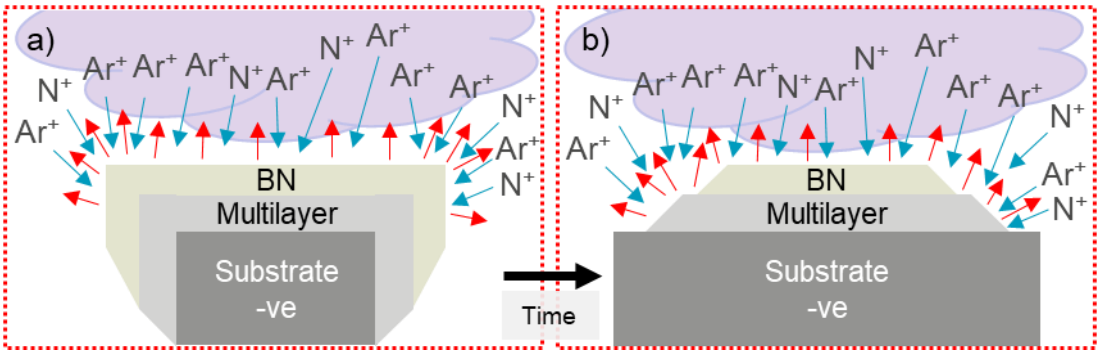

Figure 149 - Schematic detailing the preferential etching of the coating at the edges of the substrate where the electric field converges to a point, and the ratio of surface area to volume is high, a) the coating at the early stages of the BN deposition, b) the coating near the end of the BN deposition. Note that deposition of new material is omitted from this figure for clarity, in reality this mechanism is present in both the regions in Figure 148c).

So, returning to the uniformity of Coating 10, why was there deposited material remaining in the circular region in the centre of the substrate? If the net deposition is negative, the surface should appear uncoated, or coated with an interlayer, dependent on etching depth? This inhomogeneity across the surface gives a further additional indication of bombardment mechanisms. Coating 10 represents the extreme, where the coating has receded far from the edges of the 316L substrate, but the same mechanism has also happened to a lesser degree with Coatings 11 and 12.

Figure 149 presents the suggested mechanism responsible for this behaviour. At the start of the BN layer deposition, Figure 149 a), the multilayer is intact and wraps around the substrate with good step coverage (due to the randomised material flux and rotation) [1, 27, 33], with a thin layer of BN deposited. Due to the non-infinite size of the substrates, edge effects are present.

The bias potential applied to the substrates creates an electric field that is concentrated at the edges, enhancing the bombardment similar to the edging effect seen in plasma nitriding [314]. Due to the higher intensity of bombardment at the edges, the coating is resputtered such that previous layers are exposed, and the coating becomes thinner, eventually exposing the substrate. Importantly, not only is the coating removed, but the sides of each layer are exposed. It can be suggested that increasing the coating duration would eventually lead to full removal of the coating, as the net deposition of coating at the centre is reduced as the edges are removed.

This mechanism, Figure 149, and the alternating regions depicted in Figure 148, expose the limitations of this specific sputtering setup, from a research perspective. Ideally, when investigating the coating homogeneity and the formation of different BN phases, ion energy and ion current need to be controlled independently, so that only one variable is changed per investigation. This is not the case with substrate biasing

however, as the ion current and ion energy are directly linked to the voltage setpoint, and cannot be varied independently. Therefore, in order to investigate the effect of increased ion energies, the deposition rate from the BN target(s) has to increase (matching the increase in ion current) such that the same ion/atom ratios are present. Attempting this revealed a further issue caused by the design of the magnetrons used for BN deposition as the erosion of both the magnetron(s), and the erosion of the clamping ring(s) (Figure 102 b)) further limited the achievable deposition rate. At all times the power applied to the magnetron/s was being split between the target area (BN), the target clamping ring (316L, Figure 61 a)), and the erosion ring on the magnetron body behind the sheath (Cu, Figure 61 b)), (note that this split has not been quantified).

An increase of deposition rate by increasing the power density on the BN target was not possible because of the potential for sputtered steel/BN to form a physical bridge between the clamp ring and the sheath attachment, shorting the magnetron to ground, the start of which is evident in Figure 61 a), and also to prolong the lifetime of the magnetron/s. Therefore, the rationale for changing to full rotation (Coatings 8-12); increased homogeneity and process scalability, could only partially be realised, as the deposition rate was limited by the increased ion current and the maximum tested target power density of 6.86 W/cm^2 (175 W) per magnetron. In comparison to BN PVD literature, for a similar target size (2 inch diameter), 400 W was applied to the target, equating to a power density of 19.74 W/cm^2 [248, 296, 315, 316], with other studies also exceeding this with different size targets [162, 317, 318].

The modification of the substrate bias pulsing parameters, however, did reduce the ion current, from 180 ± 0 to 59 ± 2 mA (Coatings 11 and 12 respectively, Figure 48) . To the current authors knowledge a thorough study has not been undertaken varying the pulsing parameters of Pulsed-DC to assess the resulting BN structures formed. A further investigation analogous to that done by Yang et al. [319] when optimising

pulse parameters for Graphit-iC Diamond Like Carbon (DLC) coatings is needed in the future.

In contrast to the coatings discussed previously in Discussion 5.2, all coatings except for Coating 9 (100 V) deposited in this chapter degraded when exposed to atmosphere over time. This led to difficulties when measuring the B/N ratio via EDX as some coatings degraded prior to analysis. Coatings which were intact, 9 (Ar15:N5, 100 V) and 12 (Ar30:25N, 180/150 V, 50 kHz 1500 ns), had B/N ratios of 1.34 and 1.35 respectively. Whilst there are other parameter differences between the two, this indicates that an increase in the partial pressure of N_2 when depositing BN does not lead to a corresponding increase in the ratio of N in the coating. This is not unexpected, as sub-stoichiometric BN coatings are common in literature, with Reinke et al. [164] and Li et al. [187] suggesting that N preferentially resputters from the coating surface rather than B, and Kulisch et al. [43] proposing that N diffuses and desorbs from the surface during coating. Given the aforementioned issues with the balance of deposition and etching, it is likely that the former of the two mechanisms for N depletion, resputtering from previously deposited material [164, 187] is dominant here, as the relatively high ion currents would have led to removal of N. Also the temperature of the substrates was low (~100°C as measured by temperature labels) and as such diffusion of N would be minor.

The FTIR data collected after deposition gives indications of the structures formed in the coatings with varied bias/gas parameters. All coatings contained mixed BN bonding, sp2 and sp3, related to E-BN, h-BN and w-BN as summarised in Figure 150, and all spectra contain peaks which are broad, indicating nanocrystallinity. It should be noted that, as was mentioned when discussing the statically deposited coatings, Discussion 5.2, the substrate temperature was limited to below generally recognised temperatures for cubic phase nucleation [43]. This was due to reduced total power input to the magnetrons (distinct from power density), and therefore a reduced waste

heat transfer to the substrate from the plasma compared to use of large targets/magnetrons (as with the C and Cr targets 380x175 mm used for interlayers) in this system [320, 321]. This is the reason suggested for the lack of cubic vibrational modes in the FTIR spectra.

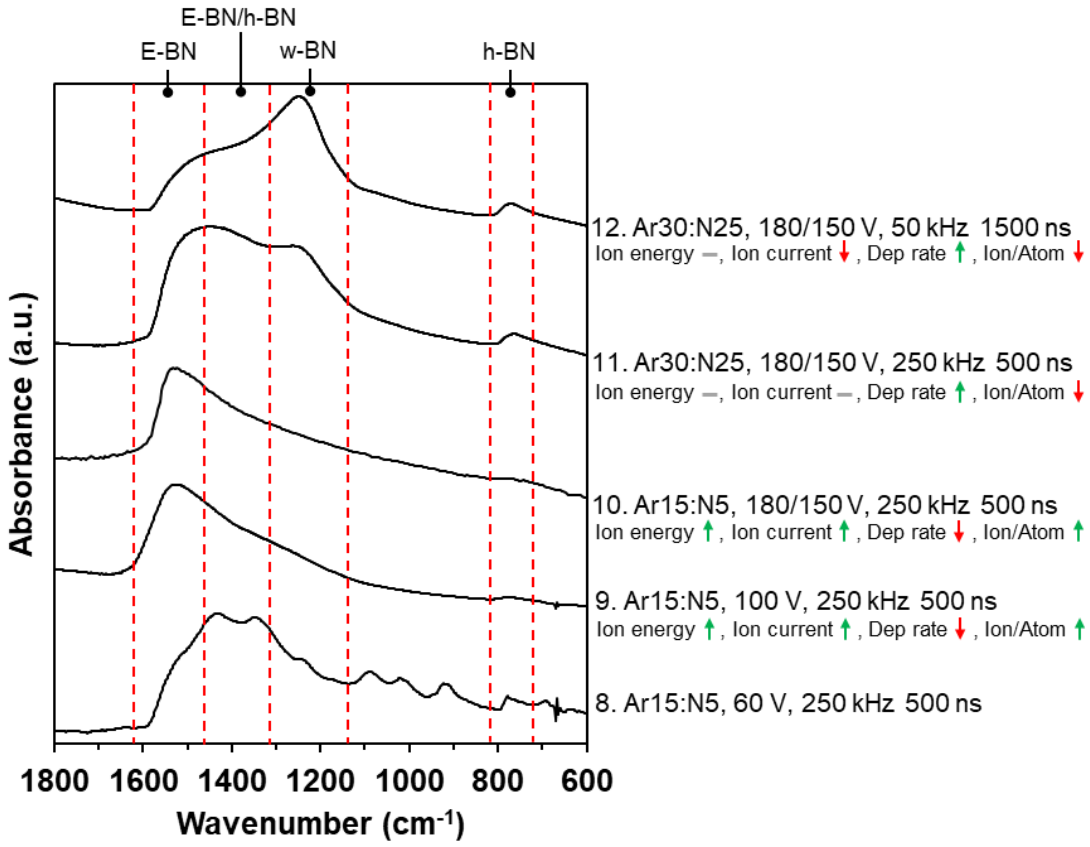

Figure 150 - Collation of the FTIR spectra (normalised) for the coatings deposited when rotating substrates. With low applied substrate bias the film has mixed bonding, as bias is increased, E-BN bonding dominates, when gas flow (sputter pressure) is increased, w-BN bonding emerges, when pulse parameters are modified, w-BN bonding dominates. The arrows indicating rising and falling of energy, current etc are relative to the previous coating, i.e. 9 has a higher ion energy than 8, 10 has a higher energy than 9 and so on.

As displayed in Figure 150, when raising the bias voltage above 60 V, the vibrational mode corresponding to E-BN becomes dominant over h-BN bonding. The mechanism for the formation of E-BN in thin films has not been conclusively published in literature, and remains unclear. One aspect that is agreed on is the nanocrystallinity of E-BN in films [160, 181, 207, 210, 243, 248], as seen in the current study. Zhu et al. [181, 322, 323] suggest a mechanism (included in the review by Batsanov [243] who originally

discovered the structure) and also referenced by Kamenetskikh et al. [201], whereby ion interaction with sputtered material within the plasma forms mixed sp2 and sp3 bonding, which then deposits as E-BN on the substrate. This mechanism is not entirely satisfactory, as the authors state that 'h-BN' [181] or 'h-BN clusters' [201] are sputtered from the target with sp2 bonding and some bonds are then changed to sp3. It is generally accepted that BN dissociates when sputtered [39], an issue which necessitates N_2 gas flow in addition to Ar flow, and as such there must be a lower energy step that forms the initial sp2 BN bonding prior to the higher energy ion interactions that cause a change to sp3 bonding. Furthermore, this mechanism is based on the E-BN structure proposed by Olszyna et al. [160] which contains mixed sp2 and sp3 bonding, rather than the updated structure proposed by Pokropiyny et al.[161], containing sp3 fullerenes.

Additionally, this mechanism does not consider the effect of O contamination on the process, seen in the current work, which could lead an alteration of the proposed mechanism. Batsanov et al. [324] report that Oxygen content stabilised the E-BN phase in their shock compression testing. Furthermore, when intentionally adding small flows of Oxygen to PVD BN processes, the FTIR spectra from Lattemann et al. [250], Choi et al. [296] and Ulrich et al. [252] show a broad shoulder in the 1400-1600 cm^{-1} wavenumber range potentially relating to E-BN, though the authors do not comment on this. Inconveniently Zhu et al. [181], Kamenetskikh et al. [201] and Pat et al. [248] have not carried out elemental analysis in their publications where E-BN is seen in FTIR for comparison.

However, taking the basic mechanism, it can be seen that there is correlation with the results seen in the current study. For Coatings 9 and 10, see Figure 150, an increase in the ion energy and ion current, and as a consequence a more intense plasma, has led to an increase in the E-BN proportion, suggesting that the plasma based modification of bonds has occurred. It can also be suggested, that as

resputtering/etching of previously deposited material from substrates has been shown to have occurred, that there could be the possibility of redeposition of material with modified bonding as well.

The parameter sets of Coating 11 (Ar30:25, 180/150V) and Coating 12 (Ar30:25, 180/150V, 50 kHz 1500 ns), where gas flows and bias pulsing parameters were modified, produced w-BN modes in the FTIR spectra (Figure 150). For the former, as the deposition rate has increased, the ion/atom ratio has also increased, for a constant ion current relative to Coating 10 (Table 32). A higher flux of B and N is reaching the substrate, and is remaining there. As an aside, the increase in pressure is also likely to have reduced bombardment from gas ions that have been neutralised and reflected from the target back at the substrate [41], due to a decrease in mean free path. Therefore, it can be suggested that the dominance of the plasma based E-BN sp2 to sp3 bond modification mechanism shifts towards surface based ion modifications/mechanisms, through adatom motion and increases of surface stresses. As w-BN is a distorted sp3 structure, the formation can be attributed to the Sputter [164, 236], Thermal spike [238] and Stress (Static and Dynamic) [239, 240] mechanisms [3], but restricted due to the low temperature deposition. The dominance of the mechanisms located at the surface further increases with a drop in ion current, as is seen from the increase in the w-BN mode over the E-BN mode for Coating 12.

Therefore, a suggested addition to the parameter space diagram published by Mirkarimi in their review [3] is contained in Figure 151. This is generalised, but from the parameters used in this current work, and the resulting materials, it is suggested that (at low temperature ~100°C) E-BN forms at high ion currents (or ion to atom ratios), low ion energies. When decreasing the ion current (reduced ion to atom ratio) w-BN formation begins to dominate.

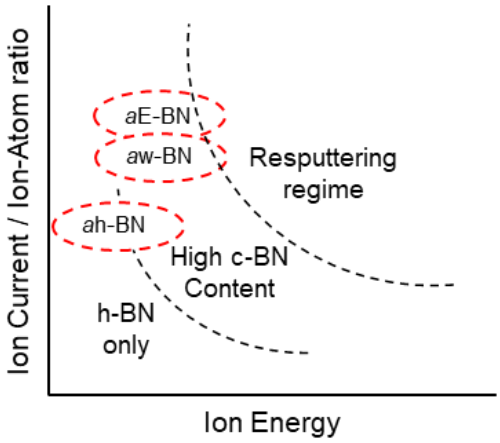

Figure 151 - General schematic showing parameter spaces for the nucleation of different BN structures, adapted from Mirkarimi et al. [3] see Figure 18, the amorphous h-BN, w-BN and E-BN bonded (sp2/sp3) structures seen in this chapter are suggested to reside in the low ion energy high ion current parameter space (at low substrate temperature).

It is still unclear as to what extent the O content in the coatings deposited in this chapter is as a consequence of O contamination during the deposition process or whether it is solely due to moisture reacting with the coating subsequent to the chamber opening. Further study, through XPS depth profiling of a coating transferred directly from the deposition chamber to the UHV XPS instrument is suggested. Surface contamination during transfer is inevitable, however in transferring with minimal time in atmosphere, time for moisture diffusion and reaction from the atmosphere would be reduced. The O content through the thickness could therefore be ascertained.

A suggestion, based upon the high degree of resputtering/etching observed, is that O could be released into the deposition chamber from the substrate holder/jigging. The substrate holder is used for many different coating batches before being thoroughly cleaned via grit blasting. Therefore, as is displayed in Figure 152, there exists a multilayer coating, composed of the previously deposited material, and oxide layers formed when the chamber is opened and substrates are exchanged. As the BN top layer progresses, the layers are gradually etched, providing a supply of oxygen into the chamber.

By using an Ellingham diagram, see sections of this in Figure 153, the ability of a reaction to occur spontaneously at a given temperature and partial pressure of a reactant gas can be ascertained. In the case of boron reacting with oxygen, the equilibrium partial pressure of oxygen at the 100°C coating temperature and at room temperature is less than 10^{-40} atm (not included on Figure 153) [325-327].

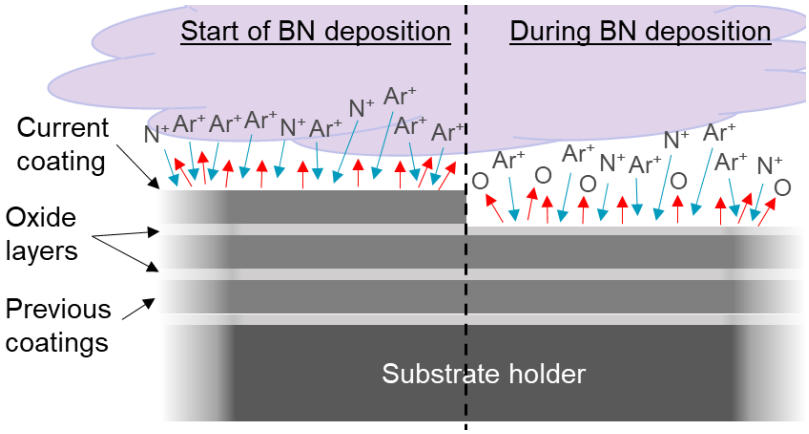

Figure 152 - Schematic detailing a potential source of Oxygen for coating contamination. Coatings from previous depositions build up on the substrate holder, oxidising when the vacuum chamber is opened, this multilayer is etched throughout the BN top layer duration, releasing oxygen into the coating environment.

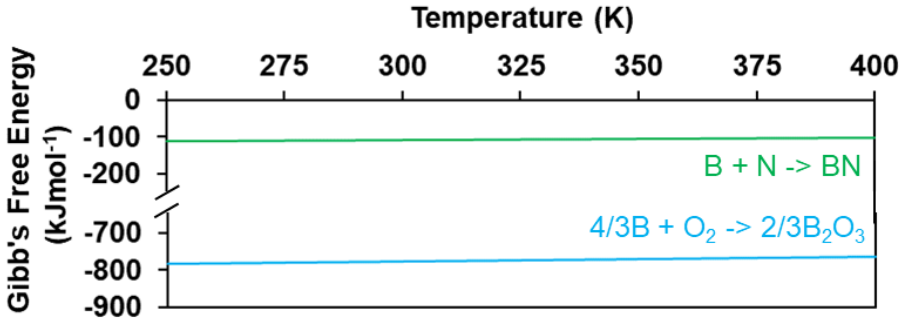

Figure 153 - Excerpt from an Ellingham diagram, showing the standard Gibb's free energy for the formation of BN and B_2O_3, data replotted from Ellingham, Howard, and Balart et al. [325-327].

Given that the Gibb's free energy of the reactions is negative, both reactions can proceed spontaneously during coating and after coating. This diagram does not, however, take into account the rate of reaction, and as the partial pressure of O_2 in the chamber was not measured, the contributions from the coating and post-coating

stages cannot be defined. This is also not necessarily applicable to the plasma based process, as this is not a standard environment.

Coatings 8, 9, 11 and 12 degraded when stored in atmosphere. Here it is important to specify degradation rather than delamination, as the latter suggests that there has been buckling, curling and peeling of the coating material as seen in the BN films deposited by Möller et al. [168]. Instead, in the current work, as is seen in the images in Figures 109, 110, 111, 123, 128 and 141, the coating has not remained intact, but has cracked into irregularly shaped islands < 50 µm wide before being lost from the surface.

The suggested mechanism for the degradation has been published previously in the review and study carried out by Mirkarimi et al. [3, 242] and the review by Batsanov [243], and is related to the reaction of moisture with the deposited coating, with the reaction at the interface of the substrate (or interlayer, whichever is in contact) and the BN layer being the critical failure point. It is suggested that the formation of hydrolised Boron Oxide, which has a lower density than BN contributes to film degradation, in conjunction with film internal stresses. The equation proposed in literature is repeated below.

$$\frac{13}{2}O_2 + 8BN + H_2O \rightarrow [(B_2O_3)_2(OH)] + 4N_2 \qquad (7)$$

This is consistent with the results in the current work, as it appears, given the EDX data in Figures 112, 124 and 142, where the clear surface has a composition similar to the BCN interlayer, that the fracture has occurred at the BCN/BN interface.

Without further analysis using X-TEM or depth profiling with XPS, the mechanism cannot by fully applied to the current work, due the aforementioned O content in the films and also the different remaining coating morphology. If the coatings already contain O are they more or less likely to degrade further, and by what mechanism?

The mechanism in the current work is likely to also be driven by attack from moisture at the edges of the films, exposed by the excessive resputtering/etching as displayed in Figure 149. Hubáček et al. [216] have suggested that dangling bonds at the periphery of structures (such as those that will be present at the film edges) are susceptible to reaction with hydroxyl molecules, with a decrease in crystallinity creating more sites for reaction. However, this is not solely responsible as Coating 8 (Ar15:5, 60 V) exhibited high surface coverage, and was seen to degrade. The stability of Coating 9 (Ar15:5, 100 V) also raises further questions, as it was the only coating to remain adhered and unchanged.

The mechanism is therefore multifactorial, and is suggested to depend on the crystallinity, bonding and composition of the interlayer/BN interface, not analysed in this chapter.

6.3 Conclusions

This chapter, following on from the previous investigation into the deposition of BN multilayer coatings, looked into first steps of scaling up for higher efficiency larger batch sizes, utilizing the enhanced ion bombardment provided by the Closed Field Unbalanced Magnetron Sputtering (CFUBMS) setup. This partially satisfied one aim of this thesis, upscaling. The optimisation of coating parameters to produce adherent coatings, stable in atmospheric humidity has also been attempted, leading to mixed results due to contamination and low deposition temperatures. The lack of success in producing c-BN layers leaves the aim of investigating BN as appropriate for tooling applications unfulfilled. The detailed conclusions are contained in bullet points below:

- All coatings deposited in this chapter were sub-stoichiometric and amorphous, with a N deficiency, regardless of the ratio of Ar/N_2 gas flow. This was suggested to be due preferential resputtering of N from the surface of the coating and low temperature respectively.
- The use of small (57 mm) targets/magnetrons for the deposition of BN, relative to the increased substrate surface area when samples were rotated was seen to promote plasma etching of previously deposited coating over deposition and modification of coating, at substrate bias potentials of > 60 V. This was driven by the use CFUBMS, which increases ion flux to the substrates during coating,
- The use of the higher bias voltages led to significant issues with surface coverage, with coatings receding from the edges, suggested to be due to enhanced etching at the edges of the substrates, exposing substrate material and the sides of coating layers.
- It has been suggested that E-BN has formed at low deposition rates with high, > 100 V, substrate bias potentials. This is due to a complex and not fully understood mechanism, that the high intensity of the plasma field, and the potential for

resputtering and subsequent redeposition of material drive the plasma based formation of mixed sp2 and sp3 BN bonding.

- The use of a blended CN/BCN/BN adhesion layer did not adhere the BN top layer to the substrate, due to the degradation of the BN into hydrolised boron oxide.
- Increasing the ion to neutral atom ratio led to a greater proportion of w-BN bonding compared to E-BN bonding, suggesting that surface based formation and modification mechanisms become more dominant with this parameter change.

7. Overall conclusions

This thesis reports on the investigations of depositing Zn, Ti, Cu and BN onto metal powders, and the deposition of BN onto planar steel substrates.

Contribution to the understanding of powder agitation under vacuum conditions whilst being coated via Magnetron Sputtering has been made. This has been through the discussion of agitation mechanisms, relating to the agglomeration of powder, dependent on material, size distribution, moisture content and rate of deposition of coating material. Three different coating morphologies, distinguished by the time spent dwelling in the coating flux, and the interaction with the container walls have been suggested. Improvements in the reflectivity of powder feedstocks used in LPBF have been realized, and the alloying of materials has been investigated by the coating of powders.

When depositing BN on planar substrates at low temperatures with high ion current at low ion energy, films with mixed phases, of h-BN, c-BN, w-BN and E-BN have been formed. A dependence on ion to atom ratio has been established in the formation of E-BN and w-BN, and mechanisms for this have been presented. Significant contamination and degradation of films was observed and assessed, and mechanisms governing these were proposed.

8. Future Work

Multiple areas of investigation have been identified in this thesis, and others are suggested based on related techniques:

- The limiting deposition rate found in the deposition of BN onto planar substrates should be overcome by the use of larger magnetrons (which allow an improved field of view) and which are designed to survive greater power densities. This would increase the deposition rate to the substrates, allow a more varied control of bias parameters and the increased total power would increase waste heat

transfer to the substrates whilst remaining below the tempering temperature of High Speed Steel tool materials.

- Subsequent to this solution being implemented, a c-BN formation parameter set should be identified, and an investigation analogous to that done by Yang et al. [319] when optimising PDC pulse parameters for Graphit-iC Diamond Like Carbon (DLC) coatings should be carried out to ascertain the dependence in structure formation on the pulsing.
- Further studies utilising the parameters for rotational BN coating used in this thesis, with a focus on the reduction of contamination during coating, and the depth profiling of coatings immediately after deposition should be undertaken to understand the role of O content in the film structures and degradation.
- In an alternative line of investigation, there is potential for investigation of superimposed RF and Pulsed DC sputtering of Boron Nitride for the investigation of improved deposition rates of BN, and the plasma intensities provided by these supplies, similar to the investigations of Stowell et al. [328] into the deposition of transparent conductive oxides
- Similarly the superposition of RF power with HiPIMS processes which provide high current ion bombardment through the ionisation of sputtered target material, and the influence this has on the structures formed at the substrate, similar to the investigation by Schmidt et al. on the HiPIMS of CN_x films [329] should be undertaken.
- Intermediate etching steps interspersed between layer deposition has been shown to increase nucleation sites by the formation of defects and the densification of deposited coating [330]. The introduction of these steps into BN coating recipes could provide a further line of investigation into stress reduction and degradation prevention.

- Plasma treatment of powders similar to the studies and suggestions from Matsubara et al. [331] and Eder et al. [120], where the powder substrate and container are biased have the potential to modify the adhesion of coatings and agitation of powders in PVD powder coating. A potential application for this would be in the reuse of waste powder from LPBF processes, where powder surfaces are contaminated. In-situ plasma etching could provide an alternative to wet chemical methods, undesirable due to harmful waste products [332].
- Optimisation of barrel geometry and agitation in the University of Nottingham powder coating equipment is essential. The initial trials contained in this thesis expose multiple flaws in the design that can be solved by paying close attention to the advances made by the group led by Abe, T. and Eisenmenger-Sittner, C.
- Following updates to the coating rig, further work in depositing BN for uniform doping of ceramic material allowing extended deposition (> 24 h) of BN with agitation should be undertaken. This can then be used to investigate uniform doping of metal powders with ceramics for LPBF for tackling segregation of powder during the recoating step.
- There is potential to combine the deposition of BN with that of AlN. This is desirable as w-AlN and c-BN have somewhat similar lattice parameters, 3.11 and 3.62 (~14 %) mismatch, which would allow epitaxial growth with dislocation formation [27, 230]. The dielectric properties of these materials could be applied to next generation thin film insulation in aircraft and power electronic systems.

9. References

1. Swann S. Magnetron sputtering. Physics in Technology. 1988;19(2):67-75. doi:10.1088/0305-4624/19/2/304.
2. Kelly PJ, Arnell RD. Magnetron sputtering: a review of recent developments and applications. Vacuum. 2000;56(3):159-72. doi:https://doi.org/10.1016/S0042-207X(99)00189-X.
3. Mirkarimi PB, McCarty KF, Medlin DL. Review of advances in cubic boron nitride film synthesis. Materials Science and Engineering: R: Reports. 1997;21(2):47-100. doi:https://doi.org/10.1016/S0927-796X(97)00009-0.
4. Mahathanabodee S, Palathai T, Raadnui S, Tongsri R, Sombatsompop N. Dry sliding wear behavior of SS316L composites containing h-BN and MoS_2 solid lubricants. Wear. 2014;316(1):37-48. doi:https://doi.org/10.1016/j.wear.2014.04.015.
5. Mahathanabodee S, Palathai T, Raadnui S, Tongsri R, Sombatsompop N. Effects of hexagonal boron nitride and sintering temperature on mechanical and tribological properties of SS316L/h-BN composites. Materials and Design,. 2013;46:588-97. doi:https://doi.org/10.1016/j.matdes.2012.11.038.
6. Mattox DM. 7. Physical Sputtering and Sputter Deposition (Sputtering). Handbook of Physical Vapor Deposition (PVD) Processing (2nd Edition): Elsevier; 2010. p. 237-86.
7. Mattox DM. 5. The Low Pressure Plasma Processing Environment. Handbook of Physical Vapor Deposition (PVD) Processing (2nd Edition): Elsevier; 2010. p. 157-93.
8. Sree Harsha KS. Chapter 9 - Nucleation and Growth of Films. In: Sree Harsha KS, editor. Principles of Vapor Deposition of Thin Films. Oxford: Elsevier; 2006. p. 685-829.
9. Sundgren J-E. Physics of Glow Discharge Plasmas and Plasma/Surface Interactions During Thin Film Growth. In: Clausing RE, Horton LL, Angus JC, Koidl P, editors. Diamond and Diamond-like Films and Coatings. Boston, MA: Springer US; 1991. p. 47-71.
10. Ohring M, Knovel. Materials Science of Thin Films: Elsevier Science; 2002.
11. Pfeiffer Vacuum. Introduction to Vacuum Technology/Fundamentals: 1.2.5 Mean Free Path; 2021 [Available from: https://www.pfeiffer-vacuum.com/en/know-how/introduction-to-vacuum-technology/fundamentals/mean-free-path/.
12. Slater JC. Atomic Radii in Crystals. The Journal of Chemical Physics. 1964;41(10):3199-204. doi:10.1063/1.1725697.
13. Mantina M, Chamberlin AC, Valero R, Cramer CJ, Truhlar DG. Consistent van der Waals Radii for the Whole Main Group. The Journal of Physical Chemistry A. 2009;113(19):5806-12. doi:10.1021/jp8111556.
14. Pranevicius L. Vapor Deposition Coating Technologies. In: Tracton A, editor. Coatings Technology Handbook. 3rd ed. Boca Raton: CRC Press; 2006. p. 31-9 to -11.
15. Sree Harsha KS. Chapter 7 - Special Sources. In: Sree Harsha KS, editor. Principles of Vapor Deposition of Thin Films. Oxford: Elsevier; 2006. p. 535-618.
16. Aufderheide BE. Sputtered Thin Film Coatings. In: Tracton A, editor. Coatings Technology Handbook. 3rd ed. Boca Raton: CRC Press; 2006. p. 30-1 to -10.
17. Window B. Recent advances in sputter deposition. Surface and Coatings Technology. 1995;71(2):93-7. doi:https://doi.org/10.1016/0257-8972(95)80024-7.
18. Laing K, Hampshire J, Teer D, Chester G. The effect of ion current density on the adhesion and structure of coatings deposited by magnetron sputter ion plating. Surface and Coatings Technology. 1999;112(1):177-80. doi:https://doi.org/10.1016/S0257-8972(98)00790-7.

19. Mattox DM. 9. Ion Plating and Ion Beam-Assisted Deposition. Handbook of Physical Vapor Deposition (PVD) Processing (2nd Edition): Elsevier; 2010. p. 301-31.
20. Cooke KE, Hampshire J, Southall W, Teer DG. Industrial Application of Pulsed Dc Bias Power Supplies in Closed Field Unbalanced Magnetron Sputter Ion Plating. Surface Engineering. 2004;20(3):189-95. doi:10.1179/026708404225016373.
21. Holmberg K, Matthews A. Coatings Tribology - Properties, Mechanisms, Techniques and Applications in Surface Engineering. 2nd ed: Elsevier; 2009.
22. Arnell RD, Kelly PJ. Recent advances in magnetron sputtering. Surface and Coatings Technology. 1999;112(1):170-6. doi:https://doi.org/10.1016/S0257-8972(98)00749-X.
23. Berg S, Nyberg T. Fundamental understanding and modeling of reactive sputtering processes. Thin Solid Films. 2005;476(2):215-30. doi:https://doi.org/10.1016/j.tsf.2004.10.051.
24. Kelly PJ, Henderson PS, Arnell RD, Roche GA, Carter D. Reactive pulsed magnetron sputtering process for alumina films. Journal of Vacuum Science & Technology A. 2000;18(6):2890-6. doi:10.1116/1.1319679.
25. D. Carter, H. Walde, G. McDonough, G. Roche. Parameter Optimization in Pulsed DC Reactive Sputter Deposition of Aluminum Oxide. 45th Annual Technical Conference Proceedings: The Society of Vacuum Coaters; 2002.
26. Sree Harsha KS. Chapter 4 - Cold Plasma Discharges. In: Sree Harsha KS, editor. Principles of Vapor Deposition of Thin Films. Oxford: Elsevier; 2006. p. 259-365.
27. Frank FC, Van Der Merwe JH, Mott NF. One-dimensional dislocations. II. Misfitting monolayers and oriented overgrowth. Proceedings of the Royal Society of London Series A Mathematical and Physical Sciences. 1949;198(1053):216-25. doi:10.1098/rspa.1949.0096.
28. Mahajan S. Growth Modes. In: Buschow KHJ CR, Flemings M, Ilshner B, Kramer E, Mahajan S, Veyssiere P, editor. Encyclopedia of Materials: Science and Technology: Elsevier; 2001. p. 3683-93.
29. Thornton JA. High Rate Thick Film Growth. Annual Review of Materials Science. 1977;7(1):239-60. doi:10.1146/annurev.ms.07.080177.001323.
30. Movchan BA, Demchishin AV. Structure and properties of thick condensates of nickel, titanium, tungsten, aluminum oxides, and zirconium dioxide in vacuum. Physics of Metals and Metallography. 1969;28:83-90.
31. Kelly PJ, Arnell RD. Development of a novel structure zone model relating to the closed-field unbalanced magnetron sputtering system. Journal of Vacuum Science & Technology A. 1998;16(5):2858-69. doi:10.1116/1.581432.
32. Anders A. A structure zone diagram including plasma-based deposition and ion etching. Thin Solid Films. 2010;518(15):4087-90. doi:https://doi.org/10.1016/j.tsf.2009.10.145.
33. Mattox DM. 10. Atomistic Film Growth and Some Growth-Related Film Properties. Handbook of Physical Vapor Deposition (PVD) Processing (2nd Edition): Elsevier; 2010. p. 333-98.
34. Panjan P, Čekada M, Panjan M, Kek-Merl D. Growth defects in PVD hard coatings. Vacuum. 2009;84(1):209-14. doi:https://doi.org/10.1016/j.vacuum.2009.05.018.
35. Panjan P, Drnovšek A, Gselman P, Čekada M, Panjan M. Review of Growth Defects in Thin Films Prepared by PVD Techniques. Coatings. 2020;10(5):447.
36. Panjan P, Drnovšek A, Mahne N, Čekada M, Panjan M. Surface Topography of PVD Hard Coatings. Coatings. 2021;11(11):1387.
37. Kelly PJ, Hall R, O'Brien J, Bradley JW, Henderson P, Roche G, et al. Studies of mid-frequency pulsed dc biasing. Journal of Vacuum Science & Technology A. 2001;19(6):2856-65. doi:10.1116/1.1410949.

38. Cooke KE, Hamsphire J, Southall W, Teer DG. The industrial application of pulsed DC bias power supplies in closed field unbalanced magnetron sputter ion plating. Surface and Coatings Technology. 2004;177-178:789-94. doi:https://doi.org/10.1016/j.surfcoat.2003.06.009.
39. Rubin B, Topper JL, Yalin AP. Total and differential sputter yields of boron nitride measured by quartz crystal microbalance. Journal of Physics D: Applied Physics. 2009;42(20):205205. doi:10.1088/0022-3727/42/20/205205.
40. Hanby BVT, Stuart BW, Grant C, Moffat J, Blissett J, Gerada C, et al. Dielectric breakdown of alumina thin films produced by pulsed direct current magnetron sputtering. Thin Solid Films. 2018;662:145-54. doi:https://doi.org/10.1016/j.tsf.2018.07.004.
41. Mattox DM. 9.4.1 Bombardment from Gaseous Plasmas. Handbook of Physical Vapor Deposition (PVD) Processing (2nd Edition): Elsevier; 2010.
42. Jimenez O, Audronis M, Leyland A, Flores M, Rodriguez E, Kanakis K, et al. Small grain size zirconium-based coatings deposited by magnetron sputtering at low temperatures. Thin Solid Films. 2015;591:149-55. doi:https://doi.org/10.1016/j.tsf.2014.05.015.
43. Kulisch W, Ulrich S. Parameter spaces for the nucleation and the subsequent growth of cubic boron nitride films. Thin Solid Films. 2003;423(2):183-95. doi:https://doi.org/10.1016/S0040-6090(02)00731-9.
44. Ngo TD, Kashani A, Imbalzano G, Nguyen KTQ, Hui D. Additive manufacturing (3D printing): A review of materials, methods, applications and challenges. Composites Part B: Engineering. 2018;143:172-96. doi:https://doi.org/10.1016/j.compositesb.2018.02.012.
45. Caffrey T, Wohlers T, Campbell I. Wohlers Report 2016. 3D Printing and Additive Manufacturing State of the Industry. Fort Collins Colorado2016.
46. Herzog D, Seyda V, Wycisk E, Emmelmann C. Additive manufacturing of metals. Acta Materialia. 2016;117:371-92. doi:https://doi.org/10.1016/j.actamat.2016.07.019.
47. Clare AT, Mishra RS, Merklein M, Tan H, Todd I, Chechik L, et al. Alloy design and adaptation for additive manufacture. Journal of Materials Processing Technology

2022;299:117358. doi:https://doi.org/10.1016/j.jmatprotec.2021.117358.
48. Gargalis L, Ye J, Strantza M, Rubenchik A, Murray JW, Clare AT, et al. Determining processing behaviour of pure Cu in laser powder bed fusion using direct micro-calorimetry. Journal of Materials Processing Technology

2021;294:117130. doi:https://doi.org/10.1016/j.jmatprotec.2021.117130.
49. Engler S, Ramsayer R, Poprawe R. Process Studies on Laser Welding of Copper with Brilliant Green and Infrared Lasers. Physics Procedia. 2011;12:339-46. doi:https://doi.org/10.1016/j.phpro.2011.03.142.
50. Jadhav SD, Fu D, Deprez M, Ramharter K, Willems D, Van Hooreweder B, et al. Highly conductive and strong $CuSn_{0.3}$ alloy processed via laser powder bed fusion starting from a tin-coated copper powder. Additive Manufacturing. 2020;36:101607. doi:https://doi.org/10.1016/j.addma.2020.101607.
51. Wilthan B, Cagran C, Pottlacher G. Combined DSC and Pulse-Heating Measurements of Electrical Resistivity and Enthalpy of Tungsten, Niobium, and Titanium. International Journal of Thermophysics. 2005;26(4):1017-29. doi:10.1007/s10765-005-6682-z.
52. Silbernagel C, Gargalis L, Ashcroft I, Hague R, Galea M, Dickens P. Electrical resistivity of pure copper processed by medium-powered laser powder bed fusion additive manufacturing for use in electromagnetic applications. Additive Manufacturing. 2019;29:100831. doi:https://doi.org/10.1016/j.addma.2019.100831.
53. Ikeshoji T-T, Nakamura K, Yonehara M, Imai K, Kyogoku H. Selective Laser Melting of Pure Copper. The Journal of The Minerals, Metals & Materials Society

2018;70(3):396-400. doi:10.1007/s11837-017-2695-x.
54. Jadhav SD, Dadbakhsh S, Goossens L, Kruth JP, Van Humbeeck J, Vanmeensel K. Influence of selective laser melting process parameters on texture evolution in pure copper. Journal of Materials Processing Technology

2019;270:47-58. doi:https://doi.org/10.1016/j.jmatprotec.2019.02.022.
55. Bidulsky R, Gobber FS, Bidulska J, Ceroni M, Kvackaj T, Grande MA. Coated Metal Powders for Laser Powder Bed Fusion (L-PBF) Processing: A Review. Metals. 2021;11(11). doi:10.3390/met11111831.
56. Jadhav SD, Vleugels J, Kruth J-P, Van Humbeeck J, Vanmeensel K. Mechanical and electrical properties of selective laser-melted parts produced from surface-oxidized copper powder. Material Design & Processing Communications. 2020;2(2):e94. doi:https://doi.org/10.1002/mdp2.94.
57. Jadhav SD, Dhekne PP, Dadbakhsh S, Kruth J-P, Van Humbeeck J, Vanmeensel K. Surface Modified Copper Alloy Powder for Reliable Laser-based Additive Manufacturing. Additive Manufacturing. 2020;35:101418. doi:https://doi.org/10.1016/j.addma.2020.101418.
58. Lindström V, Liashenko O, Zweiacker K, Derevianko S, Morozovych V, Lyashenko Y, et al. Laser Powder Bed Fusion of Metal Coated Copper Powders. Materials. 2020;13(16):3493.
59. Lassègue P, Salvan C, De Vito E, Soulas R, Herbin M, Hemberg A, et al. Laser powder bed fusion (L-PBF) of Cu and CuCrZr parts: Influence of an absorptive physical vapor deposition (PVD) coating on the printing process. Additive Manufacturing. 2021;39:101888. doi:https://doi.org/10.1016/j.addma.2021.101888.
60. Soro N, Attar H, Brodie E, Veidt M, Molotnikov A, Dargusch MS. Evaluation of the mechanical compatibility of additively manufactured porous Ti–25Ta alloy for load-bearing implant applications. Journal of the Mechanical Behavior of Biomedical Materials

2019;97:149-58. doi:https://doi.org/10.1016/j.jmbbm.2019.05.019.
61. Wang C, Tan XP, Du Z, Chandra S, Sun Z, Lim CWJ, et al. Additive manufacturing of NiTi shape memory alloys using pre-mixed powders. Journal of Materials Processing Technology

2019;271:152-61. doi:https://doi.org/10.1016/j.jmatprotec.2019.03.025.
62. Mussatto A, Groarke R, O'Neill A, Obeidi MA, Delaure Y, Brabazon D. Influences of powder morphology and spreading parameters on the powder bed topography uniformity in powder bed fusion metal additive manufacturing. Additive Manufacturing. 2021;38:101807. doi:https://doi.org/10.1016/j.addma.2020.101807.
63. Shaheen MY, Thornton AR, Luding S, Weinhart T. The influence of material and process parameters on powder spreading in additive manufacturing. Powder Technology. 2021;383:564-83. doi:https://doi.org/10.1016/j.powtec.2021.01.058.
64. Lowther M, Louth S, Davey A, Hussain A, Ginestra P, Carter L, et al. Clinical, industrial, and research perspectives on powder bed fusion additively manufactured metal implants. Additive Manufacturing. 2019;28:565-84. doi:https://doi.org/10.1016/j.addma.2019.05.033.
65. Johnson PB, Christy RW. Optical constants of transition metals: Ti, V, Cr, Mn, Fe, Co, Ni, and Pd. Physical Review B. 1974;9(12):5056-70. doi:10.1103/PhysRevB.9.5056.
66. Johnson PB, Christy RW. Optical Constants of the Noble Metals. Physical Review B. 1972;6(12):4370-9. doi:10.1103/PhysRevB.6.4370.
67. Arblaster JW. Thermodynamic Properties of Silver. Journal of Phase Equilibria and Diffusion. 2015;36(6):573-91. doi:10.1007/s11669-015-0411-5.
68. Fu S, Yang L, Wang P, Wang S, Li Z. Comparison of the Microstructure Evolution and Wear Resistance of Ti_6Al_4V Composite Coatings Reinforced by Hard

Pure or Ni-plated Cubic Boron Nitride Particles Prepared with Laser Cladding on a Ti_6Al_4V Substrate. Coatings. 2020;10(7):702.
69. Mistry PC, Grant DM, Stuart AD, Manickam K, Walker GS. Evolution of catalyst coated atomised magnesium spheres – An alternative thermal storage medium for concentrated solar power applications. International Journal of Hydrogen Energy. 2017;42(47):28453-63. doi:https://doi.org/10.1016/j.ijhydene.2017.09.095.
70. Speidel A, Wadge MD, Gargalis L, Cooper TP, Reynolds W, Grant D, et al. The interaction of volatile metal coatings during the laser powder bed fusion of copper. Journal of Materials Processing Technology

2022;299:117332. doi:https://doi.org/10.1016/j.jmatprotec.2021.117332.
71. Wadge MD, Lowther M, Cooper TP, Reynolds WJ, Speidel A, Carter LN, et al. Tailoring absorptivity of highly reflective Ag powders by pulsed-direct current magnetron sputtering for additive manufacturing processes. Journal of Materials Processing Technology

2023;317:117985. doi:https://doi.org/10.1016/j.jmatprotec.2023.117985.
72. Meyer SF, Hsieh EJ, Burt RJ. R.F. magnetron sputtering of thick platinum coatings on glass microspheres. Thin Solid Films. 1980;72(2):373-8. doi:https://doi.org/10.1016/0040-6090(80)90020-6.
73. Hsieh EJ, Meyer SF. Recent advances in Pt coating of microspheres by a batch magnetron sputtering process. Journal of Vacuum Science and Technology. 1981;18(3):1205-8. doi:10.1116/1.570894.
74. Meyer SF. Metallic coating of microspheres. Journal of Vacuum Science and Technology. 1981;18(3):1198-204. doi:10.1116/1.570893.
75. Müller HR, Ensinger W, Frech G, Wolf GK. A new approach to ion beam modification of powders. Nuclear Instruments and Methods in Physics Research Section B: Beam Interactions with Materials and Atoms. 1994;89(1):357-61. doi:https://doi.org/10.1016/0168-583X(94)95200-0.
76. Ensinger W, Müller HR. The rotating wing drum: An apparatus for ion beam treatment of powders. Review of Scientific Instruments. 1994;65(9):2963-7. doi:10.1063/1.1144585.
77. Ensinger W, Müller HR. Surface modification and coating of powders by ion beam techniques. Materials Science and Engineering: A. 1994;188(1):335-40. doi:https://doi.org/10.1016/0921-5093(94)90389-1.
78. Müller HR, Ensinger WJ. The ion-beam processing of powders. The Journal of The Minerals, Metals & Materials Society

1995;47(4):20-5. doi:10.1007/BF03221144.
79. Ensinger W, Müller HR. Noble metal deposition on aluminum oxide powder surfaces by ion beam sputtering. Nuclear Instruments and Methods in Physics Research Section B: Beam Interactions with Materials and Atoms. 1998;141(1):693-8. doi:https://doi.org/10.1016/S0168-583X(98)00173-6.
80. Ensinger W. Processing of powder surfaces by ion beam techniques. Nuclear Instruments and Methods in Physics Research Section B: Beam Interactions with Materials and Atoms. 1999;148(1):17-24. doi:https://doi.org/10.1016/S0168-583X(98)00825-8.
81. Ensinger W, Müller HR. Surface treatment of aluminum oxide and tungsten carbide powders by ion beam sputter deposition. Surface and Coatings Technology. 2003;163-164:281-5. doi:https://doi.org/10.1016/S0257-8972(02)00490-5.
82. Fernandes CM, Ferreira VM, Senos AMR, Vieira MT. Stainless steel coatings sputter-deposited on tungsten carbide powder particles. Surface and Coatings Technology. 2003;176(1):103-8. doi:https://doi.org/10.1016/S0257-8972(03)00021-5.

83. Fernandes CM, Senos AMR, Vieira MT. Particle surface properties of stainless steel-coated tungsten carbide powders. Powder Technology. 2006;164(3):124-9. doi:https://doi.org/10.1016/j.powtec.2006.03.005.
84. Castanho JM, Vieira MT, Matos M, Trindade B. Nanostructured coated powders for structural net shape components. Journal of Alloys and Compounds. 2007;434-435:383-5. doi:https://doi.org/10.1016/j.jallcom.2006.08.180.
85. Fernandes CM, Senos AMR, Vieira MT, Antunes JM. Mechanical characterization of composites prepared from WC powders coated with Ni rich binders. International Journal of Refractory Metals and Hard Materials. 2008;26(5):491-8. doi:https://doi.org/10.1016/j.ijrmhm.2007.12.001.
86. Vieira MT, Martins AG, Barreiros FM, Matos M, Castanho JM. Surface modification of stainless steel powders for microfabrication. Journal of Materials Processing Technology

2008;201(1):651-6. doi:https://doi.org/10.1016/j.jmatprotec.2007.11.162.
87. Matos M, Castanho JM, Vieira MT. Composite copper/stainless steel coated powders. Journal of Alloys and Compounds. 2009;483(1):460-3. doi:https://doi.org/10.1016/j.jallcom.2008.08.091.
88. Puga JB, Fernandes CM, Vieira MT, Senos AMR. Morphological characterization by scanning electron microscopy of WC powder particles coated with Cu. Microscopy and Microanalysis. 2013;19(S4):145-6. doi:10.1017/S1431927613001347.
89. Xu Z, Yu X, Shen Z. Coating metals on micropowders by magnetron sputtering. China Particuology. 2007;5(5):345-50. doi:https://doi.org/10.1016/j.cpart.2007.06.004.
90. Yu X, Shen Z, Xu Z, Wang S. Fabrication and structural characterization of metal films coated on cenosphere particles by magnetron sputtering deposition. Applied Surface Science. 2007;253(17):7082-8. doi:https://doi.org/10.1016/j.apsusc.2007.02.059.
91. Yu X, Xu Z, Shen Z. Metal copper films deposited on cenosphere particles by magnetron sputtering method. Journal of Physics D: Applied Physics. 2007;40(9):2894-8. doi:10.1088/0022-3727/40/9/034.
92. Yu X, Shen Z. Metal copper films coated on microparticle substrates using an ultrasonic-assisted magnetron sputtering system. Powder Technology. 2008;187(3):239-43. doi:https://doi.org/10.1016/j.powtec.2008.02.017.
93. Yu X, Shen Z. The electromagnetic shielding of Ni films deposited on cenosphere particles by magnetron sputtering method. Journal of Magnetism and Magnetic Materials. 2009;321(18):2890-5. doi:https://doi.org/10.1016/j.jmmm.2009.04.040.
94. Yu X, Shen Z. Photocatalytic TiO_2 films deposited on cenosphere particles by pulse magnetron sputtering method. Vacuum. 2011;85(11):1026-31. doi:https://doi.org/10.1016/j.vacuum.2011.03.010.
95. Smirnov I, Dolgov N, Besov A. Improved adhesion strength, corrosion and wear performance of plasma-sprayed coatings derived from pvd film-coated powders — concept and practice. Machines Technologies Materials. 2014;8(3):28-31.
96. Smirnov IV, Furman VK, Chornyi AV, Dolgov NA, Andreytsev AY, editors. Nanostructured PVD film-coated alumina powders for thermal spraying technologies. 2017 IEEE 7th International Conference Nanomaterials: Application & Properties (NAP); 2017 10-15 Sept. 2017.
97. Hara M, Hatano Y, Abe T, Watanabe K, Naitoh T, Ikeno S, et al. Hydrogen absorption by Pd-coated ZrNi prepared by using Barrel-Sputtering System. Journal of Nuclear Materials. 2003;320(3):265-71. doi:https://doi.org/10.1016/S0022-3115(03)00189-2.
98. Abe T, Akamaru S, Watanabe K. Surface modification of Al_2O_3 ceramic grains using a new RF sputtering system developed for powdery materials. Journal of Alloys

and Compounds. 2004;377(1):194-201. doi:https://doi.org/10.1016/j.jallcom.2003.12.053.
99. Abe T, Akamaru S, Watanabe K, Honda Y. Surface modification of polymer microparticles using a hexagonal-barrel sputtering system. Journal of Alloys and Compounds. 2005;402(1):227-32. doi:https://doi.org/10.1016/j.jallcom.2005.02.097.
100. Akamaru S, Higashide S, Hara M, Abe T. Surface coating of small SiO_2 particles with TiO_2 thin layer by using barrel-sputtering system. Thin Solid Films. 2006;513(1):103-9. doi:https://doi.org/10.1016/j.tsf.2006.01.056.
101. Abe T, Hamatani H, Higashide S, Hara M, Akamaru S. Surface coating of small SiO_2 particles with a WO_3 thin film by barrel-sputtering method. Journal of Alloys and Compounds. 2007;441(1):157-61. doi:https://doi.org/10.1016/j.jallcom.2006.07.132.
102. Taguchi A, Kitami T, Yamamoto H, Akamaru S, Hara M, Abe T. Surface coating with various metals on spherical polymer particles by using barrel sputtering technique. Journal of Alloys and Compounds. 2007;441(1):162-7. doi:https://doi.org/10.1016/j.jallcom.2006.07.131.
103. Taguchi A, Kitami T, Akamaru S, Abe T. Homogeneous surface coating of bolts, nuts, and screws by barrel-sputtering technique. Surface and Coatings Technology. 2007;201(24):9512-7. doi:https://doi.org/10.1016/j.surfcoat.2007.04.019.
104. Abe T, Higashide S, Inoue M, Akamaru S. Surface Modification of Fine Particles with a SnO_2 Film by Using a Polyhedral-Barrel Sputtering System. Plasma Chemistry and Plasma Processing. 2007;27(6):799-811. doi:10.1007/s11090-007-9100-4.
105. Akamaru S, Honda Y, Taguchi A, Abe T. Surface Coating on Aluminum Flakes with Titanium Nitride Layer by Barrel-Sputtering Techniques. Materials Transactions. 2008. doi:10.2320/matertrans.MRA2008014.
106. Akamaru S, Yamamoto H, Abe T. Surface coating of microparticles with tungsten carbide by using the barrel sputtering system. Vacuum. 2008;83(3):633-6. doi:https://doi.org/10.1016/j.vacuum.2008.04.052.
107. Taguchi A, Inoue M, Hiromi C, Tanizawa M, Kitami T, Abe T. Study of the surface morphology of platinum thin films on powdery substrates prepared by the barrel sputtering system. Vacuum. 2008;83(3):575-8. doi:https://doi.org/10.1016/j.vacuum.2008.04.023.
108. Honda Y, Akamaru S, Inoue M, Abe T. Development of a polygonal barrel-plasma enhanced chemical vapor deposition method for preparing powdered materials with a diamond-like carbon film. Chemical Engineering Journal. 2012;209:616-22. doi:https://doi.org/10.1016/j.cej.2012.08.051.
109. Zeng C, Sun J, Yang G, Ooki I, Hayashi K, Yoneyama Y, et al. Highly selective and multifunctional Cu/ZnO/Zeolite catalyst for one-step dimethyl ether synthesis: Preparing catalyst by bimetallic physical sputtering. Fuel. 2013;112:140-4. doi:https://doi.org/10.1016/j.fuel.2013.05.026.
110. Sun J, Li X, Taguchi A, Abe T, Niu W, Lu P, et al. Highly-Dispersed Metallic Ru Nanoparticles Sputtered on H-Beta Zeolite for Directly Converting Syngas to Middle Isoparaffins. ACS Catalysis. 2014;4(1):1-8. doi:10.1021/cs4008842.
111. Sun J, Niu W, Taguchi A, Abe T, Yoneyama Y, Tsubaki N. Combining wet impregnation and dry sputtering to prepare highly-active CoPd/H-ZSM5 ternary catalysts applied for tandem catalytic synthesis of isoparaffins. Catalysis Science & Technology. 2014;4(5):1260-7. doi:10.1039/C3CY01091K.
112. Sun J, Yang G, Ma Q, Ooki I, Taguchi A, Abe T, et al. Fabrication of active Cu–Zn nanoalloys on H-ZSM5 zeolite for enhanced dimethyl ether synthesis via syngas. Journal of Materials Chemistry A. 2014;2(23):8637-43. doi:10.1039/C3TA14936F.

113. Lu P, Sun J, Zhu P, Abe T, Yang R, Taguchi A, et al. Sputtered nano-cobalt on H-USY zeolite for selectively converting syngas to gasoline. Journal of Energy Chemistry. 2015;24(5):637-41. doi:https://doi.org/10.1016/j.jechem.2015.08.004.
114. Inoue M, Takahashi Y, Katagiri M, Abe T, Umeda M. Addition of electrical conductivity to metal oxide particles using the polygonal barrel-sputtering method. Journal of Alloys and Compounds. 2016;670:170-4. doi:https://doi.org/10.1016/j.jallcom.2016.01.224.
115. Akamaru S, Jin L, Nishimura K, Hara M, Abe T, Matsuyama M. Hydrogen sensing ability of Cu particles coated with ferromagnetic Pd–Co layer. International Journal of Hydrogen Energy. 2017;42(25):16305-12. doi:https://doi.org/10.1016/j.ijhydene.2017.05.125.
116. Hell J, Horkel M, Neubauer E, Eisenmenger-Sittner C. Construction and characterization of a sputter deposition system for coating granular materials. Vacuum. 2009;84(4):453-7. doi:https://doi.org/10.1016/j.vacuum.2009.09.007.
117. Horkel M, Mahr H, Hell J, Eisenmenger-Sittner C, Neubauer E. Determination of the thickness of metal coatings on granular diamond materials by spatially resolved optical methods. Vacuum. 2009;84(1):57-60. doi:https://doi.org/10.1016/j.vacuum.2009.04.010.
118. Schmid G, Eisenmenger-Sittner C, Hell J, Horkel M, Keding M, Mahr H. Optimization of a container design for depositing uniform metal coatings on glass microspheres by magnetron sputtering. Surface and Coatings Technology. 2010;205(7):1929-36. doi:https://doi.org/10.1016/j.surfcoat.2010.08.076.
119. Schmid GHS, Eisenmenger-Sittner C. A method for uniformly coating powdery substrates by magnetron sputtering. Surface and Coatings Technology. 2013;236:353-60. doi:https://doi.org/10.1016/j.surfcoat.2013.10.012.
120. Eder A, Schmid GHS, Mahr H, Eisenmenger-Sittner C. Aspects of thin film deposition on granulates by physical vapor deposition. The European Physical Journal D. 2016;70(11):247. doi:10.1140/epjd/e2016-70435-7.
121. Unnikrishnan R, Gardy J, Spencer BF, Kurinjimala R, Dey A, Nekouie V, et al. Functionalization of metallic powder for performance enhancement. Materials and Design

2022;221:110900. doi:https://doi.org/10.1016/j.matdes.2022.110900.
122. Lowe AT, Hosford CD. Magnetron sputter coating of microspherical substrates. Journal of Vacuum Science and Technology. 1979;16(2):197-9. doi:10.1116/1.569906.
123. Albers P, Seibold K, McEvoy AJ, Kiwi J. High-dispersion d.c. sputtered platinum-titania powder catalyst active in ethane hydrogenolysis. The Journal of Physical Chemistry. 1989;93(4):1510-5. doi:10.1021/j100341a064.
124. Schils HW, Heuberger M, Frey H, Jehn HA, Telle R, Raub CJ. Modification of alumina powders by nickel and platinum coating. Materials Science and Engineering: A. 1991;139:185-92. doi:https://doi.org/10.1016/0921-5093(91)90615-T.
125. McEachern R, Alford C, Cook R, Makowiecki D, Wallace R. Sputter-deposited be ablators for NIF target capsules. Fusion Technology. 1997;31(4):435-41. doi:10.13182/FST97-A30798.
126. Wang B, Ji Z, Zimone FT, Janowski GM, Rigsbee JM. A technique for sputter coating of ceramic reinforcement particles. Surface and Coatings Technology. 1997;91(1):64-8. doi:https://doi.org/10.1016/S0257-8972(96)03115-5.
127. Ishikawa J, Tsuji H, Mimura M, Ikemura S, Gotoh Y. Non-scattering technique of ion-implantation into vibrated micro-powders by using a negative-ion beam. Surface and Coatings Technology. 1998;103-104:173-7. doi:https://doi.org/10.1016/S0257-8972(98)00390-9.
128. Kersten H, Schmetz P, Kroesen GMW. Surface modification of powder particles by plasma deposition of thin metallic films. Surface and Coatings

Technology. 1998;108-109:507-12. doi:https://doi.org/10.1016/S0257-8972(98)00604-5.
129. Nikroo A, Baugh W, Steinman DA. Fabrication of Gas-Filled Tungsten-Coated Glass Shells. Fusion Science and Technology. 2004;45(2):202-5. doi:10.13182/FST45-202.
130. Veith GM, Lupini AR, Pennycook SJ, Ownby GW, Dudney NJ. Nanoparticles of gold on γ-Al_2O_3 produced by dc magnetron sputtering. Journal of Catalysis. 2005;231(1):151-8. doi:https://doi.org/10.1016/j.jcat.2004.12.008.
131. Florando J. Report on coating from Teer. Livermore, CA (United States): Lawrence Livermore National Lab. (LLNL); 2006.
132. Poelman H, Eufinger K, Depla D, Poelman D, De Gryse R, Sels BF, et al. Magnetron sputter deposition for catalyst synthesis. Applied Catalysis A: General. 2007;325(2):213-9. doi:https://doi.org/10.1016/j.apcata.2007.02.028.
133. Simões F, Duarte N, Trindade B. Sinterability of mechanically alloyed Ti-37.5Si (at.%) powders coated with a metallic thin layer by sputtering. Reviews on Advanced Materials Science

2008;18:293–6.
134. Baechle DM, Demaree JD, Hirvonen JK, Wetzel ED. Magnetron sputter deposition onto fluidized particle beds. Surface and Coatings Technology. 2013;221:94-103. doi:https://doi.org/10.1016/j.surfcoat.2013.01.032.
135. Fedotov AA, Grigoriev SA, Lyutikova EK, Millet P, Fateev VN. Characterization of carbon-supported platinum nano-particles synthesized using magnetron sputtering for application in PEM electrochemical systems. International Journal of Hydrogen Energy. 2013;38(1):426-30. doi:https://doi.org/10.1016/j.ijhydene.2012.09.121.
136. Yu X, Shen Z, Cai C. Millimeter wave electromagnetic interference shielding by coating expanded polystyrene particles with a copper film using magnetron sputtering. Vacuum. 2009;83(12):1438-41. doi:https://doi.org/10.1016/j.vacuum.2009.05.021.
137. Hirakawa K, Inoue M, Abe T. Methanol oxidation on carbon-supported Pt–Ru and TiO_2 (Pt–Ru/TiO_2/C) electrocatalyst prepared using polygonal barrel-sputtering method. Electrochimica Acta. 2010;55(20):5874-80. doi:https://doi.org/10.1016/j.electacta.2010.05.038.
138. Djokić SS. Fundamentals of Electroless Deposition. In: Wandelt K, editor. Encyclopedia of Interfacial Chemistry. Oxford: Elsevier; 2018. p. 161-73.
139. Vakelis A. Electroless Plating. In: Tracton A, editor. Coatings Technology Handbook. 3rd ed. Boca Raton: CRC Press; 2006. p. 27-1 to -11.
140. Li SF, Geng K, Misra RDK, Cui JY, Ye D, Liu Y, et al. Commercial Scale Uniform Powder Coating for Metal Additive Manufacturing. The Journal of The Minerals, Metals & Materials Society

2020;72(12):4639-47. doi:10.1007/s11837-020-04386-z.
141. Geng K, Yang Y, Li S, Misra RDK, Zhu Q. Enabling high-performance 3D printing of Al powder by decorating with high laser absorbing Co phase. Additive Manufacturing. 2020;32:101012. doi:https://doi.org/10.1016/j.addma.2019.101012.
142. Geng K, Yang Y, Li S, Misra RDK, Zhu Q. A General Strategy for Enhancing 3D Printability of High Laser Reflectivity Pure Aluminum Powder. Metallurgical and Materials Transactions A. 2019;50(11):4970-6. doi:10.1007/s11661-019-05436-1.
143. Zhang J, Katsui H, He Z, Goto T. Spark plasma sintering of cBN(core)/SiO_2(shell) powder prepared by rotary chemical vapor deposition. Journal of Asian Ceramic Societies. 2014;2(3):204-9. doi:https://doi.org/10.1016/j.jascer.2014.04.001.

144. Zhang J, Tu R, Goto T. Densification of SiO_2–cBN composites by using Ni nanoparticle and SiO_2 nanolayer coated cBN powder. Ceramics International. 2012;38(6):4961-6. doi:https://doi.org/10.1016/j.ceramint.2012.02.090.
145. Karches M, Morstein M, Rudolf von Rohr P. Encapsulation of abrasive particles by plasma CVD. Surface and Coatings Technology. 2003;169-170:544-8. doi:https://doi.org/10.1016/S0257-8972(03)00200-7.
146. Klein L C. Solgel Coatings. In: Tracton A, editor. Coatings Technology Handbook. 3rd ed. Boca Raton: CRC Press; 2006. p. 96-1 to -4.
147. Suffredini HB, Tricoli V, Avaca LA, Vatistas N. Sol–gel method to prepare active Pt–RuO_2 coatings on carbon powder for methanol oxidation. Electrochemistry Communications. 2004;6(10):1025-8. doi:https://doi.org/10.1016/j.elecom.2004.08.008.
148. Haraguchi M, Komatsu F, Tajiri K, Okamoto T, Fukui M, Kato S. Fabrication and optical characterization of a TiO_2 thin film on a silica microsphere. Surface Science. 2004;548(1):59-66. doi:https://doi.org/10.1016/j.susc.2003.10.037.
149. Kayani ZN, Bashir Z, Mohsin M, Riaz S, Naseem S. Sol-gel synthesized boron nitride (BN) thin films for antibacterial and magnetic applications. Optik. 2021;243:167502. doi:https://doi.org/10.1016/j.ijleo.2021.167502.
150. Rafaja D, Wüstefeld C, Motylenko M, Schimpf C, Barsukova T, Schwarz MR, et al. Interface phenomena in (super)hard nitride nanocomposites: from coatings to bulk materials. Chemical Society Reviews. 2012;41(15):5081-101. doi:10.1039/C2CS15351C.
151. Mirkarimi PB, Medlin DL, McCarty KF, Dibble DC, Clift WM, Knapp JA, et al. The synthesis, characterization, and mechanical properties of thick, ultrahard cubic boron nitride films deposited by ion-assisted sputtering. Journal of Applied Physics. 1997;82(4):1617-25. doi:10.1063/1.365961.
152. Chen K, Song B, Ravichandran NK, Zheng Q, Chen X, Lee H, et al. Ultrahigh thermal conductivity in isotope-enriched cubic boron nitride. Science. 2020;367(6477):555-9. doi:doi:10.1126/science.aaz6149.
153. Zhang XW. Doping and electrical properties of cubic boron nitride thin films: A critical review. Thin Solid Films. 2013;544:2-12. doi:https://doi.org/10.1016/j.tsf.2013.07.001.
154. Cometto O, Sun B, Tsang SH, Huang X, Koh YK, Teo EHT. Vertically self-ordered orientation of nanocrystalline hexagonal boron nitride thin films for enhanced thermal characteristics. Nanoscale. 2015;7(45):18984-91. doi:10.1039/C5NR05009J.
155. Vel L, Demazeau G, Etourneau J. Cubic boron nitride: synthesis, physicochemical properties and applications. Materials Science and Engineering: B. 1991;10(2):149-64. doi:https://doi.org/10.1016/0921-5107(91)90121-B.
156. McKenzie DR, McFall WD, Smith H, Higgins B, Boswell RW, Durandet A, et al. High pressure phases produced by low energy ion implantation with reference to cubic boron nitride. Nuclear Instruments and Methods in Physics Research Section B: Beam Interactions with Materials and Atoms. 1995;106(1):90-5. doi:https://doi.org/10.1016/0168-583X(95)00684-2.
157. Zhang WJ, Chong YM, Bello I, Lee ST. Nucleation, growth and characterization of cubic boron nitride (cBN) films. Journal of Physics D: Applied Physics. 2007;40(20):6159-74. doi:10.1088/0022-3727/40/20/s03.
158. Li Q, Zhang RQ, Marks LD, Zhang WJ, Bello I. Reactivity of different tBN environments serving as reaction sites in cBN film deposition. Diamond and Related Materials. 2002;11(7):1416-21. doi:https://doi.org/10.1016/S0925-9635(02)00037-7.
159. Batsanov SS, Batsanova LR, Doronin GS, Kutateladze SS, Moroz ÉM, Érenburg RS. Effect of explosions on matter. Formation of dense modifications of boron nitride. Journal of Structural Chemistry. 1969;9(6):913-6. doi:10.1007/BF00744389.

160. Olszyna A, Konwerska-Hrabowska J, Lisicki M. Molecular structure of E-BN. Diamond and Related Materials. 1997;6(5):617-20. doi:https://doi.org/10.1016/S0925-9635(96)00716-9.
161. Pokropivny AV. Structure of the boron nitride E-phase: Diamond lattice of $B_{12}N_{12}$ fullerenes. Diamond and Related Materials. 2006;15(9):1492-5. doi:https://doi.org/10.1016/j.diamond.2005.11.003.
162. Hahn J, Friedrich M, Pintaske R, Schaller M, Kahl N, Zahn DRT, et al. Cubic boron nitride films by d.c. and r.f. magnetron sputtering: layer characterization and process diagnostics. Diamond and Related Materials. 1996;5(10):1103-12. doi:https://doi.org/10.1016/0925-9635(95)00507-2.
163. Yamamoto K, Keunecke M, Bewilogua K, Czigany Z, Hultman L. Structural features of thick c-boron nitride coatings deposited via a graded B–C–N interlayer. Surface and Coatings Technology. 2001;142-144:881-8. doi:https://doi.org/10.1016/S0257-8972(01)01212-9.
164. Reinke S, Kuhr M, Kulisch W. Critical test of the c-BN sputter model. Surface and Coatings Technology. 1995;74-75:723-8. doi:https://doi.org/10.1016/0257-8972(95)08271-9.
165. Abbas Q, Liang H, Shi J, Chen Y, Xia X, Ahmad Au, et al. Growth and characterization of amorphous boron nitride dielectric films on Si via RF sputtering at room temperature. Materials Letters. 2018;227:284-8. doi:https://doi.org/10.1016/j.matlet.2018.05.099.
166. Abendroth B, Gago R, Kolitsch A, Möller W. Stress measurement and stress relaxation during magnetron sputter deposition of cubic boron nitride thin films. Thin Solid Films. 2004;447-448:131-5. doi:https://doi.org/10.1016/S0040-6090(03)01084-8.
167. Sell K, Ulrich S, Nold E, Ye J, Leiste H, Stüber M, et al. The constitution and properties of cubic boron nitride thin films: a comparative study on the influence of bombarding ion energy. Surface and Coatings Technology. 2003;174-175:1121-5. doi:https://doi.org/10.1016/S0257-8972(03)00533-4.
168. Möller J, Reiche D, Bobeth M, Pompe W. Observation of boron nitride thin film delamination due to humidity. Surface and Coatings Technology. 2002;150(1):8-14. doi:https://doi.org/10.1016/S0257-8972(01)01500-6.
169. Kulisch W, Freudenstein R. Deposition of thick cubic boron nitride films — Mechanisms and concepts. Thin Solid Films. 2007;516(2):216-22. doi:https://doi.org/10.1016/j.tsf.2007.06.073.
170. Hahn J, Richter F, Pintaske R, Röder M, Schneider E, Welzel T. Formation of c-BN thin films under reduced ion impact. Surface and Coatings Technology. 1997;92(1):129-34. doi:https://doi.org/10.1016/S0257-8972(96)03178-7.
171. Litvinov D, Taylor CA, Clarke R. Semiconducting cubic boron nitride. Diamond and Related Materials. 1998;7(2):360-4. doi:https://doi.org/10.1016/S0925-9635(97)00216-1.
172. Litvinov D, Clarke R. In situ texture monitoring for growth of oriented cubic boron nitride films. Applied Physics Letters. 1999;74(7):955-7. doi:10.1063/1.123421.
173. Gao W, Li Y, Zhang Y, Yin H. Exploration of Growth Window for Phase-Pure Cubic Boron Nitride Films Prepared in a Pure N_2 Plasma. Coatings. 2018;8(2):82. doi:http://dx.doi.org/10.3390/coatings8020082.
174. Bewilogua K, Keunecke M, Weigel K, Wiemann E. Growth and characterization of thick cBN coatings on silicon and tool substrates. Thin Solid Films. 2004;469-470:86-91. doi:https://doi.org/10.1016/j.tsf.2004.08.061.
175. Wang M-E, Ma G-J, Dong C, Gong S-L. Preparation and characterization of thick cubic boron nitride films. Chinese Physics B. 2014;23(6):066805. doi:10.1088/1674-1056/23/6/066805.

176. Jiang L, Fitzgerald AG, Rose MJ, Lousa A, Gimeno S. Formation of cubic boron nitride films by r.f. magnetron sputtering. Surface and Interface Analysis. 2002;34(1):732-4. doi:10.1002/sia.1399.
177. Li Q, Marks L, Lifshitz Y, Lee S, Bello I. Controlling the nucleation environment of c-BN films and their related properties. Physical Review B. 2002;30. doi:10.1103/PhysRevB.65.045415.
178. Wentzcovitch RM, Chang KJ, Cohen ML. Electronic and structural properties of BN and BP. Physical Review B. 1986;34(2):1071-9. doi:10.1103/PhysRevB.34.1071.
179. Chakrabarty K, Baker PA, Vijayan VM, Catledge SA. Bias-Enhanced Formation of Metastable and Multiphase Boron Nitride Coating in Microwave Plasma Chemical Vapor Deposition. Materials (Basel). 2021;14(23):7167. doi:10.3390/ma14237167.
180. Wang JB, Zhong XL, Zhang CY, Huang BQ, Yang GW. Explosion Phase Formation of Nanocrystalline Boron Nitrides Upon Pulsed-Laser-Induced Liquid/Solid Interfacial Reaction. Journal of Materials Research. 2003;18(12):2774-8. doi:10.1557/JMR.2003.0387.
181. Zhu PW, Zhao YN, Wang B, He Z, Li DM, Zou GT. Prepared Low Stress Cubic Boron Nitride Film by Physical Vapor Deposition. Journal of Solid State Chemistry. 2002;167(2):420-4. doi:https://doi.org/10.1006/jssc.2002.9647.
182. Eremets MI, Gauthier M, Polian A, Chervin JC, Besson JM, Dubitskii GA, et al. Optical properties of cubic boron nitride. Physical Review B. 1995;52(12):8854-63. doi:10.1103/PhysRevB.52.8854.
183. Fahy S. Calculation of the strain-induced shifts in the infrared-absorption peaks of cubic boron nitride. Physical Review B. 1995;51(18):12873-5. doi:10.1103/PhysRevB.51.12873.
184. Pascallon J, Stambouli V, Ilias S, Bouchier D, Nouet G, Silva F, et al. Microstructure of c-BN thin films deposited on diamond films. Diamond and Related Materials. 1999;8(2):325-30. doi:https://doi.org/10.1016/S0925-9635(98)00362-8.
185. Zhou ZF, Bello I, Kremnican V, Fung MK, Lai KH, Li KY, et al. Formation of cubic boron nitride films on nickel substrates. Thin Solid Films. 2000;368(2):292-6. doi:https://doi.org/10.1016/S0040-6090(00)00785-9.
186. Gimeno S, Andújar JL, Lousa A. Cubic boron nitride thin films by tuned r.f. magnetron sputtering. Diamond and Related Materials. 1997;6(5):604-7. doi:https://doi.org/10.1016/S0925-9635(96)00617-6.
187. Li Q, Zhou ZF, Lee CS, Lee ST, Bello I. Synthesis and characterization of cubic boron nitride films: substrate bias and ion flux effects. Diamond and Related Materials. 2001;10(9):1886-91. doi:https://doi.org/10.1016/S0925-9635(01)00425-3.
188. Kester DJ, Ailey KS, Lichtenwalner DJ, Davis RF. Growth and characterization of cubic boron nitride thin films. Journal of Vacuum Science & Technology A. 1994;12(6):3074-81. doi:10.1116/1.578938.
189. Ronning C, Feldermann H, Hofsäss H. Growth, doping and applications of cubic boron nitride thin films. Diamond and Related Materials. 2000;9(9):1767-73. doi:https://doi.org/10.1016/S0925-9635(00)00299-5.
190. Friedmann TA, Mirkarimi PB, Medlin DL, McCarty KF, Klaus EJ, Boehme DR, et al. Ion-assisted pulsed laser deposition of cubic boron nitride films. Journal of Applied Physics. 1994;76(5):3088-101. doi:10.1063/1.357491.
191. Schütze A, Bewilogua K, Lüthje H, Kouptsidis S, Jäger S. Cubic boron nitride films prepared by reactive r.f. and d.c. sputtering from different boron containing targets. Surface and Coatings Technology. 1995;74-75:717-22. doi:https://doi.org/10.1016/0257-8972(95)08312-X.
192. Gimeno S, Andu´jar JL, Bertran E, Lousa A. Growth of boron nitride thin films by tuned substrate RF magnetron sputtering. Diamond and Related Materials. 1996;5(3):535-8. doi:https://doi.org/10.1016/0925-9635(96)80074-4.

193. Schütze A, Bewilogua K, Lüthje H, Kouptsidis S, Gaertner M. Improvement of the adhesion of sputtered cubic boron nitride films. Surface and Coatings Technology. 1997;97(1):33-8. doi:https://doi.org/10.1016/S0257-8972(97)00373-3.
194. Ye J, Rothhaar U, Oechsner H. Conditions for the formation of cubic boron nitride films by r.f. magnetron sputtering. Surface and Coatings Technology. 1998;105(1):159-64. doi:https://doi.org/10.1016/S0257-8972(98)00479-4.
195. Yamamoto K, Keunecke M, Bewilogua K. Deposition of well adhering cBN films up to 2 µm thickness by B–C–N gradient layer system. Thin Solid Films. 2000;377-378:331-9. doi:https://doi.org/10.1016/S0040-6090(00)01364-X.
196. Schütze A, Bewilogua K, Lüthje H, Kouptsidis S. Preparation of cubic boron nitride films by reactive sputtering from a boron carbide target. Diamond and Related Materials. 1996;5(10):1130-5. doi:https://doi.org/10.1016/0925-9635(96)00530-4.
197. Ulrich S, Scherer J, Schwan J, Barzen I, Jung K, Scheib M, et al. Preparation of cubic boron nitride films by radio frequency magnetron sputtering and radio frequency ion plating. Applied Physics Letters. 1996;68(7):909-11. doi:10.1063/1.116227.
198. Kulikovsky VY, Shaginyan LR, Vereschaka VM, Hatynenko NG. Preparation of thin hard boron nitride films by r.f. magnetron sputtering. Diamond and Related Materials. 1995;4(2):113-9. doi:https://doi.org/10.1016/0925-9635(94)00224-F.
199. Zhang WJ, Matsumoto S, Li Q, Bello I, Lee ST. Growth Behavior of Cubic Boron Nitride Films in a Two-Step Process: Changing Bias Voltage, Gas Composition, and Substrate Temperature. Advanced Functional Materials. 2002;12(4):250-4. doi:10.1002/1616-3028(20020418)12:4<250::Aid-adfm250>3.0.Co;2-l.
200. Kessler G, Bauer HD, Pompe W, Scheibe HJ. Laser pulse vapour deposition of polycrystalline wurtzite-type BN. Thin Solid Films. 1987;147(1):L45-L50. doi:https://doi.org/10.1016/0040-6090(87)90046-0.
201. Kamenetskikh AS, Gavrilov NV, Koryakova OV, Cholakh SO. BN coatings deposition by magnetron sputtering of B and BN targets in electron beam generated plasma. Journal of Physics: Conference Series. 2017;857:012017. doi:10.1088/1742-6596/857/1/012017.
202. Zhou ZF, Bello I, Lei MK, Li KY, Lee CS, Lee ST. Synthesis and characterization of boron carbon nitride films by radio frequency magnetron sputtering. Surface and Coatings Technology. 2000;128-129:334-40. doi:https://doi.org/10.1016/S0257-8972(00)00600-9.
203. Singh B, Kaur G, Singh P, Singh K, Kumar B, Vij A, et al. Nanostructured Boron Nitride With High Water Dispersibility For Boron Neutron Capture Therapy. Scientific Reports. 2016;6(1):35535. doi:10.1038/srep35535.
204. Ren J, Malfatti L, Enzo S, Carbonaro CM, Calvillo L, Granozzi G, et al. Boron oxynitride two-colour fluorescent dots and their incorporation in a hybrid organic-inorganic film. Journal of Colloid and Interface Science. 2020;560:398-406. doi:https://doi.org/10.1016/j.jcis.2019.10.020.
205. Chien SC, Chattopadhyay S, Chen LC, Lin ST, Chen KH. Mechanical properties of amorphous boron carbon nitride films produced by dual gun sputtering. Diamond and Related Materials. 2003;12(9):1463-71. doi:https://doi.org/10.1016/S0925-9635(03)00175-4.
206. Tang C, Bando Y, Huang Y, Zhi C, Golberg D. Synthetic Routes and Formation Mechanisms of Spherical Boron Nitride Nanoparticles. Advanced Functional Materials. 2008;18(22):3653-61. doi:https://doi.org/10.1002/adfm.200800493.
207. Wang J, Gu Y, Li Z, Wang W, Fu Z. Growth and Optical Properties of Explosion Phase Boron Nitride Octahedron Crystals. Crystal Growth & Design. 2013;13(2):599-605. doi:10.1021/cg3012525.

208. Geick R, Perry CH, Rupprecht G. Normal Modes in Hexagonal Boron Nitride. Physical Review. 1966;146(2):543-7. doi:10.1103/PhysRev.146.543.
209. Batsanov SS, Blokhina GE, Deribas AA. The effects of explosions on materials. Journal of Structural Chemistry. 1965;6(2):209-13. doi:10.1007/BF00745942.
210. Matsuoka M, Langhi Jr. MP, Isotani S, Chubaci JFD. Fourier transform infrared spectroscopy analysis of thin boron nitride films prepared by ion beam assisted deposition. Physica Status Solidi C. 2014;11(3-4):509-12. doi:https://doi.org/10.1002/pssc.201300544.
211. Baraton MI, Merle T, Quintard P, Lorenzelli V. Surface activity of a boron nitride powder: a vibrational study. Langmuir. 1993;9(6):1486-91. doi:10.1021/la00030a011.
212. Baraton M-I, Merle T, Quintard P, Lorenzelli V. Surface Species on a submicronic boron nitride powder - a starting FT-IR characterization. Journal of Molecular Structure. 1992;267:429-34. doi:https://doi.org/10.1016/0022-2860(92)87068-7.
213. James AL, Jasuja K. Chelation assisted exfoliation of layered borides towards synthesizing boron based nanosheets. RSC Advances. 2017;7(4):1905-14. doi:10.1039/C6RA26658D.
214. Baraton MI, Boulanger L, Cauchetier M, Lorenzelli V, Luce M, Merle T, et al. Nanometric boron nitride powders: Laser synthesis, characterization and FT-IR surface study. Journal of the European Ceramic Society. 1994;13(4):371-8. doi:https://doi.org/10.1016/0955-2219(94)90013-2.
215. Kamitsos EI, Karakassides MA, Chryssikos GD. Vibrational spectra of magnesium-sodium-borate glasses. 2. Raman and mid-infrared investigation of the network structure. The Journal of Physical Chemistry. 1987;91(5):1073-9. doi:10.1021/j100289a014.
216. Hubáček M, Sato T, Ishii T. A Coexistence of Boron Nitride and Boric Oxide. Journal of Solid State Chemistry. 1994;109(2):384-90. doi:https://doi.org/10.1006/jssc.1994.1117.
217. Nose K, Oba H, Yoshida T. Electric conductivity of boron nitride thin films enhanced by in situ doping of zinc. Applied Physics Letters. 2006;89(11):112124. doi:10.1063/1.2354009.
218. Guimon C, Gonbeau D, Pfister-Guillouzo G, Dugne O, Guette A, Naslain R, et al. XPS study of BN thin films deposited by CVD on SiC plane substrates. Surface and Interface Analysis. 1990;16(1-12):440-5. doi:https://doi.org/10.1002/sia.740160191.
219. Lei MK, Li Q, Zhou ZF, Bello I, Lee CS, Lee ST. Characterization and optical investigation of BCN film deposited by RF magnetron sputtering. Thin Solid Films. 2001;389(1):194-9. doi:https://doi.org/10.1016/S0040-6090(01)00904-X.
220. Stewart DM, Lad RJ. Enhanced Crystallinity of h-BN Films Induced by Substrate Bias During Magnetron Sputtering. Physica Status Solidi B. 2018;255(3):1700458. doi:10.1002/pssb.201700458.
221. Nakao S, Sonoda T, Tsugawa K, Choi J, Kato T. Effects of nitrogen gas ratio on composition and microstructure of BCN films prepared by RF magnetron sputtering. Vacuum. 2009;84(5):642-7. doi:https://doi.org/10.1016/j.vacuum.2009.06.012.
222. Liu B, Yan S, Song Z, Liu M, Ji X, Yang W, et al. One-Step Synthesis of Boron Nitride Quantum Dots: Simple Chemistry Meets Delicate Nanotechnology. Chemistry – A European Journal. 2016;22(52):18899-907. doi:https://doi.org/10.1002/chem.201603935.
223. Huang C, Ye W, Liu Q, Qiu X. Dispersed Cu_2O Octahedrons on h-BN Nanosheets for p-Nitrophenol Reduction. ACS Applied Materials & Interfaces

2014;6(16):14469-76. doi:10.1021/am5037737.

224. Qu J, Li Q, Luo C, Cheng J, Hou X. Characterization of Flake Boron Nitride Prepared from the Low Temperature Combustion Synthesized Precursor and Its Application for Dye Adsorption. Coatings. 2018;8(6):214.
225. Chan KF, Ong CW, Choy CL, Kwok RWM. Dual ion beam deposited boron-rich boron nitride films. Journal of Vacuum Science & Technology A. 1999;17(5):2944-9. doi:10.1116/1.581965.
226. Schild D, Ulrich S, Ye J, Stüber M. XPS investigations of thick, oxygen-containing cubic boron nitride coatings. Solid State Sciences. 2010;12(11):1903-6. doi:https://doi.org/10.1016/j.solidstatesciences.2010.05.029.
227. Trehan R, Lifshitz Y, Rabalais JW. Auger and x-ray electron spectroscopy studies of hBN, cBN, and N+2 ion irradiation of boron and boron nitride. Journal of Vacuum Science & Technology A. 1990;8(6):4026-32. doi:10.1116/1.576471.
228. Bejarano G, Caicedo JM, Baca E, Prieto P, Balogh AG, Enders S. Deposition of B_4C/BCN/c-BN multilayered thin films by r.f. magnetron sputtering. Thin Solid Films. 2006;494(1):53-7. doi:https://doi.org/10.1016/j.tsf.2005.08.192.
229. Shtansky DV, gt, Yamada-Takamura Y, Yoshida T, Ikuhara Y. Mechanism of nucleation and growth of cubic boron nitride thin films. Science and Technology of Advanced Materials. 2000;1(4):219-25. doi:10.1016/S1468-6996(01)00004-3.
230. Feldermann H, Ronning C, Hofsäss H, Huang YL, Seibt M. Cubic boron nitride thin film heteroepitaxy. Journal of Applied Physics. 2001;90(7):3248-54. doi:10.1063/1.1392957.
231. Keunecke M, Yamamoto K, Bewilogua K. Mechanical and tribological properties of cBN films on silicon and tungsten carbide substrates. Thin Solid Films. 2001;398-399:142-9. doi:https://doi.org/10.1016/S0040-6090(01)01393-1.
232. Li Q, Bello I, Marks LD, Lifshitz Y, Lee ST. Orientation effects in tBN/cBN interfaces: A transmission electron microscopic study. Applied Physics Letters. 2002;80(1):46-8. doi:10.1063/1.1431394.
233. Medlin DL, Friedmann TA, Mirkarimi PB, Cardinale GF, McCarty KF. Crystallographic texture in cubic boron nitride thin films. Journal of Applied Physics. 1996;79(7):3567-71. doi:10.1063/1.361381.
234. Wong SF, Ong CW, Pang GKH, Li Q, Lau WM. Removal of sp2-boron nitride transition layer in the growth of cubic boron nitride films. Diamond and Related Materials. 2004;13(9):1632-7. doi:https://doi.org/10.1016/j.diamond.2004.01.038.
235. Bello I, Chan CY, Zhang WJ, Chong YM, Leung KM, Lee ST, et al. Deposition of thick cubic boron nitride films: The route to practical applications. Diamond and Related Materials. 2005;14(3):1154-62. doi:https://doi.org/10.1016/j.diamond.2004.12.041.
236. Reinke S, Kuhr M, Kulisch W, Kassing R. Recent results in cubic boron nitride deposition in light of the sputter model. Diamond and Related Materials. 1995;4(4):272-83. doi:https://doi.org/10.1016/0925-9635(94)05303-0.
237. Reinke S, Freudenstein R, Kulisch W. On the role of ion bombardment in cubic boron nitride deposition. Surface and Coatings Technology. 1997;97(1):263-9. doi:https://doi.org/10.1016/S0257-8972(97)00219-3.
238. Hofsäss H, Feldermann H, Merk R, Sebastian M, Ronning C. Cylindrical spike model for the formation of diamondlike thin films by ion deposition. Applied Physics A. 1998;66(2):153-81. doi:10.1007/s003390050652.
239. Mirkarimi PB, McCarty KF, Medlin DL, Wolfer WG, Friedmann TA, Klaus EJ, et al. On the role of ions in the formation of cubic boron nitride films by ion-assisted deposition. Journal of Materials Research. 1994;9(11):2925-38. doi:10.1557/JMR.1994.2925.
240. McKenzie DR, McFall WD, Sainty WG, Davis CA, Collins RE. Compressive stress induced formation of cubic boron nitride. Diamond and Related Materials. 1993;2(5):970-6. doi:https://doi.org/10.1016/0925-9635(93)90260-9.

241. McKenzie DR, McFall WD, Reisch S, James BW, Falconer IS, Boswell RW, et al. Synthesis of cubic boron nitride thin films. Surface and Coatings Technology. 1996;78(1):255-62. doi:https://doi.org/10.1016/0257-8972(95)02419-0.
242. Cardinale GF, Mirkarimi PB, McCarty KF, Klaus EJ, Medlin DL, Clift WM, et al. Effects of ambient conditions on the adhesion of cubic boron nitride films on silicon substrates. Thin Solid Films. 1994;253(1):130-5. doi:https://doi.org/10.1016/0040-6090(94)90307-7.
243. Batsanov SS. Features of phase transformations in boron nitride. Diamond and Related Materials. 2011;20(5):660-4. doi:https://doi.org/10.1016/j.diamond.2011.03.020.
244. Kim I-H, Kim S-H, Kim K-B. Delamination mechanism in relation to adhesion of cubic boron nitride. Journal of Vacuum Science & Technology A. 1998;16(4):2295-9. doi:10.1116/1.581412.
245. Lüthje H, Bewilogua K, Daaud S, Johansson M, Hultman L. Preparation of cubic boron nitride films by use of electrically conductive boron carbide targets. Thin Solid Films. 1995;257(1):40-5. doi:https://doi.org/10.1016/0040-6090(94)06341-9.
246. Ulrich S, Ye J, Stüber M. Influence of Ar–N_2 gas composition on the magnetron-sputter deposition of cubic boron nitride films. Surface and Coatings Technology. 2010;205:S96-S8. doi:https://doi.org/10.1016/j.surfcoat.2010.05.032.
247. Ding XZ, Zeng XT, Xie H. Cubic boron nitride films deposited by unbalanced RF magnetron sputtering and pulsed DC substrate bias. Thin Solid Films. 2003;429(1):22-7. doi:https://doi.org/10.1016/S0040-6090(03)00142-1.
248. Pat S, Şilik E, Musaoğlu C, Özen S, Mohammadigharehbagh R, Yudar HH, et al. Cubic BN thin film deposition by a RF magnetron sputtering. Vacuum. 2018;157:31-5. doi:https://doi.org/10.1016/j.vacuum.2018.08.027.
249. Uhlmann E, Bräuer G, Wiemann E, Keunecke M. CBN coatings on cutting tools. Annals of the German Academic Society for Production Engineering. 2004;11(No. 1):45-8.
250. Lattemann M, Ulrich S, Ye J. New approach in depositing thick, layered cubic boron nitride coatings by oxygen addition—structural and compositional analysis. Thin Solid Films. 2006;515(3):1058-62. doi:https://doi.org/10.1016/j.tsf.2006.07.069.
251. Ulrich S, Nold E, Sell K, StÜber M, Ye J, Ziebert C, editors. Nano-Scale, Multi-Functional, Cubic Boron Nitride Coatings. Functional Properties of Nanostructured Materials; 2006; Dordrecht: Springer Netherlands.
252. Ulrich S, Nold E, Sell K, Stüber M, Ye J, Ziebert C. Constitution of thick oxygen-containing cubic boron nitride films. Surface and Coatings Technology. 2006;200(22):6465-8. doi:https://doi.org/10.1016/j.surfcoat.2005.11.118.
253. Kimura T, Yamamoto K, Yugo S. Humidity Sensitive Electrical Conduction of Polycrystalline Boron Nitride Films. Japanese Journal of Applied Physics. 1978;17(10):1871-2. doi:10.1143/jjap.17.1871.
254. Hannache H, Naslain R, Bernard C. Boron nitride chemical vapour infiltration of fibrous materials from BCl_3-NH_3-H_2 or BF_3-NH_3 mixtures: A thermodynamic and experimental approach. Journal of the Less Common Metals. 1983;95(2):221-46. doi:https://doi.org/10.1016/0022-5088(83)90517-9.
255. D A. Lelonis, J W. Tereshko, C M. Andersen. Boron Nitride Powder - A High-Performance Alternative for Solid Lubrication. GE Advanced Ceramics [Internet]. 2011:[4 p.]. Available from: www.advceramics.com.
256. Madhav Reddy K, Hwang C, Ornek M, Miller SL, Mayo WE, Burgess A, et al. Observations of nanocrystalline cubic boron nitride formed with plasma spraying. Acta Materialia. 2016;116:155-65. doi:https://doi.org/10.1016/j.actamat.2016.06.038.
257. Shivalingaiah K, Sridhar KS, Sethuram D, Murthy KVS, Koppad PG, Ramesh CS. HVOF sprayed Inconel 718/cubic boron nitride composite coatings: microstructure, microhardness and slurry erosive behaviour. Materials Research Express. 2019;6(12):1265i8. doi:10.1088/2053-1591/ab7067.

258. Padmavathi G, Sarada BN, Shanmuganatan SP, Ramesha H, Padmini BV, Krishnamurthy R. A comparative assessment on the characteristics of HVOF sprayed cermet coatings. Australian Journal of Mechanical Engineering. 2022:1-23. doi:10.1080/14484846.2022.2100044.
259. Carpenter Additive. Technical Data Sheet CT PowderRange 315L F. 2019.
260. Cullity BD, Stock SR. Elements of X-ray diffraction. 3rd ed. ed. Stock SR, editor. Upper Saddle River, N.J.: Prentice Hall; 2001.
261. Schrader B. Ch2: General survey of vibrational spectroscopy. Infrared and Raman Spectroscopy: Methods and Applications: VCH Publishers. Inc; 1995. p. 7-61.
262. Kaczmarek K, Leniart A, Lapinska B, Skrzypek S, Lukomska-Szymanska M. Selected Spectroscopic Techniques for Surface Analysis of Dental Materials: A Narrative Review. Materials. 2021;14(10):2624.
263. Kendall DS. Infrared Spectroscopy of Coatings. In: Tracton A, editor. Coatings Technology Handbook. 3rd ed. Boca Raton: CRC Press; 2006. p. 8-1 to 8-.
264. Gurker N, Ebel MF, Ebel H. Imaging XPS—A new technique, I—principles. Surface and Interface Analysis. 1983;5(1):13-9. doi:https://doi.org/10.1002/sia.740050105.
265. de la Guardia M, Armenta S. Chapter 6 - Multianalyte determination in spectroscopy. In: Guardia MDL, Armenta S, editors. Comprehensive Analytical Chemistry. 57: Elsevier; 2011. p. 121-56.
266. The British Standards Institution. Metallic materials - Instrumented indentation test of hardness and materials parameters. 14577:2015: BSI Standards; 2015.
267. Boronin AI, Koscheev SV, Zhidomirov GM. XPS and UPS study of oxygen states on silver. Journal of Electron Spectroscopy and Related Phenomena. 1998;96(1):43-51. doi:https://doi.org/10.1016/S0368-2048(98)00221-7.
268. Semicore. Table of Sputtering Yield Rates, Livermore, CA: Semicore; 2022 [cited 2022. Available from: https://www.semicore.com/reference/sputtering-yields-reference.
269. Meier C, Weissbach R, Weinberg J, Wall WA, Hart AJ. Critical influences of particle size and adhesion on the powder layer uniformity in metal additive manufacturing. Journal of Materials Processing Technology

2019;266:484-501. doi:https://doi.org/10.1016/j.jmatprotec.2018.10.037.
270. Clayton J. Chapter 17 - An Introduction to Powder Characterization. In: Narang AS, Badawy SIF, editors. Handbook of Pharmaceutical Wet Granulation: Academic Press; 2019. p. 569-613.
271. Meier C, Weissbach R, Weinberg J, Wall WA, John Hart A. Modeling and characterization of cohesion in fine metal powders with a focus on additive manufacturing process simulations. Powder Technology. 2019;343:855-66. doi:https://doi.org/10.1016/j.powtec.2018.11.072.
272. Merstallinger A, Sales M, Semerad E, Dunn BD. Assessment of Cold Welding Between Separable Contact Surfaces Due to Impact and Fretting under Vacuum. ESA Scientific & Technical Memoranda. 2009;279:57.
273. Akande WO, Cao Y, Yao N, Soboyejo W. Adhesion and the cold welding of gold-silver thin films. Journal of Applied Physics. 2010;107(4):043519. doi:10.1063/1.3305791.
274. Gencoa Ltd. Universal sputter process calculator [Webpage form]. 2023 [Available from: https://www.gencoa.com/customers/apps/sputtercalc/index.php?mat_but=mat1.
275. Akamaru S, Ishikawa F, Nishimura K, Abe T, Matsuyama M. Effects of Metal (Ag, Sn and Zn) Nanoparticles Inserted into MgB_2 Grain Boundaries on Transport and Superconducting Properties. Materials Transactions. 2013;54(12):2258-64. doi:10.2320/matertrans.M2013254.

276. Inoue M, Shima A, Miyazaki K, Lu B, Sone Y, Abe T. Effects of sputtering conditions on the activities of high-performance CO_2 methanation catalysts prepared by a co-sputtering technique using the polygonal barrel system. Applied Catalysis A: General. 2020;597:117557. doi:https://doi.org/10.1016/j.apcata.2020.117557.
277. Yu J, Sun X, Tong X, Zhang J, Li J, Li S, et al. Ultra-high thermal stability of sputtering reconstructed Cu-based catalysts. Nature Communications. 2021;12(1):7209. doi:10.1038/s41467-021-27557-1.
278. Abadias G, Chason E, Keckes J, Sebastiani M, Thompson GB, Barthel E, et al. Review Article: Stress in thin films and coatings: Current status, challenges, and prospects. Journal of Vacuum Science & Technology A. 2018;36(2):020801. doi:10.1116/1.5011790.
279. Böhme O, Cebollada A, Yang S, Teer DG, Albella JM, Román E. Substrate/layer interface of amorphous-carbon hard coatings. Journal of Applied Physics. 2000;88(4):1861-6. doi:10.1063/1.1305553.
280. Field SK, Jarratt M, Teer DG. Tribological properties of graphite-like and diamond-like carbon coatings. Tribology International

2004;37(11):949-56. doi:https://doi.org/10.1016/j.triboint.2004.07.012.
281. Yang S, Li X, Renevier NM, Teer DG. Tribological properties and wear mechanism of sputtered C/Cr coating. Surface and Coatings Technology. 2001;142-144:85-93. doi:https://doi.org/10.1016/S0257-8972(01)01147-1.
282. Yang S, Teer DG. Investigation of sputtered carbon and carbon/chromium multi-layered coatings. Surface and Coatings Technology. 2000;131(1):412-6. doi:https://doi.org/10.1016/S0257-8972(00)00859-8.
283. Guanghua Y, Xinmin H, Yanqing W, Xingguo Q, Ming Y, Zuoming C, et al. Effects of heat treatment on mechanical properties of H13 steel. Metal Science and Heat Treatment

2010;52:393-5. doi:10.1007/s11041-010-9288-4.
284. Tran BH, Tieu K, Wan S, Zhu H, Cui S, Wang L. Understanding the tribological impacts of alkali element on lubrication of binary borate melt. RSC Advances. 2018;8(51):28847-60. doi:10.1039/C8RA04658A.
285. Yang L, May PW, Yin L, Smith JA, Rosser KN. Ultra fine carbon nitride nanocrystals synthesized by laser ablation in liquid solution. Journal of Nanoparticle Research. 2007;9(6):1181-5. doi:10.1007/s11051-006-9192-4.
286. Zagho MM, Dawoud HD, Bensalah N, Altahtamouni TM. A brief overview of RF sputtering deposition of boron carbon nitride (BCN) thin films. Emergent Materials. 2019;2(1):79-93. doi:10.1007/s42247-018-0018-9.
287. Harrington GF, Santiso J. Back-to-Basics tutorial: X-ray diffraction of thin films. Journal of Electroceramics. 2021;47(4):141-63. doi:10.1007/s10832-021-00263-6.
288. Zhang WJ, Bello I, Lifshitz Y, Lee ST. Recent Advances in Cubic Boron Nitride Deposition. MRS Bulletin. 2003;28(3):184-8. doi:10.1557/mrs2003.60.
289. McCaffrey JP, Phaneuf MW, Madsen LD. Surface damage formation during ion-beam thinning of samples for transmission electron microscopy. Ultramicroscopy. 2001;87(3):97-104. doi:https://doi.org/10.1016/S0304-3991(00)00096-6.
290. Kamino T, Yaguchi T, Kuroda Y, Ohnishi T, Ishitani T, Miyahara Y, et al. Evaluation of TEM samples of an Mg-Al alloy prepared using FIB milling at the operating voltages of 10 kV and 40 kV. Journal of Electron Microscopy. 2004;53(5):459-63. doi:10.1093/jmicro/dfh058.
291. Wang Z, Kato T, Hirayama T, Kato N, Sasaki K, Saka H. Surface damage induced by focused-ion-beam milling in a Si/Si p–n junction cross-sectional specimen. Applied Surface Science. 2005;241(1):80-6. doi:https://doi.org/10.1016/j.apsusc.2004.09.092.

292. Rohde SL, Hultman L, Wong MS, Sproul WD. Dual-unbalanced magnetron deposition of TiN films. Surface and Coatings Technology. 1992;50(3):255-62. doi:https://doi.org/10.1016/0257-8972(92)90009-Y.
293. Ikeda T, Kawate Y, Hirai Y. Formation of cubic boron nitride films by arc-like plasma-enhanced ion plating method. Journal of Vacuum Science & Technology A. 1990;8(4):3168-74. doi:10.1116/1.576602.
294. TEER Coatings LtD. 7. Basic coating principles for good practice. UDP 650-4 DIFFUSION PUMP RF & DC POWER SUPPLY PLATING SYSTEM - Instruction Manual. Worcestershire2005.
295. Ohtake N, Hiratsuka M, Kanda K, Akasaka H, Tsujioka M, Hirakuri K, et al. Properties and Classification of Diamond-Like Carbon Films. Materials [Internet]. 2021; 14(2).
296. Choi YH, Huh JY, Baik YJ. Nucleation retardation of cubic boron nitride films caused by the addition of oxygen in argon-nitrogen sputtering gas. Diamond and Related Materials. 2021;120:108694. doi:https://doi.org/10.1016/j.diamond.2021.108694.
297. Mirkarimi PB, McCarty KF, Cardinale GF, Medlin DL, Ottesen DK, Johnsen HA. Substrate effects in cubic boron nitride film formation. Journal of Vacuum Science & Technology A. 1996;14(1):251-5. doi:10.1116/1.579928.
298. Hori S, Niibe M, Kotaka T, Fujii K, Yoshiki K, Namazu T, et al. X-ray Absorption Studies on the Growth Process of Radio-Frequency-Magnetron-Sputtered Boron Nitride Films: Effects of Bias Voltage and Substrate Temperature. Japanese Journal of Applied Physics. 2013;52(4R):045602. doi:10.7567/JJAP.52.045602.
299. Lehtinen O, Dumur E, Kotakoski J, Krasheninnikov AV, Nordlund K, Keinonen J. Production of defects in hexagonal boron nitride monolayer under ion irradiation. Nuclear Instruments and Methods in Physics Research Section B: Beam Interactions with Materials and Atoms. 2011;269(11):1327-31. doi:https://doi.org/10.1016/j.nimb.2010.11.027.
300. Mattox DM. 7.2.1 Bombardment Effects on Surfaces. Handbook of Physical Vapor Deposition (PVD) Processing (2nd Edition): Elsevier; 2010. p. 239-42.
301. Jagielski J, Khanna AS, Kucinski J, Misra DS, Onate JI, Racolta P, et al. Surface modification of materials by ion implantations for industrial and medical applications. Vienna, Austria: International Atomic Energy Agency; 2000.
302. Friedmann TA, McCarty KF, Klaus EJ, Barbour JC, Clift WM, Johnsen HA, et al. Pulsed laser deposition of BN onto silicon (100) substrates at 600 °C. Thin Solid Films. 1994;237(1):48-56. doi:https://doi.org/10.1016/0040-6090(94)90237-2.
303. Kaltofen R, Sebald T, Weise G. Ion bombardment diagnostics in a nitrogen RF magnetron sputtering discharge. Surface and Coatings Technology. 1997;97(1):131-9. doi:https://doi.org/10.1016/S0257-8972(97)00396-4.
304. Major GH, Fairley N, Sherwood PMA, Linford MR, Terry J, Fernandez V, et al. Practical guide for curve fitting in x-ray photoelectron spectroscopy. Journal of Vacuum Science & Technology A. 2020;38(6):061203. doi:10.1116/6.0000377.
305. Fairley N. CasaXPS Manual Rev 1.2. Casa Software LtD. 2009.
306. Boyd KJ, Marton D, Todorov SS, Al-Bayati AH, Kulik J, Zuhr RA, et al. Formation of C–N thin films by ion beam deposition. Journal of Vacuum Science & Technology A. 1995;13(4):2110-22. doi:10.1116/1.579528.
307. Chen X, Wang X, Fang D. A review on C1s XPS-spectra for some kinds of carbon materials. Fullerenes, Nanotubes and Carbon Nanostructures. 2020;28(12):1048-58. doi:10.1080/1536383X.2020.1794851.
308. Lopez S, Dunlop HM, Benmalek M, Tourillon G, Wong M-S, Sproul WD. XPS, XANES and ToF-SIMS Characterization of Reactively Magnetron-sputtered Carbon Nitride Films. Surface and Interface Analysis. 1997;25(5):315-23. doi:https://doi.org/10.1002/(SICI)1096-9918(199705)25:5<315::AID-SIA238>3.0.CO;2-S.

309. Palacio C, Gómez-Aleixandre C, Díaz D, García MM. Carbon nitride thin films formation by N_2+ ion implantation. Vacuum. 1997;48(7):709-13. doi:https://doi.org/10.1016/S0042-207X(97)00036-5.
310. Keunecke M, Wiemann E, Weigel K, Park ST, Bewilogua K. Thick c-BN coatings – Preparation, properties and application tests. Thin Solid Films. 2006;515(3):967-72. doi:https://doi.org/10.1016/j.tsf.2006.07.057.
311. Stein C, Keunecke M, Bewilogua K, Chudoba T, Kölker W, den Berg Hv. Cubic boron nitride based coating systems with different interlayers for cutting inserts. Surface and Coatings Technology. 2011;205:S103-S6. doi:https://doi.org/10.1016/j.surfcoat.2011.03.016.
312. Park S-T, Han J-G, Keunecke M, Lee K. Mechanical and structural properties of multilayer c-BN coatings on cemented carbide cutting tools. International Journal of Refractory Metals and Hard Materials. 2017;65:52-6. doi:https://doi.org/10.1016/j.ijrmhm.2016.11.009.
313. Keunecke M, Bewilogua K, Wiemann E, Weigel K, Wittorf R, Thomsen H. Boron containing combination tool coatings—characterization and application tests. Thin Solid Films. 2006;494(1):58-62. doi:https://doi.org/10.1016/j.tsf.2005.08.204.
314. Li CX, Bell T. Corrosion properties of active screen plasma nitrided 316 austenitic stainless steel. Corrosion Science. 2004;46(6):1527-47. doi:https://doi.org/10.1016/j.corsci.2003.09.015.
315. Kim HS, Park JK, Lee WS, Baik YJ. Variation of residual stress in cubic boron nitride film caused by hydrogen addition during unbalanced magnetron sputtering. Thin Solid Films. 2011;519(22):7871-4. doi:https://doi.org/10.1016/j.tsf.2011.06.092.
316. Ko J-S, Park J-K, Lee W-S, Huh J-Y, Baik Y-J. Effect of radio-frequency electric power applied to a boron nitride unbalanced magnetron sputter target on the deposition of cubic boron nitride thin film. Metals and Materials International. 2013;19(6):1317-21. doi:10.1007/s12540-013-6028-5.
317. Tsuda O, Tatebayashi Y, Yamada-Takamura Y, Yoshida T. Mass and energy measurements of the species responsible for cBN growth in rf bias sputter conditions. Journal of Vacuum Science & Technology A. 1997;15(6):2859-63. doi:10.1116/1.580840.
318. Jankowski AF, Hayes JP, Makowiecki DW, McKeman MA, editors. Formation of cubic boron-nitride by the reactive sputter deposition of boron. International conference on metallurgical coatings and thin films (ICMCTF-24); 1997: Lawrence Livermore National Lab.
319. Yang S, Camino D, Jones AHS, Teer DG. Deposition and tribological behaviour of sputtered carbon hard coatings. Surface and Coatings Technology. 2000;124(2):110-6. doi:https://doi.org/10.1016/S0257-8972(99)00634-9.
320. Cooke KE, Bamber M, Bassas J, Boscarino D, Derby B, Figueras A, et al. Multilayer nitride coatings by closed field unbalanced magnetron sputter ion plating. Surface and Coatings Technology. 2003;162(2):276-87. doi:https://doi.org/10.1016/S0257-8972(02)00668-0.
321. Kok YN, Hovsepian PE, Luo Q, Lewis DB, Wen JG, Petrov I. Influence of the bias voltage on the structure and the tribological performance of nanoscale multilayer C/Cr PVD coatings. Thin Solid Films. 2005;475(1):219-26. doi:https://doi.org/10.1016/j.tsf.2004.08.042.
322. Zhu PW, He Z, Zhao YN, Li DM, Liu HW, Zou GT. Preparation of high-pressure phase boron nitride films by physical vapor deposition. Journal of Vacuum Science & Technology A. 2002;20(3):622-4. doi:10.1116/1.1458948.
323. Yang X, Li H, Li Y, Lü X, Gao S, Zhu P, et al. Dependence of RF power on the phase transformation for boron nitride films deposited on graphite at room temperature. Journal of Crystal Growth. 2009;311(14):3716-20. doi:https://doi.org/10.1016/j.jcrysgro.2009.04.041.

324. Batsanov SS, Kopaneva LJ, Lazareva EV, Kulikova IM, Barinsky RL. On the Nature of Boron Nitride E-Phase. Propellants, Explosives, Pyrotechnics. 1993;18(6):352-5. doi:https://doi.org/10.1002/prep.19930180608.
325. H J T. Ellingham. Reducibility of Oxides and Sulphides in the Metallurgical Processes. Journal of the Society of Chemical Industry. 1944;63(5):125-60. doi:https://doi.org/10.1002/jctb.5000630501.
326. S M. Howard. Ellingham Diagram Selected Oxides: Part 1. In: Standard Gibb's Energies of Formation for Oxides, editor. South Dakota: South Dakota School of Mines and Technology; 2006.
327. Balart MJ, Patel JB, Gao F, Fan Z. Grain Refinement of Deoxidized Copper. Metallurgical and Materials Transactions A. 2016;47(10):4988-5011. doi:10.1007/s11661-016-3671-8.
328. Stowell M, Müller J, Ruske M, Lutz M, Linz T. RF-superimposed DC and pulsed DC sputtering for deposition of transparent conductive oxides. Thin Solid Films. 2007;515(19):7654-7. doi:https://doi.org/10.1016/j.tsf.2006.11.166.
329. Schmidt S, Czigány Z, Wissting J, Greczynski G, Janzén E, Jensen J, et al. A comparative study of direct current magnetron sputtering and high power impulse magnetron sputtering processes for CN_x thin film growth with different inert gases. Diamond and Related Materials. 2016;64:13-26. doi:https://doi.org/10.1016/j.diamond.2016.01.009.
330. Park HS, Kappl H, Lee KH, Lee JJ, Jehn HA, Fenker M. Structure modification of magnetron-sputtered CrN coatings by intermediate plasma etching steps. Surface and Coatings Technology. 2000;133-134:176-80. doi:https://doi.org/10.1016/S0257-8972(00)00960-9.
331. Matsubara K, Danno M, Inoue M, Honda Y, Yoshida N, Abe T. Characterization of titanium particles treated with N_2 plasma using a barrel-plasma-treatment system. Physical Chemistry Chemical Physics. 2013;15(14):5097-107. doi:10.1039/C3CP44434A.
332. Speidel A, Gargalis L, Ye J, Matthews MJ, Spierings A, Hague R, et al. Chemical recovery of spent copper powder in laser powder bed fusion. Additive Manufacturing. 2022:102711. doi:https://doi.org/10.1016/j.addma.2022.102711.

10. Appendix

Table 33 - Near surface compositions of Cu powders via XPS in two size distributions uncoated and coated with Zn, summarised in Figure 38.

Sample	Concentration (at%)			
	O 1s	C 1s	Zn 2p	Cu 2p
Cu-Fine	53.0 ± 1.1	26.1 ± 1.2	0.0	20.9 ± 0.8
Cu-Zn-Fine	36.0 ± 1.2	25.2 ± 1.3	35.1 ± 1.1	3.7 ± 1.7
Cu-Coarse	46.7 ± 1.0	32.9 ± 1.2	0.0	20.4 ± 0.8
Cu-Zn-Coarse	33.6 ± 0.8	24.5 ± 0.9	40.4 ± 0.8	1.5 ± 0.5

Table 34 - EDX data for the Ag-Ti coated powders, summarised in Figure 43.

Sample	Element Concentration (wt%)			
	Ag	Ti	O	C
Ag-Ti_50W_3h	95.3 ± 2.1	1.3 ± 1.2	1.6 ± 0.7	1.7 ± 0.5
Ag-Ti_100W_1h	96.6 ± 1.5	0.3 ± 0.3	1.0 ± 0.4	1.9 ± 0.8
Ag-Ti_50W_3h_Dried	95.5 ± 1.0	1.1 ± 0.5	1.6 ± 0.5	1.8 ± 0.6

Table 35 - Near surface compositions of Ag powders via XPS coated with Ti for two parameter sets, summarised in Figure 43.

Sample	Elemental Concentrations (at%)			
	Ag 3d	Ti 2p	O 1s	C 1s
Ag-999	38.1 ± 2.4	0.0	15.0 ± 2.7	46.9 ± 3.3
Ag-Ti_50W_3h	14.8 ± 0.4	11.0 ± 0.5	37.4 ± 1.0	36.8 ± 1.1
Ag-Ti_100W_1h	19.9 ± 1.2	9.1 ± 1.6	29.0 ± 2.5	42.0 ± 3.0

Table 36 - Point EDX concentrations for multiple particles from 316L-Cu-Coarse_rot, summarised in Figure 47.

Region	Concentration (wt%)								
	Fe	Cr	Ni	Cu	C	O	Mo	Mn	Si
Top Centre	43.5 ± 22.0	12.8 ± 6.4	8.7 ± 4.7	37.6 ± 35.7	5.8 ± 1.6	0.9 ± 0.4	1.6 ± 0.9	0.7 ± 0.3	0.6 ± 0.3
Mixed	42.9 ± 14.5	12.8 ± 4.3	8.4 ± 3.1	25.9 ± 21.8	6.0 ± 2.2	1.1 ± 0.5	1.7 ± 0.6	0.6 ± 0.2	0.6 ± 0.2

Table 37 - EDX point concentrations gathered from multiple particles of 316L-Cu-Fine_rot, summarised in Figure 48.

Region	Concentration (wt%)								
	Fe	Cu	Cr	Ni	C	O	Mo	Mn	Si
Area 1.	41.4 ± 12.9	29.8 ± 20.6	12.5 ± 3.5	7.8 ± 2.7	5.0 ± 1.8	1.0 ± 0.3	1.5 ± 0.5	0.7 ± 0.2	0.5 ± 0.2
Area 2.	50.4 ± 7.8	15.3 ± 11.3	14.9 ± 2.1	10.2 ± 1.5	5.1 ± 2.3	0.7 ± 0.1	1.9 ± 0.2	0.8 ± 0.1	0.7 ± 0.1
Mixed	55.4 ± 10.3	4.4 ± 3.6	16.2 ± 2.8	10.6 ± 2.2	4.2 ± 1.4	0.7 ± 0.2	1.9 ± 0.6	0.8 ± 0.2	0.6 ± 0.2

Table 38 - Full EDX point data from 316L-Cu-Coarse_vib presented in Figure 50.

Region	Element Concentration (wt %)					
	Fe	Cr	Ni	Cu	C	O
Top Middle	58.0 ± 3.8	17.2 ± 1.1	11.6 ± 1.1	7.6 ± 4.3	2.8 ± 2.7	0.6 ± 0.3
Top left	48.6 ± 10.3	15.1 ± 4.1	9.0 ± 2.6	20.3 ± 14.4	4.0 ± 4.6	0.7 ± 0.5
Middle bulk	56.0 ± 5.7	16.5 ± 1.7	11.4 ± 1.4	6.3 ± 4.2	5.8 ± 5.7	0.7 ± 0.2
Mixed	55.6 ± 8.0	16.3 ± 2.2	11.3 ± 2.0	9.0 ± 6.6	2.9 ± 2.7	0.7 ± 0.2

Table 39 - Full EDX point data for multiple particles from 316L-Cu-Fine_vib, summarised in Figure 51.

Region	Element concentration (wt%)								
	Fe	Cr	Ni	Cu	C	O	Mo	Mn	Si
Top centre	57.7 ± 2.2	17.1 ± 0.9	11.6 ± 0.5	4.3 ± 2.5	4.6 ± 1.5	0.8 ± 0.2	2.2 ± 0.2	0.9 ± 0.1	0.8 ± 0.2
Top left	57.2 ± 2.7	16.8 ± 1.1	11.4 ± 0.7	4.9 ± 3.4	5.4 ± 1.9	0.7 ± 0.2	2.0 ± 0.4	0.9 ± 0.1	0.7 ± 0.2
Mixed	57.2 ± 2.5	16.8 ± 0.6	11.2 ± 0.6	4.8 ± 3.2	5.4 ± 1.6	0.9 ± 0.2	2.1 ± 0.2	0.9 ± 0.1	0.7 ± 0.1

Table 40 - EDX point data for multiple particles of 316L-Cu-Coarse_rot_dried, summarised in Figure 52.

Region	Element Concentration (wt%)								
	Fe	Cr	Ni	Cu	C	O	Mo	Mn	Si
Top Centre	55.1 ± 2.6	16.2 ± 0.7	11.1 ± 0.7	10.8 ± 3.7	2.3 ± 1.8	0.6 ± 0.2	2.1 ± 0.2	0.9 ± 0.1	0.7 ± 0.1
Mixed	55.9 ± 4.2	16.6 ± 1.1	11.3 ± 0.8	9.4 ± 5.3	2.2 ± 1.2	0.7 ± 0.2	2.3 ± 0.5	0.9 ± 0.1	0.8 ± 0.2

Table 41 - EDX point data for multiple particles of 316L-Cu-Fine_rot_dried, summarised in Figure 53.

Region	Element Concentration (wt%)								
	Fe	Cu	Cr	Ni	C	O	Mo	Mn	Si
Top surface	40.7 ± 16.0	31.7 ± 24.6	12.1 ± 4.5	7.8 ± 3.3	3.9 ± 1.1	0.8 ± 0.4	1.5 ± 0.6	0.6 ± 0.2	0.5 ± 0.2
Mixed	58.1 ± 2.3	3.5 ± 2.5	17.0 ± 0.6	11.6 ± 0.7	5.2 ± 1.5	0.9 ± 0.2	2.2 ± 0.1	0.9 ± 0.0	0.8 ± 0.1

Table 42 - Full EDX point data for multiple particles of 316L-BN_24h_rot_dried, summarised in Figure 54.

Region	Element Concentration (wt%)									
	Fe	Cr	Ni	B	N	C	O	Mo	Mn	Si
Top surface	59.0 ± 1.2	16.3 ± 0.2	13.4 ± 1.1	4.6 ± 0.4	0.1 ± 0.0	2.4 ± 0.6	0.5 ± 0.1	2.2 ± 0.1	0.9 ± 0.2	0.7 ± 0.1
Mix	56.8 ± 3.5	16.5 ± 1.0	13.7 ± 1.1	6.0 ± 2.2	0.1 ± 0.1	2.2 ± 1.0	0.5 ± 0.1	2.4 ± 1.0	1.0 ± 0.2	0.8 ± 0.2

Table 43 - Full EDX point scan data from 316L-BN_48h_rot_dried, summarised in Figure 55.

Region	Element Concentration (wt%)									
	Fe	Cr	Ni	B	N	C	O	Mo	Mn	Si
Top surface - multiple particles	57.1 ± 1.3	16.2 ± 0.5	13.9 ± 1.0	5.6 ± 0.4	0.1 ± 0.0	2.4 ± 0.7	0.6 ± 0.1	2.4 ± 0.2	1.0 ± 0.2	0.7 ± 0.1
Top surface - single particle	59.5 ± 0.3	18.2 ± 0.1	12.9 ± 0.4	0.0 ± 0.0	0.4 ± 0.1	4.0 ± 0.1	0.8 ± 0.0	1.9 ± 0.1	1.5 ± 0.1	0.6 ± 0.0

Table 44 - Full EDX data for the regions of Cr interlayer deposited on 316L shown in Figure 73.

	Element Concentration (at%)							
Region	Fe	Cr	Ni	O	C	Mo	Si	S
Area a/b	36.7 ± 0.9	48.2 ± 0.3	5.2 ± 0.5	4.3 ± 0.3	4.3 ± 0.6	0.8 ± 0.0	0.5 ± 0.1	0
Point 2.	36.4 ± 0.4	46.7 ± 0.9	5.3 ± 0.9	4.6 ± 0.0	5.7 ± 1.8	0.8 ± 0.1	0.5 ± 0.0	0
Area 3.	23.5 ± 5.0	49.1 ± 0.5	2.8 ± 0.3	4.3 ± 0.4	8.3 ± 0.4	0.6 ± 0.3	0.4 ± 0.1	10.9 ± 4.6

Table 45 - Full EDX data for the Cr interlayer deposited on Si substrate and shown in Figure 75.

	Element Concentration (at%)					
Region	Si	Cr	O	C	Ar	Al
Area a/b	69.0 ± 0.4	23.8 ± 0.2	2.6 ± 0.1	4.5 ± 0.6	0.1 ± 0.0	0
Point 2.	28.2 ± 4.2	23.3 ± 0.5	6.5 ± 0.6	6.6 ± 0.2	0.1 ± 0.0	35.3 ± 4.1
Area 3.	71.2 ± 0.5	24.1 ± 0.1	3.2 ± 0.2	1.5 ± 0.4	0	0

Table 46 - Full EDX data for the Cr-CrC-C coating deposited on 316L summarised in Figure 77.

	Element Concentration (at%)							
Region	Fe	Cr	Ni	O	C	Mo	Si	N
Area a/b	13.6 ± 0.5	55.2 ± 0.4	3.0 ± 1.2	2.4 ± 0.3	24.3 ± 0.2	0.4 ± 0.1	0.2 ± 0.1	1.7 ± 0.1
Point 2.	12.3 ± 0.3	54.3 ± 0.8	1.2 ± 0.3	1.8 ± 0.5	28.0 ± 0.5	0.3 ± 0.2	0	2.0 ± 0.4
Area 3.	13.3 ± 0.2	55.8 ± 0.6	0.9 ± 0.1	2.6 ± 0.4	25.0 ± 0.6	0.4 ± 0.1	0.3 ± 0.1	1.5 ± 0.4

Table 47 - Full EDX data for the Cr-CrC-C coating deposited on Si summarised in Figure 79.

	Element Concentration (at%)					
Region	Si	Cr	O	C	N	Ar
Area a/b	41.5 ± 0.6	31.1 ± 0.6	1.6 ± 0.2	23.8 ± 1.2	1.8 ± 0.1	0.1 ± 0.1
Point 2.	20.9 ± 3.1	18.7 ± 1.5	3.3 ± 0.1	51.1 ± 3.9	5.4 ± 0.4	0
Area 3.	41.7 ± 1.0	30.9 ± 1.0	1.6 ± 0.2	23.9 ± 1.6	1.9 ± 0.5	0.1 ± 0.1

Table 48 - Full EDX data for the Cr-CrC-C-BCN interlayer deposited onto 316L substrate summarised in Figure 81.

	Element Concentration (at%)								
Region	Fe	Cr	C	N	B	Mo	O	Ni	Al
Area a/b	6.7 ± 0.1	32.7 ± 0.7	47.3 ± 0.5	12.2 ± 0.1	0	0.1 ± 0.1	0.3 ± 0.2	0.1 ± 0.1	0
Area 2.	4.2 ± 1.7	20.3 ± 8.4	39.4 ± 6.0	8.4 ± 2.6	26.8 ± 19.0	0.1 ± 0.0	0.2 ± 0.2	0.3 ± 0.0	0
Point 3.	3.4 ± 0.5	24.2 ± 0.4	47.3 ± 1.2	12.5 ± 0.3	0	0	2.0 ± 0.3	0.4 ± 0.5	9.6 ± 2.4

Table 49 - Full EDX data for the Cr-CrC-C-BCN interlayer deposited on Si substrate, summarised in Figure 83.

	Element Concentration (at%)						
Region	Si	Cr	O	C	N	B	Ar
Area a/b	19.6 ± 0.1	20.1 ± 0.0	0.3 ± 0.1	48.7 ± 0.2	10.9 ± 0.4	0	0.4 ± 0.0
Point 2.	20.9 ± 0.6	5.1 ± 1.2	47.1 ± 1.7	22.1 ± 0.7	0	0	0.3 ± 0.0
Point 3.	100 ± 0.0	0	0	0	0	0	0
Area 4.	19.7 ± 0.1	20.3 ± 0.3	0.2 ± 0.2	48.5 ± 0.2	10.9 ± 0.1	0	0.3 ± 0.0

Table 50 – Full data of EDX compositions of areas and points highlighted for Coating 5 shown in Figure 90.

	Element Concentration (at%)								
Region	B	N	Cr	C	Ar	O	Fe	Ni	Si
Area a)	17.2	15.4	36.1	26.3	0.6	2.4	1.7	<1	0.0
Point 1	30.1	21.2	25.9	17.9	0.8	2.5	1.5	<1	0.0
Area c)	21.1	26.4	27.0	19.6	1.2	2.9	N/A	N/A	1.0
Point 2	30.6	38.5	6.4	13.3	0.6	10.0	N/A	N/A	0.1
Area 3	18.0	26.7	29.6	19.6	1.2	3.2	N/A	N/A	1.1

Table 51 - EDX composition of selected points and area in image of Coating 6 on 316L in Figure 91 d).

	Element Concentration (at%)							
Region	B	N	O	C	Cr	Fe	Ar	Ca
Point 1.	33.0	39.3	14.1		1.3	2.6	7.4	2.4
Area 2.	43.7	43.0	2.5		1.2	2.6	7.0	0
Point 3.	39.6	43.9	8.2		1.2	2.9	4.2	0

Table 52 - Full EDX data for the two regions of Coating 7 applied on 316L mapped in Figure 93.

	Element Concentration (at%)						
Region	B	N	O	C	Cr	Fe	Ar
Area c)	43.3	42.1	4.8	0.0	1.3	2.8	5.0
Area d)	41.6	42.5	4.6	0.0	3.0	4.0	3.8
Point 3.	42.1	39.4	11.2	0	1.5	2.9	2.5

Table 53 - Full EDX data for the regions of multilayer BN coating deposited at 60 V, on 316L and Si, summarised in Figure 112 .

	Element Concentration (at%)							
Region	B	N	O	C	Cr	Fe	Si	Ar
316L - Map Area c/d	0.0	8.3	17.0	39.5	29.3	5.2	0.2	0.4
Si - Map Area a/b	0.0	6.0	20.6	35.1	18.2	N/A	19.8	0.2
Si - Area EDX a/b	0.0	6.3	36.1	26.5	15.4	N/A	15.4	0.3
Si - Area 1.	15.5	4.3	49.6	14.3	8.3	N/A	7.9	0.2
Si - Area 2.	0.0	6.6	5.7	43.9	21.5	N/A	21.9	0.3
Si - Point 3.	30.0	2.2	38.7	9.0	10.8	N/A	9.0	0.3

Table 54 - Full EDX data for the multilayer BN coating deposited at 100 V onto 316L and silicon, summarised in Figure 118.

	Element Concentration (at%)							
Region	B	N	O	C	Cr	Fe	Ar	Si
Area a)	24.4	16.6	7.4	24.2	23.7	2.8	0.9	0.0
Area b)	21.2	15.8	7.3	24.0	27.4	3.2	1.0	0.0
Area c)	16.1	18.2	8.3	23.2	19.5	0.0	0.8	13.9
Area d)	14.1	19.2	8.6	23.3	19.7	0.0	0.9	14.2
Area e)	27.8	15.1	6.9	21.2	25.1	3.0	0.9	0.0
Area f)	28.1	14.9	6.3	21.5	25.5	2.9	0.9	0.0

Table 55 - Full EDX data for the multilayer BN coating deposited at 180-150 V bias onto 316L, data summarised in Figure 124.

	Element Concentration (at%)						
Region	O	B	N	Cr	Fe	Ar	C
Area a/b	5.4 ± 0.1	0	10.7 ± 0.0	32.5 ± 0.2	5.4 ± 0.1	0.5 ± 0.0	44.7 ± 0.1
Area 2.	3.6 ± 0.3	0	10.9 ± 0.1	34.0 ± 0.1	5.7 ± 0.3	0.5 ± 0.0	45.0 ± 0.3
Area 3.	38.4 ± 1.5	21.5 ± 0.8	5.2 ± 0.2	10.2 ± 0.2	1.2 ± 0.1	0.3 ± 0.0	23.1 ± 0.8
Points	30.0 ± 3.2	24.6 ± 2.5	3.7 ± 0.8	20.6 ± 3.9	2.6 ± 0.6	0.4 ± 0.1	18.2 ± 3.6

Table 56 - Full EDX data for the multilayer BN coating deposited at 180-150 V, with high gas flows onto 316L, summarised in Figure 129.

	Element Concentration (at%)						
Region	O	B	C	N	Cr	Fe	Ar
Area a/b	28.1 ± 4.1	0	41.5 ± 7.1	17.4 ± 2.9	24.7 ± 4.4	2.2 ± 0.6	0.3 ± 0.0
Area 2.	16.5 ± 0.1	0	43.6 ± 1.0	18.6 ± 0.6	25.8 ± 0.3	2.1 ± 0.4	0.3 ± 0.0
Area 3.	62.3 ± 0.6	33.7 ± 0.8	0	3.6 ± 0.4	0	0	0

Table 57 - Full EDX data for the multilayer BN coating applied to 316L at 180-150V, with high gas flows and modified pulse parameters, summarised in Figure 137.

	Element Concentration (at%)							
Region	O	B	C	N	Cr	Fe	Ar	Ca
Area a/b	18.0 ± 0.2	33.0 ± 0.3	13.8 ± 0.1	24.3 ± 0.1	9.8 ± 0.1	0.5 ± 0.0	0.6 ± 0.0	N/A
Point 2.	29.2 ± 3.9	24.3 ± 1.2	13.1 ± 0.9	19.9 ± 0.5	6.8 ± 3.1	0.5 ± 0.2	0.3 ± 0.1	5.9 ± 1.6
Area 3.	18.0 ± 0.2	33.2 ± 0.5	13.7 ± 0.2	24.1 ± 0.4	9.9 ± 0.1	0.5 ± 0.1	0.6 ± 0.0	N/A

Table 58 - Full EDX data for the multilayer BN coating applied to Si at 180-150V, with high gas flows and modified pulse parameters, summarised in Figure 139.

	Element Concentration (at%)								
Region	B	N	O	C	Cr	Si	Ar	Ca	P
Area a/b	32.0 ± 0.2	24.0 ± 0.2	18.5 ± 0.2	10.6 ± 0.4	9.3 ± 0.0	4.6 ± 0.1	0.7 ± 0.0	N/A	N/A
Point 2.	0.0	9.5 ± 0.6	57.3 ± 0.9	4.9 ± 0.7	6.5 ± 0.8	2.9 ± 0.3	1.0 ± 0.0	11.7 ± 0.5	6.2 ± 0.2
Area 3.	32.2 ± 0.8	24.0 ± 0.4	18.4 ± 0.2	10.7 ± 0.1	9.4 ± 0.1	4.6 ± 0.0	0.7 ± 0.0	N/A	N/A

Table 59 - Full EDX data for the BN multilayer with increased gas flow and pulse modification, applied to 316L, after 19 days, summarised in Figure 142.

	Element Concentration (at%)							
Region	O	B	C	N	Cr	Fe	Ar	Al
Point 1.	56.1 ± 3.5	34.1 ± 4.3	1.7 ± 0.8	2.9 ± 0.4	4.5 ± 2.7	0.5 ± 0.3	0.1 ± 0.1	0
Area 2.	19.0 ± 0.0	5.4 ± 0.1	36.0 ± 0.2	18.6 ± 0.2	19.3 ± 0.1	1.3 ± 0.0	0.4 ± 0.0	0
Point 3.	45.8 ± 6.3	29.9 ± 11.1	0.9 ± 1.2	1.6 ± 0.2	10.7 ± 10.9	1.0 ± 0.9	0	9.6 ± 9.2
Point 4.	12.7 ± 1.8	8.9 ± 10.6	33.4 ± 6.3	12.6 ± 4.2	40.4 ± 8.6	5.4 ± 2.4	0.4 ± 0.1	0
Area e/f	38.9 ± 0.3	20.9 ± 0.2	19.7 ± 0.2	11.6 ± 0.0	8.2 ± 0.0	0.6 ± 0.1	0.2 ± 0.0	0